COLLEGE DOCTORAL BRETAGNE — ESPACES SOCIETES CIVILISATIONS

UNIVERSITÉ RENNES 2

THESE DE DOCTORAT DE

L'UNIVERSITE RENNES 2

ECOLE DOCTORALE N° 645
Espaces, Sociétés, Civilisations
Spécialité : *Géographie*

Par

Quentin Demarquet

Long-term monitoring of Ramsar wetlands using the Landsat archive

Thèse présentée et soutenue à Rennes, le 29 Janvier 2025

Unité de recherche : UMR LETG-CNRS 6554

Rapporteurs avant soutenance :

Valery Gond	Directeur de recherche HDR, CIRAD
Julien Andrieu	Maître de conférences HDR, Université Côte d'Azur

Composition du Jury :

Examinateurs :	Aurélie Davranche	Maîtresse de conférences, Université d'Angers
	Agnès Begué	Directrice de recherche HDR, CIRAD
	Valery Gond	Directeur de recherche HDR, CIRAD
	Julien Andrieu	Maître de conférences HDR, Université Côte d'Azur
Dir. de thèse :	Laurence Hubert-Moy	Professeure des universités HDR, Université Rennes 2 - LETG
Co-dir. de thèse :	Simon Dufour	Maître de conférences HDR, Université Rennes 2 - LETG

COLLEGE DOCTORAL BRETAGNE | ESPACES SOCIETES CIVILISATIONS

UNIVERSITÉ RENNES 2

THESE DE DOCTORAT DE

L'UNIVERSITE RENNES 2

ECOLE DOCTORALE N° 645
Espaces, Sociétés, Civilisations
Spécialité : *Géographie*

Par

Quentin Demarquet

Long-term monitoring of Ramsar wetlands using the Landsat archive

Thèse présentée et soutenue à Rennes, le 29 Janvier 2025

Unité de recherche : UMR LETG-CNRS 6554

Rapporteurs avant soutenance :

Valery Gond	Directeur de recherche HDR, CIRAD
Julien Andrieu	Maître de conférences HDR, Université Côte d'Azur

Composition du Jury :

Examinateurs :	Aurélie Davranche	Maîtresse de conférences, Université d'Angers
	Agnès Begué	Directrice de recherche HDR, CIRAD
	Valery Gond	Directeur de recherche HDR, CIRAD
	Julien Andrieu	Maître de conférences HDR, Université Côte d'Azur
Dir. de thèse :	Laurence Hubert-Moy	Professeure des universités HDR, Université Rennes 2 - LETG
Co-dir. de thèse :	Simon Dufour	Maître de conférences HDR, Université Rennes 2 - LETG

A mon père, mon grand-père et ma grand-mère

ACKNOWLEDGMENTS

Je tiens à remercier ma directrice de thèse Laurence Hubert-Moy pour son aide, son encadrement pédagogique et sa passion de la recherche, ainsi que pour m'avoir donné l'opportunité de faire cette thèse en m'accordant sa confiance depuis le début du master TELENVI. Merci également à mon co-directeur Simon Dufour pour ses conseils et ses analyses pertinentes sur les plans thématiques en particulier, mais également pour son écoute et son soutien.

Un grand merci à Sébastien Rapinel qui m'a apporté son aide et son soutien et qui a fortement participé à la réussite des travaux de cette thèse, aussi bien pour son appui sur les plans techniques, thématiques que rédactionnels.

Je remercie également les chercheur.es avec qui j'ai pu collaborer au cours des différents travaux, en particulier Samuel Corgne, Damien Arvor, Jean-Yves Barnagaud et Solène Crocci. Je tiens aussi à remercier Roselyne Billy pour son aide logistique et organisationnelle au cours des missions réalisées durant la thèse.

Un grand merci à Olivier Gore de l'Etablissement Public du Marais Poitevin pour avoir apporté son expertise et ses connaissances qui ont beaucoup contribué en termes d'interprétation sur les dynamiques d'habitats sur le Marais Poitevin.

Je n'oublie bien évidemment pas mes collègues du laboratoire qui de près ou de loin m'ont aidé et m'ont apporté leur soutien au cours du doctorat : Carl Bethuel, Charlotte Brabant, Gugliermo Fernandez-Garcia, Florian Guyard, Alexandre Guyot, Théo Le Saint, Mathilde Letard, Julien Pellen, Thibaut Peres, Théo Petitjean, Roberta Rigo, Roza Taouki, Paul Vrchovsky, ainsi que tous les autres qui je l'espèrent se reconnaitront ! Un merci spécial à Daria Jirku pour avoir eu l'opportunité de participer à sa thèse et qui m'a beaucoup intéressé.

Enfin, je remercie tout particulièrement ma famille et mes amis qui m'ont soutenu pendant cette aventure et m'ont permis de vivre de bons moments de décompression. Je n'aurai pas pu finir cette thèse sans vous. Un merci tout particulier à Marine, qui partage ma vie au quotidien, et qui m'a supporté durant les moments les meilleurs comme les plus difficiles.

Trugarez vras deoc'h holl !

LIST OF ACRONYMS

AI	*Artificial Intelligence*
ALOS	*Advanced Land Observing Satellite*
ANOVA	*Analysis Of Variance*
ARTMAP	*Adaptative Resonance Theory Neural Network*
ASTER	*Advanced Spaceborne Thermal Emission and Reflection*
AVHRR	*Advanced Very High-Resolution Radiometer*
AVNIR	*Advanced Visible and Near InfraRed*
BFAST	*Breaks For Additive Season and Trend*
CBD	*Convention on Biological Diversity*
CCDC	*Continuous Change Detection and Classification*
DEM	*Digital Elevation Model*
EBV	*Essential Biodiversity Variables*
ECV	*Essential Climate Variables*
ETM+	*Enhanced Thematic Mapper Plus*
EVI	*Enhanced Vegetation Index*
FAPAR	*Fraction of Absorbed Photosynthetically Active Radiation*
GBIF	*Global Biodiversity Information Facility*
GCOS	*Global Climate Observing System*
GEDI	*Global Ecosystem Dynamics Investigation*
GEE	*Google Earth Engine*
IRS-LISS	*Indian Remote-sensing Satellite – Linear Imaging Self-scanning Sensor*
ISODATA	*Iterative Self-Organizing Data Analysis Technique*
K-ELM	*Kernel-Extreme Learning Machine*
LASSO	*Least Absolute Shrinkage and Selection Operator*
LiDAR	*Light Detection and Ranging*
LSWI	*Land Surface Water Index*
LULC	*Land Use Land Cover*
mNDWI	*Modified Normalized Difference Water Index*
MLC	*Maximum Likelihood Classification*
MODIS	*Moderate Resolution Imaging Spectroradiometer*

MSS	*Multispectral Scanner*
NASA	*National Aeronautics and Space Administration*
NDWI	*Normalized Difference Water Index*
OLI	*Operational Land Imager*
OLS	*Ordinary Least Square*
PALSAR	*Phased Array L-band Synthetic Aperture Radar*
PRISMA	*Preferred Reporting Items for Systematic Reviews and Meta-Analyses*
RIRLS	*Robust Iteratively Reweighted Least Squares*
RS-EBV	*Remote Sensing – Enabled Biodiversity Variable*
RS-ECV	*Remote Sensing – Enabled Climate Variable*
SAR	*Synthetic Aperture Radar*
SDG	*Sustainable Development Goals*
SMMI	*Soil Moisture Monitoring Index*
SPOT	*Satellite*
SRTM	*Shuttle Radar Topography Mission*
SVM	*Support Vector Machine*
TIRS	*Thermal Infra-Red Sensor*
TM	*Thematic Mapper*
USGS	*United States Geological Survey*
WOS	*Web Of Science*

TABLE OF CONTENTS

GENERAL INTRODUCTION

Long described as unhealthy environments to which legends and superstitions were attributed, wetlands, located at the interface between terrestrial and aquatic environments, are now recognised as unique ecosystems of great socio-ecological interest. They are found all over the world, except Antarctica, and cover between 5 and 8% of the Earth's surface (Mitsch et al., 2013; Mitsch and Gosselink, 2015). These environments are defined differently depending on the region and legislation around the world (Gardner and Davidson, 2011). Internationally, the Ramsar Convention, adopted in 1971, defines wetlands as « *areas of swamp, fen, peat or water, whether natural or artificial, permanent or temporary, with water that is static or flowing, fresh, brackish or saline, including areas of marine water the depth of which does not exceed six metres at low tide* ». Wetlands therefore represent a significant diversity of coastal and continental habitats, ranging from mangroves to peat bogs, marshes and wet grasslands (Finlayson et al., 2018).

Wetlands are among the world's most threatened socio-ecosystems, with an estimated global loss of approximately 3.4 million km² since 1700. An acceleration of this decline has been observed since the mid-20th century, with annual losses estimated at between -1.3 and -2.2% per year globally (Davidson, 2014; Fluet-Chouinard et al., 2023). This decline is unevenly distributed around the world, and is particularly pronounced in Asia and Europe (Hu et al., 2017). The causes of wetland loss are twofold: anthropogenic, mainly due to the expansion of cropland and urbanisation (Davidson and Finlayson, 2018; Moomaw et al., 2018a), and climatic, due to the increase in temperature, changes in precipitation patterns and sea level rise observed in the context of global climate change (L. Chen et al., 2024; Lu and Xiao, 2024; Salimi et al., 2021). The loss of wetlands is associated with the degradation of the remaining wetlands, with changes in their structure (e.g., composition, fragmentation) and functions (e.g., reduced biodiversity, less effective filtering of pollutants) (Davis and Froend, 1999; Erwin, 2009; Ramsar Convention Secretariat, 2018).

These threats are critical given that wetlands perform numerous hydrological, biogeochemical and ecological functions that provide benefits to human societies, such as flood attenuation, carbon sequestration or supporting habitats for biodiversity (Maltby, 2018; Ramsar Convention Secretariat, 2018). For example, the value of services provided by wetlands globally exceeds that of tropical forests by almost five times (Ramsar Convention Secretariat, 2018). These services are tending to decline as wetlands are reduced and degraded, leading major risks to the well-being and health of human populations at large scales (Millennium Ecosystem Assessment, 2005). It is therefore essential to monitor wetlands to describe their spatio-temporal dynamics, both in terms of structure and function, and to characterise their ecological status (Strauch et al., 2022a).

Wetland monitoring is defined in this thesis as a means of producing spatiotemporal indicators that can be used to characterise their spatial and long-term evolution. The high variability of the spatio-temporal dynamics of wetlands, particularly at a fine spatial scale, leads to difficulties in carrying out regular monitoring and characterising these ecosystems using approaches based solely on in situ observation and measurement, particularly when large wetlands are involved (Rebelo et al., 2017). Remote sensing, which makes it possible to obtain information about an object on the Earth's surface from sensors placed on mobile platforms such as satellites or drones, largely alleviates these difficulties, while saving human and financial resources (Corbane et al., 2015; Vanden Borre et al., 2011). It has been particularly used in recent decades to monitor wetlands around the world (Mahdavi et al., 2018), using optical satellite images (e.g. C. Chen et al., 2024; Jie and Wang, 2024; Yang et al., 2020) and radar (e.g. Betbeder et al., 2015; Huang et al., 2024; Zhang et al., 2024), or optical images acquired by UAVs (e.g. Doughty et al., 2021; Fu et al., 2024; Van Alphen et al., 2024). However, the vast majority of studies using these data have focused on the analysis of a single image date or images acquired over relatively short time periods, favouring the spatial resolution of the images over the repetitiveness of the observation. However, monitoring wetlands over the long term (defined here as an observation period of several decades) makes it possible to describe the historical dynamics of these ecosystems and identify the associated factors of change (Gallant, 2015).

It is particularly important to monitor wetlands over the long term, both to identify the pressures on these environments and to implement and evaluate conservation and restoration measures (Ghoddousi et al., 2022; Gillespie et al., 2015). At the international level, conservation and restoration targets to stabilise and mitigate biodiversity degradation have been defined in conventions and treaties such as the Ramsar Convention on the Conservation and Wise Use of Wetlands, the Convention on Biological Diversity (CBD) and the United Nations Sustainable Development Goals (SDGs) (Chandra and Idrisova, 2011; Hák et al., 2016). For example, the conservation and restoration of wetlands is an integral part of SDG goal 6.6 (« Protection and restoration of water-related ecosystems »), while inland wetlands are explicitly mentioned among the habitats to be conserved as defined in objectives 1 (« *Ensure all* *land, inland water and sea areas globally are under integrated biodiveristy-inclusive spatial planning addressing land-, inland water- and sea-use change [...)* and 3 (« *Ensure that at least 30 per cent globally of land, inland water and sea areas [...] are conserved through [...] systems of protected areas and other effective area-based conservation measures [...]* ») of the CBD's Post-2020 Global Biodiversity Framework (Moberg et al., 2022; Yi et al., 2024). In this context, while the number of protected areas continues to increase on a global scale, it is important to monitor them and assess the human pressures on them in order to assess whether the objectives for which they were created have been achieved (He and Wei, 2023). Similarly, ecological restoration projects for wetlands are multiplying, and it is necessary to describe their effectiveness on the basis of reliable and relevant spatio-temporal indicators in order to adapt, if necessary, the management of these ecosystems (Liu and Ma, 2024).

The Landsat archive is of particular interest for long-term monitoring of wetlands. It is the longest Earth observation data program covering the entire globe. Launched in 1972, the Landsat program has been continuously acquiring high spatial resolution images of the Earth's surface for almost 50 years, which have been used for numerous environmental applications (Hemati et al., 2021; Ojima et al., 2022; Wulder et al., 2019). These data have been available in full, free and open access since 2008 (Wulder et al., 2012), boosting the scientific interest in this archive, particularly for monitoring and characterising wetlands (Masoud Mahdianpari et al., 2020). Landsat archive provides an unprecedented temporal perspective for monitoring these ecosystems over the long term. Numerous methods for analysing Landsat time series have been developed in conjunction with artificial intelligence, in particular machine and deep learning (DeLancey et al., 2020; Jafarzadeh et al., 2022). In this context of Big Data, recent methods for the continuous analysis of image time series have been developed in order to make optimal use of satellite image time series. These methods, such as LandTrendR (Kennedy et al., 2010), BFAST (Verbesselt et al., 2010), or Continuous Change Detection and Classification (CCDC) (Zhu and Woodcock, 2014a), offer new possibilities for describing changes in ecosystems over the long term. CCDC, which was developed to exploit Landsat archive (Zhu and Woodcock, 2014), is one of the most widely used methods, as it can both produce land cover or habitat classifications at the desired frequency over the entire period studied and generate cloud-free synthetic images. However, these methods require significant computing power and the local downloading of satellite time series can be a limitation to their use. The recent development of cloud-computing platforms has facilitated access to both data and algorithms through access to remote computers, including the Google Earth Engine (GEE) platform (Gorelick et al., 2017). The recent implementation of continuous analysis methods such as CCDC (Arévalo et al., 2020) and LandTrendR (Kennedy et al., 2018) on the GEE platform represents a significant potential for monitoring wetlands over the long term using satellite image time series (e.g. Fu et al., 2022).

In this context, this thesis aims to assess the contribution of Landsat archive to the long-term monitoring and characterisation of wetlands of international importance by applying a method of continuous analysis of image time series. The thesis is structured into five chapters:

The first chapter consists of a review of the scientific literature on the use of Landsat archive for long-term wetland monitoring. For this, a systematic synthesis was carried out based on 351 articles selected according to a list of keywords relating to Landsat and wetlands. These articles were then analysed according to five main themes subdivided into 22 attributes providing information on methodological aspects (e.g., data, methods) and thematic aspects (e.g., wetland type, location, pressure and degradation factors) in order to identify recommendations and research prospects.

The second chapter describes the methodological context in which this thesis was carried out. It contains a description of the five Ramsar sites studied, the data used including reference data and remote sensing data, and the continuous analysis algorithm used to process the Landsat time series, in this case the CCDC.

The third chapter describes the application of the CCDC algorithm to monitor the long-term functioning of wetlands from the Landsat archive. More specifically, CCDC was used to generate a functional indicator for wetlands, namely ANPP, which is an indicator of net annual primary productivity. To do this, we mobilised Landsat archive over the period 1984-2021 at four contrasting Ramsar sites selected in boreal, temperate, arid and tropical regions and presenting different cloud cover and land cover conditions. We were thus able to test the sensitivity of the method to very different land cover conditions and number of Landsat images in order to assess the transferability of the method.

The fourth chapter presents the application of CCDC to study changes in wetland area and composition over a long period. To this end, we have applied the CCDC to the Marais Poitevin Ramsar site on the French Atlantic coast, in order to map changes in the main habitat types within this wetland between 1984 and 2022. We also compared the performance of the CCDC with that of a method widely used to detect changes in land use, in this case the diachronic method for detecting post-classification changes.

Finally, the fifth chapter describes the study carried out to answer the following question: are the indicators derived from the CCDC using Landsat archive useful for evaluating public conservation policies? We have used the results presented in the previous chapter to describe the annual dynamics of grassland and cropland in the Marais Poitevin, before analysing the effectiveness of public policies (creation of protected areas and implementation of agri-environmental measures) for grassland conservation.

INTRODUCTION TO CHAPTER 1

The first chapter reviews the current state of scientific knowledge to answer the question: How have Landsat archives been used for long-term wetland monitoring and characterisation?

In this review, we describe how Landsat data have been used for long-term (≥20 years) wetland monitoring. A total of 351 articles were analyzed based on 5 topics and 22 attributes that address long-term wetland monitoring and Landsat data analysis issues. This review did not include reports and articles that do not mention the use of Landsat imagery.

The future research prospects and recommendations identified from this detailed and systematic analysis of the published literature on the subject will be used to define the methodology to be implemented during the thesis to analyse the Landsat archives.

This chapter corresponds to the article published in the peer-reviewed journal *Remote Sensing:*

> Demarquet, Q., Rapinel, S., Dufour, S., Hubert-Moy, L., 2023. Long-Term Wetland Monitoring Using the Landsat Archive: A Review. *Remote Sensing* 15, 820. https://doi.org/10.3390/rs15030820

CHAPTER 1. LONG-TERM WETLAND MONITORING USING THE LANDSAT ARCHIVE: A REVIEW

Review

Long-Term Wetland Monitoring Using the Landsat Archive: A Review

by Quentin Demarquet, Sébastien Rapinel, Simon Dufour and Laurence Hubert-Moy

Submission received: 30 November 2022 / Revised: 27 January 2023 / Accepted: 29 January 2023 / Published: 31 January 2023

Abstract

Wetlands, which provide multiple functions and ecosystem services, have decreased and been degraded worldwide for several decades due to human activities and climate change. Managers and scientists need tools to characterize and monitor wetland areas, structure, and functions in the long term and at regional and global scales and assess the effects of planning policies on their conservation status. The Landsat earth observation program has collected satellite images since 1972, which makes it the longest global earth observation record with respect to remote sensing. In this review, we describe how Landsat data have been used for long-term (≥20 years) wetland monitoring. A total of 351 articles were analyzed based on 5 topics and 22 attributes that address long-term wetland monitoring and Landsat data analysis issues. Results showed that (1) the open access Landsat archive successfully highlights changes in wetland areas, structure, and functions worldwide; (2) recent progress in artificial intelligence (AI) and machine learning opens new prospects for analyzing the Landsat archive; (3) most unexplored wetlands can be investigated using the Landsat archive; (4) new cloud-computing tools enable dense Landsat times-series to be processed over large areas. We recommend that future studies focus on changes in wetland functions using AI methods along with cloud computing. This review did not include reports and articles that do not mention the use of Landsat imagery.

1.1. Introduction

Wetlands feature a wide variety of habitats, such as mangroves, swamps, fens, lagoons, and marshes, that provide many functions and ecosystem services (Xu et al., 2020). However, over several decades, agriculture, urbanization, and climate change damaged approximately half of the wetland areas worldwide (Davidson and Finlayson, 2018; Moomaw et al., 2018b) even though many conservation policies have been implemented since the Ramsar Convention in 1974. Managers need tools to monitor wetlands and to assess the effects of planning policies on their conservation status (Finlayson and Gardner, 2020; Rebelo et al., 2018). However, wetlands are difficult to identify and characterize due to their dispersal (Rebelo et al., 2017), their fine-grained pattern (Mahdavi et al., 2018), and the high spatio-temporal dynamics of the water and vegetation that shape them (Gallant, 2015). Thus, monitoring wetlands requires intra-annual observations of the Earth at high spatial resolutions for several decades and observations that cover large areas (Strauch et al., 2022b). Moreover, while there have been global mapping initiatives such as the global wetland map developed by the Center for International Forestry Research (https://www2.cifor.org/global-wetlands/, accessed on 31 January 2023), the global map of saltmarshes (Mcowen et al., 2017), or the global map of peatlands (Xu et al., 2018), there is a gap with respect to long-term monitoring efforts.

The Landsat Earth observation program continuously acquired high-spatial-resolution images worldwide for 50 years (Wulder et al., 2022). Specifically, Landsat missions comprised five sensors launched since 1972. These sensors have collected images at different spatial resolutions in panchromatic (15 m), visible (30–80 m), near-infrared (30–80 m), mid-infrared (30–80 m), and thermal infrared bands (60–120 m). The Landsat archive has been integrated into data collections, which improved the radiometric consistency and quality of images among Landsat sensors (Dwyer et al., 2018). Images have been acquired with a wide swath (185 km) every 16 days by Landsat 1–7 and every 8 days by Landsat 8–9 (Hemati et al., 2021). More than five million images have been stored in the Landsat archive (Wulder et al., 2016), including radiometrically and geometrically corrected products, cloud-free composites, and vegetation indices. The Landsat archive has been provided for free by the US Geological Survey (USGS) since 2008 (Wulder et al., 2022).

Given the characteristics of the Landsat archive, the time series of Landsat images have been used widely for a variety of applications, including long-term wetland monitoring, but a global literature review on this topic remains lacking. In this context, this study aimed to provide comprehensive insight into the benefits and challenges of using the Landsat archive for long-term wetland monitoring. To this end, we performed a systematic review of the literature that focused on long-term wetland monitoring and Landsat data analysis issues. The term "wetland" used in this study is based on the Ramsar definition: areas of marsh, fen, peatland, or water; whether natural or artificial permanent or temporary; with water that is static or flowing, fresh, brackish, or salt, including areas of marine water the depth of which at low tide does not exceed six meters (Ramsar Convention Secretariat, 2006a).

1.2. Methodology and analysis

We applied the Preferred Reporting Items for Systematic Reviews and Meta-Analyses (PRISMA) method (Moher et al., 2009) (Figure 1.2.1). Specifically, the literature search of peer-reviewed articles in English was based on expert definitions of 49 keywords divided into three topics: "Landsat", "monitoring", and "wetlands" (Appendix A). The period of the literature search ranged from 2009 (i.e., one year after the free release of Landsat images) to 1 March 2022. It was conducted globally to consider all wetland types. Only studies that monitored wetlands for at least 20 years were considered. Keywords in the title, abstract, or keyword fields were sought using queries of the Institute for Scientific Information Web of Science (WOS) and Elsevier Scopus databases. As a result, 401 and 459 articles were retrieved from WOS and Scopus, respectively. After removing duplicates, all titles and abstracts were read to remove irrelevant articles, resulting in a final selection of 351 articles (Figure 1.2.1, full list available in Appendix B).

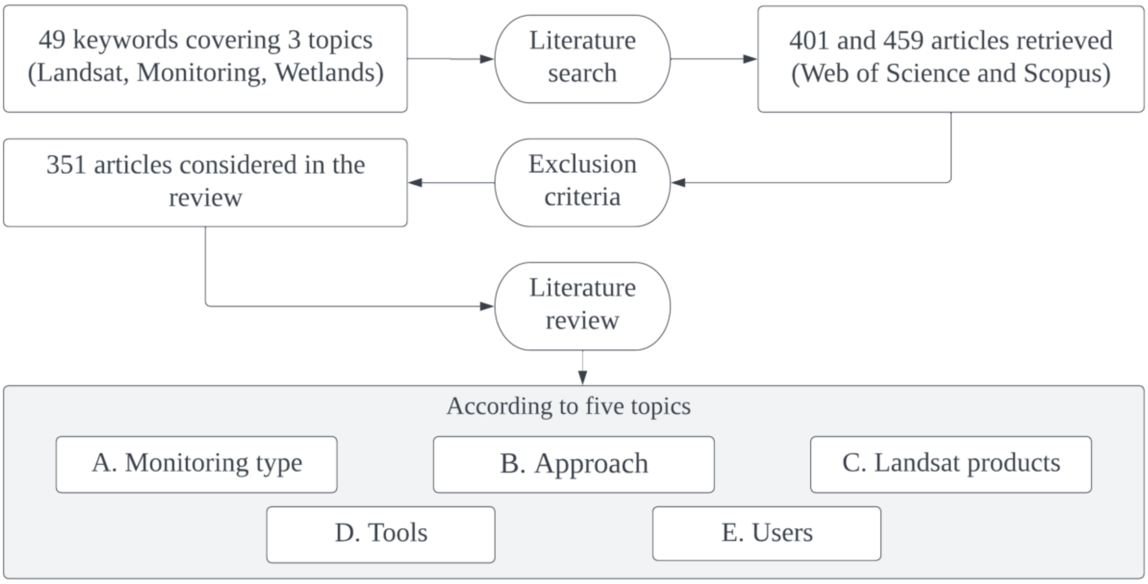

Figure 1.2.1: Flowchart used to search and review the literature on Landsat, monitoring, and wetlands (time span: 2009–2022).

The review was based on an analysis grid of 5 topics and 22 attributes qualified by categories (Table 1.2.1; see Appendix C for a full description of the categories). Attribute B1 "Wetland type" was characterized according to the Ramsar classification system (Ramsar Convention Secretariat, 2006a) (Appendix D). When the wetland type was missing or uncertain in an article, Google Earth images were used to provide a visual interpretation of the studied wetland(s). When the wetland type changed over time, all wetland types in the article were considered. Attributes B6 and B7 were essential biodiversity variables (EBVs) and essential climate variables (ECVs), respectively. EBVs, which are spatial indicators recognized by the scientific community, characterize the ecosystem's structure and functions, species, and plant communities (Skidmore et al., 2021a). Similarly, ECVs address climate monitoring via atmospheric, land, and ocean observations (Bojinski et al., 2014). From this perspective, EBVs and ECVs are valuable indicators for monitoring the functions and services provided by wetlands.

Table 1.2.1: Topics, attributes, and categories used in the literature review (see Appendix C for a full description of categories). LULC: land use/land cover change; FAPAR: fraction of absorbed photosynthetically active radiation.

Topic	Attribute	Categories
A. Landsat data analysis	A1. Change detection	Diachronic; Multitemporal; Time series
	A2. Methods	Classification; Regression; Profile analysis
	A3. Artificial intelligence	Yes; No
	A4. Deep learning	Yes; No
	A5. Supervised method	Yes; No
	A6. Validation	Field data; Visual image interpretation; Both; None
B. Wetland monitoring	B1. Wetland type	Defined based on level 2 Ramsar classification
	B2. Spatial extent	Local; Regional; Continental; Global
	B3. Topic	LULC; Fragmentation and connectivity; Biophysical parameters; Hazards; Ecosystem services; Biodiversity; Hydrology
	B4. Drivers of change	LULC changes; Climate change; Invasive species; Restoration and/or conservation; Combination; No drivers of change
	B5. Essential Biodiversity Variables	Species population; Species traits; Community composition; Ecosystem function; Ecosystem structure
	B6. Remote Sensing—Essential Biodiversity Variables	Species phenology; Species morphology; Species physiology; Population structure by age/size class; Species distribution; Species abundance; Community diversity; Species composition; Ecosystem phenology; Ecosystem physiology; Ecosystem disturbances; Spatial configuration; Habitat structure
	B7. Remote Sensing—Essential Climate Variables	Lakes; Soil moisture; River discharge; Groundwater; Glaciers; Ice sheets and shelves; Snow cover; Permafrost; Albedo; Land use/land cover; Above-ground biomass; Land surface temperature; Evapotranspiration; Fire; Leaf area index; Soil carbon; FAPAR; Anthropogenic greenhouse gas fluxes; Human water use

	B8. Intra-annual observations	Yes; No
	B9. Study period	20–30 years; 30–40 years; More than 40 years
C. Landsat products	C1. Satellite	Landsat 1-2-3 (MSS); Landsat 4-5 (MSS-TM); Landsat 7 (ETM+); Landsat 8 (OLI-TIRS)
	C2. Spectral domain	Visible; Infrared; Thermal; Combination
	C3. Pre-processing level	Level 1; Level 2; Derived products; Composite
D. Tools	D1. Cloud computing	Yes; No
	D2. Open-source software	Yes; No
E. Users	E1. Users	Scientists; Managers; Both
	E2. Journal discipline	Remote sensing; Geography; Earth and planetary science; Forestry; Aquatic, marine and water science; Environmental science; Sociology; Ecology; Multidisciplinary science; Computer science; Land management; Climatology

Given the benefits of using cloud computing to analyze Landsat time series (M. Mahdianpari et al., 2020), we explored whether articles using this approach (attribute D1) provided new insights on long-term wetland monitoring. To this end, a v-test was calculated to compare the distribution of each category (Table 1.2.1) in the articles based on cloud computing to the overall distribution in all articles (Husson et al., 2017). An absolute v-test value of 1.96 corresponds to a p-value of 0.05. The higher the v-test value, the more the category was typical of using cloud computing. Statistical analysis was performed using R software (R. Core Team, 2019) with the *FactoMine R* package (Lê et al., 2008). It is important to note that this review focuses exclusively on Landsat imagery and did not include reports or articles that did not mention the use of Landsat imagery. Hence, some approaches developed for long-term wetland monitoring such as the evaluation of wetland habitat change that was conducted by the US Fish and Wildlife Service (Dahl, 2004) were ignored.

1.3. Long-term Wetland Monitoring

1.3.1. Spatial Extent and Global Distribution

The spatial extent of the reviewed studies varied by world region (Figure 1.3.1). Overall, most studies (73%) focused on the local scale, while only 27% focused on the regional scale. At the local scale, most studies were performed in Asia, especially China (15%) and India (8%), followed by Africa (8%), North America (5%), South America (4%), Oceania (3%), and Europe (2%). At the regional scale, a similar trend was observed, with most studies being performed in China (7%), followed by the United States (USA) (3%), India (2%), and Canada (2%). Three studies were performed at the continental scale, specifically North America (Ju and Masek, 2016), Central and South America (Cavanaugh et al., 2018), and Europe (Laengner et al., 2019). Conversely, no studies were performed on a global scale, although Schwatke et al. (Schwatke et al., 2019) monitored the extent of 32 lakes around the world. Comparing the locations of the studies to those of wetlands highlighted several gaps (Figure 1.3.1): Many large wetlands have not been monitored in the long term, particularly in South America, Equatorial Africa, Oceania, and Russia. Moreover, the comparison between the distribution of reviewed studies and wetland areas according to the world temperature domains (Figure 1.3.2) emphasizes that polar, cool temperate, and especially boreal domains were understudied. Conversely, warm temperate, sub-tropical, and tropical domains were covered by numerous long-term Landsat studies, although they were mostly focused on intertidal swamp forests (Figure 1.3.3).

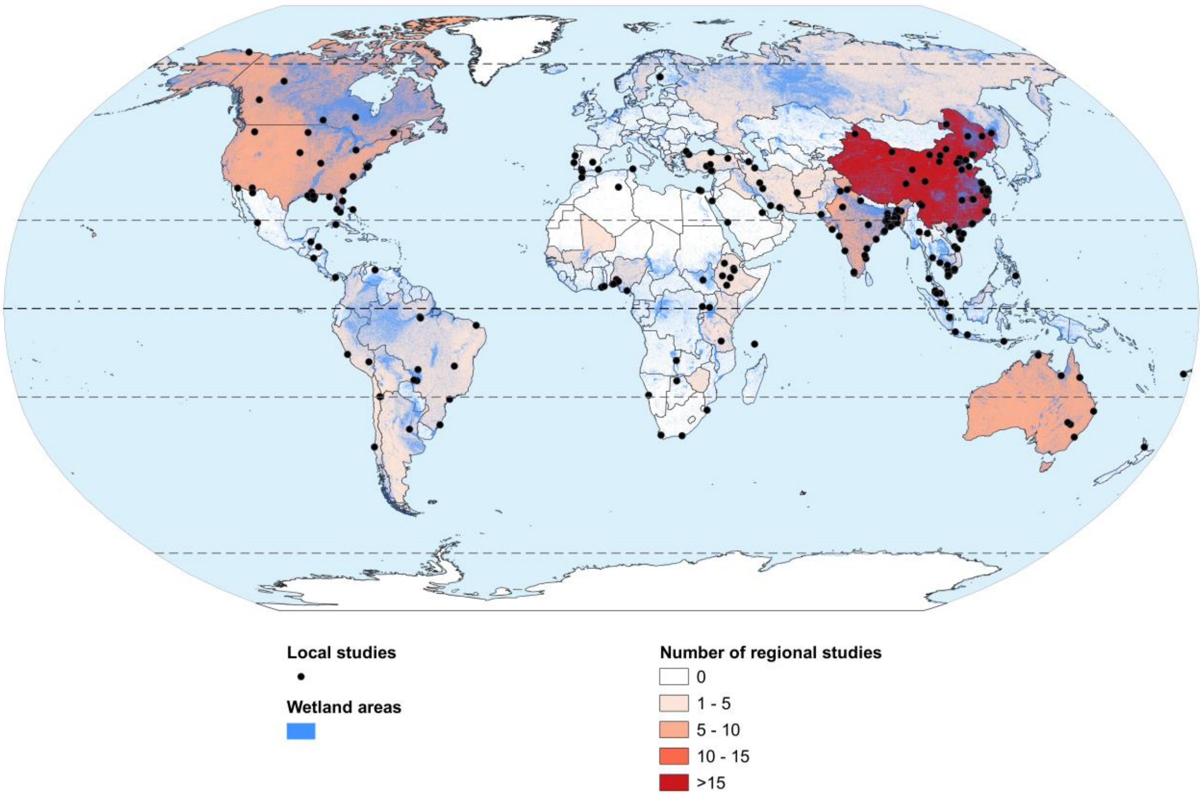

Figure 1.3.1: Spatial distribution of the reviewed studies. Source of the global wetland map: (Tootchi et al., 2018).

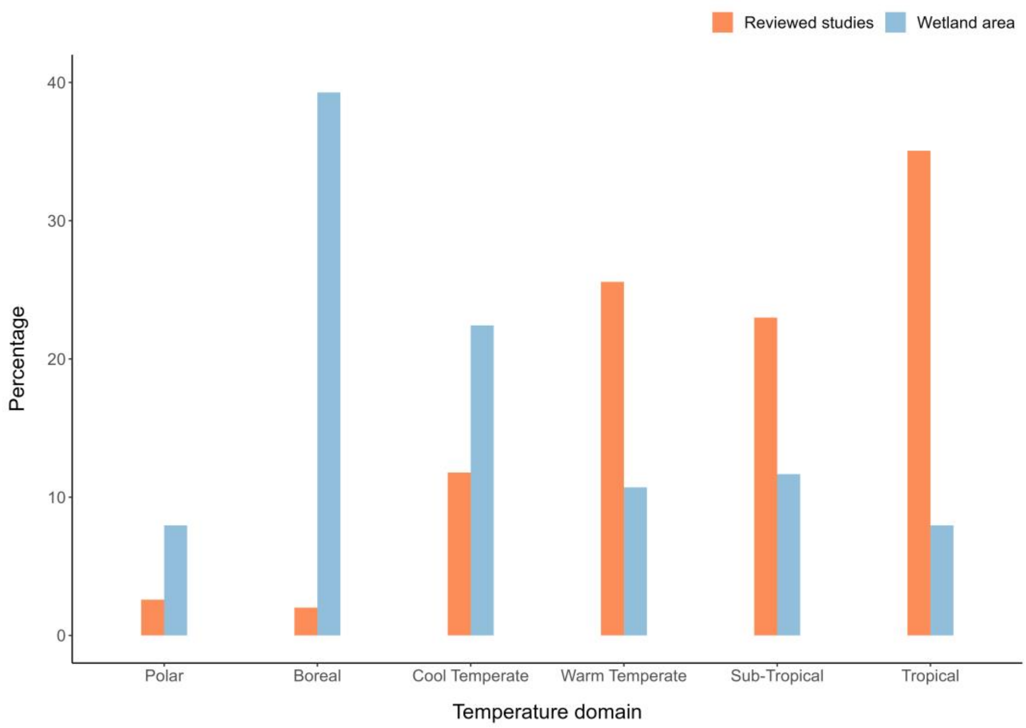

Figure 1.3.2: Distribution of the 351 reviewed studies and wetland areas (Tootchi et al., 2018) according to world temperature domains (Sayre et al., 2020).

Figure 1.3.3: Percentage of wetland types investigated in the reviewed studies classified by levels 1 and 2 of the Ramsar wetland classification (Ramsar Convention Secretariat, 2006a). Seas.: seasonal; Perm.: permanent.

1.3.2. Wetland Types

The percentage of wetland types surveyed in this review varied by Ramsar classification (Figure 1.3.3). Globally (Level 1), inland wetlands (48%) and marine/coastal wetlands (33%) were studied the most, while human-made wetlands (19%) were studied the least. Among the marine/coastal wetlands, intertidal swamp forests (8%), intertidal mudflats (6%), tidal salt/brackish/freshwater marshes (6%), and estuarine waters (4%) were studied the most. Conversely, freshwater lagoons and marine aquatic beds were rarely studied, e.g., Lopes et al. (2019); Zefrehei et al. (2021). Among inland wetlands, permanent freshwater marshes (10.5%), seasonal freshwater marshes (8.5%), permanent freshwater rivers (8%), and lakes (7%) were studied the most. Conversely, many inland wetland types, such as tundra wetlands, inland deltas, and freshwater springs, were rarely studied (<1%) (Chouari, 2021; Hiernaux et al., 2021; Wells et al., 2021). Among human-made wetlands, aquaculture ponds (5%), irrigated land (3.5%), ponds (3%), and salt pans (2.5%) were studied the most, while seasonally flooded agricultural land, which includes pastures, was rarely studied (e.g., Dang et al. (2021)).

1.3.3. Long-term Wetland Changes

The distribution of the reviewed studies according to categories of long-term wetland changes is shown in Figure 1.3.4.

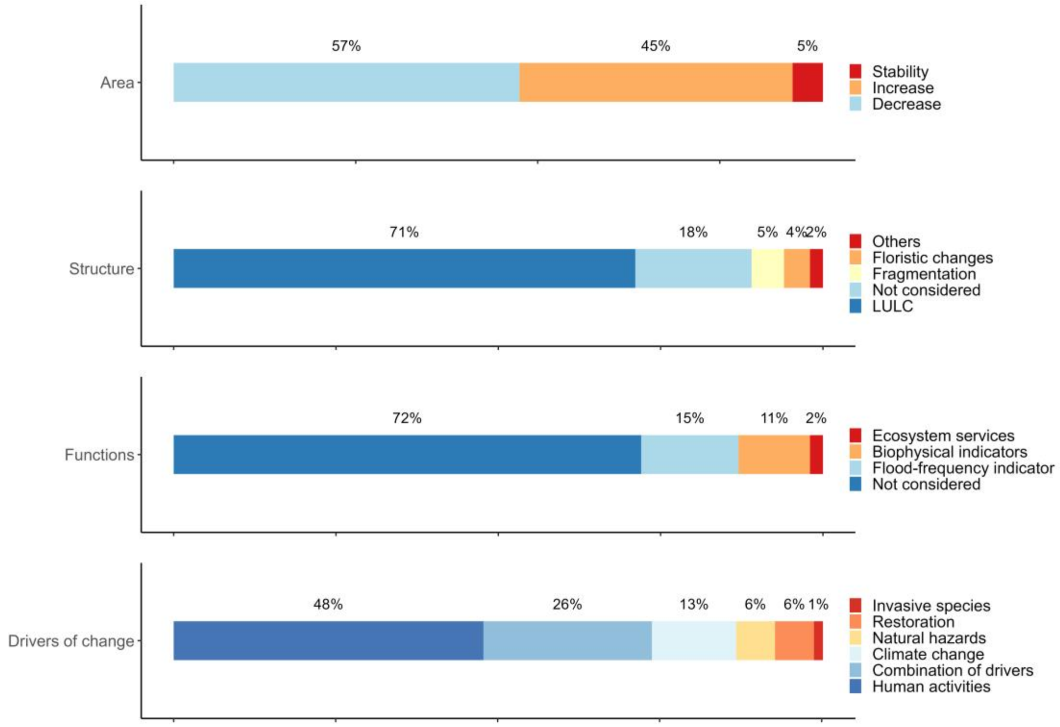

Figure 1.3.4: Distribution of the reviewed studies according to categories of long-term wetland change.

1.3.3.1. Area

A decrease in wetland area was the most frequent change reported worldwide (57% of the reviewed studies; Figure 1.3.4), including mangroves in West Africa (Carney et al., 2014), Belize (Cherrington et al., 2020), India (Mabwoga and Thukral, 2014), Vietnam (Nguyen et al., 2013), and Madagascar (Rakotomavo and Fromard, 2010), as well as estuarine wetlands (Dipson et al., 2015) and lakes (Koshale and Mahato, 2020) in India, wet forests in Nigeria (Tope-Ajayi et al., 2016), freshwater marshes in Uganda (Kabiri et al., 2020), and tundra wetlands in Canada (Campbell et al., 2018). Conversely, 45% of the studies reported an increase in wetland areas, including mangroves in China (Hu et al., 2018), Vietnam (Son et al., 2016), and Australia (Asbridge et al., 2016), and alpine wetlands (Dangles et al., 2017) and glacial lakes in the Andes Mountains (Veettil et al., 2017). To a lesser extent, wetland areas remained stable in 5% of the studies, including mangroves in Bangladesh (Islam et al., 2019) and sand bars in India (Talukdar et al., 2020). Interestingly, Tiné et al. (2019) described a long-term increase in wetland areas in Quebec due to an increase in the beaver population, which created new hydrological conditions that promoted wetland expansion.

1.3.3.2. Structure

The fragmentation of wetlands was described in 5% of the reviewed studies (Figure 1.3.4). Most of these studies indicated an ongoing increase in wetland fragmentation over time, such as for waterbodies in India (Paul and Pal, 2020), the Prairie Pothole Region of North America (Krapu et al., 2018), coastal wetlands in China (Tian et al., 2017), and Ghana (Ekumah et al., 2020), as well as lakes on the Tibetan Plateau (Qiu et al., 2009). Conversely, some studies emphasized an increase in wetland connectivity, such as for floodplains in Australia (Bishop-Taylor et al., 2017) and mangroves in Pakistan (Gilani et al., 2021).

The long-term monitoring of floristic changes within wetlands was addressed in 4% of the studies. For example, O'Donnell and Schalles (O'Donnell and Schalles, 2016) showed a decrease in the biomass of *Spartina alterniflora (syn. Sporobolus alterniflorus)*, especially for small patches in salt marshes on the coast of Georgia, USA. Lucas et al. (Lucas et al., 2020) indicated that variations in biomass were explained by the age of *Rhizophora* spp. in a mangrove in Malaysia. In the Sundarbans mangroves in Bangladesh, Ghosh et al. (2017) described a decrease in *Heritiera fomes* and *Excoecaria agallocha* cover from 1977 to 2015 but an increase in *Ceriops decandra*, *Xylocarpus mekongensis*, and *Sonneratia apelatala* cover.

The other parameters of wetland structure were monitored less frequently. For example, an increase in above-ground mangrove biomass was measured in Vietnam (Lap et al., 2021), and the percentage of mangrove canopy cover was monitored in Australia (Lymburner et al., 2020). The dynamics of natural habitats within wetlands were monitored in shallow lakes in Argentina (Gayol et al., 2019), boreal wetlands in Canada (Amani et al., 2021), and floodplains in China (Dong and Chen, 2021).

1.3.3.3. Functions

Many of the reviewed studies derived functional indicators from the Landsat archive. A flood-frequency indicator was explored the most (15% of the studies; Figure 1.3.4). Overall, studies highlighted a decrease in flood frequency, such as in floodplain wetlands in India (Mondal and Pal, 2016), in shallow intermittent lakes in Nebraska, USA (Tang et al., 2016), and in the Macquarie Marshes in Australia (Thomas et al., 2011). However, a few studies described an increase in flood frequency, such as in the northern part of the Doñana Marshes in Spain (Díaz-Delgado et al., 2016). Interestingly, Cai et al. (2017) described an alluvial wetland in Zambia for which floods had recently increased in the area, which disturbed wetland ecosystems and Indigenous populations. Biophysical indicators that characterize wetland functioning were derived from the Landsat archive in 11% of the studies. For example, the normalized difference vegetation index (NDVI) derived from Landsat time series revealed decreasing productivity in the Andes in southern Peru (Mazzarino and Finn, 2016) but increasing productivity in the Tapacarí Province of Bolivia (Hartman et al., 2016). The biophysical properties of lakes have also been monitored worldwide: Zefrehei et al. (2020) described increasing chlorophyll-a concentrations and turbidity in the Choghakhor wetland in Iran; Ho et al. (2017) observed decreasing extents of the phytoplankton bloom from 1984 to 1991 and then a significantly increasing extent from 1991 to 2011 in Lake Erie (North America); Alademomi et al. (2020) observed an increase in lagoon temperature in Nigeria using thermal Landsat bands. Less than 2% of the studies investigated changes in wetland functions and ecosystem services. For example, two studies used the NDVI trend to reveal a decrease in carbon storage in mangroves in Fiji (Avtar et al., 2021) and in coastal wetlands in China (Zhao et al., 2017). Duncan et al. (2021) used the NDVI trend in Cuba to explore the relation between mangrove productivity and extent, considering the habitat function for threatened mammal species. Interestingly, Ekumah et al. (2020) described a decrease in coastal wetland ecosystem health in Ghana by combining functional indicators related to habitat fragmentation, vegetation phenology, flooding frequency, and land use/land cover (LULC) persistence. Changes in the monetary valuation of ecosystem services were investigated in a mangrove in Iran based on the NDVI trend (Ashournejad et al., 2019) and in a lake in the Xinjiang region of China based on LULC changes (Yushanjiang et al., 2018).

1.3.4. Drivers of change

1.3.4.1. Human activities

The most common driver of wetland changes identified using the Landsat archive was LULC changes related to human activities (47.8%; Figure 1.3.4). Decreases in wetland areas were mainly due to urbanization (e.g. Blanchette et al., 2018; Mialhe et al., 2019), agriculture (e.g. Fickas et al., 2016; Kabiri et al., 2020), and industrialization (e.g. Wang et al., 2016) or coastal land reclamation (e.g. Ding et al., 2020) to a lesser extent. The development of artificial wetlands (e.g., aquaculture ponds) is also responsible for the decrease in the area of natural wetlands worldwide, such as in China (Xie et al., 2017), Indonesia (Eddy et al., 2017), Vietnam (Hong et al., 2019), India (Jayanthi et al., 2018), and Egypt (Masria et al., 2020). The consumption of natural resources related to water management (e.g. Gao et al., 2022; Karim et al., 2019) or deforestation (Villate Daza et al., 2020) was also identified as a negative driver of change. Conversely, LULC changes may increase the area of natural wetlands, such as when a dam is constructed (e.g. Ablat et al., 2019; Zheng et al., 2020) or when farmland is abandoned (Fitoka et al., 2020).

1.3.4.2. Natural Hazards

Natural hazards were reported as a driver of change in wetlands in 6% of the reviewed studies. Several studies monitored post-fire conditions in wetlands: (Darmawan et al., 2020) observed the natural restoration of mangroves in Indonesia, and (Mexicano et al., 2013) described a significant increase in primary production the year after a fire. Other studies focused on the impacts of hurricanes on coastal wetlands: (Carle and Sasser, 2016) observed a significant decrease in vegetation productivity in Wax Lake Delta (LA, USA), and (Zhang et al., 2016) observed that mangroves took 2–6 years to reach their full extent in the Biscayne National Park (FL, USA). Sedimentation is recognized as a key factor in increasing the area of wetlands in floodplains (Chouari, 2021; Pirali Zefrehei Ahmad Reza et al., 2020). In addition, many studies highlighted erosion and accretion in coastal wetlands, such as in mangroves in Vietnam (Long et al., 2021), as well as in lagoons in Namibia (Behling et al., 2018), China (Jia et al., 2018), and Turkey (Kuleli et al., 2011).

1.3.4.3. Climate change

Climate change was identified as a driver of change in 13% of the reviewed studies. Changes in precipitation varied among climatic regions. In Australia, precipitation increased in the northeast tropical region, which increased the area of mangroves (Asbridge et al., 2016), but decreased in the southeast temperate region, which decreased the area of lakes (Banerjee et al., 2016). The impact of rising temperatures in wetlands increased worldwide. For example, increased phenological activity has been observed in boreal regions of Canada in tundra (Ju and Masek, 2016) and peatlands (Dearborn and Baltzer, 2021) and in oases in the arid region of northwestern China (Pan et al., 2018). In the tropics, rising temperatures have driven changes in the floristic composition of mangroves in Bangladesh (Ghosh et al., 2017). Rising temperatures caused glaciers to melt, with new lakes appearing in the Andes cordilleras (Dangles et al., 2017), and sea levels to rise, resulting in the loss of some coastal marshes in Virginia, USA (Sun et al., 2018).

1.3.4.4. Restoration and/or Conservation Policies

Overall, 6% of the reviewed studies used the Landsat archive to monitor the impacts of conservation or restoration policies. The studies showed positive effects, such as the restoration of lost wetlands (Darmawan et al., 2020; Gilani et al., 2021), improved vegetation functioning (Charters et al., 2019; Wilson and Norman, 2018), the maintenance of flood cycles (Bishop-Taylor et al., 2017; Díaz-Delgado et al., 2016), greater connectivity (Bishop-Taylor et al., 2017; Gilani et al., 2021), and improved bird habitat function (Li et al., 2013). Most studies focused on mangroves (e.g. Misra et al., 2015; Tuholske et al., 2017), but restoration or conservation policies also succeeded on floodplains (Bishop-Taylor et al., 2017; Wilson and Norman, 2018), alpine wetlands (Hartman et al., 2016), coastal marshes (Díaz-Delgado et al., 2016), and peat swamp forests (Charters et al., 2019).

1.3.4.5. Invasive Species

Invasions of alien plant species in wetlands were successfully observed using the Landsat archive. For example, the expansion of *S. alterniflora* was monitored in coastal wetlands (Wu et al., 2018; Yan et al., 2021), the effects of *Azolla filiculoides* growth on ecosystem services of lagoons were assessed (Marzvan et al., 2021), and the invasion of *Eichhornia crassipes* was mapped in lakes in Rwanda (Ndayisaba et al., 2017).

1.3.4.6. Combination of Drivers of Change

In the reviewed studies, 26% of wetland changes were due to a combination of several drivers (Figure 1.3.4). For example, water consumption by agriculture and industries, combined with a decrease in precipitation, resulted in a decrease in the area of wetlands in China (Huo et al., 2017). In an arctic archipelago of Canada, climate change and the expansion of a bird species resulted in wetland degradation (Campbell et al., 2018). In addition, the combination of the expansion of invasive species and LULC changes decreased the area of water bodies (Y. Liu et al., 2020; Zefrehei et al., 2021). Interestingly, many studies highlighted that a combination of drivers of change can both decrease and increase the area of wetlands. For example, LULC changes combined with sea level rise increased the area of salt marshes but decreased that of salt pans (Hamandawana et al., 2020). In China, Wu et al. (Wu et al., 2015) found that climate change combined with agricultural development could decrease or increase the area of wetlands depending on the conservation policy.

1.4. Landsat Data Analysis

The distribution of the reviewed studies according to categories of Landsat data analysis is shown in Figure 1.4.1.

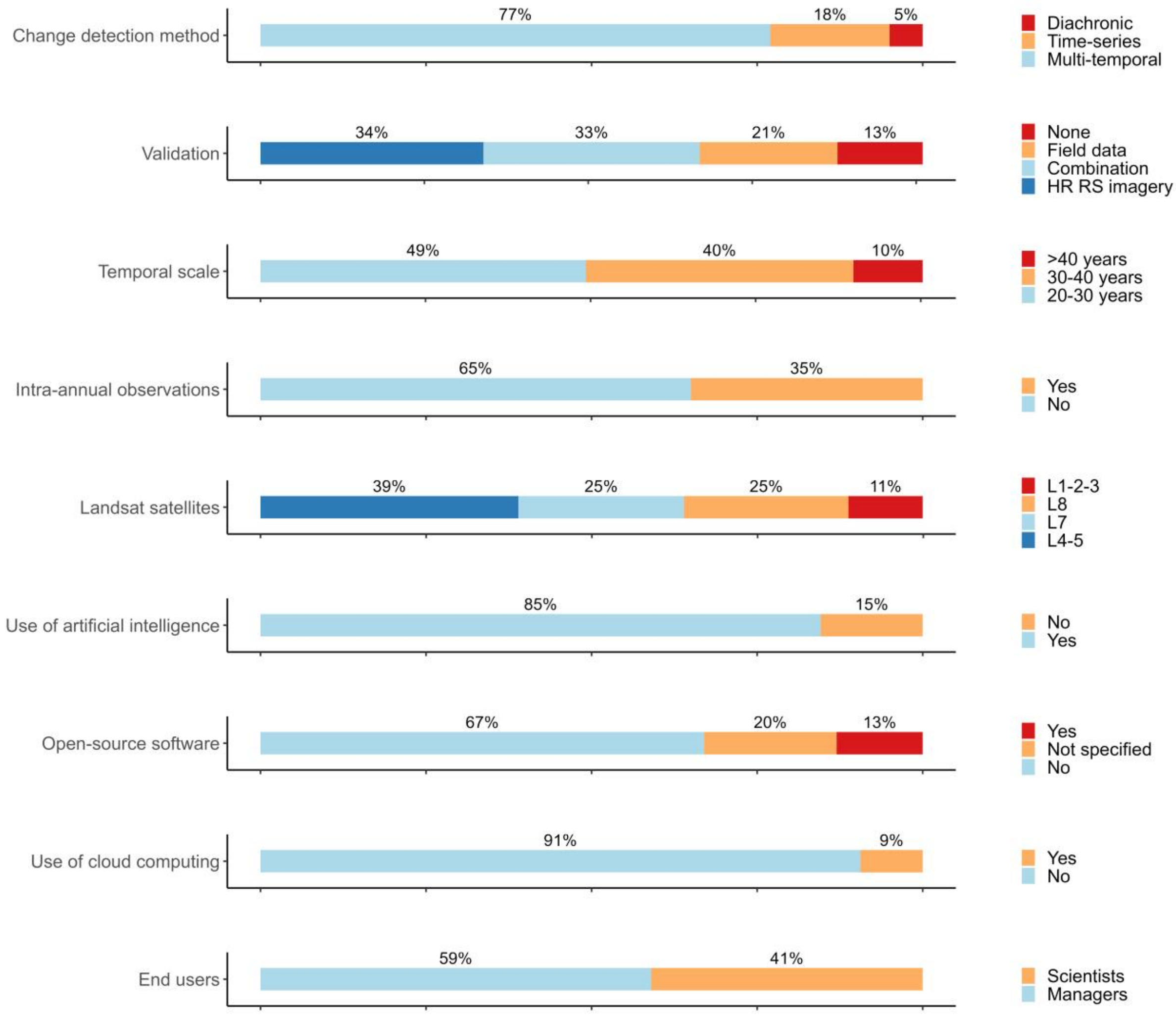

Figure 1.4.1: Distribution of the reviewed studies according to categories of Landsat data analysis.

1.4.1. Change detection method

Changes in wetlands were detected mainly using multi-temporal approaches (77.5%), followed by time-series analyses (18%) (e.g. Diniz et al., 2019; Tahsin et al., 2019), and the diachronic approach (5%) (e.g. Dervisoglu et al., 2017; Zelelew et al., 2021) (Figure 1.4.1). The diachronic approach (change detection by processing two images of different dates) widely used to map LULC, although fast and simple, does not consider the intra- and inter-annual variability of wetland water and vegetation, which leads to errors in wetland area estimation and habitat classification. While the multi-temporal approach (processing of more than two images for several different dates), which is also fast and simple to implement, improves the results obtained with the diachronic approach, only remote sensing data time series (processing of most available images) that consider the intra- and inter-annual variability of wetland water and vegetation can help assess wetland functions. However, the use of time series poses the challenge of developing methods that are able to process such amounts of data.

1.4.2. Validation

Landsat-derived maps and products were validated mainly by visual interpretation of high-resolution remote sensing imagery (34%), such as those available on Google Earth. In 33% of the studies, visual interpretation was combined with field data. Only 21% of the studies used field data for validation (Hason et al., 2020; Rakotomavo and Fromard, 2010). Surprisingly, ca. 13% of the studies did not mention a validation procedure (Figure 1.4.1).

1.4.3. Temporal Scale of Studies

The study period was 20–30, 30–40, and more than 40 years for 49.3%, 40.5%, and ca. 10.5% of the reviewed studies (Figure 1.4.2). Notably, (Kawser et al., 2021) analyzed the impacts of the great Assam earthquake (1950) on an estuarine floodplain in Bangladesh by processing historical toposheets combined with the Landsat archive from 1942 to 2019. (Gopalakrishnan et al., 2021) explored changes in mangroves in Peninsular Malaysia using historical records and the Landsat archive for a 74-year period (1944–2018).

From 2009 to 2021, the number of studies published per year with periods of 20–30, 30–40, and more than 40 years increased from 2 to 27, from 1 to 36, and from 1 to 7, respectively (Figure 1.4.2).

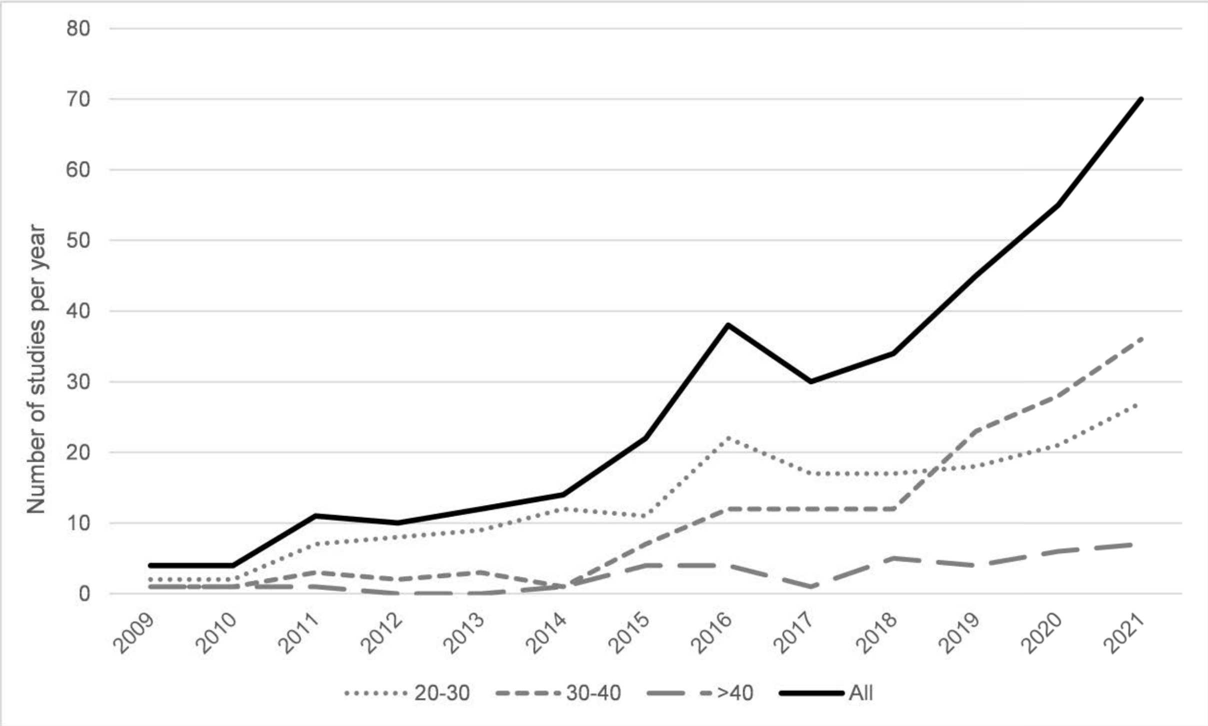

Figure 1.4.2: Number of reviewed studies published per year from 2009 to 2021 by the duration of the study period (years).

1.4.4. Intra-Annual Observations

Only 35% of the reviewed studies used intra-annual observations (Figure 1.4.1). Notably, (Borro et al., 2014) mapped shallow lakes in South America from 1987 to 2010 using 1–8 images from Landsat 5 and 7 per year. (Ouyang et al., 2014) investigated the impacts of drought on the extent of surface water in the USA from 1984 to 2011 using 1–5 images from Landsat 5 and 7 per year. Other studies used more images per year, such as (Liang and Li, 2019), who investigated changes in lakes in China from 1988 to 2014 using 12 images from Landsat 5, 7, and 8 per year.

1.4.5. Use of Landsat Sensors

All Landsat sensors were used in the reviewed studies but in different percentages (Figure 1.4.1). Landsat 4–5 (MSS/TM) images were used the most (38.9% of the studies), while Landsat 1-2-3 (MSS) images were used the least (11.2%). Landsat 7 ETM+ and Landsat 8 OLI/TIRS images were used in 25% and 24.8% of the studies, respectively. Visible and infrared bands were used in 49% of the studies. Conversely, only 2% of the studies used thermal bands (e.g. M. Mahdianpari et al., 2020; Pedreros-Guarda et al., 2021).

The Landsat bands were used at different pre-processing levels. While 20.5% of the studies did not specify a pre-processing level, most (63%) used Level 1 (radiometrically and geometrically corrected) Landsat data. Conversely, 16% of the studies used Level 2 (atmospherically corrected) Landsat data. Fewer than 1% of the studies used Landsat composites (Rossi et al., 2020; Wulder et al., 2018).

The combination of the Landsat archive and data derived from other remote sensing sensors was shown in 34.7% of the reviewed studies. Various topographic information derived from DEM data can be combined with spectral data to capture additional wetland characteristics not captured by spectral data alone (Tortini et al., 2020). More precisely, 17.4% of the reviewed studies used DEMs derived from remote sensing data, such as SRTM (e.g. Ndayisaba et al., 2017); ASTER (e.g. Veettil et al., 2017); TanDEM-X (e.g. Lucas et al., 2020); ALOS PALSAR (e.g. Lucas et al., 2020); or LiDAR (e.g. Kolari et al., 2021), to characterize topography, vegetation, or water height. In 19.7% of the reviewed studies, optical or radar variables from other sensors such as MODIS (e.g. Wu et al., 2018); AVHRR (e.g. Ju and Masek, 2016); ALOS AVNIR (e.g. Mozumder et al., 2014); IRS-LISS II/III/IV (e.g. Dipson et al., 2015); SPOT 2/4/5 (e.g. Tran Thi et al., 2014); or Sentinel-1/2 (e.g. Wang et al., 2021), were combined with Landsat data. In 2% of the cases, studies used both DEMs and spectral variables (e.g. Shi et al., 2021).

1.4.6. Use of Artificial Intelligence

Artificial intelligence (AI) was used in 84.6% of the reviewed studies for the classification (64.3%), regression (15.9%), and profile analysis (4.4%) of Landsat data (Figure 1.4.1). Supervised classification was the approach used most frequently. For example, (Parihar et al., 2013) classified Landsat MSS and TM data from 1973 to 2010 in West Bengal, India, applying a supervised maximum likelihood classifier, one of the classification methods used the most in the studies. Their classifications had an overall accuracy of 73.8–79.3%. (Han et al., 2015) investigated changes in vegetation in Poyang Lake, China, from 1973 to 2013 using inter-annual classification applied to data from Landsat 1-2-3 to Landsat 8. A comparison of several supervised classification algorithms showed that support vector machine (SVM) had the highest accuracy, with a Kappa index of >0.9. More recently, (Berhane et al., 2020) used the random forest algorithm to monitor LULC in the wetlands of the Midwestern USA. They classified 1749 Landsat data with an overall classification accuracy of 81–89%. The studies also used unsupervised classification methods. For example, (Dewidar, 2011) classified Landsat MSS, TM, and ETM+ data by using the ISODATA algorithm to monitor temporal changes in the area of water in lagoons in Egypt from 1972 to 2007, with an overall accuracy of ca. 97.5%. (Fitoka et al., 2020) mapped wetland areas in Greece by combining Sentinel-2 and Landsat 5 TM data from 1986 to 2017. They combined classification trees with expert rules to distinguish 31 wetland classes with an overall accuracy of more than 90% over a total area of more than 2 million ha.

(Raynolds and Walker, 2016) applied regression methods to Alaska, USA, from 1985 to 2011. They calculated and estimated the NDVI trend across the study area and observed a significantly negative regional trend in NDVI, mainly due to the development of the oil industry. (Dingle Robertson et al., 2015) applied spectral mixture analyses to 26 Landsat 5 TM images from 1984 to 2010 in Canada. The results showed a decrease in wetland areas, mainly due to the extension of recreational and agricultural activities and encroaching development. Regression models can also provide information on abiotic and anthropogenic factors that influence wetlands. For example, the Breaks for Additive Season and Trend algorithm was used for long-term monitoring (Verbesselt et al., 2010) to identify global temporal trends in wetlands (e.g., vegetation greenness) and provide information on seasonal components and abrupt changes.

(Lv et al., 2019) investigated wetland loss in a region of China from the 1980s to 2015 by performing a profile analysis of 3 spectral indices (the normalized difference vegetation index (NDVI), the normalized difference water index (NDWI), and the soil moisture monitoring index (SMMI)) derived from 27 Landsat images. Results showed a decrease in the wetland area of ca. 13.8% over three distinct periods. Among studies that used machine learning, nine used deep-learning algorithms. For example, (Lin et al., 2018) investigated changes in wetlands in Shanghai, China, from 1986 to 2013 using the Kernel Extreme Learning Machine (K-ELM) algorithm on six Landsat 5 TM images and compared its accuracy to those of Extreme Learning Machine, MLC, and SVM algorithms. Results showed that K-ELM performed the best, with an overall accuracy of 86%. (Ehsani and Shakeryari, 2021) used a fuzzy ARTMAP neural network to process Landsat MSS, TM, ETM+, and OLI images to investigate changes in wetlands from 1977 to 2014. They observed a decreasing trend in wetland area, with a Kappa index of 0.84–0.89.

AI was also used to detect and remove pixels from cloudy Landsat images and then fill these gaps with other images. It achieved denser cloud-free time series that improved modeling quality (M. Mahdianpari et al., 2020). For example, (Schwatke et al., 2019) increased the accuracy of spatial models of lakes by 41% by developing an automated tool to extract water areas and that detects and removes clouds in Landsat images and fills in some gaps with Sentinel-2 images.

Conversely, 15.7% of the studies did not use AI approaches, such as visual interpretation and digitization or band thresholding. For example, (Xie et al., 2012) investigated LULC changes in a nature reserve in China from 1988 to 2008 based on the visual interpretation of Landsat TM data. (Chen et al., 2013) applied Otsu's method to obtain an optimal threshold of Landsat bands to classify and monitor mangrove changes in Honduras from 1985–2013 (Kappa index = 0.82). (Almahasheer et al., 2016) thresholded NDVI to monitor mangroves on the coast of the Red Sea from 1972 to 2013, with 91% overall accuracy.

1.4.7. Open-Source Software

The Landsat archive has been processed less often using open-source software (13% of the reviewed studies; Figure 1.4.1). For example, (Otero et al., 2019) created maps of changes in mangrove cover in Malaysia from 1988 to 2015 from Landsat TM, ETM+, and OLI using R software. (Tin et al., 2019) processed and classified Landsat images using QGIS software to describe historical changes in mangroves in Vietnam from 1973 to 2016. Notably, (Schaffer-Smith et al., 2017) investigated dynamics of the area of water in wetlands in California, USA, from 1983 to 2015. They analyzed Landsat 4, 5, 7, and 8 data using Python to pre-process images and R software to classify images and assess accuracy, along with commercial ArcGIS software. Notably, 20% of the studies did not name which software they used.

1.4.8. Cloud Computing

Overall, 9.4% of the reviewed studies used cloud computing for long-term wetland analysis, of which all used the Google Earth Engine (GEE) cloud-computing platform (Gorelick et al., 2017) (Figure 1.4.1). Comparing cloud-computing studies to local-computing studies revealed statistically significant differences in several attributes (Table 1.4.1). Studies that used cloud computing performed more change detections using time series and thus used more intra-annual images. Similarly, they combined Landsat TM, ETM+, and OLI/TIRS data more often and at pre-processing Level 2. Cloud-computing studies were conducted more often at regional and continental scales than at the local scale. Regarding study periods, 30–40-year periods were more common for cloud-computing than local-computing studies. Cloud-computing studies did not use more open-source software than local-computing studies did. Cloud-computing studies were published more often (+17.8%) in remote sensing journals.

Several studies used GEE. For example, (Cavanaugh et al., 2018) investigated the sensitivity of mangrove extent relative to climate variability from the Atlantic coast of North America to the Pacific coast of South America from 1984 to 2011 using the Enhanced Vegetation Index from Landsat 5 TM and Landsat 7 ETM+ images available in GEE. (Laengner et al., 2019) used GEE to investigate changes in the area of salt marshes at the continental scale at 125 sites of ca. 20 km^2 each across Europe from 1986 to 2010. (Shi et al., 2021) assessed the impacts of historical changes on wetland areas in Zhenlai County (5350 km^2), China, from 1985 to 2018 using 2562 images and spectral indices including NDVI, enhanced vegetation index (EVI), land surface water index (LSWI), normalized difference water index (NDWI), and modified normalized difference water index (mNDWI) derived from Landsat 5 TM, Landsat 7 ETM+, and Landsat 8 OLI/TIRS surface reflectance and combined with Sentinel-1 SAR and Sentinel-2 MSI data. (Wang et al., 2021) described spatio-temporal variations in coastal wetlands in China from 1984 to 2018 using 62,000 images from Landsat 5 TM, Landsat 7 ETM+, and Landsat 8 OLI/TIRS.

Table 1.4.1: Frequency (percentages) of attributes in studies that used Google Earth Engine that differed significantly (|v-test| > 1.96) from the frequency in all studies reviewed. "Class": Studies that used Google Earth Engine; "Class/Mod": studies with the attribute and belonging to the class; "Mod/Class": studies belonging to the class and with the attribute; "Overall": frequency of the attribute in all studies, regardless of the class; EBVs: essential biodiversity variables.

Attribute	Class/Mod	Mod/Class	Overall	*v*-Test
Change detection using time series	38	73	18	7.3
Use of intra-annual observations	23	85	34	6.2
Level 2 of pre-processing	31	51	15	5.1
Use of L4-5 TM AND L7 ETM+ AND L8 OLI/TIRS images	18	51	27	3.1
Regional-scale study	18	48	25	3.0
Open-source software not used	12	85	65	2.6
Continental-scale study	50	9	2	2.5
Remote sensing journal	17	40	22	2.4
Study period of 30–40 years	14	61	40	2.4
Ecosystem function EBVs	24	15	6	2.0
Forces driving change not specified	21	18	8	1.99
Spectral domain of the Landsat archive not specified	0	0	9	−2.0
Local-scale study	5	39	73	−4.2
Change detection using multi-temporal images	3	27	77	−6.4

1.4.9. End Users

The results of the reviewed studies targeted mainly the scientific community and stakeholders/policy makers (59%), providing information for management and economic and social policies that protect wetlands and/or improve wetland conservation (Figure 1.4.1). The remaining studies (41%) targeted only scientific communities primarily for modeling and for developing basic knowledge to better understand spatio-temporal dynamics of wetlands (Mao et al., 2021; Umarhadi et al., 2022).

1.5. Progress and Recommendations

1.5.1. Using the Landsat Archive for the Extensive Monitoring of Wetland Extent and Type

This review highlights that wetlands have been monitored worldwide over large areas, ranging from local to continental scales. However, certain areas with high wetland density, such as boreal wetlands in Russia, tropical inland wetlands in Africa, and cool temperate wetlands in Europe, were monitored less often in the long-term and should be studied more extensively.

Nearly all wetland types in the Ramsar level 2 classification system were monitored using the Landsat archive. Mangroves and inland freshwater marshes were the types monitored the most, but rarer wetland types such as lagoon seabed vegetation (Lopes et al., 2019) and freshwater springs (Chouari, 2021) were also monitored. However, other wetland types that are widely distributed around the world have been monitored less often and should be studied more in the future. This includes tundra wetlands, which cover ca. 25% of the global area of lakes (Lehner and Döll, 2004) and face major conservation issues related to climate change (Liljedahl et al., 2016).

1.5.2. Using the Landsat Archive to Improve Monitoring of Wetland Areas, Structure, and Functions

1.5.2.1. Landsat Archive Enables the Monitoring of Wetland, Area, Structure, and Functions

Changes in wetland areas, structure, and functions must be monitored to assess the conservation status of these ecosystems (Delbosc et al., 2021). This review highlights that the Landsat archive is suitable for this purpose: (1) Many studies highlighted changes in wetland area; (2) changes in wetland structure were described using multiple indicators related to fragmentation, floristic composition, biomass, and percentage canopy cover; (3) changes in functions were described using indicators related to flooding frequency, vegetation productivity, chlorophyll-a concentration, and surface temperature. Some studies emphasized changes in functions such as carbon storage or support for bird habitats. This review revealed that the Landsat archive can also be used to identify drivers of wetland changes over long-term periods of time. Unsurprisingly, human activities and climate change are the main threats to wetland conservation. Interestingly, the long-term effectiveness of conservation and restoration policies has been successfully measured using the Landsat archive.

1.5.2.2. The Need for Crosswalks to Common Operational Frameworks

This review highlights advantages for the scientific community of using the Landsat archive for long-term wetland monitoring; however, wetland structure and functions are rarely considered in assessments of wetland conservation status (Davidson et al., 2020). This may be due to several reasons, including a lack of correspondence between indicators derived from the Landsat archive and those developed from common operational frameworks based on in situ observations. For example, indicators of area, structure, or functions identified from the Landsat archive were frequently similar to most EBVs (Table 1.5.1) and ECVs (Table 1.5.2). Correspondence with EBVs and ECVs should be explicitly mentioned in future research to provide better information on the potential to derive and monitor these indicators using the Landsat archive.

Table 1.5.1: Number and percentage of reviewed studies by remote sensing essential biodiversity variable (RS-EBV) as defined by (Skidmore et al., 2021a). The total number of studies exceeds 351 because some studies mentioned several EBVs.

Class	RS-EBV	Number of Studies	Percentage of All Reviewed Studies	Example References
Species traits	Species phenology	0	0%	
	Species morphology	0	0%	
	Species physiology	1	0.2%	(O'Donnell and Schalles, 2016)
Species population	Population structure by age/size class	2	0.4%	(Lucas et al., 2020; O'Donnell and Schalles, 2016)
	Species distribution	0	0%	
	Species abundance	0	0%	
Community composition	Community diversity	0	0%	
	Species composition	8	1.9%	(Ghosh et al., 2017, 2016; Kolari et al., 2021; Lin et al., 2018; Luo et al., 2016; Marzvan et al., 2021; Ndayisaba et al., 2017; Yan et al., 2021)
Ecosystem functioning	Ecosystem phenology	7	1.8%	(Broich et al., 2018; Ekumah et al., 2020; Jordan et al., 2012; Mo et al., 2020; Wu et al., 2018)
	Ecosystem physiology	33	7.9%	(Dearborn and Baltzer, 2021; Díaz-Delgado et al., 2016; Wilson and Norman, 2018; Zhang et al., 2016)
	Ecosystem disturbances	8	2.0%	(Aljahdali et al., 2021; Darmawan et al., 2020; Mexicano et al., 2013; Shaeri Karimi et al., 2021)
Ecosystem structure	Spatial configuration	25	6.1%	(Dou and Cui, 2014; Qiu et al., 2009; Vanderhoof et al., 2018; Zhang et al., 2009)
	Habitat structure	326	79.7%	(Cetin, 2009; Eslami-Andargoli et al., 2010; Gong et al., 2013; Mabwoga and Thukral, 2014; Soliman and Soussa, 2011)

Table 1.5.2: Number and percentage of reviewed studies by remote sensing essential climate variable (RS-ECV) as defined by (GCOS, 2010). The total number of studies exceeds 351 because some studies mentioned several ECVs. FAPAR: Fraction of absorbed photosynthetically active radiation.

Domain	RS-ECV	Number of Studies	Percentage of All Reviewed Studies	Example References
Hydrosphere	Lakes	57	14.6%	(Liang and Li, 2019; Taravat et al., 2016)
	Soil moisture	20	5.1%	(Hiernaux et al., 2021; Thomas et al., 2011)
	River discharge	0	0%	
	Groundwater	0	0%	
Cryosphere	Glaciers	2	0.4%	(Dangles et al., 2017; Veettil et al., 2017)
	Ice sheets and shelves	0	0%	
	Snow cover	0	0%	
	Permafrost	0	0%	
	Albedo	0	0%	
Biosphere	Land use/land cover	278	71.1%	(Behling et al., 2018; Hamandawana et al., 2020; Lipp-Nissinen et al., 2018)
	Above-ground biomass	3	0.8%	(Lap et al., 2021; Lucas et al., 2020)
	Land surface temperature	2	0.5%	(Alademomi et al., 2020; Cai et al., 2016)
	Evapotranspiration	2	0.5%	(Liu and Hu, 2019; Mexicano et al., 2013)
	Fire	0	0%	
	Leaf area index	0	0%	
	Soil carbon	0	0%	
	FAPAR	0	0%	
Anthroposphere	Anthropogenic greenhouse gas fluxes	0	0%	
	Human water use	0	0%	
No ECVS in the reviewed study		27	6.9%	

While this review shows that functional indicators have been derived from the Landsat archive, it also highlights that wetland functions and ecosystem services have rarely been assessed in long-term monitoring, and when they have, the assessment used an expert-based approach. Future studies should assess changes in wetland ecosystem functions and services using recognized and operational approaches, such as functional assessment (Maltby and Barker, 2009) or the Rapid Assessment of

Wetland Ecosystem Services (McInnes and Everard, 2017). However, it should be kept in mind that the spatial resolution of Landsat is insufficient for delineating small wetlands and/or small hydrogeomorphic units within wetlands and for assessing their functions. This is especially true for Landsat MSS images that have a spatial resolution of 80 m. In these cases, it is necessary to use a field approach. In addition, some wetland functions cannot yet be assessed from space because canopies prevent the direct observation of important features such as soil bacteria.

1.5.3. Extend the Monitoring Period backwards and forwards in Open Access

This review highlights that the Landsat archive can be used to map long-term and fine-grained changes in patterns, such as the spread of invasive species or the phenological response of vegetation after natural hazards, which would have been difficult to observe over shorter periods and/or at a larger scale. Although the Landsat archive has been available for 50 years, most studies that used it, including the most recent ones, covered 20–30 years. This could be due to the challenge of combining Landsat MSS images, which have different spatial and spectral resolutions than Landsat TM, ETM+, and OLI images. However, MSS images provide the ability to look back an additional decade, which would be valuable for improving the understanding of responses of wetlands to human development and climate change. Future research should extend the temporal monitoring period to at least 50 years by including not only new Landsat 9 images but also older MSS images, although some wetlands may not be detected and monitored due to the broad spatial resolution of these data.

The combination of topographic data with spectral data significantly improves wetland delineation, and several high spatial resolution global DEMs are available in open access (Uuemaa et al., 2020). Moreover, the future monitoring of wetland structure and function could be improved by using new variables such as the global canopy height model derived from GEDI and Landsat data (Potapov et al., 2021) or Sentinel-1 interferometric coherence time series (Minotti et al., 2021).

The large number of long-term wetland monitoring studies in this review from 2009 to 2022, especially in developing countries, shows the positive effect of providing open access Landsat archive data for wetland conservation worldwide, especially in developing countries where managers have limited resources and funds for monitoring highly threatened wetlands (Rebelo et al., 2018). In this context, we remind practitioners that they should always acknowledge the USGS for making the Landsat data freely available.

1.5.4. The Era of AI and Cloud Computing

1.5.4.1. Progress in AI and Cloud Computing Provide New Opportunities for Long-Term Wetland Monitoring

This review illustrates how recent advances in AI (e.g., cloud masking, classification, and regression) have been used to analyze Landsat archive data automatically. Nevertheless, two points of progress must be discussed. The first concerns the use of reference data, which remain challenging to collect in some regions and/or for the past. This may explain why the accuracy of indicators derived from earlier Landsat images was rarely assessed. Future studies could make greater use of archive field databases, such as the Global Biodiversity Information Facility (GBIF, 2022) for flora and fauna or the GlobalSoilMap (Rossiter, 2016) for soils, to further calibrate and validate models. As an alternative to field surveys, several tools such as TimeSync and CollectEarth support the collection of reference points via the visual interpretation of high-spatial-resolution images (Stehman and Foody, 2019).

The second point concerns the analysis approach used. This review found that most studies used only cloud-free Landsat images, which discards a large amount of imagery, and that each year was modeled individually, which increases uncertainty in detecting change. Future research should focus on modeling the temporal profile using most images available in the Landsat archive. Cloud removal methods are now available that allow denser Landsat time series to be used over the entire globe, which can improve long-term monitoring, including in tropical areas. For example, (Arévalo et al., 2020) recently developed a set of tools in Google Earth Engine for this purpose. We calculated the normalized difference vegetation index (NDVI) time series in the Iraqi Hammar Marsh (Ramsar site ID 2242) from the Landsat archive for the period 1984–2022 as an example (Figure 1.5.1). Filtering Landsat data contributes to maintaining a high-quality time series, because it reduces the redundancy of information, residual noises in the images, and processing time and space.

This review also shows the relevance of cloud computing for processing the Landsat archive over large areas (Hemati et al., 2021). Cloud computing is an opportunity to reduce the technology gaps between countries in the Global North and South. All studies that used cloud computing chose the GEE for its easy access and use and for the availability of the entire Landsat archive pre-processed for surface reflectance (Level 2). However, future studies could also use the lesser-known NASA Earth Exchange (Nemani, 2012) or Microsoft Planetary Computer platforms, which are open access alternatives to GEE.

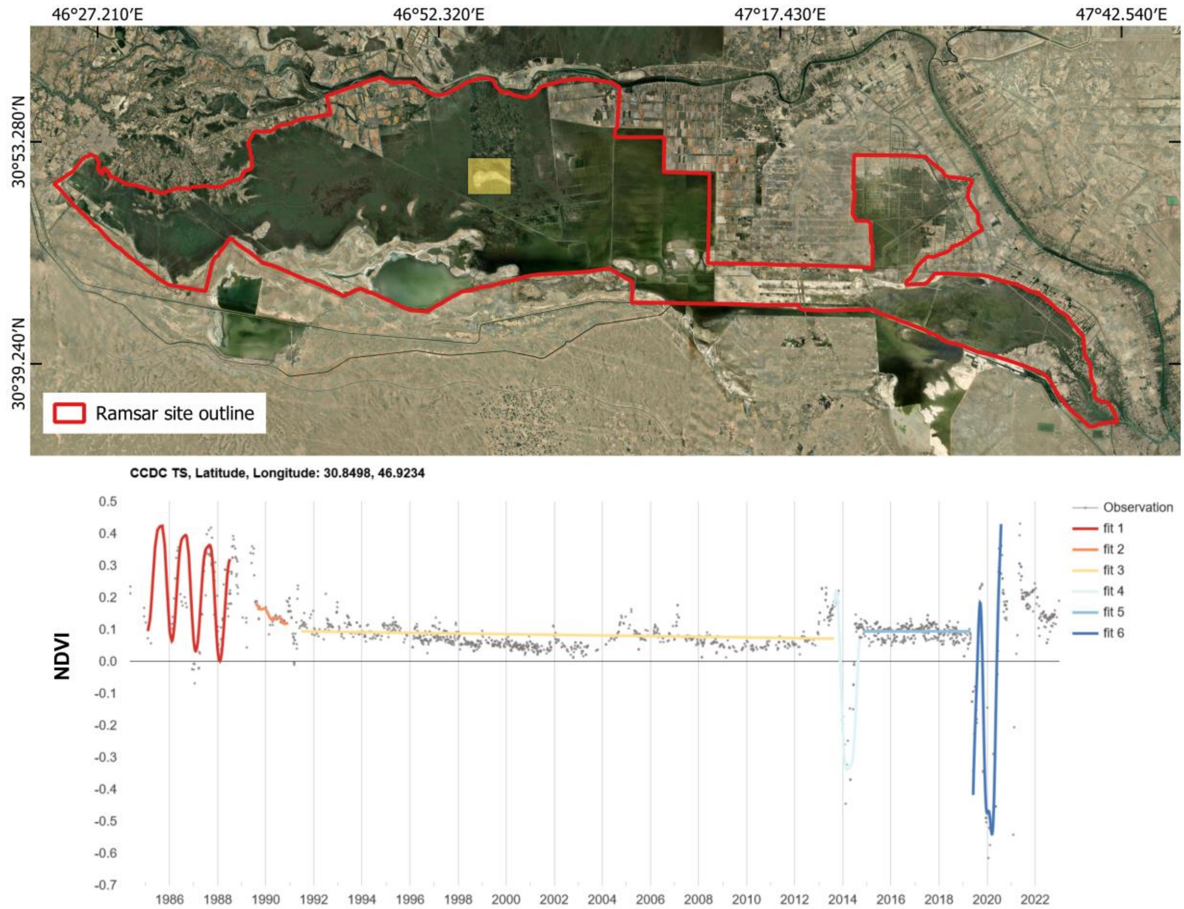

Figure 1.5.1: Example of the normalized difference vegetation index (NDVI) time series for a pixel (yellow rectangle) in the Iraqi Hammar Marsh (Ramsar site ID 2242) derived from the Landsat archive from 1984 to 2022 obtained using the CCDC algorithm developed by Arévalo et al. (2020) in Google Earth Engine. Grey dots indicate Landsat observations available in the pixel and used for harmonic regression of the time series. The fits in the colored lines indicate time segments detected by the CCDC algorithm: a change in color indicates a change in land cover/land use.

1.5.4.2. Bridging the Gap between Remote Sensing and Wetland Monitoring

This review emphasizes that the analysis and interpretation of the Landsat archive differs among scientific disciplines. Studies published in environmental journals used field observations to provide new insights on wetland ecosystem functioning but rarely used the most advanced AI or cloud-computing tools. Conversely, studies published in remote sensing journals used innovative methods to analyze large datasets from the Landsat archive, but the changes detected were rarely interpreted or validated using the visual interpretation of high-spatial-resolution images. Thus, as described by Pettorelli et al. (2014), scientists in environmental and remote sensing communities need to share skills and knowledge even more to facilitate and improve ecosystem monitoring using methods known to be effective. In this context, using open-source solutions provides more effective ways to share methods and thus increases reproducibility by providing widely available methods.

1.6. Conclusions

This review highlighted that the Landsat archive was used in hundreds of scientific studies for the global long-term monitoring of wetlands, especially in developing countries where managers have limited resources and funds for monitoring highly threatened wetlands. The continuity of Landsat missions since 1972 enables the monitoring of wetland areas, structure, and functions including fine-grained changes in patterns, which would have been difficult to observe over shorter periods and/or at a broader spatial resolution. This review also emphasizes that new cloud-computing tools enable dense Landsat times series to be processed over large areas. Future research should study more extensively certain areas or wetland types that are still poorly explored, extend the monitoring period backwards and forwards, make greater use of archive field databases to further calibrate and validate models, focus on modeling the temporal profile using most of the images available in the Landsat archive, crosswalk to common operational frameworks such as functional assessment procedure or essential biodiversity variables, and bridge the gap between environmental and remote sensing scientific communities.

CONCLUSION TO CHAPTER 1

In this chapter, we have reviewed the state of scientific knowledge on the use of Landsat archives for long-term wetland monitoring. This state of the art has led us to make several recommendations on this issue, in particular to increase the diversity of wetlands studied and to foster the use of continuous time series analysis algorithms, especially through the use of cloud computing.

Since Landsat archives have been made openly available, they have been increasingly used to monitor wetlands. Although technological advances make AI-based remote sensing data processing and analysis methods increasingly powerful and accessible, a significant number of studies are still conducted using the traditional diachronic approach. This approach typically uses only two or three images to analyse land cover and land use change, whereas newer time series analysis methods make optimal use of the Landsat archive because they are based on continuous approaches. In particular, several studies have demonstrated the value of CCDC (Continuous Change Detection and Classification), which can be used on the Google Earth Engine cloud computing platform to detect changes in land cover.

These observations led to the following two main research questions:

- Can the CCDC method be used to study the evolution of wetlands in terms of area, composition, and functions based on the Landsat archive?

- Is the CCDC method, still using the Landsat archive, applicable to wetlands worldwide despite the diversity of bioclimatic and meteorological conditions?

To answer these questions, we selected five Ramsar sites with different bioclimatic conditions and habitat conservation issues. The CCDC was first applied to four of these sites to assess the wetlands from a long-term functional point of view (Chapter 3). It was then applied to the fifth site to identify changes in the area and composition of its wetlands over several decades (Chapter 4) and to analyse these changes in the light of public policy (Chapter 5).

CHAPTER 2. STUDY AREAS AND MATERIALS

This chapter aims to present the study sites, data, and tools used in this thesis. Firstly, the five Ramsar study sites in four countries are described: one in Sweden, two in France, one in Algeria, and one in Brazil. Secondly, the remote sensing data (i.e. resolutions, products) and the reference data used for the different analyses are presented. Then, the principle and functioning of the Continuous Change Detection and Classification (CCDC) algorithm are described in detail, as well as the programming code used and produced.

2.1. Ramsar sites

The sites investigated are all Ramsar sites.

2.1.1. The Ramsar Convention

The Ramar Convention, whose full name is the Convention on Wetlands of International Importance Especially as Waterfowl Habitat, is an international treaty for the conservation and wise use of inland and marine wetlands. Established in 1971 in Ramsar, Iran, it is currently the oldest multilateral international environmental agreement and the only treaty covering a single ecosystem (Bridgewater and Kim, 2021). The number of Parties to the Ramsar Convention has increased from 18 in 1971 to 172 in 2024, representing almost 90% of the countries recognized by the United Nations (Gardner and Davidson, 2011; "The Ramsar Convention on Wetlands," 2024). Parties are committed to three main obligations: (i) to designate at least one wetland of international importance, (ii) to use and apply the concept of 'wise use' of wetlands, and (iii) to participate in international cooperation (Gardner and Davidson, 2011). According to Article 1, wetlands under the Convention are any "area of marsh, fen, peatland, or water; whether natural or artificial permanent or temporary; with water that is static or flowing, fresh, brackish, or salt, including areas of marine water the depth of which does not exceed six meters" (Ramsar Convention Secretariat, 2006a). As stated in Article 3, the wise use of wetlands is the first pillar of the Convention and is defined as "the maintenance of their ecological character, achieved through the implementation of ecosystem approaches, within the context of sustainable development". This definition can be organized around several mechanisms that can be activated by stakeholders, such as the implementation of national wetland legislation, research and monitoring programmes, and awareness and education projects (Gardner and Davidson, 2011). Wetland of International Importance designation is the second pillar, with a total of 2,517 Ramsar sites worldwide as of June 5, 2024, covering nearly 257,289,430 hectares (Figure 2.1.1) (Ramsar Convention Secretariat, 2024). Lastly, the third pillar relates to international cooperation, particularly the creation of observatories and international and interregional programmes on wetlands, such as the Mediterranean Wetlands Initiative (MedWet) launched in 1991 ("MedWet," 2024).

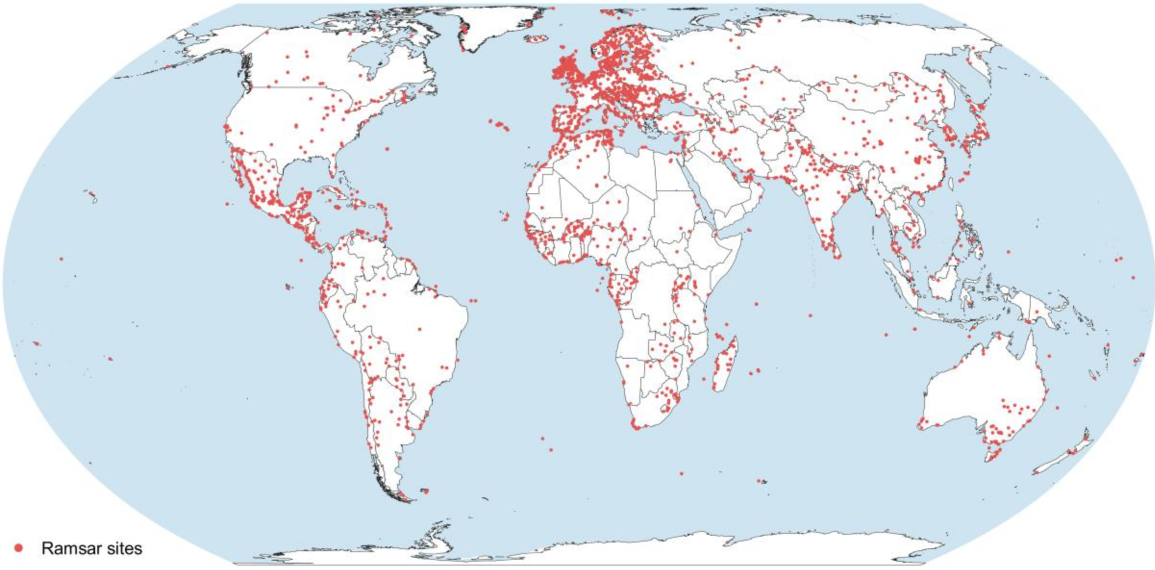

Figure 2.1.1: Ramsar sites location worldwide (n = 2517). Source: Ramsar Sites Information Services (https://rsis.ramsar.org/?language=en&pagetab=0)

Ramsar Convention's mission can be summarised as the "conservation and wise use of wetlands through local and national actions and international cooperation, as a contribution towards achieving sustainable development throughout the world." (Ramsar Convention Secretariat, 2016). To carry out this mission, several major objectives have been defined within a strategic plan during the COPs (Conference of Parties) for a given period. These objectives also correspond to those defined within the framework of other conventions and multilateral agreements, such as the Sustainable Development Goals (SDGs). Since the first Ramsar Strategic Plan in 1997, three others have followed before the 4th was defined. In the context of this 4th Plan established for the 2016-2024 period, the priorities are three strategic objectives and one operational objective (Ramsar Convention Secretariat, 2016): (1) Addressing the drivers of wetland loss and degradation; (2) Effectively conserving and managing the Ramsar site network; (3) Wisely using all wetlands; and (4) Enhancing implementation. Various data acquired by the stakeholders are then used to inform qualitative and quantitative indicators, which in turn provide information on the achievement of these objectives. In this way, stakeholders produce national reports every three years before each COP and send them to the Ramsar Secretariat (Davidson et al., 2019). Monitoring and measurements are carried out on Ramsar sites and, more generally, on all of a country's wetlands. Stakeholders then provide a qualitative assessment of changes in the ecological character of wetlands, providing a wealth of information that can be analysed over time (Davidson et al., 2019). However, the proper implementation of these reports and the sharing of up-to-date data remain a challenge for some stakeholders, and the relevance and effectiveness of the indicators used to assess wetlands are frequently questioned by the scientific community (Bridgewater and Kim, 2021; Davidson et al., 2019). Despite the international application and implementation of the Ramsar Convention, wetlands continue to decline, with 35% of the world's wetlands having disappeared since 1970 (Courouble et al., 2021).

2.1.2. Ramsar sites characteristics

Each stakeholder may select one or more sites, the choice being motivated by ecological, faunistic, floristic, or hydrological issues, as specified in Article 2 (Gardner and Davidson, 2011). Nine criteria define whether or not a wetland is relevant from the perspective of the Ramsar Convention, based on the presence of habitats and/or species associated with wetlands and being endangered (Table 2.1.1) (Stroud and Davidson, 2021).

Table 2.1.1: Summary of the nine criteria used in the Ramsar Convention for designating a new Ramsar site. Based on (Stroud and Davidson, 2021)

Type	Criteria	Description
Criteria based on species and ecological communities	Criterion 1	A wetland should be considered internationally important if it contains a representative, rare, or unique example of a natural or near-natural wetland type found within the appropriate biogeographic region.
	Criterion 2	A wetland should be considered internationally important if it supports vulnerable, endangered, or critically endangered species or threatened ecological communities.
	Criterion 3	A wetland should be considered internationally important if it supports populations of plant and/or animal species important for maintaining the biological diversity of a particular biogeographic region.
	Criterion 4	A wetland should be considered internationally important if it supports plant and/or animal species at a critical stage in their life cycles, or provides refuge during adverse conditions.
Specific criteria based on waterbirds	Criterion 5	A wetland should be considered internationally important if it regularly supports 20,000 or more waterbirds.
	Criterion 6	A wetland should be considered internationally important if it regularly supports 1% of the individuals in a population of one species or subspecies of waterbird.
Specific criteria based on fish	Criterion 7	A wetland should be considered internationally important if it supports a significant proportion of indigenous fish subspecies, species or families, life history stages, species interactions, and/or populations that are representative of wetland benefits and/or values and thereby contribute to global biological diversity.
	Criterion 8	A wetland should be considered internationally important if it is an important source of food for fishes, spawning ground, nursery, and/or migration path on which fish stocks, either within the wetland or elsewhere, depend
Specific criteria based on other taxa	Criterion 9	A wetland should be considered internationally important if it regularly supports 1% of the individuals in a population of one species or subspecies of wetland-dependent non-avian animal species.

The Ramsar Convention has its own classification system for wetlands, which includes three main types: marine/coastal, inland, and human-made wetlands (Table 2.1.2) (Ramsar Convention Secretariat, 2006a). Marine/coastal wetlands include habitats ranging from sandbanks and mudflats to mangroves and coral reefs. Inland wetlands include flowing and permanent surface waters (e.g. rivers, lakes), marshes, peat bogs, and alluvial forests. Lastly, artificial wetlands include rice paddies, quarries, and dam reservoirs.

Table 2.1.2: Ramsar Classification System of wetlands (Ramsar Convention Secretariat, 2006a). A single asterisk (*) indicates floodplain wetlands, such as seasonally flooded grasslands (including natural wet meadows), shrublands, woodlands, or forests. Double asterisks (**) indicate intensively managed or grazed wet meadows or pastures.

Level 1	Level 2	Description
Marine/ Coastal wetlands	A	Permanent shallow marine waters less than six meters deep at low tide; includes sea bays and straits.
	B	Marine subtidal aquatic beds; includes kelp beds, sea-grass beds, tropical marine meadows
	C	Coral reefs
	D	Rocky marine shores; includes rocky offshore islands and sea cliffs.
	E	Sand, shingle, or pebble shores; includes sand bars, spits, and sandy islets; includes dune systems.
	F	Estuarine waters; permanent water of estuaries and estuarine systems of deltas
	G	Intertidal mud, sand, or salt flats
	H	Intertidal marshes; includes salt marshes, salt meadows, saltings, and raised salt marshes; includes tidal brackish and freshwater marshes.
	I	Intertidal forested wetlands; includes mangrove swamps, nipah swamps, and tidal freshwater swamp forests.
	J	Coastal brackish/saline lagoons; brackish to saline lagoons with at least one relatively narrow connection to the sea
	K	Coastal freshwater lagoons; includes freshwater delta lagoons.
Inland wetlands	L	Permanent inland deltas
	M	Permanent rivers/streams/creeks; includes waterfalls.
	N	Seasonal/intermittent/irregular rivers/streams/creeks
	O	Permanent freshwater lakes (over 8 ha); includes large oxbow lakes.
	P	Seasonal/intermittent freshwater lakes (over 8 ha); includes floodplain lakes.
	Q	Permanent saline/brackish/alkaline lakes
	R	Seasonal/intermittent saline/brackish/alkaline lakes and flats*
	Sp	Permanent saline/brackish/alkaline marshes/pools
	Ss	Seasonal/intermittent saline/brackish/alkaline marshes/ pools*
	Tp	Permanent freshwater marshes/pools; ponds (below 8 ha), marshes, and swamps on inorganic soils; with emergent vegetation water-logged for at least most of the growing season
	Ts	Seasonal/intermittent freshwater marshes/pools on inorganic soil; includes sloughs, potholes, seasonally flooded meadows, and sedge marshes*
	U	Non-forested peatlands; includes shrub or open bogs, swamps, fens
	Va	Alpine wetlands; includes alpine meadows, and temporary waters from snowmelt.
	Vt	Tundra wetlands; includes tundra pools, temporary waters from snowmelt
	W	Shrub-dominated wetlands; Shrub swamps, shrub-dominated freshwater marsh, shrub carr, alder thicket; on inorganic soils*
	Xf	Freshwater, tree-dominated wetlands; includes freshwater swamp forests, seasonally flooded forests, and wooded swamps; on inorganic soils*

	Xp	Forested peatlands; peat swamp forest*
	Y	Freshwater springs; oases
	Zg	Geothermal wetlands
	Zk	Subterranean karst and cave hydrological systems
Human-made wetlands	1	Aquaculture (*e.g.* fish/shrimp) ponds
	2	Ponds; includes farm ponds, stock ponds, and small tanks; (generally below 8 ha)
	3	Irrigated land; includes irrigation channels and rice fields
	4	Seasonally flooded agricultural land**
	5	Salt exploitation sites; salt pans, salines, etc.
	6	Water storage areas; reservoirs/barrages/dams/impoundments; (generally over 8 ha)
	7	Excavations; gravel/brick/clay pits; borrow pits, mining pools
	8	Wastewater treatment areas; sewage farms, settling ponds, oxidation basins
	9	Canals and drainage channels, ditches

In addition to national reports, the data and information for a Ramsar site are made available to the public on the Ramsar Sites Information Service website (https://rsis.ramsar.org/about?language=en). Each site is listed with its geographical boundaries, the different habitats that it includes, and a summary of the reasons for its Ramsar designation.

2.1.3. Selected Ramsar sites

In this section, five Ramsar sites are described: four sites in Chapter 4 (i.e., Pirttimysvuoma, Marais Vernier et Vallée de la Risle Maritime, Oasis de Ouled Saïd, and Taiamã Ecological Station), and one site in Chapters 5 and 6 (i.e., the Marais Poitevin). Those four study sites were chosen because of their different bioclimatic conditions and levels of cloud cover, while the Marais Poitevin was chosen because it represents the largest French Atlantic coastal wetland and has been subject to strong anthropogenic pressures for several decades.

2.1.3.1. Pirttimysvuoma

Located in northern Sweden, Pirrtimysvuoma was designated as a Ramsar site in 2013 (no 2177; center coordinates 68°16′N 20°44′E) and is a mire, bogs, and fen complex of 2,586 ha (Figure 2.1.2). Elevation varies between 500 and 700 meters and the climate is subarctic (Köppen Dfc classification). Wetland habitats listed in the Ramsar Convention include wooded (Xp) and non-wooded peatlands (U), permanent rivers (M), lakes (O), and permanent freshwater marshes (Tp). There are no artificial wetlands within this site. Few human activities are present, apart from extensive reindeer grazing.

Regarding remote sensing data, this site intersects four Landsat tiles (WRS Path/Row 194/12, 195/12, 196/12 et 197/12). Still, due to its high latitude, the number of available images per tile is lower than other sites, with an average of 340 images available over the 1984-2021 period from all satellites combined (i.e., Landsat 4 to 8).

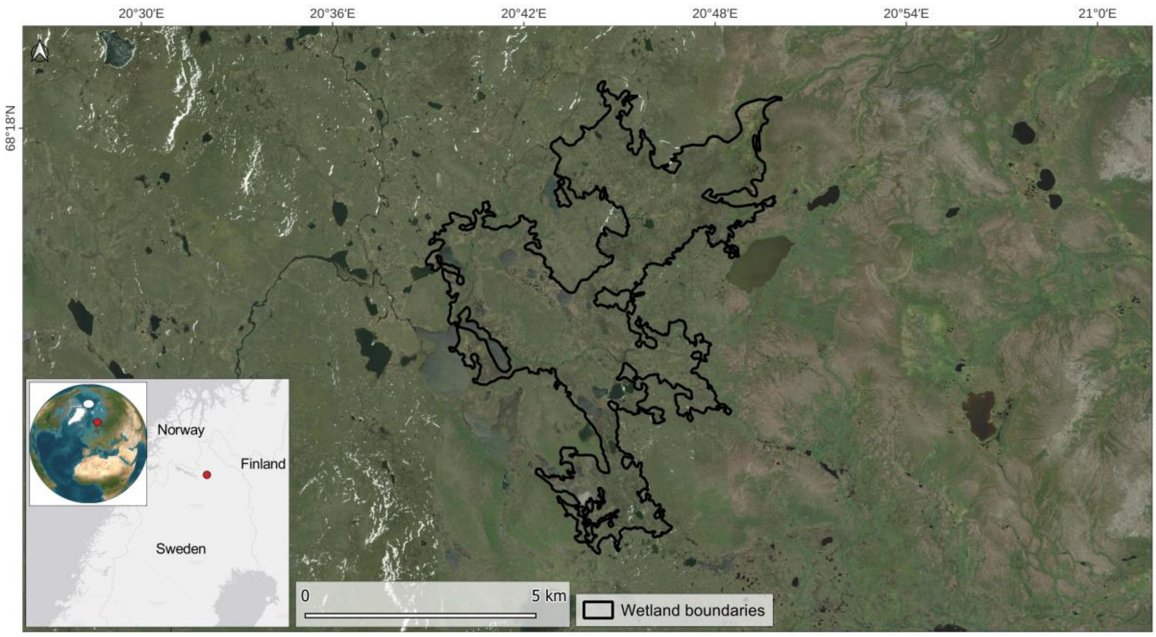

Figure 2.1.2 : Location and delineation of the Pirrtimysvuoma Ramsar site (no 2177), Sweden. Basemap: ESRI.

2.1.3.2. Marais Vernier et Vallée de la Risle Maritime

Located near the entrance to the Seine estuary, the Marais Vernier et Vallée de la Risle Maritime site (no 2247; center coordinates 49°25'N 00°28'E) is a wetland located in France on the north coast of the English Channel (Figure 2.1.3). Elevation is very low, ranging from 0 to 10 meters, and the climate is oceanic temperate (Köppen Cfb classification). Designated as a Ramsar site in 2015, this 9,565-ha wetland forms a complex of freshwater and brackish habitats with a high conservation value for amphibians, fish, and natural habitats such as peat bogs (Lautier and Meurisse, 2003). Wetland habitats listed in the Ramsar Convention include wooded (Xp) and non-wooded peatlands (U), permanent rivers (M), lakes (O), permanent freshwater marshes (Tp), estuarine waters (F) and intertidal mud, sand, or salt flats (G). Human-made wetlands are represented by seasonally flooded agricultural land (4), ponds (2), and canals and drainage channels (9). Human activities such as shipping, agriculture, and water management and use such as drainage are significant, with the added risks of pollution and the development of invasive species. Conservation measures have been implemented to reduce the impact of these threats, including species and habitat management programmes, and hydrological restoration.

This site intersects three Landsat tiles (WRS Path/Row 200/26, 201/25, et 201/26), each with around 640 images available from all sensors combined over the 1984-2021 period.

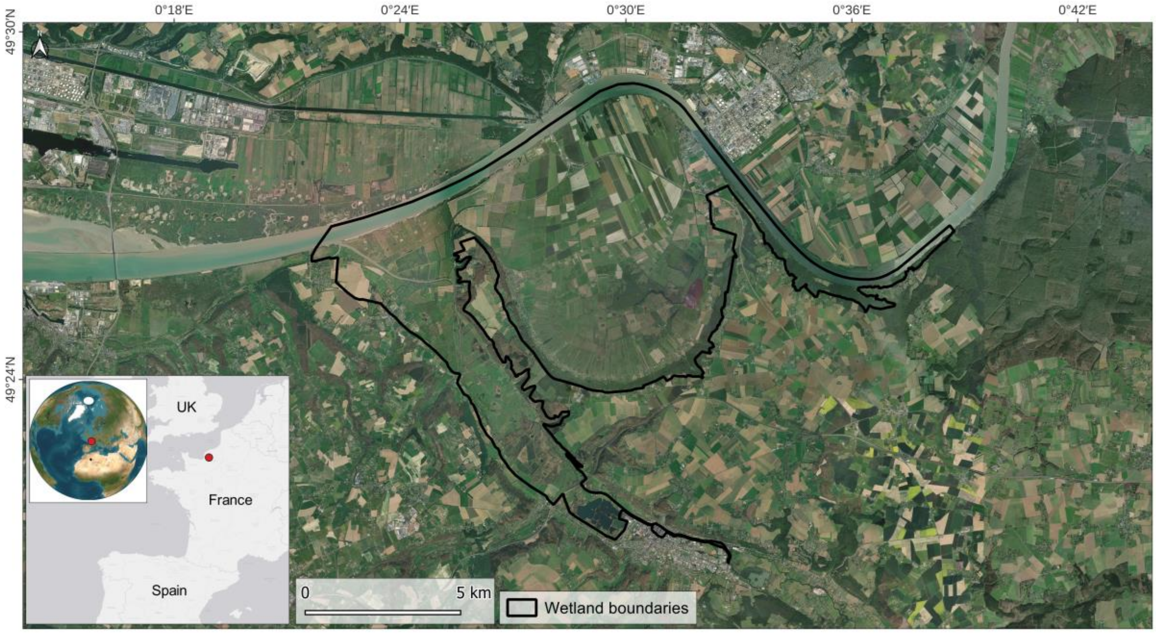

Figure 2.1.3: Location and delineation of the Marais Vernier et Vallée de la Risle Maritime Ramsar site (no 2247), France. Basempa: ESRI.

2.1.3.3. Oasis de Ouled Saïd

The Oasis de Ouled Saïd site (no 1060 ; center coordinates 29°26’N 00°17’E) is an anthropogenic wetland located in the Algerian Sahara (Figure 2.1.4). Designated as a Ramsar site since 2001, this oasis covers 24,400 ha in a arid climate (Köppen BWh classification) at an elevation ranging from 240 to 330 meters. A historical remnant of an ancient river has formed a topographical depression in the form of a diagonal running from the north-east to the south-west of the site, which is mainly made up of desert areas. The water management system that has been developed is specific to the hydrological conditions of the oasis: a system known as “foggara”, which consists of digging galleries beneath the surface of the ground to channel water to crops and dwellings (“Oasis de Ouled Saïd | Ramsar Sites Information Service,” 2023). Wetland habitats under the Ramsar Convention include freshwater springs (Y), karst and other subterranean hydrological systems (Zkb), followed by permanent (Ts), and seasonal

(Ss) natural ponds. Human-made wetlands are irrigated cropland (3), water storage areas (6), and canals (9). Water use has become one of the main threats affecting the wetland, along with droughts and desertification. However, it is also this active water management that can counter these threats.

This site intersects three Landsat tiles (WRS Path/Row 196/40, 197/39, et 197/40), and due to the high level of annual sunshine, the average number of available images is close to 1,000 per tile for all sensors combined over the 1984-2021 period.

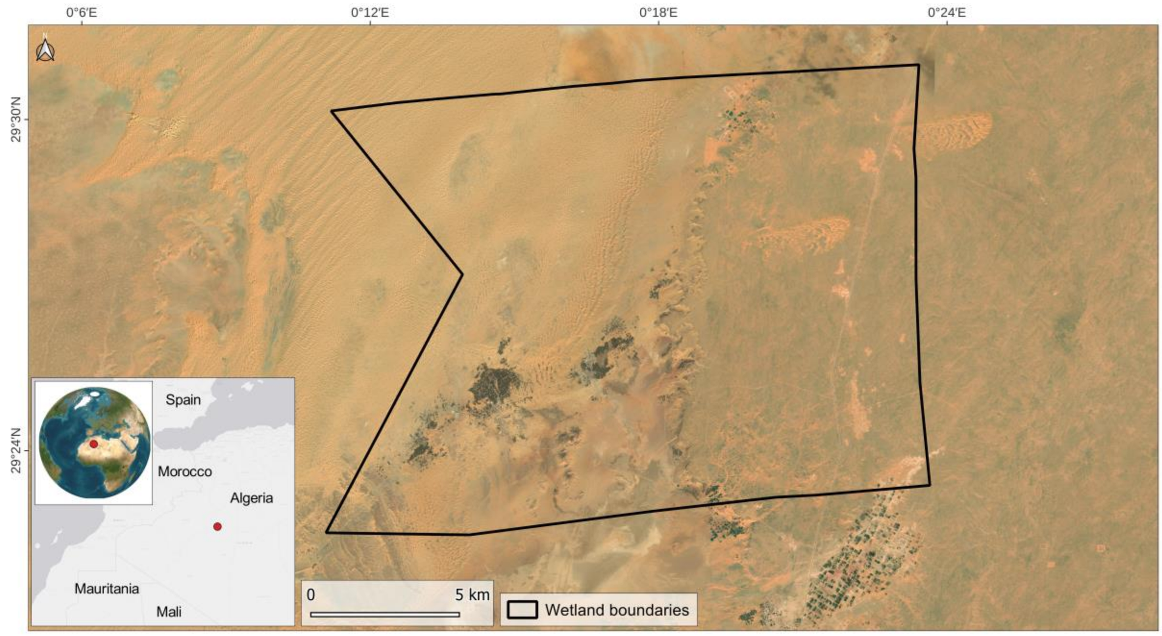

Figure 2.1.4: Location and delineation of the Oasis d'Ouled Saïd Ramsar site (no 1060), Algeria. Basemap: ESRI.

2.1.3.4. *Taiamã Ecologocial Station*

The Taiamã Ecological Station site (no 2363; center coordinates 16°51'S 57°30'W) is located in the Brazilian part of the Pantanal, one of the world's largest wetlands (Figure 2.1.5). Designated as a Ramsar site in 2018, this 11,555-hectare inland wetland presents major biodiversity challenges, with a high abundance of birds and fish, as well as the presence of endangered mammals such as the Jaguar. Flooding from the River Paraguay plays a key role in the functioning of the site and, more broadly, of the Pantanal, resulting in the dominance of various seasonally flooded habitats, while continuously flooded habitats account for between 20% and 30% of the total surface area. The climate is humid tropical monsoonal (Köppen Am classification) and the elevation ranges from 90 to 110 meters. Wetland habitats under the Ramsar Convention include permanent freshwater marshes (Tp), and seasonal freshwater marshes (Ts), followed by wet forests (Xf) and permanent freshwater lakes (O). There are no human-made wetlands on the site. There are many threats around the site, such as livestock farming, hunting and fishing, tourism, and water management and use, but the main threat is fire.

This site intersects a single Landsat tile (WRS Path/Row 227/72) with more than 970 available images for all sensors combined over the 1984-2021 period.

Figure 2.1.5: Location and delineation of the Taiamã Ecological Station Ramsar site (no 2363), Brazil. Basemap: ESRI.

2.1.3.5. *Marais Poitevin*

The Marais Poitevin (no 2363; center coordinates 46°21'N 01°01'W) is located on the Atlantic coast and is the second-largest wetland in France (Figure 2.1.6). Designated as a Ramsar site since 2023, it covers around 100,000 ha in a temperate oceanic climate (Köppen Cfb classification) and has an elevation ranging from 0 to 10 meters. Once covered by the sea, this marsh was created by the construction of dykes and canals from the 13th century onwards for agriculture and urban development (Godet and Thomas, 2013; Pouzet et al., 2015). Wetland habitats under the Ramsar Convention include estuarine waters (F), intertidal mud, sand, or salt flats (G), permanent (M) and seasonal (N) rivers, followed by peat bogs (U), and wet forests (Xf). Human-made wetlands include irrigated land (3), canals and ditches (9), and seasonally flooded agricultural areas (4). Significant conservation issues are present, particularly for wet grassland habitats and the avifauna that depend on them for breeding and migration. However, agricultural intensification and urbanisation have led to a significant loss of these grasslands, particularly during the second half of the 20th century (Godet and Thomas, 2013), although this degradation continues nowadays.

The site intersects two Landsat tiles (WRS Path/Row 200/28 et 201/28) with around 800 available images per tile for all sensors combined over the 1984-2021 period.

It is important to note that the analyses are based on the official wetland boundary used by policymakers and managers, and not just the official Ramsar site boundary, which follows the contours of the Natura 2000 site ("Marais Poitevin | Ramsar Sites Information Service," 2024).

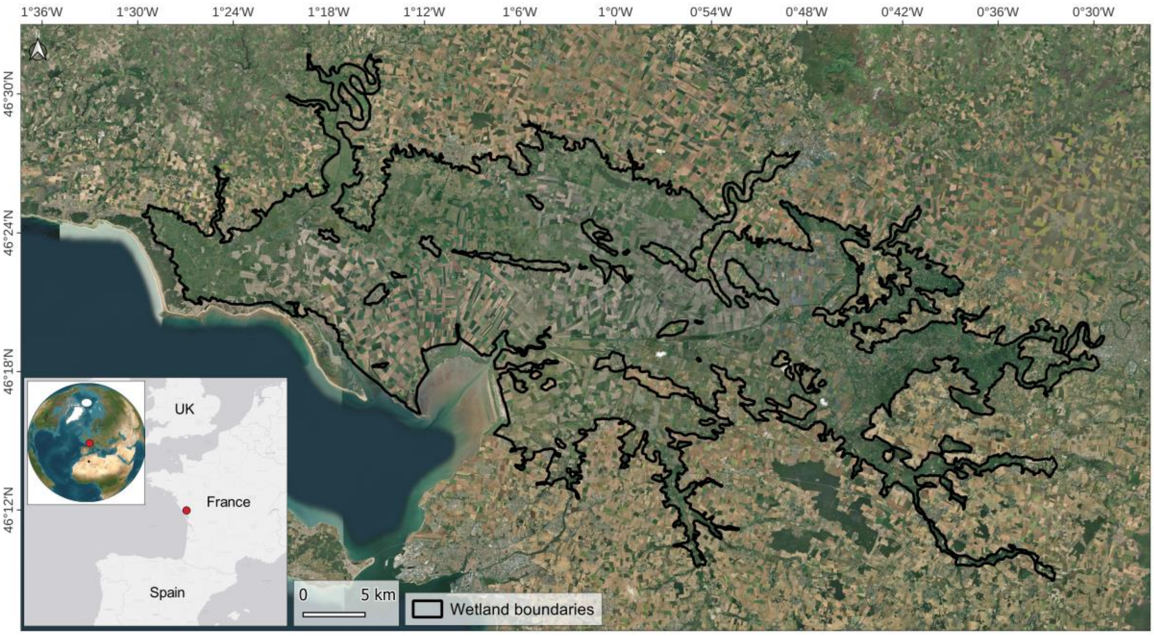

Figure 2.1.6: Location and delineation of the Marais Poitevin Ramsar site (no 2531), France. Basemap: ESRI.

2.2. The Landsat archive

The satellite remote sensing data used in this thesis are exclusively from the Landsat archive. In this section, the characteristics and resolutions of the Landsat time series are described, together with the type of pre-processed products used.

2.2.1. The Landsat mission

The Landsat mission is the longest Earth observation program available to date, providing nearly 50 years of continuous satellite imagery across the globe (Wulder et al., 2022). Jointly administered by the US Geological Survey (USGS) and the National Aeronautics and Space Administration (NASA), this program was the first in history to focus specifically on observation of the Earth's surface, with the launch of the first Landsat 1 satellite in 1972. This was followed by eight more satellites, until today with the launch of Landsat 9 in 2021 (Masek et al., 2020) (Figure 2.2.1).

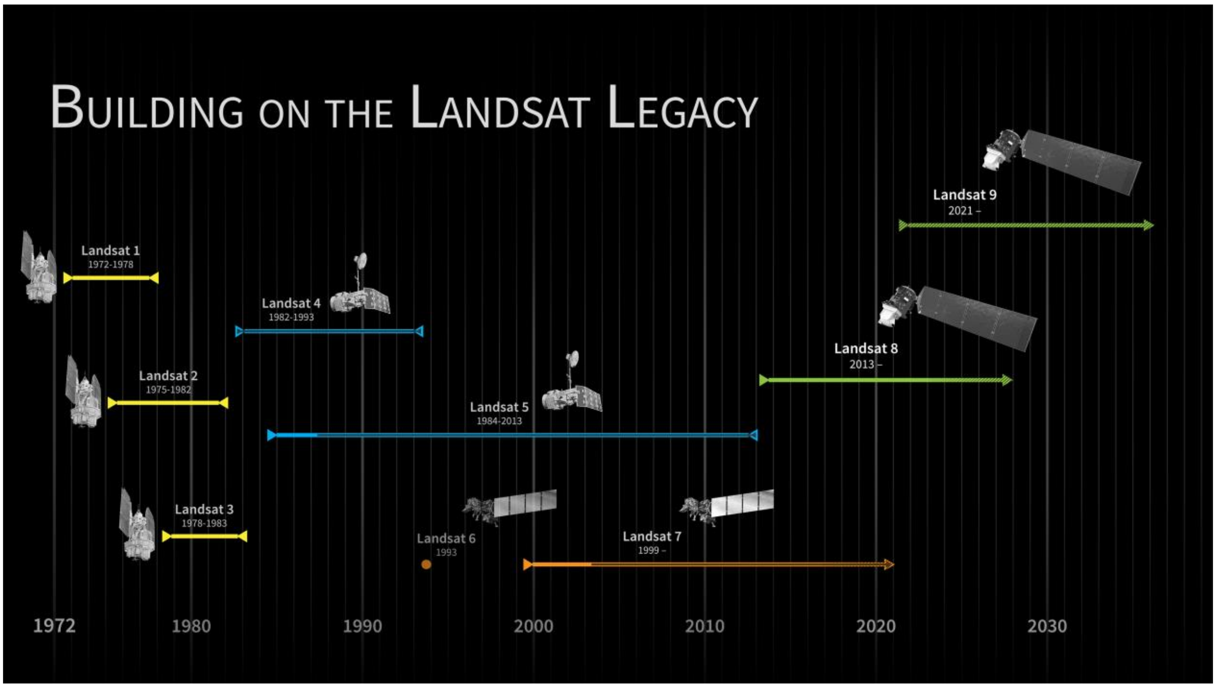

Figure 2.2.1: Summary of the Landsat satellite launch timeline from the start of the program in 1972 to the present day. Note that Landsat 6 was lost during launch. Credits: NASA's Scientific Visualization Studio (https://svs.gsfc.nasa.gov/11433)

The special feature of the program lies in its aim to ensure continuity between the various satellites, enabling temporal analyses to be carried out using images from different sensors without interruption (Wulder et al., 2016). Landsat satellites are all launched into low Earth orbit (ranging from 700 to 900 km of altitude) in sun-synchronous orbit, enabling them to capture images with an average swath of 185 km and high spatial resolution, covering the entire Earth's surface. The average revisit time for sensors at the same location is 16 days but can be reduced to 8 days with the overlapping of Landsat 8 and 9 (Wulder et al., 2022). Since 2008, the Landsat archive has been available in open access for free from the start of the program to the present day, giving access to more than 21 million in August 2024 (https://landsat.usgs.gov/landsat-archive-dashboard; on 14/08/2024) (Wulder et al., 2012) (Figure 2.2.2).

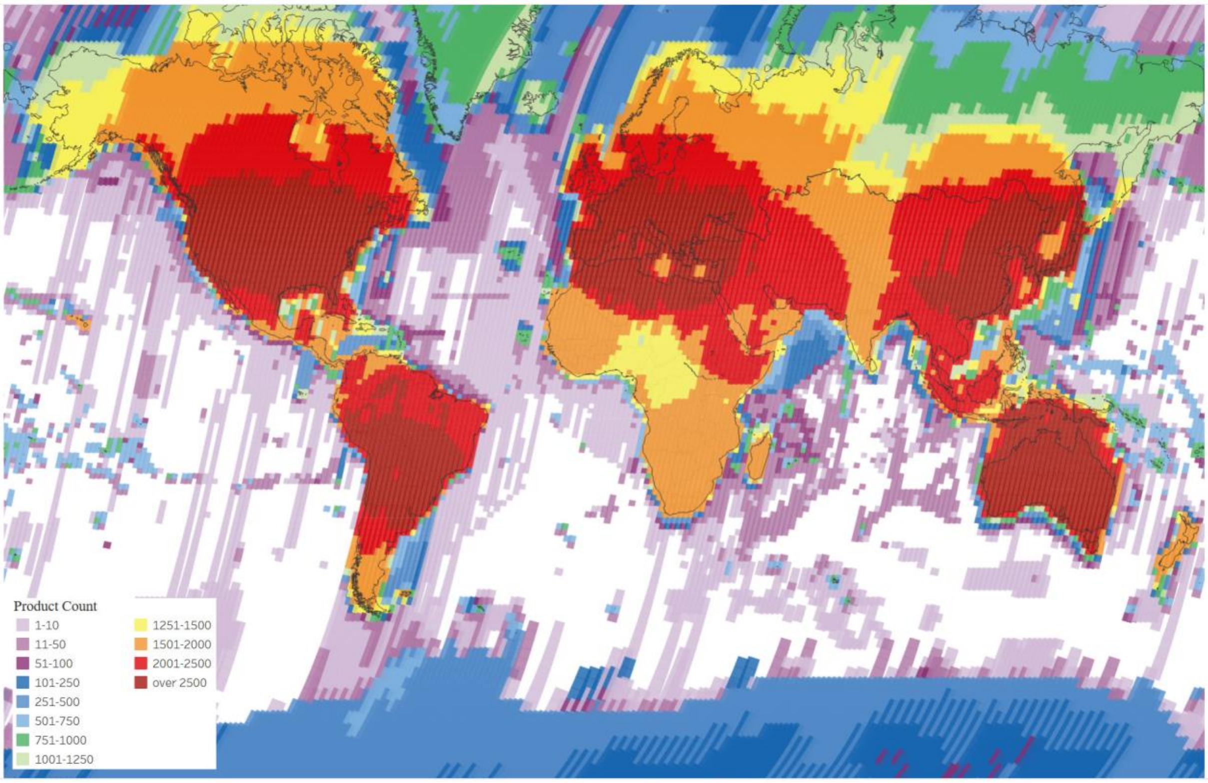

Figure 2.2.2: Landsat archive total sum of images (all collections combined) per tile, from Landsat 4 to 9 on the 20th August 2024. Source: USGS ([https://landsat.usgs.gov/landsat-archive-dashboard)](https://landsat.usgs.gov/landsat-archive-dashboard).

2.2.2. The Landsat sensors

Throughout the development of the program, new remote sensing sensors were developed to continue the monitoring of the Earth's surface initiated at the beginning of the 1970s, while at the same time improving certain technical characteristics (Table 2.2.1). After the first Multispectral Scanner (MSS) sensor, onboard Landsat 1-5 satellites, and capturing images in 4 bands at 80m spatial resolution, the Thematic Mapper (TM), implemented from 1982 onwards, showed a marked improvement. The number of visible and multispectral bands increased to six, and radiometric and spatial resolution improved from 6 to 8 bits and from 60 to 30 meters respectively. The first thermal infrared band also appeared, with a resolution of 120 meters. Following the failed launch of Landsat 6 in 1993, which carried the Enhanced Thematic Mapper (ETM) sensor, Enhanced Thematic Mapper Plus (ETM+) was developed and launched on Landsat 7 six years later, showing further improvements over its predecessor: a panchromatic band with 15m resolution was added and the resolution of the thermal infrared band was doubled to 60m. However, ETM+'s Scan Line Correction (SLC) system failed on 31 May 2003 and has since proved to be permanent, leading to gaps (i.e. masked pixels) in images taken when the satellite is moving. In 2013, Operational Land Imager and Thermal Infrared Sensor (OLI-TIRS) was put into orbit on Landsat 8 with new features. Using a pushbroom sensor, which was not the case for its predecessors, OLI-TIRS offers 12-bit radiometric resolution of images, enabling encoding on 4096 grey levels, and therefore providing more precise and better differentiated spectral information. At the same time, two new multispectral bands have been added, ultra-blue band 1 and cirrus band 9, for improved cloud detection. Finally, Landsat 9 was launched in 2021 carrying OLI2-TIRS2, a version that is almost identical to OLI-TIRS but with better radiometric resolution of 14 bits for encoding on 16,384 grey levels, as well as an improvement to TIRS2 for better atmospheric corrections and more accurate surface temperature measurements.

Table 2.2.1. Summary of the characteristics of the various sensors on board past and present Landsat satellites

Bands		Wavelength (μm)	Spatial resolution (m)	Radiometric resolution	Acquisition years	Repeat cycle
Multispectral Scanner (MSS)						
L1-3	*L4-5*					
B1 (Green)	B4 (Green)	0.50 – 0.60	60	6-bit (64 levels)	1972–2013	18 days (L1-3) 16 days (L4-5)
B2 (Red)	B5 (Red)	0.60 – 0.70	60			
B3 (NIR1)	B6 (NIR1)	0.70 – 0.80	60			
B4 (NIR2)	B7 (NIR2)	0.80 – 1.10	60			
Thematic Mapper (TM)						
Landsat 4-5						
B1 (Blue)		0.45 – 0.52	30	8-bit (256 levels)	1982–2013	16 days
B2 (Green)		0.52 – 0.60	30			
B3 (Red)		0.63 – 0.69	30			
B4 (NIR)		0.76 – 0.90	30			
B5 (SWIR1)		1.55 – 1.75	30			
B6 (TIR)		10.4 – 12.5	120			
B7 (SWIR2)		2.08 – 2.35	30			
Enhanced Thematic Mapper (ETM+)						
Landsat 7						
B1 (Blue)		0.45 – 0.52	30	8-bit (256 levels)	1999–2022	16 days
B2 (Green)		0.52 – 0.60	30			
B3 (Red)		0.63 – 0.69	30			
B4 (NIR)		0.77 – 0.90	30			
B5 (SWIR1)		1.55 – 1.75	30			
B6 (TIR)		10.40 – 12.50	60			
B7 (SWIR2)		2.08 – 2.35	30			
B8 (PAN)		0.52 – 0.90	15			

Operational Land Imager and Thermal Infrared Sensor (OLI/TIRS)					
Landsat 8-9					
B1 (Deep Blue)	0.43 – 0.45	30	12-bit (4096 levels) (L8) 14-bit (16 384 levels) (L9)	2013–Ongoing	16 days
B2 (Blue)	0.45 – 0.51	30			
B3 (Green)	0.53 – 0.59	30			
B4 (Red)	0.64 – 0.67	30			
B5 (NIR)	0.85 – 0.88	30			
B6 (SWIR1)	1.57 – 1.65	60			
B7 (SWIR2)	2.11 – 2.29	30			
B8 (PAN)	0.50 – 0.68	15			
B9 (Cirrus)	1.36 – 1.38	30			
B10 (TIR1)	10.60 – 11.19	100			
B11 (TIR2)	11.50 – 12.51	100			

2.2.3. Data preprocessing and accessibility

Landsat archives are available in different types of collections and levels of pre-processing. During this thesis, images from the TM, ETM+ and OLI-TIRS sensors at L2 Tier 1 quality level from Collection 2 were analysed (Figure 2.2.3). The images in Collection 1 have undergone a series of pre-processing operations (e.g., terrain and radiometric corrections) before being included in the catalogue for downloading. Collection 2, which appeared in 2020, offers improved pre-processing, such as more accurate geographical corrections or ortho-rectification, or the integration of Landsat 9 data (Crawford et al., 2023). Collection 1 has been reprocessed into Collection 2, and Collection 1 has not been made available by the USGS since December 2022 (https://www.usgs.gov/landsat-missions/landsat-collection-1).

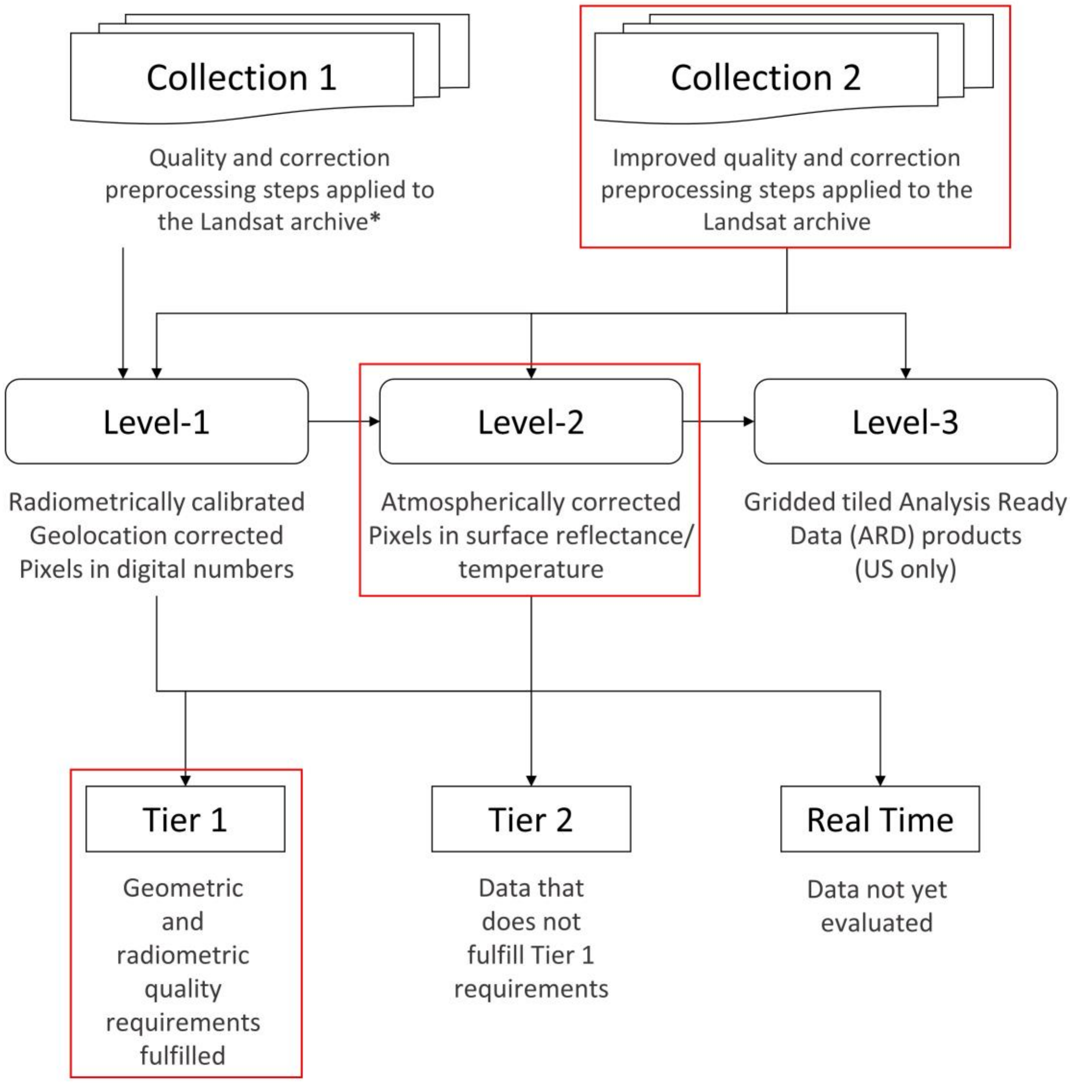

Figure 2.2.3: Summary of collections and Landsat product types available for downloading and analysis. Red squares indicate which data was selected. Asterisk indicates that Collection 1 is no longer available since December 30, 2022. Based on https://www.usgs.gov/landsat-missions/landsat-collection-2

L2 pre-processing level images are provided in reflectance and surface temperature corrected for geometric, radiometric and atmospheric effects. Tier 1 quality images are those that have received the first pre-processing and meet the geometric and radiometric accuracy conditions required to be added to the collection. Conversely, Tier 2 quality images have lower geometric and radiometric accuracies, requiring additional pre-processing. Before analysis, the CFMask algorithm was applied to the Landsat time series in order to mask pixels containing noise, clouds or cast shadows that would bias the temporal analysis (Foga et al., 2017). This algorithm is a C-coded version of version 3.3 of the FMask algorithm (Zhu and Woodcock, 2012).

An additional multi-temporal mask was used, but as it is an integral part of the method used to analyse the Landsat archives, it is described in this section (see section 2.4.2).

Traditionally, the Landsat archive is available for download from the USGS EarthExplorer website (https://earthexplorer.usgs.gov/), but it is also available remotely on cloud-computing platforms without the need to download it. During this thesis, the Landsat archive was accessed through the Google Earth Engine (GEE) cloud-computing platform, which contains several petabytes of remote sensing data at a global scale in open access (Gorelick et al., 2017). This platform includes the entire Landsat 2 collection and enables image processing (e.g., thresholding, calculation of vegetation indices, classifications) to be carried out directly on remote servers, and results to be exported in various formats (e.g., raster, vector, or csv). Using these cloud computing platforms offers several technical and operational benefits: (1) Direct access to Landsat images without the need to download them; (2) Access to remote servers across large study sites and over time to run power and energy-intensive algorithms; and (3) the ability to share code easily and create/use thematic application program interfaces (APIs). Several platforms have been created for several years and are similar to GEE, such as Nasa Earth Exchange (Nemani, 2012), Amazon Web Services (Jackson et al., 2010), or Microsoft Planetary Computer (Lukacz, 2024). However, the availability of the CCDC algorithm and the existence of a dedicated API to run it on GEE motivated the choice to use this platform rather than another. It is important to note that using GEE relies on the use of its javascript-based API and therefore requires basic programming skills. However, user-friendly APIs are available and have been specifically designed to be ready to use with a dedicated user interface with no programming skills required.

2.2.4. Spectral indices and bands transformation

In addition to the spectral and thermal bands provided in the Landsat archive, a set of spectral indices were calculated and band transformations applied: three vegetation indices (i.e., NDVI, EVI, and EVI2), two indices sensitive to bare soil and vegetation (i.e., NBR and NDFI), as well as the three components derived from the Tasseled Cap Transformation applied to the spectral bands (Table 2.2.2). This selection comes from the CCDC API developed by Arévalo et al. (2020) which was used during this thesis, and we have decided to keep these indices by default.

Table 2.2.2: Summary of spectral indices and transformations derived from the Landsat archive used in Chapter 4.

Indices	Description	Source
NDVI	Normalized Difference Vegetation Index: used to quantify vegetation health and density related to photosynthesis	Myneni et al. (1995)
EVI	Enhanced Vegetation Index: used to quantify vegetation health and density with higher sensitivity in high-biomass regions; related to canopy structure	Huete et al. (2002)
EVI2	Two-band Enhanced Vegetation Index: EVI calculated without the blue spectral band to calculate EVI based on sensors lacking a blue band (e.g., AVHRR)	Jiang et al. (2008)
NBR	Normalized Burn Ratio: used to identify burned areas and quantify fire severity	Key and Benson (2006)
NDFI	Normalized Difference Fraction Index: used to monitor forest degradation and deforestation; sensitive to canopy state. Calculated from green vegetation (GV), non-photosynthetic vegetation (NPV), soil, and shade fractions obtained from spectral mixture analysis.	Souza Jr et al. (2005)
Greenness vegetation index	Greenness fraction: extracted by tasseled cap transformation; corresponds to vegetation fraction	Crist (1985)
Brightness vegetation index	Brightness fraction: extracted by tasseled cap transformation; corresponds to soil fraction	Crist (1985)
Wetness vegetation index	Wetness fraction: extracted by tasseled cap transformation; corresponds to the relation between soil and canopy wetness	Crist (1985)

2.3. Reference and ancillary data

2.3.1. LULC data

Land Use and Land Cover (LULC) data used during the thesis come from a variety of sources:

The ESA WorldCover 2021 version 200 product, which is a raster map of land cover and land use in 2021 at 10 m spatial resolution derived from Sentinel-1 and 2 time series (Zanaga et al., 2022) was used. It contains 11 LULC classes corresponding to the Land Cover Classification System established by the UN-FAO and has an overall accuracy of 77%. These LULC data were collected on the four Ramsar sites investigated in Chapter 3 to study the influence of land cover on the net annual primary production derived from Landsat time series analyses.

Data from the Land Use and Cover Area frame Survey (LUCAS), the temporal monitoring of LULC in European countries (Gallego and Delincé, 2010), has been downloaded from the Eurostat website (https://ec.europa.eu/eurostat/web/lucas).

Initiated in 2001, these field surveys carried out by several observers provide observation data on the LULC, photos of the associated landscapes, and environmental parameters (*e.g*. soil parameters) at systematically defined points within the Member States of the European Union. (Palmieri, 2016). There have been numerous field campaigns since 2006 (involving 11 Member States), and the most recent in 2022 (involving all 27 Member States). These data were used to study LULC changes in the Marais Poitevin (Chapter 4), which were available on this site for the years 2006, 2012, and 2018, with a total of 130, 70, and 69 observation points, respectively.

Data from the Land Parcel Identification System (LPIS) was used. Serving as a reference for the appraisal of financial aid under the European Union's Common Agricultural Policy (CAP), this geographical data contains farmers' annual declarations giving information on the type of crop and plant cover present at the parcel level (European Court of Auditors, 2016). This data, updated every year since 2007, describes around thirty classes, including permanent and temporary grassland. It was accessed via a WMS feed directly into the QGIS software to assess changes in LULC in the Marais Poitevin (Chapter 4).

Finally, two vector data supplied by local managers relating to the conversion of parcels of arable land to grassland were used to study LULC changes in the Marais Poitevin (Chapter 4) and to assess the effectiveness of public policies for the conservation of wet grasslands on this same study site (Chapter 5). The first concerns 563 parcels of arable land restored to grassland over the periods 2001-2003 and 2005-2015, while the second provides information on the extensive grazing of 17.4 km² of grassland located in communal marshes between 2003 and 2013.

2.3.2. Climate data

Climate data come from the NOAA Climate Prediction Center's Global Historical Climatology Network - Daily (GHCN-d) dataset ("Gridded Climate: NOAA Physical Sciences Laboratory," 2024), which contains records at 0.5° spatial resolution from over 100,000 weather stations located in more than 180 countries and territories worldwide (Menne et al., 2012). From the CPC Global Unified Temperature product, the minimum and maximum daily temperatures (T_{min} and T_{max}) were extracted and used to derive the mean daily temperature (T_{mean}), which was then averaged annually from 1984 to 2021. Daily precipitation (P_{mm}) was collected from the CPC Global Unified Gauge-Based Analysis of Daily Precipitation and summed annually over the study period. These climate data were used at the four Ramsar sites studied in Chapter 3 to investigate the influence of climate on annual net primary production derived from Landsat time series analyses.

2.3.3. Environmental data

The use of environmental data in addition to satellite images is an interesting way of improving the output of classification algorithms (Demarquet et al., 2023a). To this end, three topographic data derived from DEM SRTM at 30m spatial resolution (Farr et al., 2007) were incorporated to the CCDC algorithm (i.e. elevation, aspect, and slope) for the EUNIS habitat classification. The DEM was obtained and processed directly from GEE. Locally, the distance to the nearest sea was also calculated at a spatial resolution of 30m from the highest water line (IGN and SHOM, 2009) and fed into GEE for inclusion in the model.

These environmental data were collected to study LULC changes in the Marais Poitevin (Chapter 4).

2.3.4. Vegetation data

Vegetation data from field surveys were used to study LULC changes in the Marais Poitevin (Chapter 4). Specifically, these surveys included vegetation maps downloaded from the Institut National du Patrimoine Naturel (INPN) and produced at the scale of the five nature reserves present on the site (1:5000 scale), covering a total area of 18 km² and conducted between 2006 and 2015 (Robert and Brosseau, 2022). Habitats are described under both classification systems EUNIS 2004 (Davies et al., 2004) and Progrome of French Vegetation (PVF) (Bioret et al., 2013). Habitat mapping for the Natura 2000 site, providing spatial information on the CORINE biotope habitats (1:15,000 scale), was obtained from the site managers for the 2001-2005 period (Devillers et al., 1991). In addition, 821 phytosociological *relevés* conducted between 2001 and 2015 were used, principally collected on grasslands by local botanists and scientists, and accessed from both the local managers and the VegFrance database (Bonis and Bouzillé, 2012). A final step of harmonisation between the different nomenclatures was carried out to automatically assign the surveys to an EUNIS class using the EUNIS-ESy expert system (Chytrý et al., 2020).

Furthermore, the maps of EUNIS level 1 habitats generated for the Marais Poitevin over the 1984-2022 period in Chapter 4 have been used as a reference to calculate annual changes in grassland (EUNIS E) and cropland (EUNIS I) areas to evaluate the effectiveness of conservation policies (Chapter 5).

2.3.5. Aerial photographs

Historical aerial photographs can be used to collect LULC data by visual photo-interpretation. A total of 16 aerial photographs covering different areas of the Marais Poitevin site over the 1984-1997 period have been downloaded from the Institut Géographique National (IGN) website, available in open access (https://remonterletemps.ign.fr/) to study LULC changes in this site (Chapter 4). Several thousand aerial photographs dating back to the 1950s are available for free download, although they must be georeferenced prior to use. Specifically, 6 black and white photographs (scale 1:30,000) from 1984 and 10 colour photographs (scale 1:21,000 to 1:26,000) from 1990 and 1997 were downloaded and then georeferenced from the 2022 georeferenced aerial photograph, achieving an average RMSE (root mean square error) of 3.58m.

2.3.6. Protected area data

Geographic information layers on protected areas have been used on the Marais Poitevin site to assess the value of using Landsat time series to evaluate public policies for grassland conservation on this site (Chapter 5). These data were obtained from the World Database on Protected Area (WDPA), a database accessible from the Protected Planet website (https://www.protectedplanet.net/en), which lists all the available data on protected areas worldwide (UNEP-WCMC and IUCN, 2024). This information is provided by the secretariats of international conventions, governements, and NGOs, and covers all the different categories of protected areas as defined by the IUCN. Attribute tables provide information on site names, date of creation or management type, where available. Natura 2000 and nature reserves layers were obtained from this data. At the same time, land-purchased perimeters layers from the Coastal and Lakeshore Protection Agency have been collected from the French Ministry of Environment website (https://geoservices.ign.fr/services-web-experts-environnement). Finally, land-purchased perimeters from the Natural Area Conservation Societies were collected from the local managers.

2.4. CCDC algorithm

2.4.1. Principle of the algorithm

The CCDC algorithm, which stands for Continuous Change Detection and Classification, enables LULC or habitat mapping based on satellite time series (Zhu and Woodcock, 2014a). This is a temporal segmentation method that groups multiple observations into representative periods, called time segments, to which a model is applied in the same way as in spatial segmentation algorithms (Pasquarella et al., 2022). Its principle is to extract a time series within a pixel and iteratively apply a harmonic regression to it (Figure 2.4.1). Initialised at the beginning of the study period, the model is applied to each spectral band or index derived from the satellite image (e.g., surface reflectance, vegetation index, surface temperatures) and detects a change when the difference between predicted and observed values exceeds a given threshold on several consecutive occurrences. Such significant and consecutive changes within a satellite time series are then considered likely to be due to a LULC change. The date of the event is noted and the regression is then reset to apply to the remaining data in the time series. Harmonic regression coefficients are thus derived for each pixel in the satellite image series. Secondly, a Random Forest (RF) image classification algorithm integrates these coefficients as input and learns the relationship between the value of these coefficients and the reference data of LULC classes. Finally, in addition to producing image classifications and synthetic images, the algorithm can produce several outputs related to the magnitude and date of the changes detected. These characteristics make CCDC a computationally intensive algorithm compared with other time series analysis methods such as LandTrendR (Pasquarella et al., 2022).

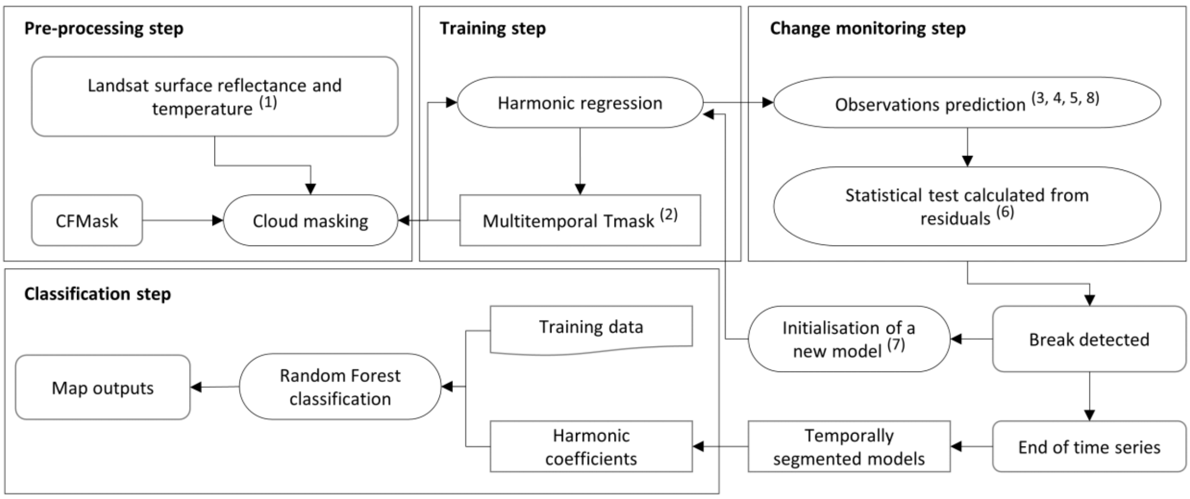

Figure 2.4.1: Workflow of the CCDC algorithm. Numbers indicate the CCDC parameter described in Table 2.4.1 and associated with the component. Inspired from and based on ("Continuous Change Detection and Classification CCDC," 2024).

The CCDC source code is available in two forms. The first is local, when sufficient computing and storage resources are available, using the Python code dedicated to this algorithm available in open access (https://code.usgs.gov/lcmap/pyccd) (e.g. Xian et al., 2022). The second is remote, on the servers of the GEE platform, where the algorithm has been programmed and made available either directly by calling the dedicated function (ee.Algorithms.TemporalSegmentation.Ccdc; https://developers.google.com/earth-engine/apidocs/ee-algorithms-temporalsegmentation-ccdc), or through an API developed to facilitate its use (Arévalo et al., 2020). It is this second option, reused and partially modified, that has been chosen for the work in this thesis. The parameterisation of the harmonic regression requires the input of several variables in order to apply a multi-temporal mask to the time series and to select the type of regression and its sensitivity for change detection (Table 2.4.1).

Table 2.4.1: Harmonic regression parameters used in the CCDC and associated values used in the thesis. Asterisks indicate non-default values.

Parameter ID	Parameter	Meaning	Value
1	*breakpointBands*	The name or index of the bands used to detect change	All
2	*tmaskBands*	The name or index of the bands used to detect clouds and noise iteratively (*TMask*)	Green, SWIR2
3	*MinObs*	Moving window size used to detect breaks	5
4	*Seg*	Maximum number of temporal segments in the entire time-series	6
5	*Lambda*	Penalty parameter for LASSO regression	0.005
6	*ChiSquareProbability*	Chi-square probability threshold for break detection	0.99*
7	*MinNumOfYearsScaler*	Factor of minimum number of years to apply a new regression model	1.33
8	*MaxIterations*	Maximum number of runs for LASSO regression convergence	10 000*

Each step of the CCDC application in GEE and the associated parameters are described in detail in the following sections.

2.4.2. Pre-processing step

The first step is to retrieve the satellite images and extract the time series for each selected band on a pixel-by-pixel basis (*breakpointBands* ; parameter 1). The algorithm was initially developed specifically for the Landsat archive, due to the long temporal availability of the images. However, it can be applied to all types of satellite data, such as Sentinel or MODIS images (e.g. Fu et al., 2022; Giannetti et al., 2021). Unlike the traditional diachronic approach, which consists of selecting a few clear and cloud-free images, the CCDC algorithm takes into account all the available images, with and without clouds, making optimum use of the Landsat archive as a whole because it is applied at pixel scale. Precisely, a pixel may be covered by a valid observation at a date *n* but not at a date *n+1*, making it potentially different from other pixels in the image which may be covered at date n+1 (Figure 2.4.2). In this way, the algorithm exploits all the cloud-free pixel data available, rather than focusing on a selection of a few entirely clear images. The CFMask algorithm (Foga et al., 2017) was used to mask pixels covered by clouds and cast shadows (see section 2.2.3).

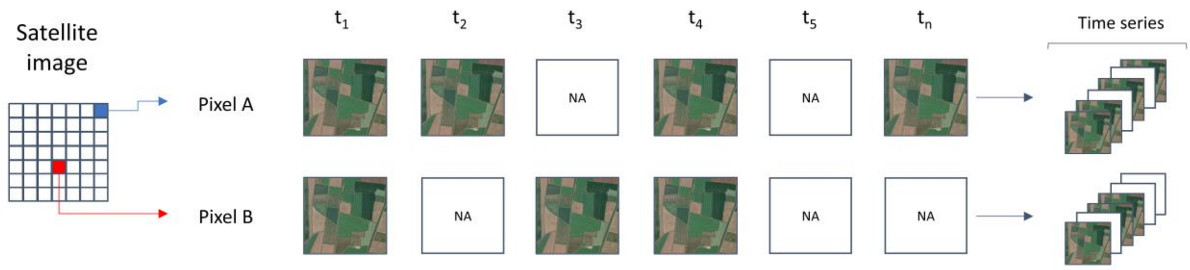

Figure 2.4.2: Schematic representation of the extraction of time series from a Landsat band for the application of harmonic regression. The time indications t represents the dates of image acquisition by the satellite. NA pixels represent pixels masked by clouds or cast shadows.

This cloud extraction and masking step was applied for each pixel of the Landsat image and for each spectral band, thermal band and index calculated.

2.4.3. Training step

Once the masked time series has been extracted from the bands selected to compute the regression (*breakpointBands*), the additional multitemporal mask TMask (Zhu and Woodcock, 2014b) can be applied from the green and short-wave infrared 2 (SWIR2) spectral bands (*tmaskBands ;* parameter 2). This is applied throughout the regression on the time series in order to detect and mask outliers not previously detected by the *CFMask* algorithm. *TMask* is a simple time series analysis algorithm designed to estimate the reflectance values of the bands selected for the mask, i.e., the green and SWIR2 bands. Various coefficients are estimated using Robust Iteratively Reweighted Least Squares (RIRLS) to eliminate the influence of outliers on the model (Street et al., 1988; Zhu and Woodcock, 2014b). They are used to capture seasonality and global reflectance, as well as changes in LULC over time (Equation 1). This last point is critical in order to prevent the algorithm from considering a real change in LULC as a noisy or cloudy pixel (Zhu and Woodcock, 2014b).

Equation 1: TMask algorithm equation from Zhu and Woodcock (2014b)

$$\rho(i,x) = a_{0,i} + a_{1,i}cos\left(\frac{2\pi}{T}x\right) + b_{1,i}sin\left(\frac{2\pi}{T}x\right) + a_{2,i}cos\left(\frac{2\pi}{NT}x\right) + b_{2,i}sin\left(\frac{2\pi}{NT}x\right)$$

Where:

x	The Julian date
i	The Landsat Band i in Top-op-Atmosphere reflectance (Green or SWIR2)
T	The number of days per year (T=365)
N	The number of years
$a_{0,i}$	The coefficient for the overall value for Landsat Band i
$a_{1,i}$, $b_{1,i}$	The coefficients for intra-annual change for Landsat Band i
$a_{2,i}$, $b_{2,i}$	The coefficients for inter-annual change for Landsat Band i

The final harmonic regression model resembles Equation 1 but takes into account three harmonic components: an annual component, a bimodal component (over 6 months) and a third trimodal component (over 4 months). Taking these three levels into account provides the best performance compared to models with fewer harmonics and refines the regression better (Zhu and Woodcock, 2014a).

Equation 2: Harmonic regression model used per time series during the CCDC workflow

$$\rho_{i,t} = a_{0,i} + \sum_{k=1}^{n}\left(a_{k,i}\,cos\left(\frac{2k\pi}{T}t\right) + b_{k,i}sin\left(\frac{2k\pi}{T}t\right)\right) + c_{1,i}t$$

Where $\rho_{i,t}$ is the predicted reflectance/temperature/index value for a Landsat band i and for a given Julian date t; $a_{0,i}$ represents the overall value of the i th band reflectance; $a_{k,i}$ and $b_{k,i}$ represents the coefficient of the intra-annual variation term of the reflectance of band i (k depends of the harmonics considered, in our case bimodal and trimodal); $c_{1,i}$ represents interannual variation of a Landsat band i, which is the long-term slope; and T represents the number of days during one year (defined to 365 days, by default). This regression calculates a number of nine coefficients and derivatives for a same time segment (Zhu and Woodcock, 2014a) (Table 2.4.2), These include:

- The intercept (INTP), which corresponds to the average surface reflectance, temperature, or spectral index on which the regression is applied;

- The slope (SLP), which informs on the long-term trend of the modelled time segment;
- The three harmonic components are taken into account and combined to model the time segments: unimodal (over an entire year; COS and SIN), bimodal (over 6 months; COS2 and SIN2), and trimodal (over 4 months; COS3 and SIN3);
- The Root Mean Square Error (RMSE), which correspond to the error calculated between the Landsat observations and the predicted values from the regression;
- The amplitude (AMPLITUDE), which is derived from cosine and sine and corresponds to the seasonal variability over the year (as well as for the bi- and tri-modal harmonics AMPLITUDE 2 and AMPLITUDE3, respectively).
- The phase (PHASE), which corresponds to the phenology of the time segment, also derived from the cosines and sines for the three harmonic components (PHASE2 and PHASE3).

Table 2.4.2: Continuous change detection and classification (CCDC) outputs used as predictor variables for random forest classification of natural habitats. The acronyms correspond to those defined in the Google Earth Engine CCDC application programming interface (Arévalo et al., 2020).

CCDC output type	Acronym	Description
Coefficients	INTP	Intercept: Intercept of the time series. Mean reflectance for spectral bands or mean value for spectral indices and indicators.
	SLP	Slope: Long-term trend of the time series
	SIN COS	Sine and cosine: Harmonic coefficients for intra-annual change
	SIN2 COS2	Sine and cosine: Harmonic coefficients for intra-annual bimodal change
	SIN3 COS3	Sine and cosine: Harmonic coefficients for intra-annual trimodal change
	RMSE	Root mean square error: The error between the observed and CCDC fitting values. Corresponds to non-seasonal variability.
Derivatives	AMPLITUDE	Magnitude of the time series. Corresponds to seasonal variability. Derived from COS and SIN.
	PHASE	Phenological timing of the time series. Derived from COS and SIN.
	AMPLITUDE2	Bimodal magnitude of the time series. Derived from COS2 and SIN2.
	PHASE2	Bimodal phenological timing of the time series. Derived from COS2 and SIN2.
	AMPLITUDE3	Trimodal magnitude of the time series. Derived from COS3 and SIN3.
	PHASE3	Trimodal phenological timing of the time series. Derived from COS3 and SIN3.

2.4.4. Change monitoring step

As the regression progresses in the time series of a pixel and for each band/spectral index, the residuals are calculated between each clear Landsat observation and the value predicted by the harmonic model, giving the RMSE. When these residuals are significantly different from the threshold of three times the RMSE (*ChiSquareProbability*; parameter 6) on several consecutive occurrences (*minObs*; parameter 3), a break is detected in the time series (Figure 2.4.3).

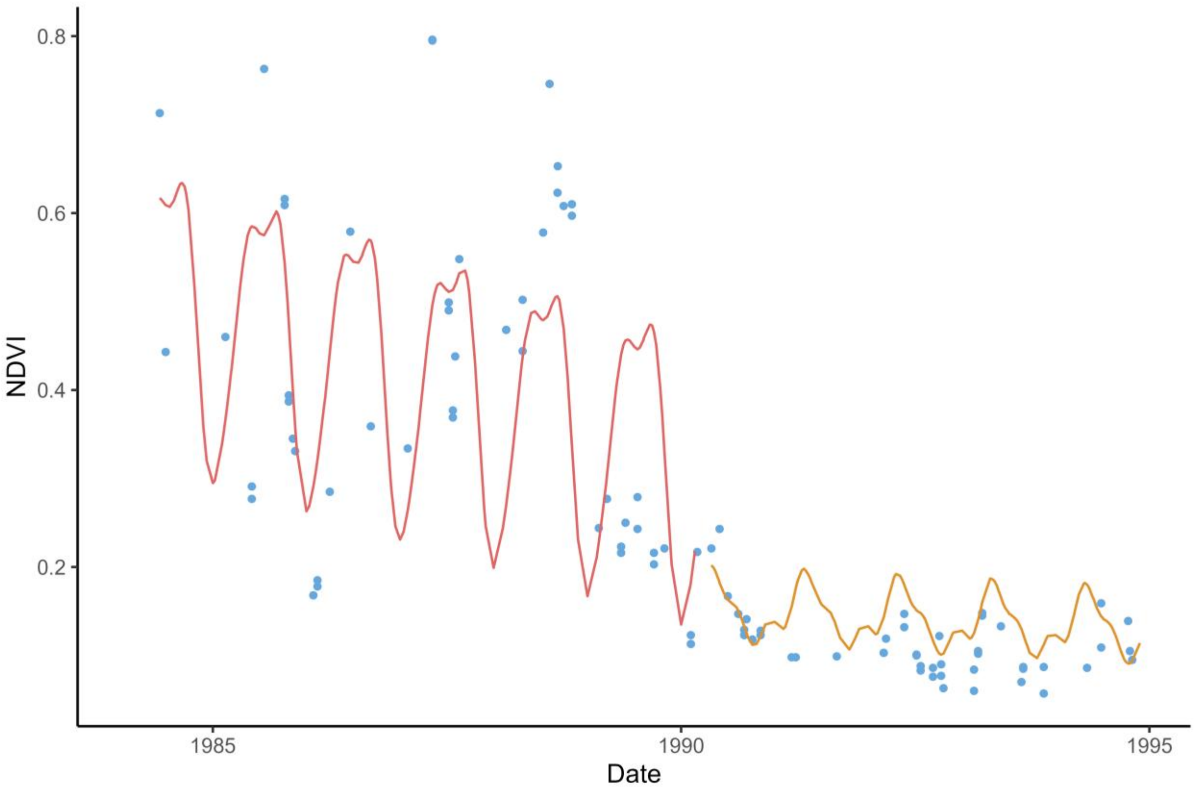

Figure 2.4.3: Example of the application of harmonic regression to an NDVI time series from the Landsat archive between 1984 and 1995. The blue dots indicate the clear Landsat observations within the selected pixel. The coloured lines indicate the time segments detected by the harmonic regression. More specifically, an initial segment (in red) is modelled from 1984 to around 1990. A break is then detected and a new temporal segment (in yellow) is initialized.

The regression initialization is repeated to model a new time segment and so on until the end of the series and for a maximum number of defined segments (*Seg*; parameter 4). Two types of regression can be used to model time segments according to a degree of penalty to be defined (*Lambda*; parameter 5). When there is no penalty (i.e., Lambda = 0), a conventional Ordinary Least Squares (OLS) regression is applied, whereas when Lambda increases, a Least Absolute Shrinkage and Selection Operator (LASSO) regression is applied (Zhu et al., 2015). This regression method with penalty automatically selects several variables from a set, with the possibility of forcing the regression coefficients to be equal to zero by minimising the residual sum of squared errors (Tibshirani, 1996). In this way, the LASSO regression is more advantageous for the CCDC because it avoids overfitting the model while adapting to the available

Landsat data, which is a benefit in areas with high cloud cover (Zhu et al., 2015). For these reasons, we chose the LASSO regression for our analyses, which is also the default method in the source code used, with a Lambda parameter set to 0.005.

2.4.5. Classification step

Once the regression is complete and the time segments have been modelled with all the coefficients for each Landsat band, the classification step can begin. To do this, a simple geomatic process is used to extract the coefficients and derivatives of the harmonic regression for each reference training datum. These data then contain the LULC class, the reference year, and all the temporal coefficients for each Landsat band, representing the dataset on which the classification algorithm is trained. Of the algorithms available, Random Forest was chosen for its ability to manage a large number of input variables and its low sensitivity to outliers and overfitting (Belgiu and Drăguţ, 2016). The version that is available and usable on GEE is the function from the Statistical Machine Intelligence and Learning Engine (SMILE) package (ee.Classifier.smileRandomForest), and only one parameter related to the number of random trees generated has been increased from the default setting to 500. For a more detailed description of the RF algorithm, see Breiman (2001)

2.4.6. CCDC outputs

Once trained, the RF model is applied to the entire study area to generate LULC class maps derived from the classification for any year within the study period. For a given date, the model produces a LULC map based on its learning from the coefficients of the time segments. On the other hand, if the requested date does not correspond to a time segment (e.g., because of the time required to initialise the model after a break or because the number of Landsat observations is too small), there are no regression coefficients, and the model uses a forward or back-filling approach to fill in these periods without segments and define the corresponding LULC class (Pasquarella et al., 2022). This LULC map is then subjected to an evaluation process to assess its accuracy by generating confusion matrices (Olofsson et al., 2014). This validation requires the use of reference data that has not been used to train the Random Forest model in order to derive accuracy indicators such as Overall accuracy, User's accuracy and Producer's accuracy (Olofsson et al., 2013). This approach was used in the Chapter 4.

Another CCDC output concerns the generation of synthetic images derived from harmonic regression. Once the regression has been applied to a time series, it is possible to retrieve the value predicted by the model at a given date, whether or not a clear observation is available. Zhu et al. (2015) showed a low RMSE between the synthesised images and the real Landsat images compared, the best accuracy being obtained with the visible bands (i.e., blue, green and red, around 0.01) while the RMSE was higher for the SWIR (between 0.01 and 0.02) and NIR (between 0.02 and 0.03) bands. An example of this approach is provided in Figure 2.4.4 on the Ramsar site Marais Vernier et Vallée de la Risle Maritime. In this example, the date of 11 June 2000 was taken as an example because of its heavy cloud cover (Figure 2.4.4B). Any pixel in the image on the site would therefore be masked by the CFMask and TMask. The coefficients of the time segments coinciding with this same date can be used to replace the masked value with the value predicted by the harmonic regression (Figure 2.4.4C). In this way, it is possible to recreate an image (Figure 2.4.4C) and to measure its accuracy with the RMSE coefficients (Arévalo et al., 2020). This approach was used in the Chapter 3.

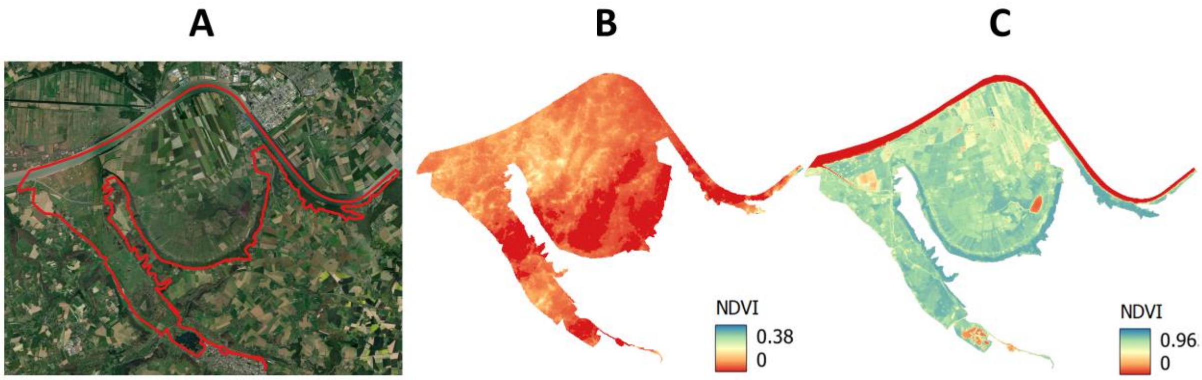

Figure 2.4.4: Example of a synthetic image generation from the CCDC algorithm on the Marais Vernier et Vallée de la Risle Maritime Ramsar site. From left to right: (A) satellite view from Google Earth; (B) Landsat 5 TM NDVI image on the 11th of june, 2000; (C) synthetic NDVI image generated on the 11th of June, 2000.

2.4.7. CCDC API on GEE

The API developed by Arévalo et al. (2020) has been programmed in several scripts enabling all the steps described above to be performed. The respective codes are freely accessible in the GEE code editor, only as readers and users, through this link (https://code.earthengine.google.com/?scriptPath=users%2Fparevalo_bu%2Fgee-ccdc-tools%3AAPPS%2Ftstools_basic), as well as on GitHub (https://github.com/parevalo/gee-ccdc-tools). This API is divided in five tools:

1) Two time-series display modules (*tstools_basic* and *tstools_advanced*), which provide access to the Landsat archive as well as Sentinel-1 and 2 archives,

and enable time regression to be calculated 'on the fly' via the GEE interface at the pixel level;

2) A CCDC execution module (*submit_ccdc*) that allows the algorithm to be run over a given geographical area and time period. The result is exported either as an asset or directly to a predefined Google Drive file;
3) A module for displaying the results of the CCDC (*visualize_ccdc*), enabling the most significant amplitudes of change, the value of the regression coefficients for a given date, or the RMSEs to be displayed in the form of images;
4) A module for classifying the time segments obtained after harmonic regression (*classify_app*), enabling the Random Forest algorithm to be trained to assign a LULC class to the segments on the basis of the regression coefficients;
5) A module for generating LULC maps based on classification (*landcover_app*).

In addition, there are scripts containing the functions called in these different modules, all located in the *ccdcUtilities* module. A website dedicated to the use of the API can also be consulted, with examples of applications and use of the functions (https://gee-ccdc-tools.readthedocs.io/en/latest/). The entire API was used as the main basis for the programming work. Using the functions created by Arévalo et al. (2020), modifications have been made to meet the needs of the thesis. The most notable changes include the integration of Landsat 9 into the GEE collection call and the ability to select the geographic extent of images by loading a shapefile. The scripts produced and used are available in Appendix E and Appendix F.

1

INTRODUCTION TO CHAPTER 3

Chapter 3 describes the application of the CCDC algorithm to monitor long-term wetland ecosystem functioning from Landsat archives over four contrasting Ramsar wetlands selected from boreal, temperate, arid and tropical regions.

Specifically, the Landsat archive was used to produce an indicator of net annual primary productivity (NDVI-I) between 1984 and 2021 by exploiting the capacity of the CCDC to generate synthetic images. In addition, the sensitivity of the method to significantly different conditions of land cover and number of available Landsat images was tested in order to describe the transferability of the algorithm. Thus, we describe in this chapter how land cover/use and the number of unambiguous Landsat observations available affect the accuracy of the harmonic regression performed during the CCDC. We also assess the relevance of the method for generating functional indicators for wetlands with contrasting bioclimatic conditions and over long time periods.

This chapter corresponds to the article published in the peer-reviewed journal *Sustainability*:

> Demarquet, Q., Rapinel, S., Arvor, D., Corgne, S., Hubert-Moy, L., 2024. Satellite Long-Term Monitoring of Wetland Ecosystem Functioning in Ramsar Sites for Their Sustainable Management. *Sustainability* 16, 6301. https://doi.org/10.3390/su16156301

CHAPTER 3. SATELLITE LONG-TERM MONITORING OF WETLAND ECOSYSTEM FUNCTIONING IN RAMSAR SITES FOR THEIR SUSTAINABLE MANAGEMENT

Article

Satellite Long-Term Monitoring of Wetland Ecosystem Functioning in Ramsar Sites for Their Sustainable Management

by Quentin Demarquet, Sébastien Rapinel, Damien Arvor, Samuel Corgne and Laurence Hubert-Moy

Submission received: 29 June 2024 / Revised: 17 July 2024 / Accepted: 19 July 2024 / Published: 23 July 2024

Abstract

The long-term monitoring of wetland ecosystem functioning is critical because wetlands, which provide multiple services, can be affected by human activities and climate change. The aim of this study was to monitor wetland ecosystem functioning in the long-term using the Landsat archive. Four contrasting Ramsar wetlands were selected in boreal, temperate, arid, and tropical areas. First, the annual sum of the normalized difference vegetation index (NDVI-I) was calculated as an indicator of annual net primary productivity for the period 1984–2021 using the continuous change detection and classification (CCDC) algorithm. Next, the influence of the number of Landsat images and class of land use and land cover (LULC) on the accuracy of the CCDC was investigated. Finally, correlations between annual NDVI-I and climate were analyzed. The results revealed that NDVI-I accuracy was influenced mainly by the LULC class and to a lesser extent by the number of cloud-free Landsat observations. Infra- and inter-site variations in NDVI-I were high and showed an overall increasing trend. NDVI-I was positively correlated with the mean temperature. This study shows that this approach applied in contrasting sites is robust for the long-term monitoring of wetland ecosystem functioning and can be used to improve the implementation of international biodiversity conservation policies.

3.1. Introduction

Although wetlands support many functions and ecosystem services (Xu et al., 2020), they have been increasingly threatened over the past several decades due to climate change and human pressure (Fluet-Chouinard et al., 2023). In this context, international biodiversity conservation policies have been implemented, such as the Ramsar Convention (Ramsar Convention on Wetlands, 2015), the Aichi Targets of the Convention on Biological Diversity (CBD Secretariat, 2010), the UN Sustainable Development Goals (United Nations, 2015), and the Paris Climate Agreement (Viñuales, 2016). However, these policies are difficult to implement due to the incomplete evaluation of the ecological character of wetlands, which considers the composition and structure of these ecosystems but not their functioning (Geijzendorffer et al., 2019; Lock et al., 2021). However, the scientific community has shown that indicators of the long-term functioning of wetlands can be derived from satellite time series (Kingsford et al., 2021; Lock et al., 2021). A number of wetland conservation initiatives based on Earth Observation (EO) data have been implemented worldwide, such as the Globwetland Program (Jones et al., 2009), the Satellite-Based Wetland Observation Service Project (Weise et al., 2020), and the Ramsar Reporting Convention (MacKay et al., 2009). The studies conducted as part of these initiatives highlighted the need for the systematic assessment of the accuracy, relevance, and transferability of EO-derived products, as well as for the long-term continuous monitoring of wetlands at high spatial resolution using an EO archive (Rebelo et al., 2018).

While different open access satellite data sources could be used for long-term wetland monitoring, Landsat imagery was selected because it combines a long observation period (40 years) with a high spatial resolution (30 m) (Wulder et al., 2022) compared to Sentinel-2 imagery (9 years, 10 m) or MODIS imagery (23 years, 250 m). The Landsat program provides unique capabilities for observing the entire Earth for 40 years at 30 m spatial resolution (Wulder et al., 2022). Landsat images were acquired every 16 days by Landsat 4–7 (1984–2022) and have been acquired every 8 days by Landsat 8–9 (2013–present). The Landsat archive, which the U.S. Geological Survey has provided free of charge since 2008 (Woodcock et al., 2008), can be easily accessed and processed using cloud-computing platforms such as the Google Earth Engine (GEE) (Mutanga and Kumar, 2019). Although the Landsat archive is increasingly used for the long-term monitoring of wetlands, it has not been fully exploited, as cloudy images and images influenced by the failure of the SLC on Landsat 7 have been discarded. This has resulted in discontinuous time series that may exclude periods when ecosystems changed greatly (Demarquet et al., 2023a).

The entire Landsat archive can now be turned into a continuous time series to generate a synthetic image for any date using harmonic regression methods (Li et al., 2021). Among these methods, the CCDC algorithm is the most widely used for ecosystem monitoring using Landsat data (Pasquarella et al., 2022), as it is suited to time series with many missing observations at the pixel scale (Awty-Carroll et al., 2019a) and is easily accessible using cloud-computing tools (Arévalo et al., 2020). While the CCDC algorithm has been widely used for classification, it has been under-used for producing synthetic images (Pasquarella et al., 2022) to derive indicators of ecosystem functioning (Cabello et al., 2012). For example, continuous long-term time series derived from the Landsat archive using the CCDC algorithm have better captured subtle changes and seasonal variations in biomass in tropical (Arévalo et al., 2023) and semi-arid (Liao et al., 2022) forests, or phenology in a temperate marsh (Fu et al., 2022). However, the worldwide relevance and transferability of the CCDC in producing continuous long-term indicators of ecosystem functioning such as annual net primary productivity (ANPP) has not been evaluated.

In this study, wetland ecosystem functioning refers to their annual greenness cycle of vegetation, and the NDVI-I index was used as a surrogate of ANPP. This index is a reliable indicator of wetland ecosystem functioning, such as carbon storage and fluxes (Bansal et al., 2023) or habitat support (Radeloff et al., 2019). ANPP has high spatial and temporal variability in wetlands and responds to human and climate disturbances (Dąbrowska-Zielińska et al., 2022; Rapinel et al., 2019). ANPP can be derived from continuous satellite-based time series of the NDVI, as the latter, which is strongly correlated with above-ground net primary productivity, is a linear estimator of the fraction of photosynthetically active radiation absorbed by vegetation, the main driver of primary production (Pettorelli et al., 2005). Thus, the annual NDVI integral (NDVI-I), which equals the sum of NDVI and represents ANPP, can be used as an integrated indicator of wetland ecosystem functioning (Cabello et al., 2012). To date, monitoring ANPP using EO data in wetlands has meant a trade-off between the duration of monitoring and spatial resolution: either long-term at low spatial resolution (Fernandez-Carrillo et al., 2019) or short-term at high spatial resolution (Dąbrowska-Zielińska et al., 2022). However, the long-term monitoring of ANPP at high spatial resolution is now possible using the Landsat archive (L. Zhang et al., 2022).

The aim of this study was to monitor long-term changes in wetland ecosystem functioning using the Landsat archive and the CCDC algorithm. Specifically, we explored the influence of the LULC class and the number of available cloud-free Landsat observations for each pixel on the accuracy of the NDVI-I, as harmonic regression methods are likely to perform better when applied to stable ecosystems with many cloud-free observations. Four Ramsar wetlands were selected in boreal, temperate, arid, and tropical biomes to cover a wide range of LULC classes and cloud-free Landsat observation numbers.

3.2. Materials and Methods

3.2.1. Study sites

This study focused on four Ramsar wetlands that covered a wide range of wetland types and cloud-free Landsat observation numbers due to bioclimatic conditions (Figure 3.2.1). The first site is a 2586 ha unexploited tundra mire complex in northern Sweden (*Pirttimysvuoma*, Ramsar ID 2177) frequently grazed by reindeer. Due to the site's high latitude and boreal climate, it had the fewest cloud-free Landsat observations (Figure 3.2.1A).

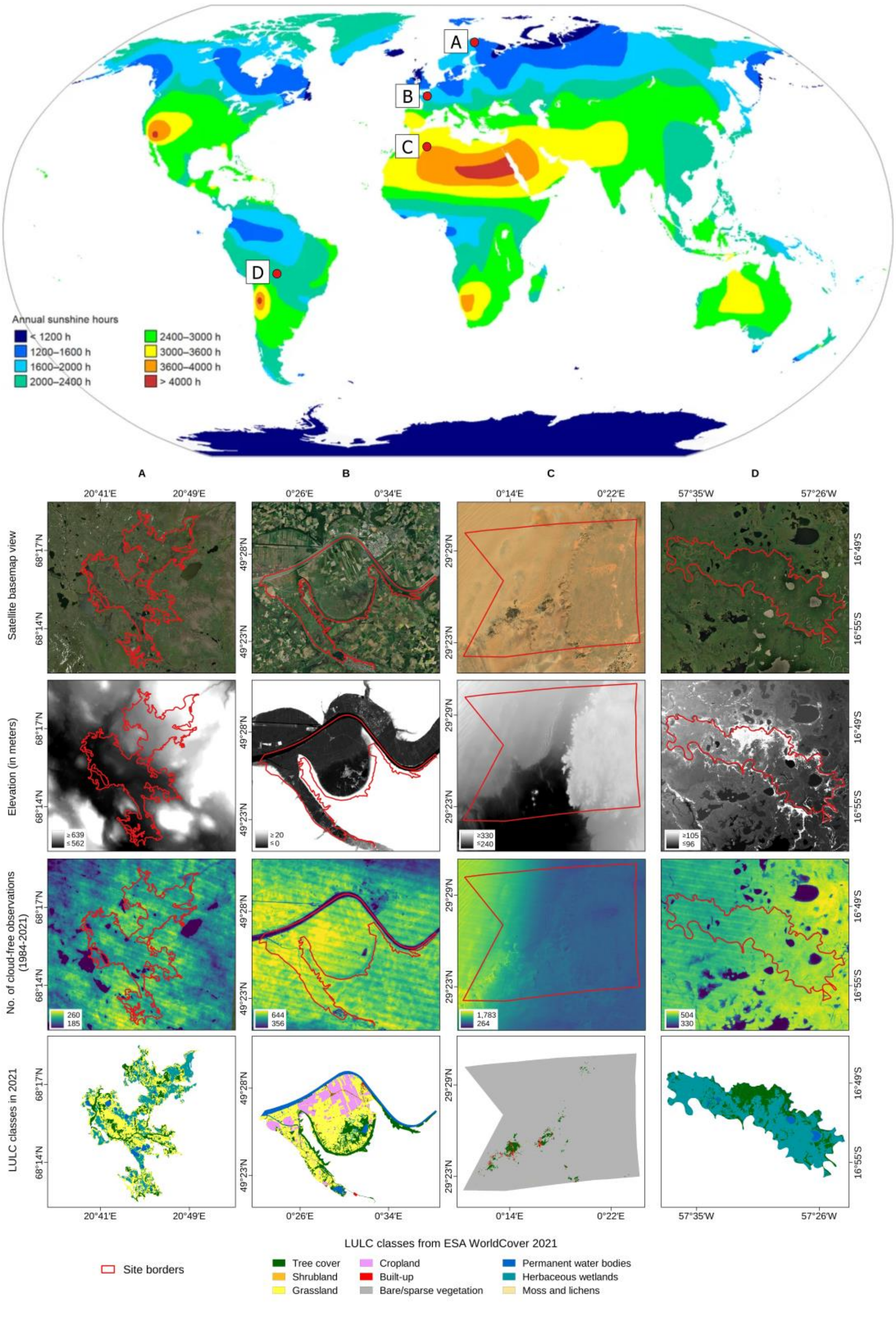

Figure 3.2.1. Top: Location of the four Ramsar wetland sites on a world map of the annual hours of sunshine (Landsberg and Pinna, 1978). Bottom: View of the four Ramsar wetland sites as Google Earth images (first row), the elevation derived from the Copernicus DEM (second row), the number of cloud-free Landsat observations (third row), and the LULC classes in 2021 (fourth row). A: Pirttimysvuoma; B: Marais Vernier; C: Ouled Saïd; D: Taiamã Ecological Station.

The second site, the Marais Vernier et Vallée de la Risle Maritime (Ramsar ID 2247), is located in France and has a temperate climate. This 9565-ha site is dominated by seasonally flooded agricultural land. A moderate number of cloud-free Landsat observations were available for this site (Figure 3.2.1B).

The third site, Oasis de Ouled Saïd (Ramsar ID 1060), is located in the Sahara Desert. This 25,400-ha oasis wetland developed in a former channel bed. Due to this site's arid climate, many cloud-free Landsat observations were available for it (Figure 3.2.1C).

The fourth site, the Taiamã Ecological Station (Ramsar ID 2363) covers 11,555 ha in the Pantanal wetland (Figure 3.2.1D). This tropical wetland is dominated by seasonal and permanent freshwater marshes and is frequently threatened by fires. Few cloud-free Landsat observations were available due to the frequency of tropical rainfall.

A more detailed description of each site is provided on the Ramsar Sites Information Service website (https://rsis.ramsar.org/ ; accessed on 17 July 2024).

3.2.2. Data

3.2.2.1. Landsat archive

Level-2 Landsat atmospherically corrected surface reflectance images were extracted for 1984–2021 from the Landsat Collection 2 archive (Lubke et al., 2021), which is available in the GEE (Gorelick et al., 2017). Specifically, the images were acquired using the Landsat 4-5 thematic mapper (TM), Landsat 7 enhanced thematic mapper (ETM+), and Landsat 8-9 operational land imager (OLI) sensors (Figure 3.2.2). The Landsat 1–2–3 Multispectral Scanner archive was not used in this study because the spectral and spatial characteristics of this sensor differ greatly from those of the other Landsat sensors. All available images were considered, including cloudy images and Landsat 7 SLC-off images, as the CCDC algorithm contains a two-step cloud, cloud shadow, and snow-masking tool to eliminate "noisy" observations (Zhu and Woodcock, 2014a). In total, 1263, 2090, 2715, and 929 Landsat images were used for the Pirttimysvuoma, Marais Vernier, Ouled Saïd, and Taiamã, respectively (Figure 3.2.2, Appendix G).

Landsat images were pre-processed in the CCDC GEE application program interface (API) (Arévalo et al., 2020) using a two-step procedure: noisy pixels were masked using the quality-assessment band, and clouds, cloud shadows, and snow cover were removed using *CFmask* (Foga et al., 2017), a C programming language translation of the *Fmask* version 3.2 algorithm (Zhu and Woodcock, 2012) (Figure 3.2.3).

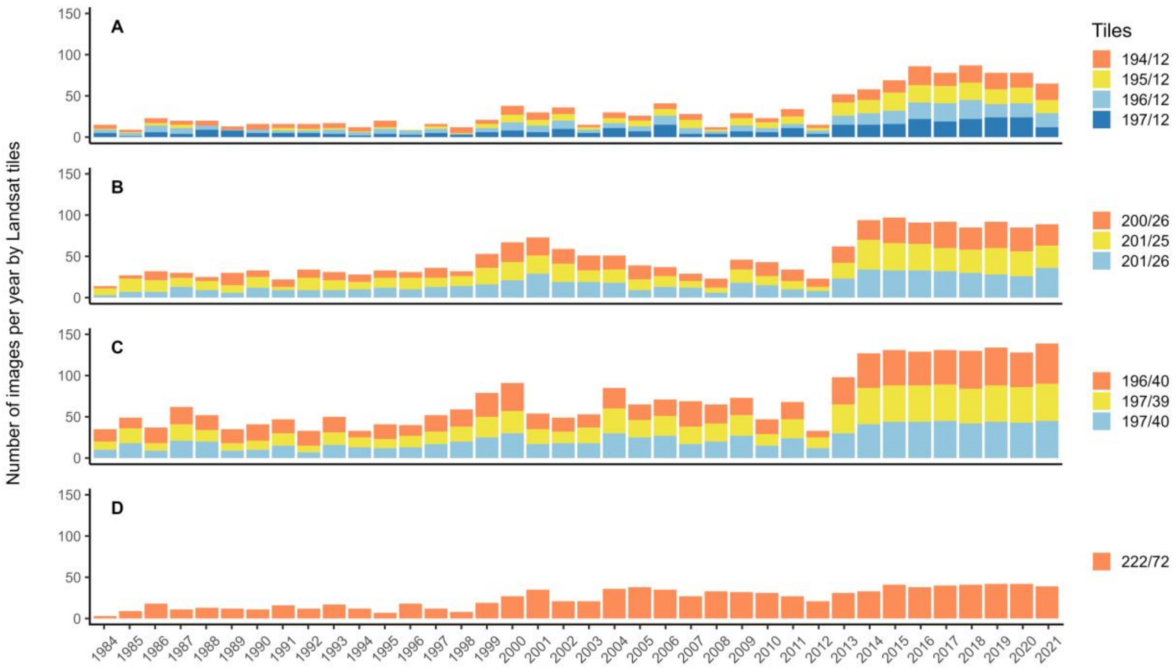

*Figure 3.2.2. Number of Landsat images by tile per year for each site: (**A**) Pirttimysvuoma; (**B**) Marais Vernier; (**C**) Ouled Saïd; (**D**) Taiamã Ecological Station.*

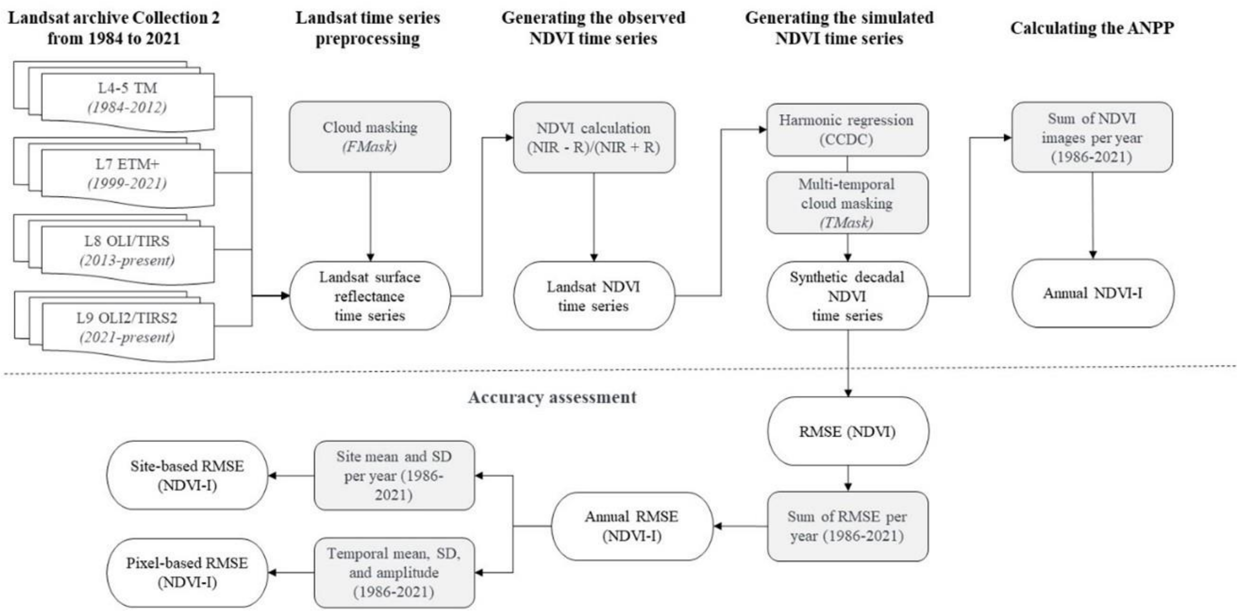

Figure 3.2.3. The method used to calculate the annual normalized difference vegetation index integral (NDVI-I) as an indicator of annual net primary productivity (ANPP) using the continuous change detection and classification (CCDC) application program interface (Arévalo et al., 2020). RMSE: root-mean-square error, SD: standard deviation.

3.2.2.2. LULC Data

The ESA WorldCover 2021 version 200 raster map was downloaded from the Zenodo repository (Zanaga et al., 2022). The map, which contains 11 LULC classes aligned with the UN-FAO Land Cover Classification System, was produced from the Sentinel-1&2 time series. It has a spatial resolution of 10 m and an overall accuracy of 77%.

3.2.2.3. Climatic Data

Gridded climate data were retrieved for 1984–2021 at 0.5° spatial resolution from the Global Historical Climatology Network Daily (GHCN-d) dataset (Menne et al., 2012) of the NOAA Climate Prediction Center (CPC) (NOAA, n.d.), which contains records from more than 100,000 stations in 180 countries and territories. These climate data were gridded using the Shepard algorithm. The distance of Pirrtimysvuoma, Marais Vernier, Ouled Saïd, and Taiamã Ecological Station to the nearest GHCN meteorological station was 61, 26, 23, and 29 km, respectively. Daily minimum (T_{min}) and maximum (T_{max}) temperatures were extracted for each site from the CPC Global Unified Temperature product and then averaged per year. Daily mean temperature (T_{mean}) was calculated as the mean of daily T_{min} and daily T_{max} and then averaged per year. Daily precipitation (P_{mm}) was extracted for each site from the CPC Global Unified Gauge-Based Analysis of Daily Precipitation product and then summed per year.

3.2.3. Calculating Indicator of Wetland Ecosystem Functioning

As a reliable indicator of ecosystem primary productivity (Pettorelli et al., 2005), a continuous time series of the NDVI was calculated in the cloud using the CCDC API (Arévalo et al., 2020) to estimate the ANPP (Figure 3.2.3).

3.2.3.1. Generating the Observed NDVI Time Series

A discontinuous time series was generated for each 30 m pixel by calculating the NDVI from each cloud-masked Landsat image using the following equation:

$$NDVI = (NIR - Red)/(NIR + Red) \quad (1)$$

Where NIR corresponds to the near-infrared spectrum (band 4: 0.76–0.90 μm for the TM and ETM+ sensors and band 5: 0.85–0.88 μm for the OLI sensor) and Red to the red spectrum (band 3: 0.63–0.69 μm for the TM and ETM+ sensors and band 4: 0.64–0.67 μm for the OLI sensor).

3.2.3.2. Generating the Simulated NDVI Time Series

A continuous simulated NDVI time series was generated for each 30 m pixel using a harmonic regression model that was fit to a stable historical period at the beginning of the observed NDVI time series. Next, new observations (pixels) were added to the model iteratively, and their residuals were compared to the root-mean-square error (RMSE) of the historical period. When the predictions differed significantly from the observations on six consecutive dates (i.e., when residuals of future observations exceeded a chi-square threshold value), a break (indicating a potential change in the structure or functioning of the wetland) was flagged, and a new model was initialized. This process was repeated for the remaining observations of the NDVI time series (Figure 3.2.4). The multi-temporal Tmask algorithm (Zhu and Woodcock, 2014b) was also applied during this procedure to remove aberrant observations not detected by the Fmask algorithm before fitting the harmonic model.

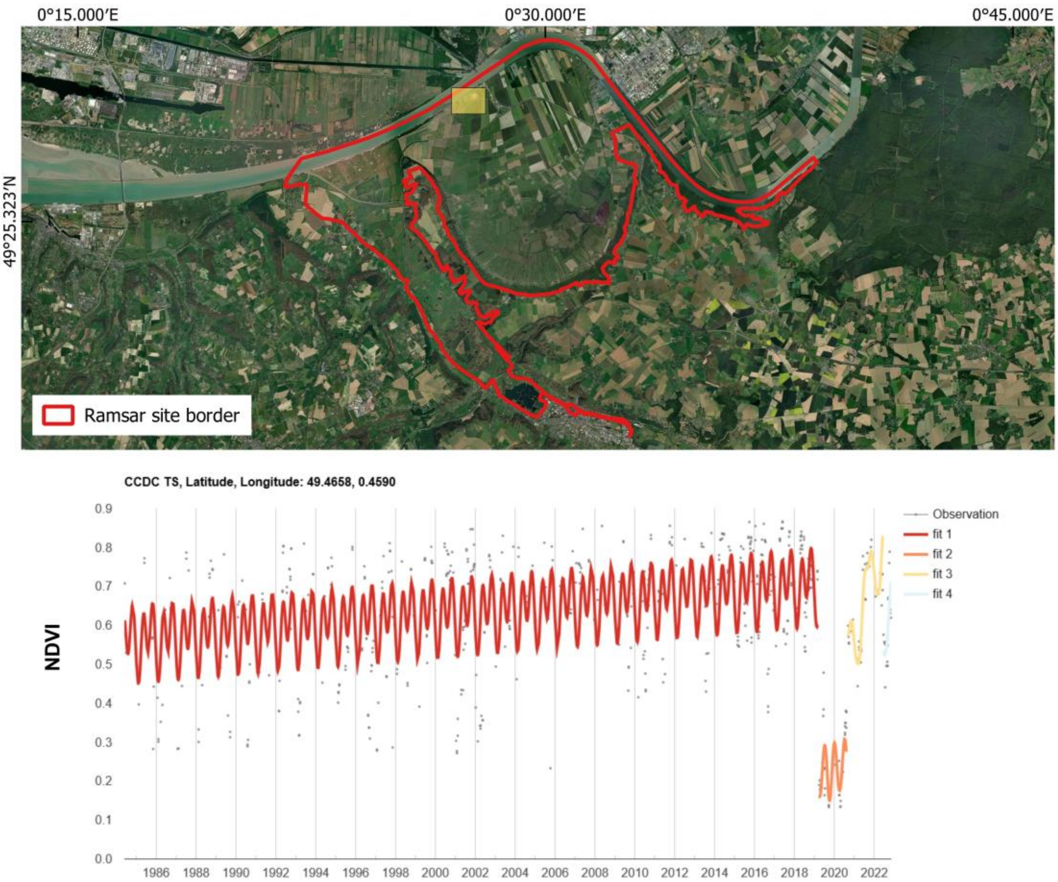

Figure 3.2.4. Example of the normalized difference vegetation index (NDVI) time series (TS) extracted from the Landsat archive for 1984–2021 at the Marais Vernier Ramsar site. The yellow rectangle identifies the pixel from which the time series was extracted and analyzed using the continuous change detection and classification (CCDC) algorithm. The colored lines indicate fits during time segments detected by the CCDC algorithm; a change in color indicates a change in land cover/land use.

The CCDC API provides two types of harmonic models: ordinary least-square regression and least absolute shrinkage and selection operator (LASSO) regression. The latter was selected because it has a regularization parameter that reduces overfitting (Tibshirani, 1996) and remains robust when only a few cloud-free Landsat images are available during a year (Zhu et al., 2015). CCDC also provides the RMSE for each band, which indicates the accuracy with which the observed reflectance was predicted.

To evaluate the transferability of the CCDC algorithm, it was applied with the default parameters set in the API (Table 3.2.1) to each Landsat pixel for specific dates each year for each study site. It should be noted that the default parameters in the help document (https://developers.google.com/earth-engine/apidocs/ee-algorithms-temporalsegmentation-ccdc) (accessed on 17 July 2024) and given in the literature (Arévalo et al., 2023; Pasquarella et al., 2022) differed slightly from those in the submit_CCDC script used (https://code.earthengine.google.com/?accept_repo=users/parevalo_bu/gee-ccdc-tools) (accessed on 17 July 2024). In total, 1388 synthetic mean NDVI images at a 10-day time step were generated for each site from 1984 to 2021. This decadal interval was considered a reasonable trade-off between temporal resolution and computing requirements. The model RMSE per period and the number of breaks in the time series were retrieved from CCDC outputs for each Landsat pixel of the four sites.

Table 3.2.1. Parameters for the continuous change detection and classification algorithm and default values set in the API submit_ccdc script (https://code.earthengine.google.com/?accept_repo=users/parevalo_bu/gee-ccdc-tools) (accessed on 17 July 2024) applied to the four study sites. Asterisks indicate non-default values.

Parameter	Meaning	Value
breakpointBands	The name or index of the bands used for change detection	NDVI *
tmaskBands	The name or index of the bands used for iterative TMask cloud detection	Green, SWIR2
MinObs	Moving window size for break detection	5
Lambda	Penalty parameter for LASSO regression	0.005
ChiSquareProbability	Chi-square probability threshold for break detection	0.99 *
MinNumOfYearsScaler	Minimum number of years before applying a new fitting	1.33
Seg	Maximum number of temporal segments in the entire time series	6
MaxIterations	Maximum number of runs for LASSO regression convergence	10,000 *

3.2.3.3. Calculating NDVI-I

The NDVI-I is a reliable indicator of the ANPP (Alcaraz et al., 2006). Before calculating the NDVI-I, the years 1984–1985 were removed as they corresponded to the initialization of the first harmonic model, which had predicted many "no data" values on the synthetic NDVI images. The NDVI-I was then calculated for each year and each site by setting negative NDVI values to zero (to avoid water-related biases) and summing the decadal synthetic NDVI images. As a result, the NDVI-I theoretically ranged from 0.0 (0 × 36 images) to 36.0 (1 × 36 images), and as NDVI-I values increased, ANPP increased.

To investigate spatiotemporal variations in the accuracy of NDVI-I, annual cumulative RMSE images—corresponding to the sum of the RMSE of model predictions of decadal synthetic NDVI images for the year—were generated per pixel for each site. Spatiotemporal variations in the NDVI-I for 1986–2021 were assessed for each site by calculating, for each pixel, the temporal mean, temporal standard deviation (SD), and temporal amplitude of NDVI-I, as well as the two years with the minimum and maximum NDVI-I.

3.2.4. Influence of LULC Class and Number of Cloud-Free Landsat Observations on NDVI-I Accuracy

To investigate the influence of LULC on NDVI-I accuracy, we used the 2021 ESA WorldCover map (Zanaga et al., 2022) instead of the CCDC classification output to ensure independence between LULC and NDVI-I values. The cumulative RMSE of the synthetic NDVI images for 2021, the LULC classes, and the number of Landsat cloud-free observations available in 2021 (divided into five classes using the Jenks natural breaks method: very small (0–6), small (7–19), moderate (20–35), large (36–63), and very large (64–113)) were extracted for each Landsat pixel at each site. Under-represented (<100 pixels per site) combinations of LULC class and observation number (e.g., grasslands and very large) were removed from the analysis. Eighty pixels were then randomly selected from each combination of LULC class and observation number. For each site, permutational Type II analysis of variance (ANOVA) (i.e., with no assumptions about normality or heteroscedasticity (Anderson, 2014)) was performed with the selected pixels to estimate the RMSE as a function of LULC class and the number of observations. The size of RMSE variance explained by each factor and their interaction was expressed by the partial eta-squared index (η^2) (Richardson, 2011) as follows:

$$\eta^2 = SS_{effect}/(SS_{effect} + SS_{error}) \tag{2}$$

where SS_{effect} is the sum of squares associated with the effect of the factor, and SS_{error} is the sum of squares error (i.e., unexplained variance) in the ANOVA model.

To reduce the bias due to sample balancing, pixels were randomly selected, and the ANOVA was repeated 500 times.

3.2.5. Correlation between NDVI-I and Climate Data

For each site, the correlation between annual climate variables (i.e., mean T_{min}, mean T_{max}, mean T_{mean}, and cumulative P_{mm}) and spatially averaged annual NDVI-I for 1986–2021 was assessed using the Pearson correlation coefficient. Statistical analyses were performed using R software version 4.2.2 (R Core Team, 2022) with the terra (Hijmans, 2022), FactoMineR (Lê et al., 2008), and lmPerm (Wheeler et al., 2016) packages.

3.3. Results

3.3.1. CCDC Sensitivity

The sensitivity of the CCDC algorithm for the wetland sites varied at the site scale (Figure 3.3.1) and pixel scale (Figure 3.3.2). At the site scale, the CCDC algorithm was consistently accurate when generating NDVI-I for 1986–2021. The slope of the trend in RMSE ranged from −0.010 for Taiamã (Figure 3.3.1D) to 0.002 for Marais Vernier (Figure 3.3.1B). NDVI-I accuracy was higher and less variable for Ouled Saïd (mean RMSE: 0.44–0.49, SD of RMSE: 0.17–0.19) (Figure 3.3.1C) and Pirrtimysvuoma (mean RMSE: 2.63–2.70, SD of RMSE: 0.49–0.51) (Figure 3.3.1A) than for Marais Vernier (mean RMSE: 3.80–4.03, SD of RMSE: 1.38–1.54) (Figure 3.3.1B) and Taiamã (mean RMSE: 1.89–2.38, SD of RMSE: 0.94–1.51). For Taiamã, the RMSE decreased continuously beginning in the 2000s (Figure 3.3.1D).

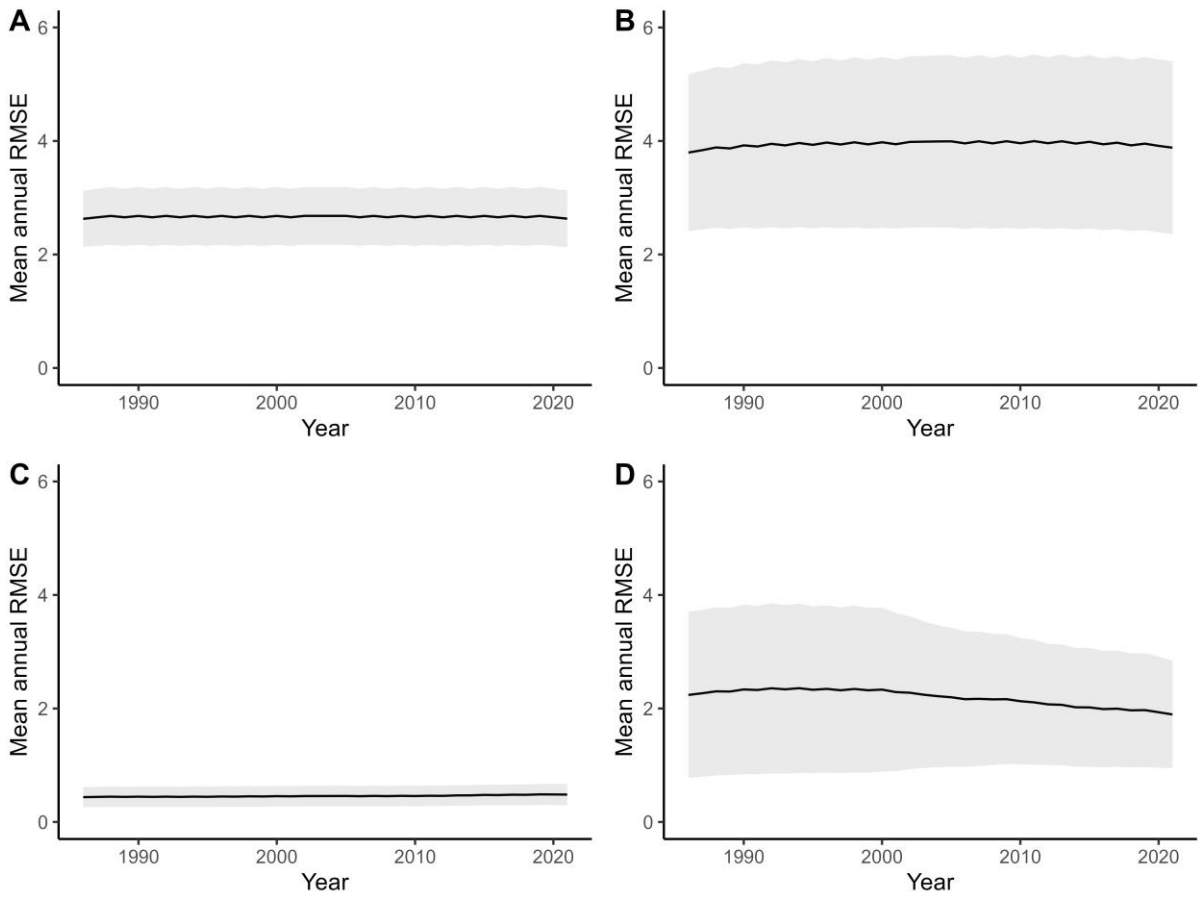

*Figure 3.3.1. Annual variation in spatially averaged root-mean-square error (RMSE) of the annual normalized difference vegetation index integral (NDVI-I) (black line) and standard deviation (grey area) calculated from all pixels for each site from 1986 to 2021: (**A**) Pirttimysvuoma; (**B**) Marais Vernier; (**C**) Ouled Saïd; (**D**) Taiamã Ecological Station.*

At the pixel scale, NDVI-I accuracy had a fine-grained pattern for all sites (Figure 3.3.2). For Pirttimysvuoma, scattered patches of larger RMSE (mean ≥ 3.90, SD ≥ 0.05, and amplitude ≥ 0.1) and more breaks (≥1) were observed for water bodies and herbaceous wetlands. For Marais Vernier, the southern part (i.e., grassland and woodland) clearly differed from the northern part (i.e., cropland), which had larger RMSE (mean ≥ 7.80, SD ≥ 1.30, and amplitude ≥ 4.20) and more breaks (≥2). For Ouled Saïd, bare soil and vegetated areas differed greatly, with the latter having a larger mean RMSE (≥0.70) and amplitude (≥0.10). Interestingly, the largest SD of RMSE and the highest number of breaks (≥2) were observed in the center of the site along a northeast/southwest line, which corresponded to a depression (Figure 3.2.1). Site-specific stretching of these images also revealed linear patterns in the northwestern part that may have been due to the Landsat 7 SLC-off images. In comparison, Taiamã had many patches with large RMSE (mean ≥ 5.00, SD ≥ 0.50, and amplitude ≥ 5.00) and many breaks (≥3). Similarly, for Pirttimysvuoma, these patches covered water bodies and herbaceous wetlands.

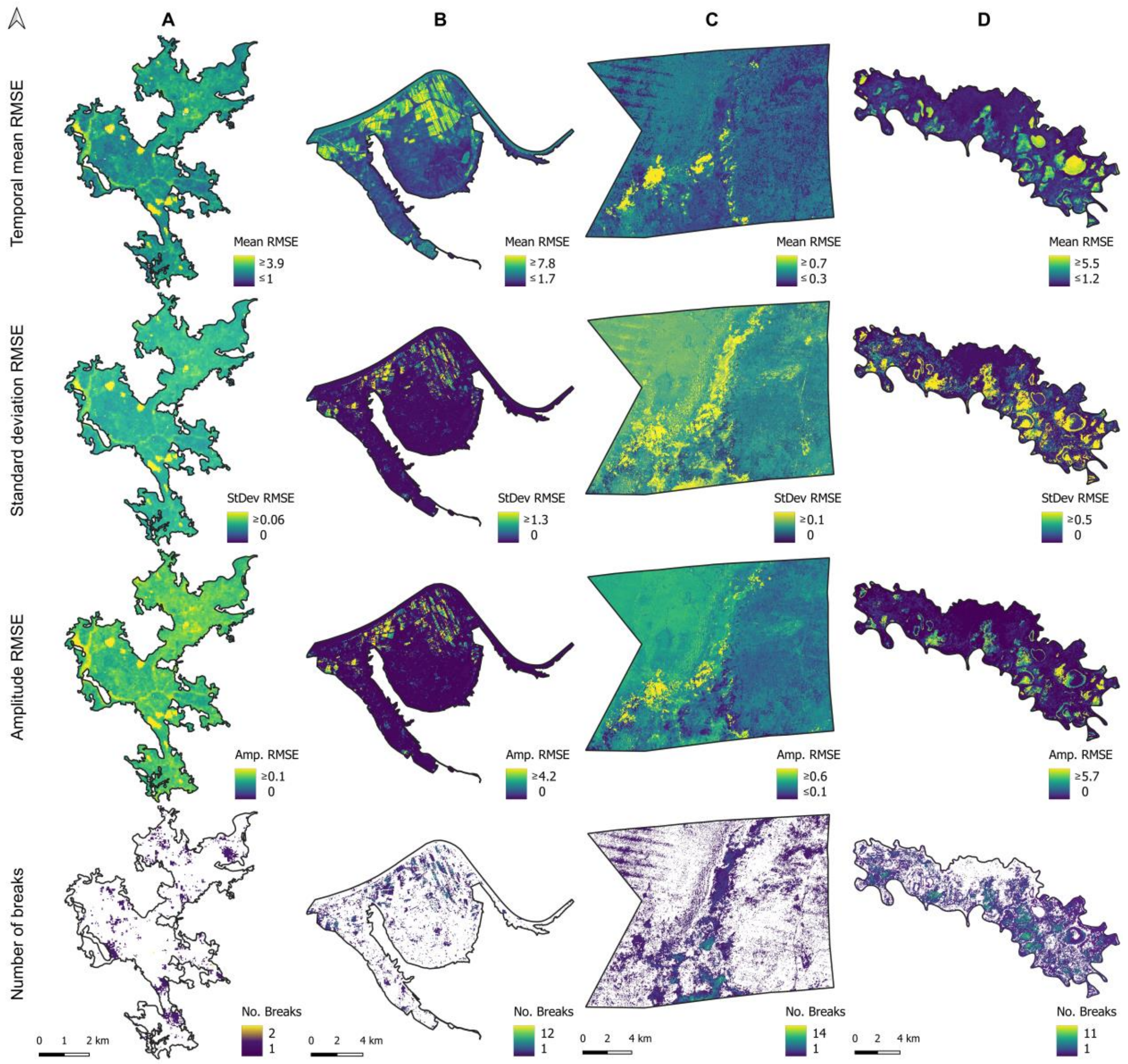

Figure 3.3.2. Temporal mean, standard deviation (StDev), and amplitude (Amp.) of the annual normalized difference vegetation index integral (NDVI-I) root-mean-square error (RMSE) and number of breaks (No. Breaks) detected in the NDVI time series using the continuous change detection and classification algorithm for the four study sites from 1986 to 2021. Image stretching was applied to each site to highlight its spatial pattern. (A) Pirttimysvuoma; (B) Marais Vernier; (C) Ouled Saïd; (D) Taiamã Ecological Station.

The ANOVA confirmed that LULC class had a large influence on NDVI-I accuracy for the four sites (η^2: 0.37–0.56), whereas the number of Landsat observations had a small influence on this value for Marais Vernier (η^2: 0.01) but a moderate influence on those for the other three sites (η^2: 0.09–0.12) (Table 3.3.1). The interaction between the two factors had a small (η^2: 0.02–0.05) but significant influence on NDVI-I accuracy for Marais Vernier, Ouled Saïd, and Taiamã.

*Table 3.3.1. Results of two-factor permutational analysis of variance to quantify the variance (expressed as mean partial eta-squared based on 500 iterations) in the accuracy (root-mean-square error) of the annual normalized difference vegetation index integral (NDVI-I) in 2021 for each Ramsar site explained by land use and land cover class (LULC), number of Landsat observations (NLO), and their interaction. *** p < 0.001, "ns" p ≥ 0.05.*

Ramsar Site	**Factors**		
	LULC	**NLO**	**LULC × NLO**
Pirttimysvuoma	0.37 ± 0.05 ***	0.10 ± 0.03 ***	ns
Marais Vernier	0.56 ± 0.03 ***	0.01 ± 0.01 ***	0.02 ± 0.01 ***
Ouled Saïd	0.40 ± 0.03 ***	0.09 ± 0.02 ***	0.05 ± 0.02 ***
Taiamã Ecological Station	0.37 ± 0.03 ***	0.12 ± 0.02 ***	0.05 ± 0.02 ***

Analysis of the interaction plots provided details about variations in NDVI-I accuracy as a function of LULC class and the number of Landsat observations (Figure 3.3.3). As expected, the mean RMSE was largest (≥3.40) for water bodies and cropland and smallest (<3.00) for tree cover, bare/sparse vegetation, and built-up areas. Interestingly, the RMSE values by LULC class were similar among the sites; for example, the mean RMSE for permanent water bodies ranged from 4.03 to 4.86 for Pirttimysvuoma and from 4.25 to 4.53 for Marais Vernier. The larger number of Landsat observations resulted in a smaller RMSE for permanent water bodies (Pirttimysvuoma and Taiamã), cropland (Marais Vernier), herbaceous wetland (Taiamã), and tree cover (Ouled Saïd and Taiamã).

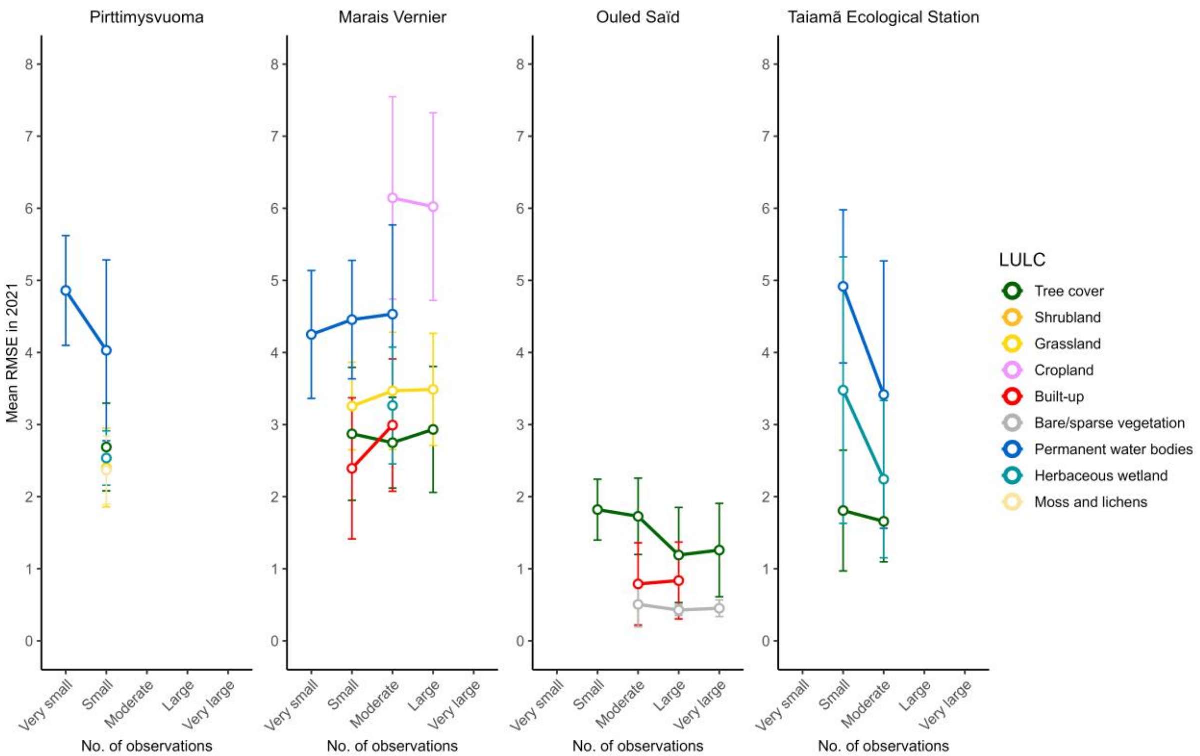

Figure 3.3.3. Influence of the number of Landsat observations (very small: 0–6; small: 7–19; moderate: 20–35; large: 36–63; very large: 64–113), land use and land cover (LULC) class, and their interaction on the accuracy of the continuous change detection and classification algorithm (median and standard deviation of the root-mean-square error (RMSE) for each wetland site). Lines that are nearly parallel indicate weak interactions.

3.3.2. Spatiotemporal Dynamics of NDVI-I

At the site scale, the temporal trends indicated that mean NDVI-I was highest for Taiamã (23.94–28.19) and Marais Vernier (19.45–22.26) and lowest for Pirttimysvuoma (16.76–20.18) and especially Ouled Saïd (2.85–3.16) (Figure 3.3.4). The mean annual NDVI-I increased over time, except for Ouled Saïd, whose trend was stable. In addition, spatial variability was higher for Marais Vernier (SD: 6.65–7.69) and Taiamã (SD: 4.74–6.11) than for Pirttimysvuoma (SD: 2.69–2.80) and Ouled Saïd (SD: 0.77–0.96).

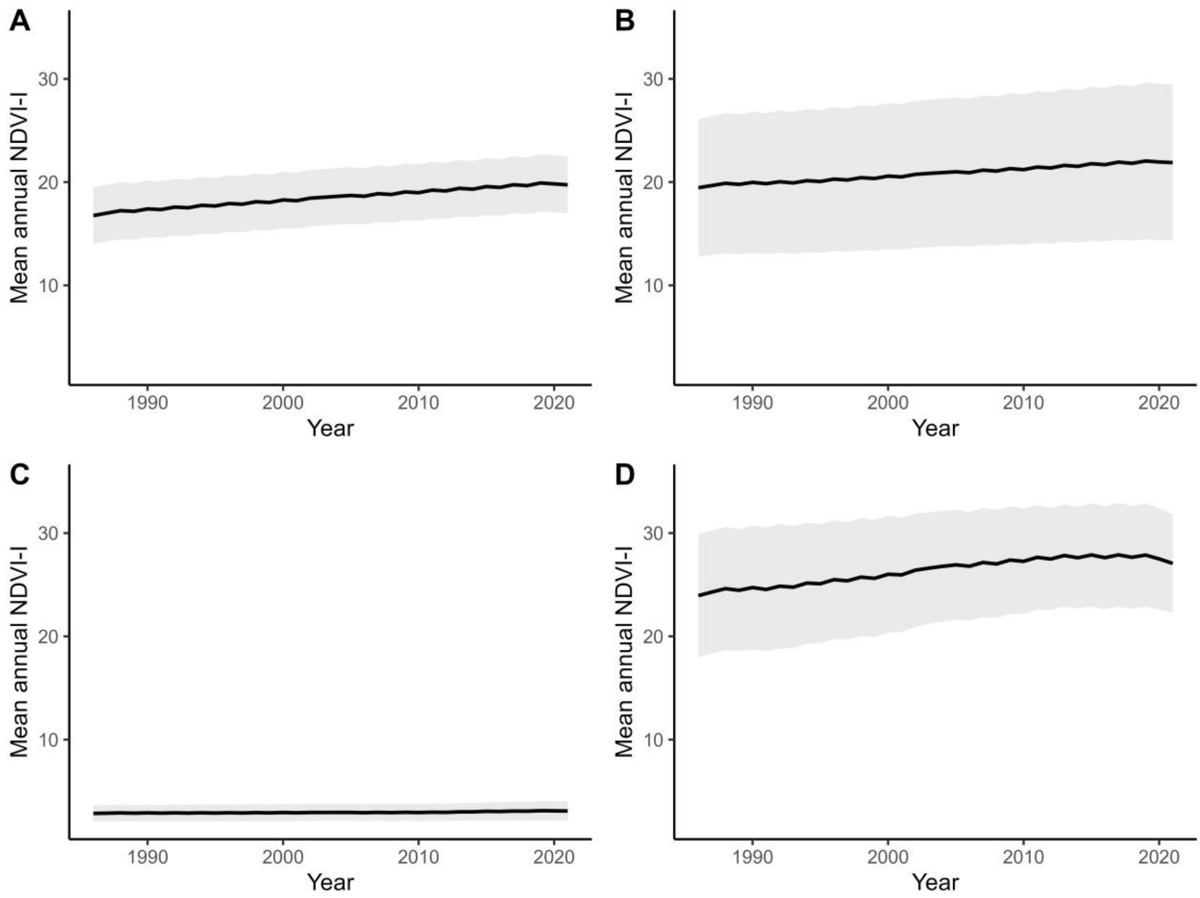

*Figure 3.3.4. Annual variation in spatial mean annual normalized difference vegetation index integral (NDVI-I) (black line) and standard deviation of the annual variation in spatial mean NDVI-I (grey area) for each site for 1986–2021. (**A**) Pirttimysvuoma; (**B**) Marais Vernier; (**C**) Ouled Saïd; (**D**) Taiamã Ecological Station.*

This high spatial variability in NDVI-I was highlighted at the pixel scale for each site (Figure 9). For Pirttimysvuoma, mean NDVI-I was highest for grassland (>21.40) and lowest (≤1.50) for permanent water bodies. The variability in NDVI-I differed greatly among pixels, as illustrated by the fine-grained pattern of SD and amplitude images. NDVI-I tended to increase over time over nearly the entire site (minimum in ~1986, maximum in ~2021).

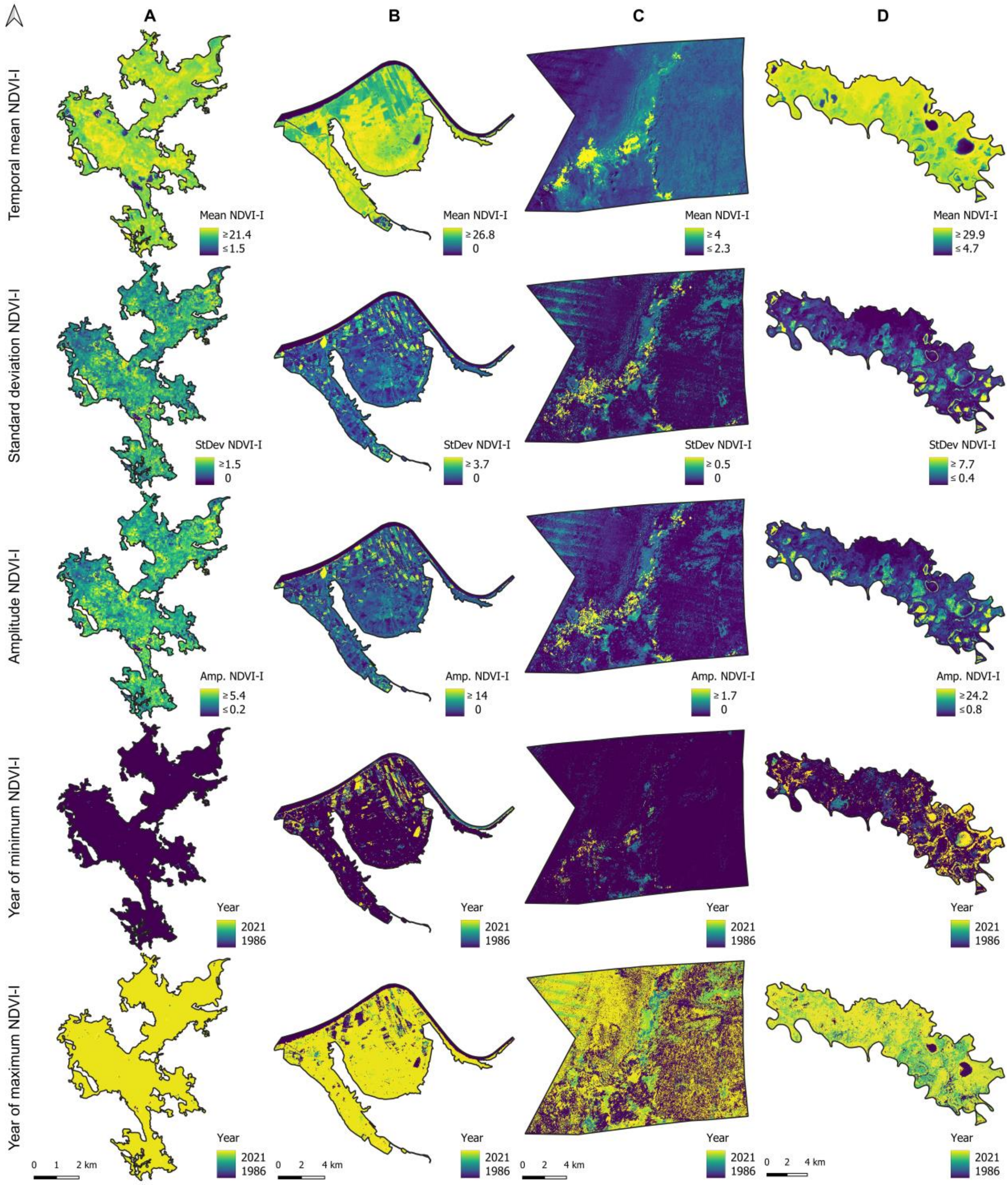

*Figure 3.3.5. Temporal mean, standard deviation (StDev), amplitude (Amp.) of NDVI-I, and years of minimum and maximum NDVI-I for the four study sites for 1986–2021: (**A**) Pirttimysvuoma; (**B**) Marais Vernier; (**C**) Ouled Saïd; (**D**) Taiamã Ecological Station. Image stretching was applied to each site to highlight its spatial pattern.*

For Marais Vernier, the mean NDVI-I was highest for grassland and tree cover (>26.80), lower for cropland (16.00–19.00), and lowest for water bodies (≤3.00). The NDVI-I clearly varied the most over time for cropland (SD ≥ 2.50, amplitude ≥ 10.00).

Unlike the rest of the site, cropland often had a decreasing trend in NDVI-I, with the minimum and maximum values observed in ~2021 and ~1986, respectively.

For Ouled Saïd, the mean NDVI-I was highest for vegetated areas (≥4.00), intermediate in the central depression (3.00–3.50), and lowest throughout the rest of the site (≤2.50). The NDVI-I generally varied little, although it varied more (SD ≥ 1.00, amplitude ≥ 3.00) for vegetated areas. Overall, NDVI-I increased over time, but the year with maximum NDVI-I varied greatly among pixels. Interestingly, linear patterns were observed in the northwestern part, likely due to the Landsat 7 SLC-off images.

For Taiamã, the NDVI-I was highest for tree cover (≥29.00), lower for herbaceous wetland (22.00–27.00), and lowest for permanent water bodies (≤10.00). NDVI-I values varied more (SD ≥ 3.80, amplitude ≥ 8.00) for these flooded LULC classes. Overall, NDVI-I values increased over time (minimum ~1986, maximum ~2021), but they decreased for flooded classes (herbaceous wetlands and permanent water bodies).

3.3.3. Relationship between NDVI-I Temporal Trends and Climate

Correlations between the climate variables and the NDVI-I were significant (Table 3). For temperature variables, the mean annual T_{max} (r: 0.53–0.62) and, to a lesser extent, T_{mean} (r: 0.47–0.59) were strongly positively correlated with the annual NDVI-I for all sites, whereas the mean annual T_{min} was positively correlated only for Pirttimysvuoma and Marais Vernier (r = 0.39 and 0.57, respectively). P_{mm} was negatively correlated only with the annual mean NDVI-I for Taiamã (r = −0.38).

*Table 3.3.2. Pearson correlations between annual mean NDVI-I and climate variables per study site. T_{min}: mean annual minimum temperature; T_{max}: mean annual maximum temperature; T_{mean}: mean annual mean temperature; P: cumulative annual precipitation. * $p < 0.05$, ** $p < 0.01$, "ns" $p \geq 0.05$.*

Climate Variable	Pirttimysvuoma	Marais Vernier	Oasis de Ouled Saïd	Taiamã Ecological Station
T_{min}	0.39 *	ns	0.57 **	ns
T_{max}	0.53 **	0.62 **	0.57 **	0.60 **
T_{mean}	0.47 **	0.49 **	0.59 **	0.51 **
P_{mm}	ns	ns	ns	−0.38 *

3.4. Discussion

The sensitivity of the CCDC algorithm can be influenced by the parameter values defined in the GEE API (Arévalo et al., 2020). Consequently, we performed an exploratory calibration step before the analyses, as recommended by Pasquarella et al. (2022). Increasing the number of consecutive observations needed to identify a break (minObservations) from five (default value) to eight greatly decreased the number of breaks detected. Conversely, increasing the chi-square probability threshold at which changes were detected from 0.90 (default value) to 0.99 decreased the identification of false breaks. However, increasing the penalty parameter for LASSO regression lambda from 0.005 (default value) to 0.10 decreased the amplitude of the temporal profiles significantly. We decreased the maxIteration parameter from 25,000 to 10,000, as doing so slightly decreased calculation times without increasing the RMSE. This exploratory step demonstrated that the default parameters in the submit_CCDC script were generally appropriate. We could have performed site-specific hyper-calibration to increase the accuracy of the synthetic images, even though the CCDC algorithm is not highly sensitive to small parameter changes (Pasquarella et al., 2022), but we used the same parameter values for all sites to emphasize the algorithm's generality. However, no break was identified for much of the Pirttimysvuoma and Marais Vernier sites, which seems unusual given the length of the study period and the dynamic characteristics of wetlands, which highlights the CCDC's limited ability to detect subtle changes, such as vegetation regrowth (Pasquarella et al., 2022). CCDC customizations such as DECODE (Detection and Characterization of Coastal Tidal Wetlands Change) have been developed recently to detect this type of change (Yang et al., 2022), but they have not yet been integrated into a cloud-based solution.

One major advantage of the CCDC algorithm over other approaches was its ability to use all Landsat archive images, including those with high cloud cover and/or SLC-off, to better capture wetland dynamics. For example, it was able to use 929 images for Taiamã instead of only the 91 images without clouds and was not influenced by the failure of the Landsat 7SLC sensor. However, one disadvantage was that cloudy and noisy areas were over-masked at the expense of flooded areas, as indicated by the few Landsat observations retained over water (Figure 1D). The over-detection of cloud shadows over water bodies was observed for CFmask (Foga et al., 2017), and although it was partially corrected in Fmask version 4.0 (Qiu et al., 2019), it has not yet been integrated into the CCDC API of GEE. In addition, the Tmask used in CCDC sometimes confuses ephemeral floods with temporal artifacts. Because the developers of TMask acknowledged this limitation (Zhu and Woodcock, 2014a), we initially considered disabling Tmask to better monitor flood dynamics, but preliminary tests indicated that it removed noise effectively from the time series.

Overall, using CCDC to simulate decadal synthetic NDVI images (from 1984 to 2021) enabled an accurate estimation of ANPP in wetlands. The results support previous studies that used CCDC to generate synthetic images for continuous monitoring of wetland ecosystem functioning over the long term (Fu et al., 2022). However, Fu et al. (2022) did not explore the sensitivity of the CCDC algorithm. The present study demonstrated that the accuracy (mean RMSE) of NDVI synthetic images ranged from 0.01 (0.46/36 dates) for the arid wetland to 0.11 (3.94/36 dates) for the tropical wetland. These results are similar to those of Liao et al. (2022) for wooded vegetation in Australia (mean RMSE of 0.13 in the NIR band). The present study provided a deeper analysis, highlighting that the RMSE generally remained constant over time (1984–2021) but not over space. The high variations among and within sites were due to the LULC classes and the number of Landsat observations available.

Studies have recently highlighted the sensitivity of the CCDC algorithm to the number of observations available, but that number should be described more precisely than as "a sufficient number" (Pasquarella et al., 2022). The present study highlights that the increase in the number of Landsat images available (Figure 2), due to the launch of Landsat 7 in 1999 and Landsat-8 in 2013, has not increased the accuracy of the CCDC algorithm, except for Taiamã (Figure 5). For this site, which is covered by only one Landsat tile and thus had the fewest images, the mean and SD of the RMSE decreased significantly in the early 2000s. This period corresponds to the increase in the mean number of annual observations (from 12 for 1984–1999 to 33 for 2000–2021) due to the launch of Landsat 7. This result was not observed for Pirttimysvuoma, even though it also had few Landsat observations available. This may have been due to the contrasting dynamics of these sites: Pirttimysvuoma is covered mainly by extensive grasslands ("Pirttimysvuoma | Ramsar Sites Information Service," n.d.), whose relatively stable dynamics can be captured accurately with a few Landsat observations (6–19/years), unlike those of the herbaceous wetlands that are periodically flooded by the Paraguay River (Frota et al., 2017) and cover much of the Taiamã site (Figure 7). Thus, increasing the number of Landsat observations is the best way to increase the accuracy of CCDC for LULC classes with irregular or hazard-related dynamics, such as herbaceous wetlands, water bodies, and cropland.

The ANOVA indicated that the LULC class explained a large percentage of the variation in CCDC accuracy, likely due, as before, to the irregular and/or hazard-related dynamics of each LULC class caused by hydrodynamics and/or agricultural practices. CCDC was most accurate for the tree cover and grassland LULC classes, as they have relatively stable and linear dynamics. Interestingly, the RMSE for grasslands was larger for Marais Vernier, where grasslands were alternately grazed and mowed, which resulted in highly irregular seasonal cycles, than for Pirttimysvuoma, where grasslands were only grazed extensively. Conversely, the CCDC algorithm was less accurate for water bodies, herbaceous wetlands, and cropland, perhaps due to the algorithm itself, which assumes linear variations and constant amplitudes within a given time segment, which is not the case for crop rotations or floods. As reported by Liao et al. (2022), this results in the over-detection of breaks and thus larger RMSE values (Figure 6). Approaches based on generalized additive models can also improve the continuous monitoring of frequently flooded areas (Wen et al., 2023), but these models are sensitive to outliers and discontinuous observations.

The present study identified a long-term increase in the NDVI-I at all four wetland sites, in coherence with the global “greening” phenomenon widely documented in the literature (Piao et al., 2020) and related to climate change, particularly in boreal regions (Ju and Masek, 2016). Unsurprisingly, the Pirttimysvuoma boreal wetland showed the largest increase in the NDVI-I. The greening phenomenon also occurred at Marais Vernier, accentuated by fertilizer inputs for agriculture (Piao et al., 2020). At Taiamã, the greening phenomenon has been observed in the Pantanal (de Souza Miranda et al., 2017), but NDVI-I values decreased in 2020 and 2021 (Figure 8), potentially due to drought and wildfires in 2020 (Correa et al., 2022). Conversely, a relatively stable trend was observed for the arid Ouled Saïd site, which agrees with the observations of Wen et al. (2023) for semi-arid marshes in Australia. However, recent studies of wetlands have highlighted that the greening phenomenon varies locally, with larger temporal amplitudes in water levels in flooded areas (Fu et al., 2022; Wen et al., 2023). This was particularly evident for Taiamã, in which large amplitudes and negative trends in NDVI-I were observed in areas that flooded frequently (Figure 9) (Ivory et al., 2019). It also explains the negative correlation between rainfall and NDVI-I at Taiamã. Furthermore, the relationship between the NDVI and primary productivity can be biased in wetlands due to the decrease in spectral reflectance caused by water absorption (Bansal et al., 2023). Although the present study addressed this bias for flooded areas by reclassifying negative NDVI values to zero, it may remain for semi-submerged vegetated areas.

This study shows that the implemented method for the long-term monitoring of wetland ecosystem functioning is robust under contrasting bioclimatic conditions. The method is based on the cloud computing use of a large volume of open access satellite data and algorithms, making it an easily accessible tool to improve the long-term monitoring and management of wetlands considering the dimension of their ecosystem functioning (Geijzendorffer et al., 2019; Kingsford et al., 2021; Lock et al., 2021). For example, this tool could improve the implementation of target 5 "maintenance of ecological character" of the Ramsar Strategic Plan 2016–2024 (Ramsar Convention on Wetlands, 2015), Aichi target 1 "conserve biodiversity" of the Convention on Biological Diversity (CBD Secretariat, 2010), or target 6.6 "protect and restore water-related ecosystems" of the UN Sustainable Development Goals (United Nations, 2015).

CONCLUSION TO CHAPTER 3

In this chapter we have assessed the potential of the CCDC to generate a functional indicator of wetlands from the Landsat archive. Specifically, we calculated NDVI-I, an indicator of annual net primary productivity, continuously over a 38-year period.

The results revealed that NDVI-I accuracy was influenced mainly by the LULC class and to a lesser extent by the number of cloud-free Landsat observations. Infra- and inter-site variations in NDVI-I were high and showed an overall increasing trend. NDVI-I was positively correlated with the mean temperature. This study shows that this approach applied in contrasting sites is robust for the long-term monitoring of wetland ecosystem functioning and can be used to improve the implementation of international biodiversity conservation policies.

While the CCDC can be used to generate functional indicators of wetlands from Landsat archives, the question remains as to whether this method can also be used to study the evolution of wetlands in terms of area and composition, still based on Landsat archives. Chapters 5 and 6 are devoted to answering this question.

INTRODUCTION TO CHAPTER 4

In the previous chapter we described how the CCDC could be used to generate a spatialised functional indicator of wetlands from Landsat archives. Chapter 5 examines whether this method is also suitable for studying changes in wetland area and composition over a long time period.

Unlike the previous chapter, which explored the ability of the algorithm to generate synthetic images, in this chapter we have attempted to use the CCDC to produce annual maps of habitats and to measure changes in their area and structure in a Ramsar site. We have chosen to compare CCDC with a more traditional method that is still widely used, namely post-classification. This study was carried out on the 5th site studied in this thesis, the Marais Poitevin on the Atlantic coast of France.

This chapter corresponds to the article published in the peer-reviewed journal *International Journal of Applied Earth Observation and Geoinformation*:

> Demarquet, Q., Rapinel, S., Gore, O., Dufour, S., Hubert-Moy, L., 2024. Continuous change detection outperforms traditional post-classification change detection for long-term monitoring of wetlands. *International Journal of Applied Earth Observation and Geoinformation* 133, 104142. https://doi.org/10.1016/j.jag.2024.104142

CHAPTER 4. CONTINUOUS CHANGE DETECTION OUTPERFORMS TRADITIONAL POST-CLASSIFICATION CHANGE DETECTION FOR LONG-TERM MONITORING OF WETLANDS

Article

Continuous change detection outperforms traditional post-classification change detection for long-term monitoring of wetlands

by Quentin Demarquet, Sébastien Rapinel, Olivier Gore, Simon Dufour and Laurence Hubert-Moy

Submission received: 10 April 2024 / Revised: 27 August 2024 / Accepted: 1 September 2024 / Published: 6 September 2024

Abstract

Accurate long-term monitoring of wetlands using satellite archives is crucial for effective conservation. While new approaches based on temporal profile classification have been useful for long-term monitoring of wetlands, their advantages over traditional classification approaches have not yet been demonstrated. This study aimed to compare continuous change detection (using the continuous change detection and classification (CCDC) algorithm) to traditional post-classification change detection for monitoring wetland changes between 1984 and 2022 in a temperate coastal marsh (Marais Poitevin, France) from the Landsat archive. The reference dataset was collected mainly from field observations and used to train and test a random forest classifier. The accuracy of the resulting change map was then assessed for both approaches using validation points collected *via* visual interpretation of historical aerial photographs and Landsat temporal profiles. The change map derived from CDDC had much higher unbiased overall accuracy (0.86 ± 0.02) than that derived from post-classification change detection (0.51 ± 0.03). In addition, wetland loss was much higher than wetland gain (18% and 2% of the area, respectively) and was due mainly to conversion of grassland to cropland and urbanization. The study demonstrated that, unlike traditional post-classification change detection, continuous change detection provides maps of wetland changes sufficiently accurate for operational use by managers. The study also confirmed the ongoing impact of agricultural intensification and artificialization on wetland degradation in Europe.

4.1. Introduction

Wetlands, defined as "areas that are inundated or saturated at a frequency to support, and which normally do support, plants adapted to saturated and/or inundated conditions" (Brinson, 1993), provide 40 % of the total value of ecosystem services on Earth (Xu et al., 2020). However, the amount of ecosystem services provided has decreased continuously for several decades due to human pressure on wetlands, as well as climate change (Yang et al., 2023). From a conceptual viewpoint, it is useful to distinguish existing wetlands that are slightly or not impacted by human or climate disturbances from damaged wetlands degraded by changes in land use and land cover (LULC) and from habitat types, such as crops or permanent ponds, in which restoration can be performed (Rapinel et al., 2018). Long-term (i.e. several decades) mapping of LULC or habitat types is therefore a key indicator for monitoring the structure of wetlands and ultimately their ability to provide ecosystem services and support human well-being (Yang et al., 2023).

Earth observation (EO) data, which provide standardized, repeated measurements with wide spatial coverage, have been extensively used to detect long-term changes in wetlands (Jafarzadeh et al., 2022). Among EO data, archive images from Landsat missions are of particular interest for long-term monitoring, since Landsat images have been collected every 16 days at 30 m spatial resolution since 1984, making them the longest EO record worldwide (Wulder et al., 2022). In addition, the Landsat archive is freely available and integrated into cloud-computing platforms such as Google Earth Engine (Gorelick et al., 2017).

Currently, using the Landsat archive to detect changes in wetlands is based mainly on two methods: traditional post-classification change detection or continuous change detection (Demarquet et al., 2023a). The former involves classifying LULC or habitat types for two separate years from one or a few cloud-free images or one composite image, then detecting changes between the two years by combining the classifications in post-processing (Zhu, 2017). The value of this simple method is that it requires few images and therefore few computational resources (Zhu, 2017). The latter method, which is more recent, identifies and classifies temporal segments (each corresponding to one LULC/habitat type) identified from a dense Landsat time-series containing several hundred observations. This method has been developed using a variety of algorithms, such as LandTrendr (Kennedy et al., 2010) or continuous change detection and classification (CCDC) (Zhu and Woodcock, 2014a). The advantage of continuous change detection is that it can produce a LULC/habitat map for any year in the period under consideration from a single classifier. Initially, continuous change detection was rarely used due to the high computation time and number of images needed; however, it is increasingly used due to the recent development of cloud-computing application programming interfaces (APIs) (Pasquarella et al., 2022).

Although continuous change detection would appear more effective than post-classification change detection, the latter remains the most widely used method for monitoring long-term changes in wetlands (Demarquet et al., 2023a; Jafarzadeh et al., 2022). Moreover, recent studies that used the Landsat archive for long-term wetland monitoring emphasized that the overall accuracy of LULC or habitat maps was high (>0.80) regardless of the method. For example, LULC maps of a coastal wetland had an overall accuracy of 0.90–0.97 using post-classification change detection (Hotaiba et al., 2024) and 0.88 using continuous change detection (Peng et al., 2021). Similarly, LULC maps of an inland marsh had an overall accuracy of 0.82–0.88 using post-classification change detection (Liu et al., 2021) and 0.84 using continuous change detection (Fu et al., 2022). These results indicate two main reasons why choosing the most appropriate method to detect wetland change can be difficult: (i) the classification accuracy obtained for one site using a given method cannot be strictly compared to that obtained for another site using another method, since accuracy depends on the structural and functional characteristics of the site, and (ii) the accuracy of change maps is rarely specified for post-classification change detection (Demarquet et al., 2023a).

The objective of the present study was to determine which method detected long-term wetland changes most accurately. To this end, the two methods used the Landsat archive to detect changes in a coastal marsh in France between 1984 and 2022. Specifically, continuous change detection was performed using the most widely used CCDC algorithm (Pasquarella et al., 2022). We then assessed the overall accuracy of the change map generated by each method and also assessed strengths and weaknesses of each method.

4.2. Materials and Methods

4.2.1. Rationale of the approach

Continuous and post-classification change detection methods were performed in parallel (Figure 4.2.1) using the same Landsat archive, environmental variables, and reference datasets. The first reference dataset (Dataset 1), which included field archive data supplemented with points extracted from visual interpretation of historical aerial photographs, was used to evaluate the accuracy of annual habitat maps. The second reference dataset (Dataset 2), which included points extracted from visual interpretation of aerial photographs, satellite images from Google Earth, and temporal profiles derived from the Landsat archive, was used to evaluate the accuracy of the change detection maps. Continuous change detection was performed using the API developed by (Arévalo et al., 2020) in the Google Earth Engine (GEE) cloud-computing platform (Gorelick et al., 2017).

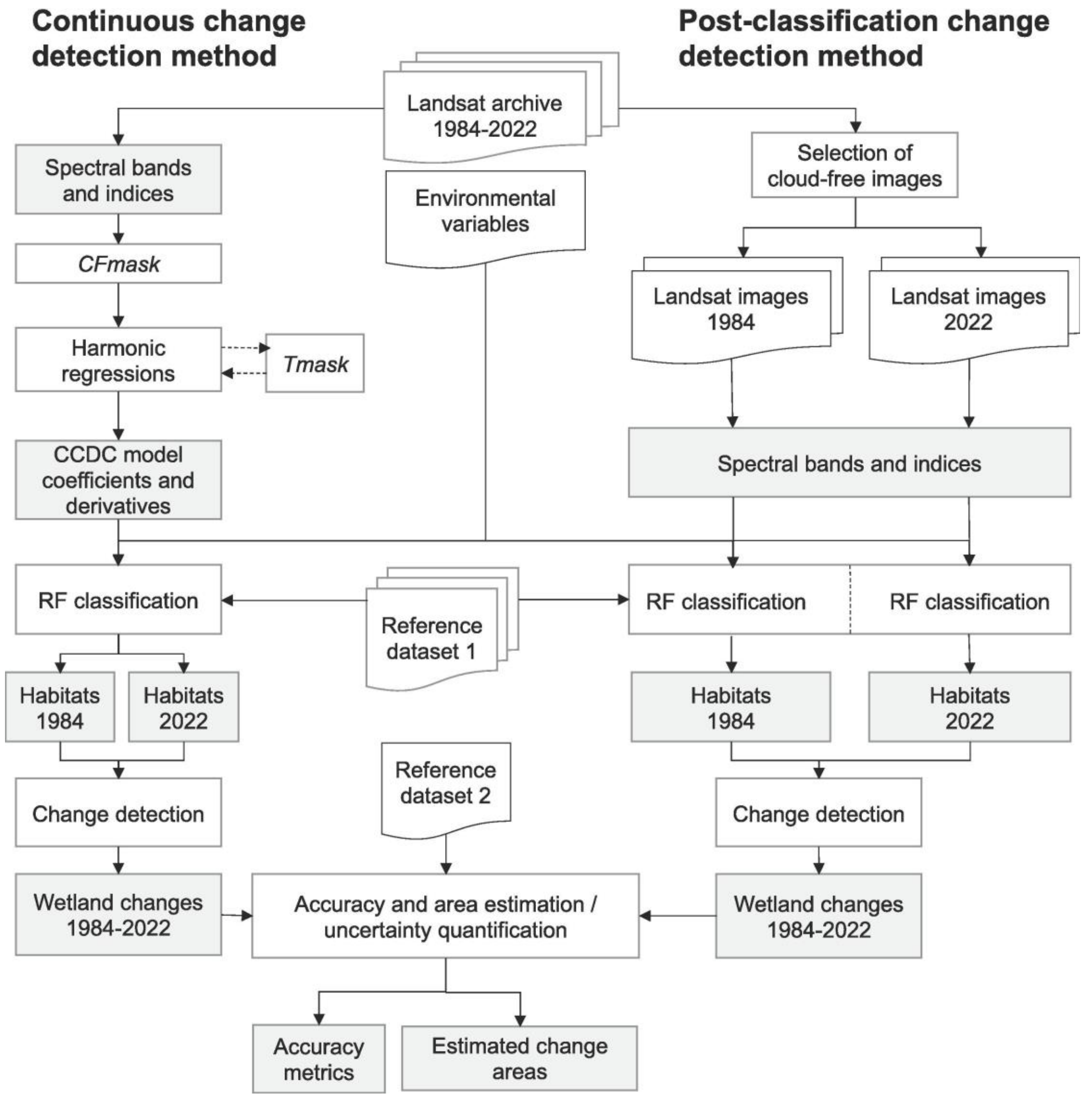

Figure 4.2.1. Framework for monitoring long-term changes using the Landsat archive and the continuous change detection and classification (CCDC) algorithm and comparison with the post-classification change detection method. RF: random forest.

Habitats were characterized using the hierarchical European Nature Information System (EUNIS) level 1 classification (Davies et al., 2004). EUNIS classes were grouped into two classes (i.e., damaged wetlands or existing wetlands, which were strongly altered by or protected from human disturbance, respectively) to describe wetland changes (Rapinel et al., 2018).

4.2.2. Study site

The Marais Poitevin, located on the Atlantic coast of France (Figure 4.2.2), is the second largest wetland in the country (ca. 100 000 ha). This coastal wetland complex has a temperate climate and flat topography whose elevation ranges from 0 to 10 m. Construction of dikes and canals for agriculture and urbanization since the 13th century has resulted in marsh drainage (Godet and Thomas, 2013; Pouzet et al., 2015). Today, the Marais Poitevin includes three contrasting areas: a western area with marine and coastal habitats, a central area with wet grasslands and cropland, and an eastern area with wet grasslands and woodlands (Rapinel et al., 2015). Pressure from tourism and farming has prompted the creation of several protected areas over the past few decades (i.e., Natura 2000 sites, nature reserves, and regional nature parks). Nonetheless, the wetlands have generally degraded over time despite these conservation measures (Duncan et al., 1999).

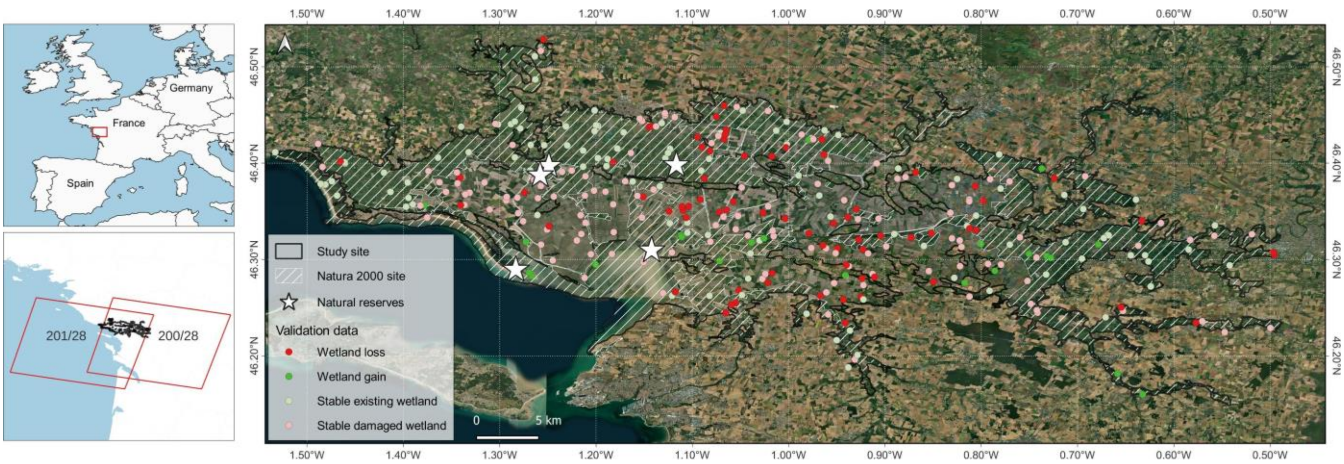

Figure 4.2.2. Location of the study area and Landsat tile overlay (left) and reference Dataset 2 used to assess the unbiased accuracy of the change map (right).

4.2.3. Data

4.2.3.1. Landsat archive

Landsat TM, ETM+, OLI/TIRS, and OLI2/TIRS2 atmospherically corrected surface images (Tier 1, Collection 2, Level 2) acquired from 1984 to 2022 were used and accessed through GEE (USGS, 2021). The images were selected because enhanced geometric correction and radiometric calibration and harmonization among sensors makes the images suitable for time-series analysis (Dwyer et al., 2018). The study site was covered by two tiles – path/row 200/28 and 201/28 (Figure 4.2.2) – for which 800 and 784 images were retrieved, respectively. Optical and thermal band time series were used as input data. Optical bands were used to generate the eight spectral indices that were set by default in the Google Earth Engine CCDC application programming interface (Arévalo et al., 2020) (Table 4.2.1). Clouds, shadows, and noise were removed from Landsat images using the *CFMask* algorithm (Foga et al., 2017), which is a C version of the popular *FMask* algorithm v3.3 (Zhu and Woodcock, 2014a).

Table 4.2.1. Summary of spectral bands and indices derived from the Landsat archive used in the study.

Input data	Description	Source
Spectral bands	Landsat spectral bands (visible, NIR, SWIR) in surface reflectance, and thermal bands in surface temperature	-
NDVI	Normalized Difference Vegetation Index for vegetation health and density quantification related to photosynthesis activity	(Myneni et al., 1995)
EVI	Enhanced Vegetation Index for vegetation health and density quantification with an improved sensitivity in high biomass regions, related to canopy structure	(Huete et al., 2002)
EVI2	Two-bands Enhanced Vegetation Index EVI computation without the blue spectral band to calculate EVI with sensors lacking a blue band (e.g. AVHRR)	(Jiang et al., 2008)
NBR	Normalized Burn Ratio For the identification of burned areas and quantification of fire severity	(Key and Benson, 2006)
NDFI	Normalized Difference Fraction Index For forest degradation and deforestation monitoring, sensitive to canopy state. Computed from Green Vegetation (GV), Non-Photosynthetic Vegetation (NPV), Soil, and Shade fractions obtained from spectral mixture analysis	(Souza Jr et al., 2005)
Greenness vegetation index	Greenness fraction Extracted by tasseled cap transformation, corresponds to vegetation fraction	(Crist, 1985)
Brightness vegetation index	Brightness fraction Extracted by tasseled cap transformation, corresponds to soil fraction	(Crist, 1985)
Wetness vegetation index	Wetness fraction Extracted by tasseled cap transformation, corresponds to the relationship between soil and canopy moisture	(Crist, 1985)

4.2.3.2. *Environmental variables*

Environmental variables were added to the Landsat data to better distinguish wetland habitats (Demarquet et al., 2023a). They included three topographic variables (i.e., elevation, slope, and aspect) derived from the DEM SRTM at 30 m resolution (Farr et al., 2007), as well as the distance to the sea calculated at 30 m spatial resolution from the highest sea level (IGN and SHOM, 2009).

4.2.3.3. *Historical aerial photographs*

A total of 16 aerial photographs covering different parts of the study site from 1984–1997 were downloaded from the French National Geographic Institute (IGN) website available in open access (https://remonterletemps.ign.fr/): 6 black-and-white photographs from 1984 (1:30 000 scale) and 10 RGB color photographs from 1990 and 1997 (ranging from 1:21 000 to 1:26 000 scale). The photographs were georeferenced using ground control points obtained from 2022 aerial photographs orthorectified using QGIS software (QGIS Development Team, 2018), achieving an average root mean square error of 3.58 m.

4.2.3.4. *Field data*

Field vegetation and LULC data were collected from several international, national, and local archive databases (Table 4.2.2). Field vegetation data included vegetation maps and phytosociological relevés. Local botanists have produced vegetation maps since the early 2000s to monitor protected areas. Vegetation maps of natural reserves (EUNIS 2004 and PVF) and the Natura 2000 habitat map described vegetation at the habitat or phytosociological unit scale. The former map covered 18 km^2 on five nature reserves (Figure 4.2.2), while the latter covered the entire site. The vegetation relevés (EUNIS 2020) consisted of 821 phytosociological relevés collected mainly on grasslands by local botanists and scientists. The relevés were automatically assigned to EUNIS habitats using the EUNIS-ESy expert system (Chytrý et al., 2020).

Table 4.2.2. Summary and description of field vegetation data used in the study. LULC: land use and land cover.

Name	Type	Format	Ca. Scale/accuracy	Nomenclature	Time Range	Source
Vegetation maps of natural reserves	Vegetation	Polygons	1:5 000	EUNIS 2004 (Davies et al., 2004) Regional classification of vegetation (Delassus et al., 2014)	2006, 2009, 2012, 2013, 2015	INPN (Robert and Brosseau, 2022)
N2000 habitat map	Vegetation	Polygons	1:15 000	CORINE Biotopes (Devillers et al., 1991)	2001-2005	Local managers
Vegetation relevés	Vegetation	Points	1 m	EUNIS 2020 (Chytrý et al., 2020)	2001, 2002, 2004, 2005, 2006, 2014, 2015	VegFrance (Bonis and Bouzillé, 2012) and local managers
LPIS	LULC	Polygons	1: 5 000	LPIS	2007, 2010, 2015	IGN (https://geoservices.ign.fr/rpg)
LUCAS	LULC	Points	5 m	LUCAS	2006, 2012, 2018	ESDAC (https://esdac.jrc.ec.europa.eu/projects/lucas)
Arable land conversion	LULC	Polygons	1:5 000	-	2001-2003, 2005-2015	Local managers
Communal grasslands	LULC	Polygons	1:5 000	-	2003-2013	Local managers

Field LULC data were obtained from the land parcel information system (LPIS), the land use and cover area frame survey (LUCAS), and two local GIS layers related to agri-environmental measures (i.e., “arable land conversion” and “communal grasslands”). The LPIS contains farmers' annual declarations of crop type in each field, in the framework of the European Union’s Common Agricultural Policy (CAP) (European Court of Auditors, 2016). This geographic information layer, released every year since 2007, describes ca. 30 crop classes, including grassland. Each year, it lists several hundred fields in the Marais Poitevin. The LUCAS database provided field observations of LULC types from a regular sampling campaign across Europe in 2006, 2012, and 2018 (Palmieri, 2016), which included 103, 70, and 69 points in the Marais Poitevin, respectively. The two local GIS layers described 563 fields that were converted from arable land to grassland from 2001 to 2003 and 2005 to 2015 (“arable land conversion") and 17.4 km^2 of communal grasslands where extensive grazing was encouraged from 2003 to 2013 ("communal grasslands").

4.2.4. Annual habitat mapping

4.2.4.1. Generating the reference dataset

Dataset 1 was generated from field data and historical aerial photographs to train and test the habitat classification models in 1984 and 2022 for the CCDC and diachronic methods. While the time difference between the date of the Landsat images and that of the reference data must be as small as possible for the diachronic method, this is not required for CCDC. Consequently, Dataset 1 contained all points collected from 1984 to 2022, regardless of the date.

A three-step workflow was performed to extract reference points from field data. First, all field data were converted to the EUNIS classification system at level 1 (Davies et al., 2004), which describes seven major habitat types (Appendix O). Specifically, we used the guide of (Delassus et al., 2014) for the regional classification of vegetation, the French Habref reference guide (Clair et al., 2017) for the CORINE Biotopes classification systems, the crosswalk table of Chytrý et al. (2020) for the EUNIS 2020 classification system, and the two crosswalk tables of (Buck et al., 2015) and the European Environmental Agency (EEA, 2014) to convert the LUCAS classification system to CORINE Land cover and then to the EUNIS classification system. For the LPIS data, all crop types were assigned to habitat I (i.e., *Regularly or recently cultivated agricultural, horticultural and domestic habitats*), except for old pastures, which were assigned to habitat E (i.e., *Grasslands and lands dominated by forbs, mosses or lichens*). The fields in the "arable land conversion" and "communal grasslands" layers were also assigned to habitat E.

In the second step, the EUNIS classification system was adjusted for habitats C (i.e., *Inland surface waters*) and J (*Constructed, industrial and other artificial habitats*), since they included spectrally heterogeneous habitats. More specifically, we merged habitats C1 (i.e., *Surface standing waters*) and J5 (i.e., *Highly artificial manmade waters and associated structures*), since they have similar spectral signatures. In addition, habitat C3 (i.e., *Littoral zone of inland surface waterbodies*) was considered separately because its spectral signature differs from that of surface water, and habitat C2 (i.e., *Surface running waters*) was excluded because it was undetectable at the study site due to Landsat's low spatial resolution. Thus, the final classification system contained eight habitat types:

- *A – Marine habitats*
- *B – Coastal habitats*
- *C1/J5 – Natural permanent surface waters* and *Artificial permanent surface waterbodies*
- *C3 – Littoral zone of inland surface waterbodies*
- *E – Grasslands and lands dominated by forbs, mosses or lichens*
- *G – Woodland, forest and other wooded land*
- *I – Regularly or recently cultivated agricultural, horticultural and domestic habitats*
- *J – Constructed, industrial and other artificial habitats*

In the third step, reference points were visually extracted from field GIS layers so that they lay entirely within a Landsat pixel (30 × 30 m). Field data in polygon format were overlaid on a vector grid of Landsat image pixel contours to automatically select all pixels that lay completely within the polygons. For field data in point format, the reference data corresponded to points manually identified in vegetation patches that lay entirely within a Landsat pixel. The vegetation patches had been previously delineated via visual interpretation of aerial photographs taken on the date closest to that on which the field data had been collected. A total of 100 reference points, corresponding to the approximate number of available points for the least represented habitats (A, B, and C3), were randomly selected per habitat per year to balance Dataset 1.

Due the lack of field data before 2001 and after 2016, Dataset 1 was supplemented with points obtained from visual interpretation of historical (1984, 1990, and 1997) and recent (2022) aerial photographs to cover the entire period. For each year, 100 reference points per EUNIS habitat were selected within all vegetation patches that lay completely within a Landsat pixel. The relatively low quality of the historical aerial photographs prevented unambiguous identification of habitats B (i.e., Coastal habitats) and C3. For these habitats, the 1990 and 1997 reference points were discarded since they were optional for CCDC and not used for the diachronic method. Conversely, the 1984 reference points were retained since they were required for the diachronic method (Table 4.2.3). Ultimately, Dataset 1 contained 4 200 points collected from 1984–2022 (Table 4.2.3) that were randomly divided per year and habitat into training (80 %) and testing (20 %) samples.

Table 4.2.3. Number of reference points per year and EUNIS habitat type (level 1). Gray cells indicate reference points for 1984–1997 and 2022 that were collected from visual interpretation of historical aerial photographs and recent aerial photographs, respectively, due to the lack of field reference data before 2001 and after 2016.

	Years										
EUNIS class	1984	1990	1997	2001	2002	2005	2006	2015	2016	2022	All
A	100	100	-	-	-	-	100	100	-	100	500
B	100	-	-	-	100	-	100	-	-	100	400
C1/J5	100	100	100	-	100	-	-	-	100	100	600
C3	100	-	-	100	100	-	-	-	-	100	400
E	100	100	100	100	-	100	100	-	-	100	700
G	100	100	100	100	-	-	-	-	-	100	500
I	100	100	100	100	-	-	-	-	-	100	500
J	100	100	100	-	100	-	100	-	-	100	700
All	800	600	500	400	400	100	400	100	100	800	4200

4.2.4.2. Continuous change detection and classification

4.2.4.2.1. Harmonic regression

A continuous simulated time-series for 1984–2022 was produced for each Landsat spectral band and index (Table 4.2.1) using a harmonic regression model (Zhu and Woodcock, 2014b). Specifically, the least absolute shrinkage and selection operator (LASSO) was selected as regression type, since it rarely overfits (Tibshirani, 1996) and remains robust when using infrequent observations (Zhu et al., 2015). The Google Earth Engine CCDC application programming interface includes two versions with slightly different default parameter values (Arévalo et al., 2020). During the preliminary calibration step, we tested the default values of these two versions for all parameters and retained the best values based on a visual interpretation of the results (Table 4.2.4).

*Table 4.2.4. Harmonic regression parameters used in the continuous change detection and classification and set in the scripts of the Google Earth Engine CCDC application programming interface. Exponent letters [a] and [b] indicate respectively default values from version 1 * and 2 ** of the application programming interface.*

Parameter	Meaning	Value
breakpointBands	The name or index of the bands to use for change detection	All[ab]
tmaskBands	The name or index of the bands to use for iterative *TMask* cloud and noise detection	Green, SWIR2[ab]
MinObs	Moving window size for break detection	5[a]
Seg	Maximum number of temporal segments over the entire time-series	6[ab]
Lambda	Penalty parameter for LASSO regression	0.005[a]
ChiSquareProbability	Chi-Square probability threshold for break detection	0.99[b]
MinNumOfYearsScaler	Factor of minimum number of years to apply new fitting	1.33[ab]
MaxIterations	Maximum number of runs for LASSO regression convergence	10,000[b]

*https://code.earthengine.google.com/?scriptPath=users%252Fparevalo_bu%252Fgee-ccdc-tools%253AAPPS%252Fsubmit_ccdc and https://code.earthengine.google.com/?scriptPath=users%252Fparevalo_bu%252Fgee-ccdc-tools%253AccdcUtilities%252Finputs.js

-

*https://code.earthengine.google.com/?scriptPath=users%252Fparevalo_bu%252Fgee-ccdc-tools%253AAPPS%252Ftstools_advanced

For each pixel, the model was fitted to a stable historical period at the beginning of the time series. The model was then fitted iteratively to the next set of clear Landsat observations until the fitted values differed significantly from the values observed on five consecutive dates, which indicated a potential change in natural habitat. When a break was detected, a new temporal segment was begun using a new harmonic regression model (Figure 4.2.3). This process was then repeated until the end of the time series. The *TMask* multitemporal algorithm (Zhu and Woodcock, 2014b) was applied throughout the process to detect and discard any noisy Landsat observations previously missed by the *CFMask* algorithm.

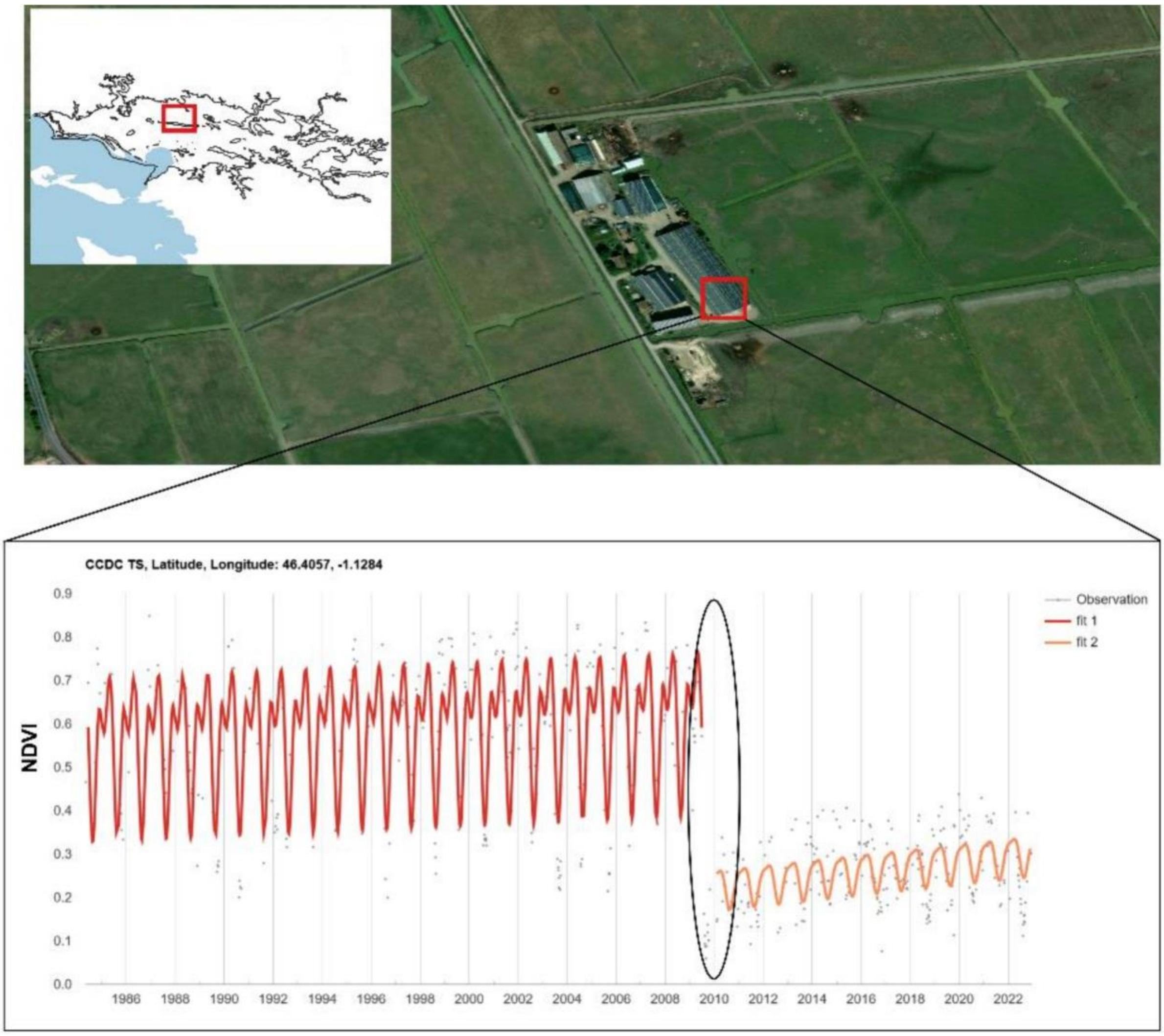

Figure 4.2.3. Example of a one-pixel NDVI time-series extracted from the Landsat archive for the Marais Poitevin from 1984–2022. The fits in the colored lines indicate temporal segments detected by the continuous change detection and classification (CCDC) algorithm. A change in color indicates a change in land cover/land use. The red segment corresponds to the NDVI signal from grasslands until a break in ca. 2010 (black ellipse), when grasslands were converted to built-up areas (orange segment).

A total of 15 CCDC algorithm coefficients and derivatives characterizing each temporal segment per pixel were calculated for each spectral band and index (Table 4.2.5).

Table 4.2.5. Continuous change detection and classification (CCDC) outputs used as predictor variables for random forest classification of natural habitats. The acronyms correspond to those defined in the Google Earth Engine CCDC application programming interface (Arévalo et al., 2020). See Zhu and Woodcock (2014a) for more detailed description of each coefficient and derivative.

CCDC output type	Acronym	Description
Coefficients	INTP	Intercept: Intercept value of the time series. Average reflectance for spectral band or average value for spectral indices and indicators.
	SLP	Slope: Long-term trend of the time series.
	SIN COS	Sine and cosine: Harmonic coefficients for intra-annual change.
	SIN2 COS2	Sine and cosine: Harmonic coefficients for intra-annual bimodal change.
	SIN3 COS3	Sine and cosine: Harmonic coefficients for intra-annual trimodal change.
	RMSE	Root means square error: Error between observation and CCDC fitting value. Corresponds to non-seasonal variability.
Derivatives	AMPLITUDE	Magnitude of the time series. Corresponds to seasonal variability. Derived from COS and SIN.
	PHASE	Phenological timing of the time series. Derived from COS and SIN.
	AMPLITUDE2	Bimodal magnitude of the time series. Derived from COS2 and SIN2.
	PHASE2	Bimodal phenological timing of the time series. Derived from COS2 and SIN2.
	AMPLITUDE3	Trimodal magnitude of the time series. Derived from COS3 and SIN3.
	PHASE3	Trimodal phenological timing of the time series. Derived from COS3 and SIN3.

4.2.4.2.2. Random forest classification

CCDC algorithm coefficients and derivatives of the seven Landsat bands and eight indices, as well as the three environmental variables, were used as input variables for classifying habitats. The random forest (RF) classifier can manage many input variables from different sources and has little sensitivity to outliers or over-fitting (Belgiu and Drăguţ, 2016). RF classification was performed using the GEE *ee.Classifier.smileRandomForest* function, using all default parameters, except for the maximum number of trees, which was increased to 500. All training samples collected for 1984–2022 were used to calibrate the classifier. Although the CCDC algorithm could have generated habitat maps for any year of the study period, we generated habitat maps only for 1984 and 2022 to detect changes over the longest time span in order to compare its predictions to those of the traditional post-classification method. The two annual habitat classifications may have contained a few no-value (NA) pixels due to initializing harmonic regression at the beginning of the period or immediately after a break (e.g., black ellipse, Figure 4.2.3). These NA pixels were assigned to the dominant habitat type using a modal filter with a 5 × 5 sliding window.

4.2.4.3. Traditional classification

4.2.4.3.1. Selection of cloud-free Landsat images

Cloud-free images were first automatically selected for 1984 and 2022 using a cloud-cover criterion (0 %) and then visually checked to discard images that covered only part of the site and/or contained haze or residual noise. For 1984, two L5 TM images (18 Aug, path/row 201/28; 30 Oct, path/row 200/28) were mosaicked to obtain one early-autumn composite image. Specifically, pixels of the most recent image were used first in the mosaic, and missing pixels were filled in with pixels of the oldest image using the Google Earth Engine *ee.ImageCollection.mosaic()* function. For 2022, four L8-9 OLI/TIRS images were selected to obtain one mid-summer composite (10 Jul, path/row 201/28; 11 Jul, path/row 200/28) and one late-summer composite (20 Sep, path/row 201/28; 21 Sep, path/row 200/28). The eight spectral indices were then calculated for each composite (Table 4.2.1).

4.2.4.3.2. Random forest classification

RF classification was performed for 1984 and 2022 separately using spectral bands and spectral indices derived from each year's composites, as well as environmental variables. RF classifications were performed using the same GEE function and parameters used for CCDC, but each RF classifier was calibrated using only training samples collected for the corresponding year. This method generated two habitat maps: one for 1984 from the first RF classifier and one for 2022 from the second RF classifier.

4.2.5. Change detection

The change detection analysis described and compared wetland dynamics between 1984 and 2022 and then compared continuous and post-classification change detection methods. A two-step procedure was applied in parallel for each method. First, wetlands in annual habitat maps 1984 and 2022 were simplified into "existing wetland" (habitats A, B, C3, E, and G) or "damaged wetland" (habitats C1/J5, I, and J) based on Rapinel et al. (2018). In the second step, the wetland change map was derived by subtracting the 2022 two-class map from the 1984 map. Four classes were identified from the change map: (i) "wetland loss", which described a change from existing to damaged wetland; (ii) "wetland gain", which described a change from damaged to existing wetland; (iii) "stable existing wetland", which described stability of an existing wetland; and (iv) "stable damaged wetland", which described stability of a damaged wetland.

4.2.6. Accuracy assessment

The accuracy of the 1984 and 2022 habitat classifications was determined for the two methods using the same testing sample for the given year (i.e., 1984 or 2022) extracted from Dataset 1. For each date (1984 or 2022), we calculated a confusion matrix, the overall accuracy, user's accuracy (UA), and producer's accuracy (PA) per habitat (Appendices G-J).

The unbiased accuracy and estimated area of the wetland-state change map were calculated for the two methods according to Olofsson et al. (2014), which provided the magnitude of the classification errors needed to adjust the area estimator. To this end, stratified validation sampling (Dataset 2) was performed based on the change map derived from continuous change detection. Specifically, the number of samples per class of change was defined as a function of the expected standard deviation of overall and class-specific accuracy. First, the expected standard deviation of overall accuracy was set at 0.015 to achieve a trade-off between the required minimum of 50 samples per class and a rapid strategy for visual interpretation. The expected standard deviation for each class was then set to be higher for under-represented classes: 0.2, 0.3, 0.4, and 0.5 for "stable damaged wetland", "stable existing wetland", "wetland loss", and "wetland gain", respectively. A total of 326 validation samples were automatically assigned (i.e., 62, 54, 101, and 109 for "wetland loss", "wetland gain", "stable existing wetland", and "stable damaged wetland", respectively). Each validation sample included visual interpretation of aerial photographs for 1984 and 2022 and very high spatial resolution satellite imagery available in Google Earth Pro, supplemented with Landsat NDVI time series supplied by the API CCDC visualizer (Arévalo et al., 2020). The unbiased overall accuracy, UA, PA, and estimated area for each change detection class were calculated using the R package *mapaccuracy* (Costa, 2022).

4.3. Results

4.3.1. Habitat map accuracy

While the overall accuracy of habitat maps derived from CCDC and post-classification was high for both years (Table 4.3.1), that of post-classification was higher for 1984 (0.93 and 0.86, respectively) but was much lower for 2022 (0.75 and 0.91, respectively). Accuracies for habitat types A, B, C1/J5, G, and J were high (UA and PA > 0.75). Conversely, for 2022, accuracies for habitat E were moderate for CCDC (UA = 0.61 and PA = 1.00) and low for post-classification (UA = 0.45 and PA = 0.75). Similarly, for 1984, accuracies for habitat I were high for CCDC (UA = 1.00 and PA = 0.95) and moderate for post-classification (UA = 0.66 and PA = 0.95). For 2022, accuracies for habitat C3 were low for CCDC (UA = 1.00 and PA = 0.40) and even lower for post-classification (UA = 80.20 and PA = 0.05).

Table 4.3.1. User's accuracy (UA) and producer's accuracy (PA) of habitat maps in 1984 and 2022 obtained using continuous change detection and classification (CCDC) and post-classification. Bold text indicates the highest accuracy per year and habitat.

	1984				2022			
	CCDC		Post-classification		CCDC		Post-classification	
Habitat types	UA	PA	UA	PA	UA	PA	UA	PA
A	0.90	0.90	**1.00**	**0.95**	**1.00**	**0.95**	0.74	0.85
B	0.85	0.85	**1.00**	**1.00**	1.00	**1.00**	1.00	0.75
C1/J5	1.00	1.00	1.00	1.00	1.00	**1.00**	1.00	0.95
C3	1.00	0.40	1.00	**0.91**	**1.00**	**0.40**	0.20	0.05
E	0.73	**0.95**	**0.80**	0.84	**0.61**	**1.00**	0.45	0.75
G	0.80	**1.00**	**1.00**	0.83	**1.00**	1.00	0.91	1.00
I	**0.88**	0.75	0.80	**0.89**	**1.00**	0.95	0.66	0.95
J	**0.83**	1.00	0.81	1.00	0.95	**1.00**	**1.00**	0.70
Overall Accuracy (%)	0.86		**0.93**		**0.91**		0.75	

The post-classification accuracy has varied strongly (0.93 in 1984 and 0.75 in 2022), while the CCDC accuracy has remained constant over time (0.86 in 1984 and 0.91 in 2022). This could be explained by the characteristics of the two classification methods: the first is based on the discriminant capacity of the pair of composite images used, which varied from one year to another, while the second is based on a sequence of images, which makes it more stable over time. The analysis of the confusion matrix for habitat types in 2022 derived from the post-classification change detection (Appendix I) showed that most classification errors occurred between E and C3 habitats, and to a lesser extent between I and E habitats, highlighting that the dates of the Landsat images used (mid- and late-summer composites) were not optimal for discriminating these habitats in 2022. In contrast, the date of the image composite (early autumn) was more appropriate for discriminating these habitats in 1984 (Appendix J). The variability in the accuracy of the post-classification method explained why the accuracy of this method was slightly higher than that of the CCDC in 1984, whereas the accuracy of the CCDC was significantly higher than that of the post-classification in 2022.

4.3.2. Change detection accuracy

The unbiased accuracies of the wetland change maps (Table 4.3.2) calculated using the method of Olofsson et al. (2014) indicated a low uncertainty in the accuracy estimate, with a 95 % confidence interval between 0.01 and 0.08. Continuous change detection outperformed post-classification change detection (overall accuracy = 0.86 ± 0.02 and 0.51 ± 0.03, respectively), highlighting the value of the former method based on the analysis of temporal profiles and the main limitation of the latter method due to the sum of the classification errors. Specifically, stable existing wetlands were accurately classified using continuous change detection (UA 0.83–0.90 and PA 0.90–0.96) and less accurately using post-classification change detection (UA 0.58–0.69 and PA 0.26–0.81), whereas wetland loss and gain were classified with moderate accuracy using continuous change detection (UA 0.48–0.93 and PA 0.56–0.62) and very low accuracy using post-classification change detection (UA 0.21–0.39 and 0.19–0.58).

Table 4.3.2. User's accuracy (UA) and producer's accuracy (PA) of continuous and post-classification change detection using the method of Olofsson et al. (2014).

Change detection approach	**Continuous**		**Post-classification**	
	UA	PA	UA	PA
Wetland loss	0.93±0.04	0.56±0.05	0.39±0.05	0.58±0.05
Wetland gain	0.48±0.08	0.62±0.08	0.21±0.08	0.19±0.07
Stable wetland	0.83±0.04	0.96±0.01	0.58±0.04	0.81±0.03
Stable damaged wetland	0.90±0.03	0.90±0.02	0.69±0.07	0.26±0.03
Overall Accuracy (%)	0.86±0.02		0.51±0.03	

Applying the two methods to detect change between 1984 and 2022 using aerial photography for areas dominated by two change classes in the Marais Poitevin (i.e., stable degraded wetlands vs. wetland loss due to conversion of grasslands to cropland) indicated that continuous change detection accurately detected both classes, unlike post-classification change detection (Figure 4.3.1).

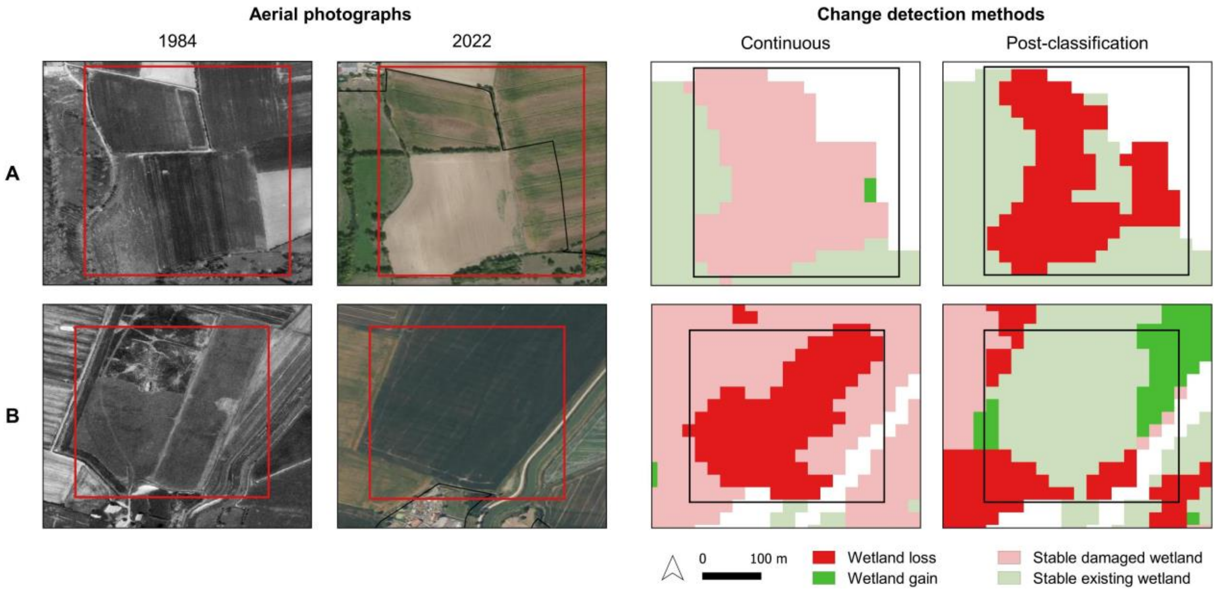

Figure 4.3.1. Comparison of continuous and post-classification change detection between 1984 and 2022 for two areas of the Marais Poitevin: area A (46° 19′ N, 0° 33′ W), with a stable degraded wetland due to the presence of arable land, and area B (46° 23′ N, 1° 10′ W), with wetland loss, since grassland in 1984 had been converted to arable land by 2022. A 3 × 3 modal filter was applied to the change maps in post-processing to reduce the salt-and-pepper effect. Source of aerial photographs: French National Geographic Institute (IGN).

4.3.3. Areas of wetland change

Areas of wetland change between 1984 and 2022 mapped using continuous change detection (Table 4.3.3) highlighted that wetland state changed over ca. 20 % of the Marais Poitevin. Wetland loss was much larger than wetland gain (ca. 18 % and 2 %, respectively). Damaged wetlands covered the largest area of the Marais Poitevin in 2022. Conversely, the percentage of existing wetland area in 1984 decreased by 16 percentage points to cover less than half (ca. 41 %) of the Marais Poitevin in 2022.

Table 4.3.3. Unbiased estimate of wetland area (in ha and percentage of total site area) with 95 % confidence intervals for the four wetland-change classes between 1984 and 2022 using continuous change detection and classification.

Item	Wetland loss	Wetland gain	Stable existing wetland	Stable damaged wetland
Unbiased area estimation (ha) and CI95%	18 286 ± 3 365	2 234 ± 1 248	40 808 ± 3 492	37 659 ± 2 888
Percentage of total site area and CI95%	18.5 ± 1.7	2.2 ± 0.6	41.2 ± 1.8	38.0 ± 1.5

Locations of wetland changes between 1984 and 2022 using continuous change detection varied (Figure 4.3.2). Most stable existing wetlands were located inside the Natura 2000 protected site, while stable degraded wetlands were located outside of it. Wetland losses were concentrated mainly in the east-central part of the Marais Poitevin within the large areas of stable degraded wetlands. Conversely, most of the wetland gains were scattered throughout the Natura 2000 site.

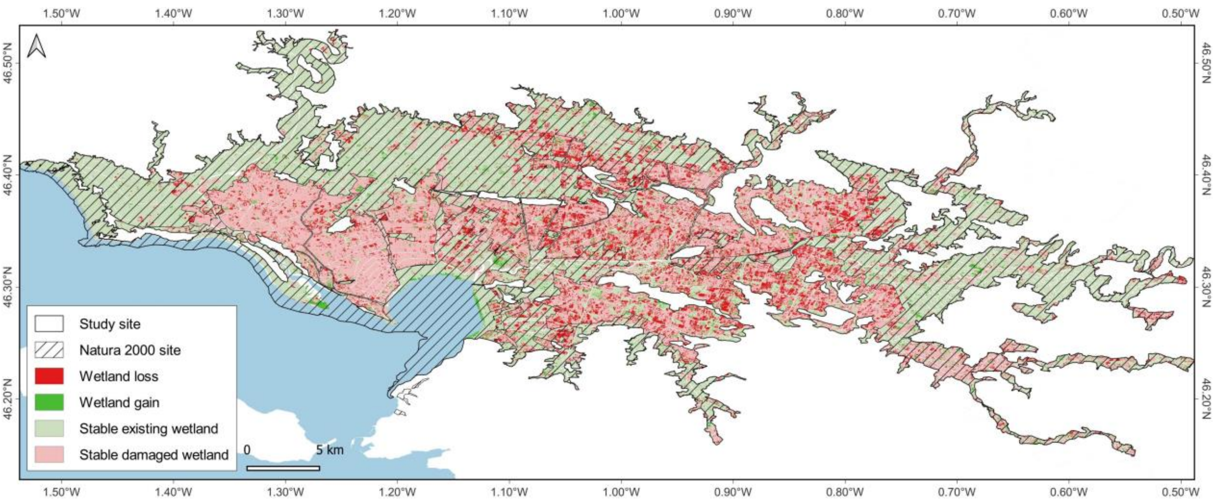

Figure 4.3.2. Wetland changes detected in the Marais Poitevin site between 1984 and 2022 using continuous change detection.

Analysis of the drivers of wetland change revealed that wetland loss was due mainly to conversion to arable land (ca. 95 %) and, to a lesser extent, constructed habitats and creation of artificial waterbodies (ca. 4 % and 1 % of the area of wetland loss, respectively). Conversely, wetland gain was due to both natural (e.g., sediment accumulation) and human drivers (e.g., conversion, abandoning farming practices). More specifically, most wetland gain was due to grassland expansion (ca. 80 %), followed by an increase in habitat A (i.e., *Marine habitats*) (ca. 11 %) from 1984 to 2022. To a lesser extent, the area of habitat C3 increased by ca. 5 %, followed by that of habitats G (ca. 4 %) and B (i.e., *Coastal habitats*) (ca. 2 %). We highlighted examples of wetland loss (Figure 4.3.3) and gain (Figure 4.3.4) due to these drivers of change.

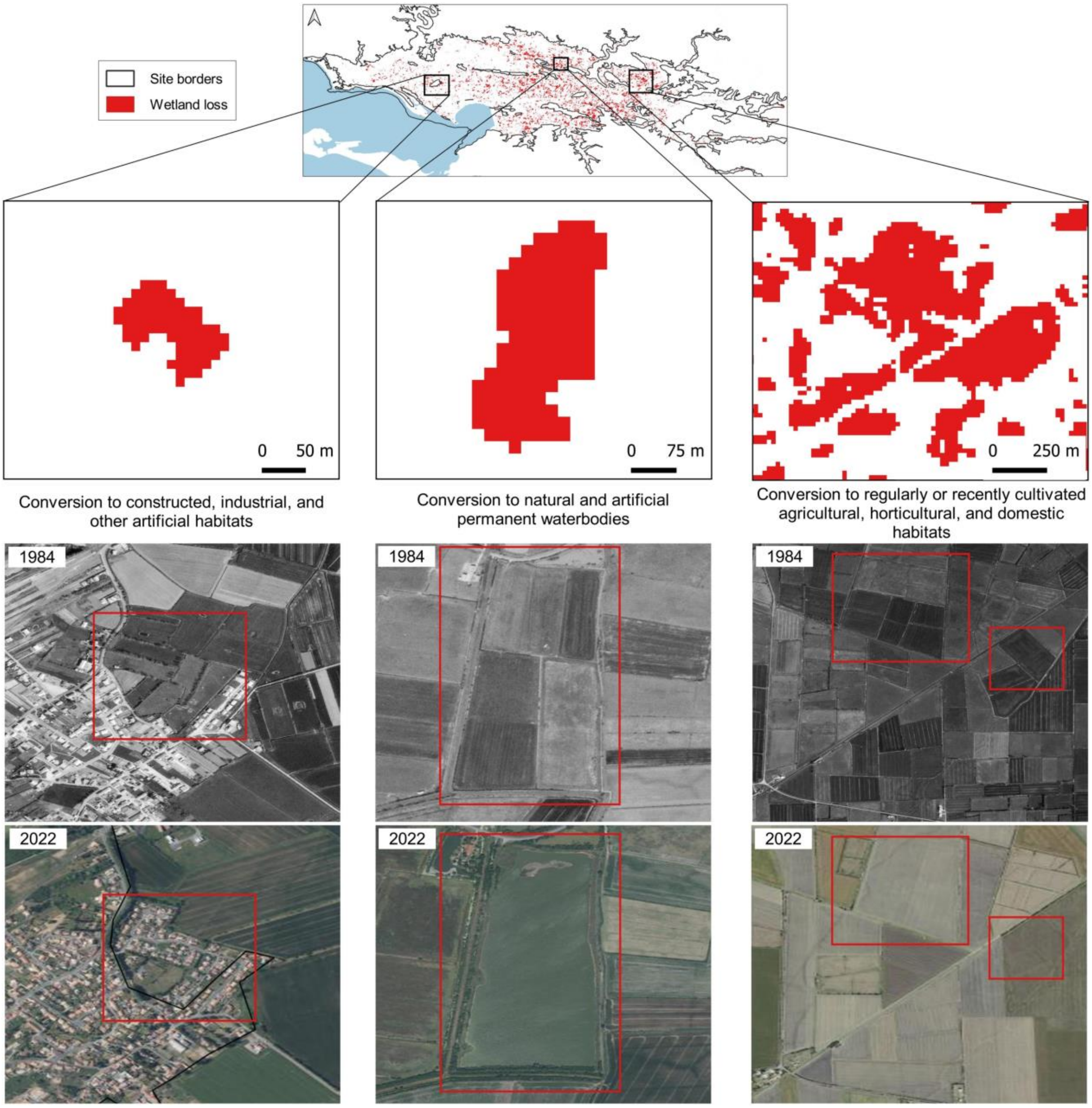

Figure 4.3.3. Examples of wetland loss between 1984 and 2022 due to urbanization (left), conversion to natural and artificial waterbodies (middle), and conversion to arable land (right) derived from continuous change detection, and aerial photographs (IGN). A 3 × 3 modal filter was applied to the change map in post-processing to reduce the salt-and-pepper effect.

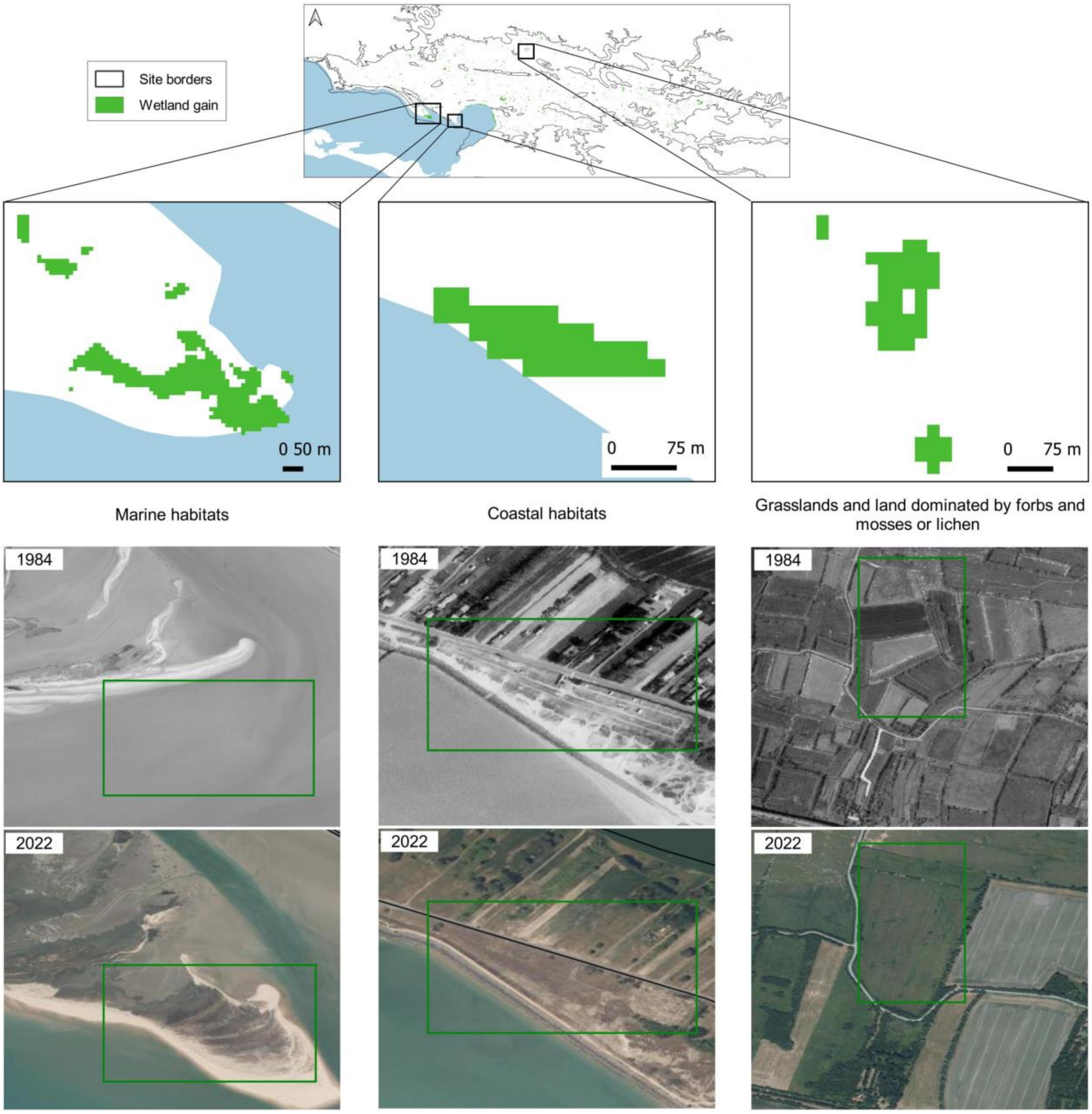

Figure 4.3.4. Examples of wetland gain between 1984 and 2022 due to natural coastal sedimentation (left); conversion of constructed, industrial, and other artificial habitats to coastal habitats (middle); and conversion of arable land to grasslands (right) derived from continuous change detection, and aerial photographs (IGN). A 3 × 3 modal filter was applied to the change map in post-processing to reduce the salt-and-pepper effect.

4.4. Discussion

4.4.1. Continuous vs. post-classification change detection approaches

This study highlights the value of using continuous change detection rather than post-classification change detection to detect changes in wetlands over a 39-year interval. The accuracy of the annual maps obtained using continuous change detection was satisfactory and similar to that obtained using post-classification change detection. Specifically, the overall accuracy of the annual habitat maps obtained with continuous change detection was high (> 0.85) and similar to that obtained for coastal wetlands in China (He et al., 2022; Peng et al., 2021; Wang et al., 2023), Bangladesh (Awty-Carroll et al., 2019b), and the USA (Yang et al., 2022), confirming the generic nature of the CCDC algorithm for coastal wetlands. The largest classification errors were for grassland habitats (E), which are the most difficult to classify (M. Liu et al., 2020; Xie et al., 2022). Some of them were classified as habitat C3 (i.e., *Littoral zone of inland surface waterbodies*), since the physiognomy of some unmanaged wet grasslands can resemble that of C3 vegetation, making it difficult to distinguish the two habitats.

However, accuracy was higher for the change maps obtained using continuous change detection than using post-classification change detection. This could have been due to the cumulative misclassification of the two annual habitat maps (7 % in 1984 and 25 % in 2022) obtained using the latter, which inevitably led to the detection of false changes (Fuller et al., 2003; Gómez et al., 2016). The most frequent confusion was between cropland (I) and grassland (E) habitats (Figure 4.3.1, Appendix I-Appendix J), which resulted in inadequate characterization of changes in wetland conservation.

Continuous change detection avoided most of these misclassification errors, making it possible to classify the temporal profile of the entire study period by using all Landsat archive images, including partially cloudy images and those acquired by the ETM+SLC-off sensor, totaling several hundred clear observations per pixel (Appendix H). Another advantage of continuous change detection is that it uses the temporal profile of the entire study period to make predictions for the years selected (here, 1984 and 2022) using asynchronous reference data with a single classifier. In this way, all field data collected during the study period (2000–2010) were used to classify wetlands before (1984) and after (2022) reference data had been collected.

These two advantages explain the much higher overall accuracy of the wetland change map obtained using continuous change detection (0.86) than that obtained using post-classification change detection (0.51). However, accuracy was lower for the maps of wetland change (i.e., “wetland gain” and “wetland loss”) than for the maps of wetland stability (i.e., “stable existing wetland” and “stable damaged wetland”) (Appendix M). Several studies achieved similar results when using the CCDC algorithm and Landsat archive images for urban (Xie et al., 2022), forest (Chen et al., 2021), or wetland (Yang et al., 2022) ecosystems. In agreement with Chen et al. (2021), the PA errors could have been due to the few clear Landsat observations at the beginning of the time series, which resulted in a poor fit of the harmonic regression model that led to false break detection when the number of observations increased. The UA errors could have occurred because the CCDC algorithm did not detect a break in the time series, or detected a break, but the magnitude of the change was lower than the detection threshold (*ChiSquareProbability*).

This study is the first to highlight the higher performance of the continuous method over the post-classification method for change detection in wetlands. Although these two methods are among the most popular (Gómez et al., 2016; Pasquarella et al., 2022) other ones have recently shown interest in wetland monitoring, such as the Detection and Characterisation of Coastal Tidal Wetland Change (DECODE) (Yang et al., 2022) or the Domain Adaptive and Interactive Differential Attention Network (DA-IDANet) (Ji et al., 2024) and deserve to be further compared. In addition, our study which was applied to a small coastal marsh of about 1000 km^2 in Europe should be further tested on other types of wetlands and in other geographical areas to assess the sensitivity of these methods to wetland dynamics and to field and satellite data availability.

4.4.2. Landsat archive and CCDC algorithm for monitoring wetlands

This study confirmed the value of using Landsat archive images to monitor wetlands over the long term (Demarquet et al., 2023a). While the spatial resolution of Landsat images limited the ability to detect changes in linear habitats, such as in habitats C3 or G, it was sufficient for detecting the main changes of human origin (e.g., urban sprawl, agricultural intensification) or natural origin (e.g., coastal sedimentation). In addition, the cloud and outlier masks implemented in the CCDC algorithm yielded many clear Landsat observations per pixel (i.e., 238–760), despite the high frequency of cloud cover in Western Europe. However, the number of clear observations was significantly lower over the sea and lakes, as well as over arable land, suggesting an over-detection of shadows on water and bare soil (Appendix H). This problem, recognized by the authors of *CFmask* (Foga et al., 2017) and *Tmask* (Zhu and Woodcock, 2014b), was not an issue in the present study, since the minimum number of clear observations (238) was sufficient to detect habitat changes. However, this could be an issue when monitoring wetlands at sites with high cloud cover and/or frequent flooding.

The CCDC algorithm was able to detect abrupt habitat changes by identifying significant breaks in the temporal profile. For this reason, parameterization of the CCDC algorithm is crucial, in particular (i) the minimum number of consecutive observations for break detection (*minObs*) and (ii) the threshold value for break detection (*ChiSquareProbability*) (Pasquarella et al., 2022). We set the default value of the *ChiSquareProbability* parameter to 0.99, as (Yang et al., 2022) did for coastal wetlands in the USA. Conversely, the default values of parameters *minObs* and *lambda* were suitable for our study site, while Yang et al. (2022) increased *minObs* to 6 and Awty-Carroll et al. (2019) increased *lambda* to 1 when monitoring mangroves. Thus, there seems to be no consensus on parameter values, since the CCDC algorithm must be parameterized for the structural and functional characteristics of the area studied. In our study the classification accuracy could also be improved using a hyper tuning procedure of the CCDC parameters as demonstrated in Yang et al. (2022) instead of using default values.

The method applied in this study was able to assess changes in wetland state based on a map of the main habitat types (Rapinel et al., 2018). However, it was unable to assess the natural vs. artificial character of certain habitats, especially natural (habitat C1) and artificial (habitat J5) waterbodies, as well as wooded areas (habitat G), which indicate wetland state. We considered habitat C1/J5 a poor indicator of wetland state, since many of the waterbodies were waterfowl-hunting ponds created in the 1980s (Duncan et al., 1999). Future studies could analyze changes in wetland state in greater detail by detecting progressive changes within the same habitat (e.g., eutrophication of grasslands) based on recent continuous change detection methods, such as object-based continuous monitoring of land disturbances (OB-COLD) (Ye et al., 2023), DECODE (Yang et al., 2022), or new deep learning methods (Huang et al., 2022; Ji et al., 2024; Liu et al., 2022; Sun et al., 2021).

CCDC has been successfully and widely used to map land cover and land cover change at regional scale (Friedl et al., 2022). Our study confirmed the value of the CCDC approach by showing its effectiveness in detecting habitat change within a Ramsar wetland compared to the traditional method. However, in our study, a large number of Landsat images were available, which is not always the case: for example, in some regions of the world, such as Siberia, the Pacific Islands or West Africa, the number of clear observations per year is insufficient (<4) to fit robust CCDC models (Y. Zhang et al., 2022). In this case, the traditional method based on composites using available historical Landsat data is an option (Potapov et al., 2012). In addition, we had a large number of high-quality field observations, which is essential to train high-quality classification models (Friedl et al., 2022). The availability of new crowdsourced data, such as the GeoWiki Global Land Cover and Land Use reference dataset (Fritz et al., 2017), which contains over 150,000 100-m grid cells, can partially compensate for the lack of field observations in wetlands.

4.4.3. Continuous change detection for conservation

Results of the present study agree with those of previous studies that have highlighted the degradation of wetland state in the Marais Poitevin due to conversion of grasslands to cropland (Duncan et al., 1999; Godet and Thomas, 2013) and increasing urbanization in the littoral zone (Pouzet et al., 2015) since 1950. In addition, wetland loss at this site was also related to the construction of artificial waterbodies, such as hunting ponds (Duncan et al., 1999) and wastewater treatment ponds. Conversely, wetland gain, although small, was due mainly to conversion of arable land to grassland, which highlights the conservation efforts of site managers as well as the agri-environmental incentives offered to farmers under the CAP (Petit et al., 2022). The wetland gain of shore meadows was due to sediment accumulation caused by construction of dykes at the entrance of the marsh (Regnauld et al., 2015).

More generally, continuous change detection based on dense Landsat time-series has enabled standardized (i.e., same data and method) long-term monitoring of wetland ecosystem structure, which is essential for biodiversity (Skidmore et al., 2021a). This method overcomes the biases currently encountered in Ramsar (Davidson et al., 2019) or the European Union's Habitat Directive (Delbosc et al., 2021), whose monitoring has not yet been standardized (e.g. changes in field observers, different data sources and methods). In addition, combining the free Landsat archive (Wulder et al., 2022) and CCDC API (Arévalo et al., 2020) with an intuitive graphical interface on the GEE platform makes this method simple to use by non-specialists in remote sensing such as wetland managers or policy makers seeking to assess the impact of restoration measures or wetland health indicators, including those in developing countries.

4.5. Conclusion

This study, focused on a coastal marsh in France, highlights that while continuous change detection and post-classification change detection had similar overall accuracy, the wetland change maps of the former between 1984 and 2022 were much more accurate. We recommend further testing continuous change detection to detect changes in wetlands, especially since APIs are now freely available in cloud computing, which makes processing straightforward. Future research will focus on detecting changes, including subtle ones, in other wetland types and geographical areas, comparing CCDC with various change detection methods, including deep learning algorithms. This will support the monitoring of wetland health to meet conservation plans, such as Ramsar reporting.

CONCLUSION TO CHAPTER 4

In this chapter we have demonstrated the ability of the CCDC to generate an indicator of wetland area and structure from Landsat archives. Specifically, we produced annual habitat maps for a Ramsar site between 1984 and 2022. We extracted the long-term annual dynamics of the main habitat classes, which is not possible using the diachronic image post-classification method. The CCDC makes it possible to generate habitat maps for years for which reference data are not available, thanks to the classification of temporal segments derived from harmonic regression and not only from pixel reflectance values. In addition, the change map derived from CDDC had a much higher overall unbiased accuracy than that derived from post-classification change detection. Based on these results, we were able to describe the evolution of pressures on natural and semi-natural habitats, such as grasslands, associated with agricultural intensification and urban development.

The CCDC is therefore a relevant method for generating indicators of the surface area, structure and functioning of Ramsar wetlands over a long time period. These indicators can be used to characterise the ecological status and pressures on wetlands, both at a given time and in the past, using Landsat archives. The changes in area and structure that have been detected in wetlands using CCDC can also be analysed in the light of public policy.

1

INTRODUCTION TO CHAPTER 5

In the previous chapter, the CCDC was used to produce an indicator of ecosystem structure (natural habitat maps) over the long term. In this chapter, the habitat maps generated annually with the CCDC are used to assess the effectiveness of agri-environmental policies and protected areas for the conservation of grassland habitats in the Marais Poitevin. The methodology used in this chapter was developed in collaboration with one of the managers of the Marais Poitevin, who was also involved in the analysis of the results.

This chapter corresponds to the article submitted to the peer-reviewed journal *Applied Geography* in November 2024.

Chapter 5. Evaluating the Effectiveness of Agri-Environmental and Protected Area Policies for Grassland Conservation Using Continuous Long-Term Satellite Monitoring: a Case Study in the Poitevin Marsh (France).

Article

Evaluating the effectiveness of agri-environmental and protected area policies for grassland conservation using continuous long-term satellite monitoring: a case study in the Poitevin marsh (France)

by Quentin Demarquet[1], Olivier Gore[2], Sébastien Rapinel[1], Laurence Hubert-Moy[1], and Simon Dufour[1]

[1] Université Rennes 2, LETG UMR 6554 CNRS, place du recteur Henri Le Moal, 35000 Rennes, France

[2] Établissement Public du Marais Poitevin, 1 Rue Richelieu, 85400 Luçon, France

Abstract

While grasslands provide many ecosystem services, they are under threat from human and climatic pressures, agri-environmental and protected area policies have been implemented for several decades to protect them. However, assessing the effectiveness of these policies is challenging due to the lack of extensive and continuous data to monitor grassland evolution, resulting in a poor understanding of trends in grassland conservation status and threats. Recent advances in artificial intelligence and the availability of satellite image archives enable continuous, long-term, and high-resolution monitoring of grassland. This study aims to assess the effectiveness of agri-environmental and protected area policies for the conservation of a coastal grassland marsh (France) based on long-term continuous satellite monitoring. Annual natural habitat maps at 30 m spatial resolution derived from Landsat time series classification for 1984-2022 were analyzed with protected area maps, agri-environmental scheme data, and key events to highlight the long-term dynamics of grassland and cropland. The results showed: (i) a significant effect of anticipation of the 1992 reform of the European Common Agricultural Policy, which lead to a major conversion of grassland to cropland at the end of the 1980s, (ii) an increase in grassland areas as a result of agri-environmental schemes, (iii) a stability of grassland areas

within protected areas. This study highlights the interest of long-term monitoring of grassland conditions using Landsat open archive and cloud computing tools to more effectively assess agri-environmental and protected area policies.

5.1. Introduction

Although grasslands are rich in biodiversity and provide numerous ecosystem services such as climate regulation, pollination and maintenance of water resources, they are under serious threat from human pressures and climate change (Bengtsson et al., 2019; Elliott et al., 2024). Protected area (Gohr et al., 2022) and agri-environmental (Wuepper et al., 2024) policies have been implemented for several decades to limit the degradation and loss of these ecosystems. Protected area policies, widely developed since the 1950s, aim to conserve nature by applying legal or contractual means to geographical areas covered by management plans (Dudley et al., 2013). Agri-environmental policies, more recently developed in the 1990s, aim to develop environmentally friendly farming practices on a voluntary basis using financial incentives paid to farmers (Wuepper et al., 2024). Although the value for ecosystem conservation has been reported for both protected areas (Geldmann et al., 2021; He and Wei, 2023) and agri-environmental policies (Batáry et al., 2015; Kleijn and Sutherland, 2003), their effectiveness depends on their management (Esbah et al., 2010; Gibbes et al., 2009), pressures) (Anzoategui et al., 2023; Rodríguez-Rodríguez and Sinoga, 2022) and also adaptation and targeting to local characteristics (Batáry et al., 2015).

Assessing the effectiveness of protected areas and agri-environmental policies is challenging due to the lack of extensive and continuous data, leading to a poor understanding of trends in conservation status and threats (Geldmann et al., 2021; Hoffmann, 2022). This requires continuous, long-term spatio-temporal indicators (He and Wei, 2023; Martínez-López et al., 2021). In the case of grasslands, monitoring their spatio-temporal dynamics makes it possible to describe changes in ecosystem structure, which is a key indicator for assessing the effectiveness of conservation policies (Parracciani et al., 2024). Two studies have shown the effect of agri-environmental policies implemented as part of the Common Agricultural Policy (CAP) in Germany (Haensel et al., 2023) and the European network of protected areas Natura 2000 in Denmark (Levin et al., 2018) on changes in grassland areas based on the analysis of the Land Parcel Information System (LPIS). However, the LPIS, which has a high spatial resolution (parcel scale) and an annual update frequency, has two main limitations: the period over which parcels are monitored is relatively short (since the 2000s) and it is not spatially exhaustive (lack of parcels not subsidised by the CAP).

Open access satellite remote sensing data, which have been standardised and available worldwide, have been widely used to assess the status of protected areas

(Gohr et al., 2022). Many studies have focused on monitoring changes in grasslands within protected areas using layers of major habitat types derived from satellite imagery. For example, the Corine Land Cover product at 100 m spatial resolution, updated every 6/10 years since 1990, has been used to assess the effectiveness of protection levels in national parks (Kubacka et al., 2022), nature reserves (Rodríguez-Rodríguez et al., 2019) and protected areas of the European Natura 2000 network (Ferrarini et al., 2021; Hermoso et al., 2018; Kubacka and Smaga, 2019; Rodríguez-Rodríguez and Sinoga, 2022; Ursu et al., 2020). The effectiveness of European protected areas has also been assessed using the MODIS Land Cover Types product at 500 m spatial resolution, updated annually since 2001 (Cheţan and Dornik, 2021). Although these products contain ready-to-use GIS layers and cover a long time period, their spatial resolution is too coarse to detect grasslands in fragmented landscapes (Lopes et al., 2017). Conversely, high spatial resolution (20-30 m) satellite imagery acquired since the 1980s with a 10-day observation frequency is *a priori* well suited for long-term grassland monitoring (Vannoppen et al., 2023). However, grassland monitoring using these images or derived products has so far been carried out using a discontinuous change detection approach (Demarquet et al., 2024b), which limits monitoring to a ten-year frequency. For example, grasslands have been monitored using one Landsat image and two IRS-LISS images acquired in 1977, 1998 and 2006 in a national park in India (Sarma et al., 2008), one SPOT-2 image and one ASTER image acquired in 1994 and 2005 respectively in a natural park in Turkey (Esbah et al., 2010), and more recently several hundred Landsat images acquired over three periods (1999-2001, 2009-2011, and 2019-2021) in a Natura 2000 site in Italy (Parracciani et al., 2024).

The development of cloud computing has facilitated the processing of large amounts of satellite images, making it possible to detect continuous long-term changes using artificial intelligence. The most widely used method for analysing continuous image time series is the Continuous Change Detection and Classification (CCDC) (Pasquarella et al., 2022). The CCDC algorithm identifies and classifies, at the scale of each pixel, homogeneous temporal segments from the analysis of the time series comprising all the available satellite images, which has two advantages: (i) the possibility of generating a map of land cover or natural habitats at any date during the period studied, and (ii) the reduction in the detection of false changes (Demarquet et al., 2024b; Reynaert et al., 2024). Despite these advantages, to our knowledge, the CCDC has never been used to monitor the effectiveness of agri-environmental measures. It has also been little used to assess the effectiveness of protected areas (Mao et al., 2020), although first case studies applied to forest ecosystems have recently been reported (e.g. Bullock et al., 2020; He et al., 2022; Long et al., 2024).

This study aims to assess the effectiveness of protected areas and agri-environmental schemes for the conservation of grassland in the largest Atlantic coastal marsh in France, based on a long-term continuous satellite monitoring. Annual habitat maps derived from Landsat time-series classification for 1984 – 2022 were combined with protected areas maps (Natura 2000, nature reserves, purchased land) and agri-environmental schemes data to describe the long-term dynamics of grassland and cropland. This study was conducted jointly by researchers and a site manager in order to better analyse the results.

5.2. Material and methods

5.2.1. Study site

The Marais Poitevin, covering an area of around 100,000 hectares, is the largest Atlantic coastal wetland in France. It has been a Ramsar-listed site since 2023, due to its strategic role in the migration of waterfowl and its rich diversity of habitats. It has a temperate climate and a relatively low average altitude, generally between 0 and 10 metres. Human activities have profoundly altered the marsh since the 13th century, with the construction of dykes, canals and channels that have led to a retreat of the sea and the drainage of part of the marsh (Godet and Thomas, 2013; Pouzet et al., 2015).

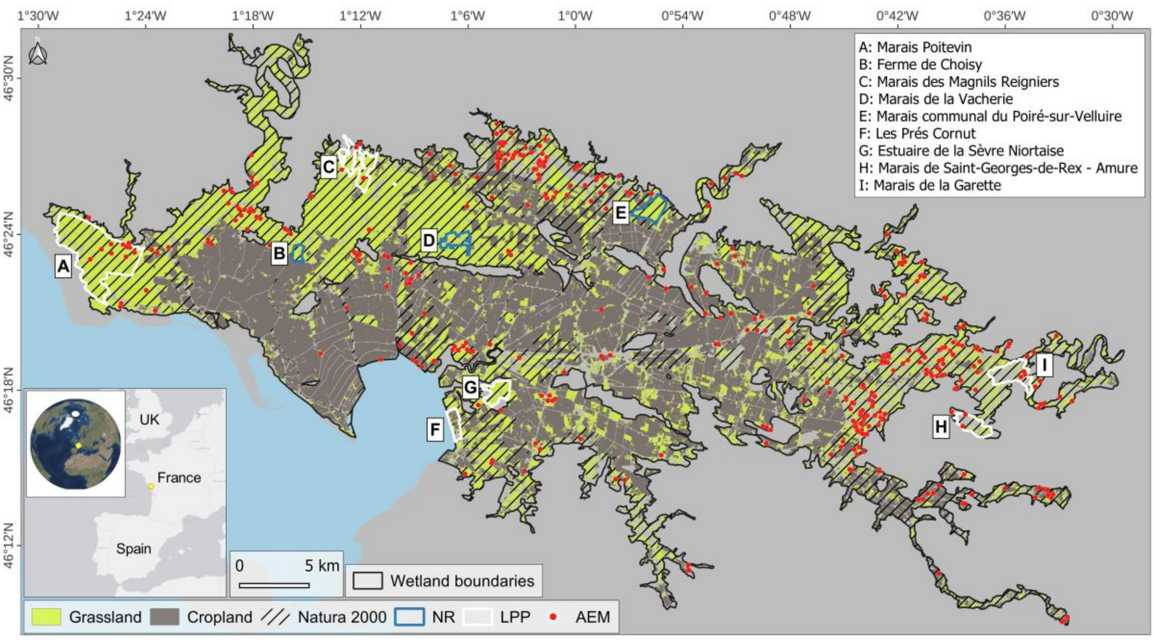

Figure 5.2.1: Location of the study site and selected protected measures used in evaluation assessment. LPP: land-purchased perimeters; NR: Natura reserves; AEM: Agro-Environmental Measures. The map of grassland and crops was produced for the year 2022 with the Change Detection and Classification algorithm using Landsat archive (Demarquet et al., 2024b).

Since the 1950s, the area of wet grassland has been declining, mainly as a result of agricultural intensification and urbanisation (Duncan et al., 1999; Godet and Thomas, 2013). Their conservation is therefore a major issue for this site (Ouisse and Barnier, 2021). The main conservation actions implemented over the last forty years (Figure 5.2.2) have involved the creation of three main types of PAs: (i) regulatory protection (e.g. nature reserves, biological reserves) based on legislation, (ii) contractual protection (e.g. Natura 2000, Regional Nature Park) based on contracts between owners and managers, and (iii) land protection areas (e.g. Natural Area Conservation Societies and Coastal and Lakeshore Protection Agency acquisition areas) within which managers of natural areas are granted a priority right of pre-emption in the event of the sale of plots of land.

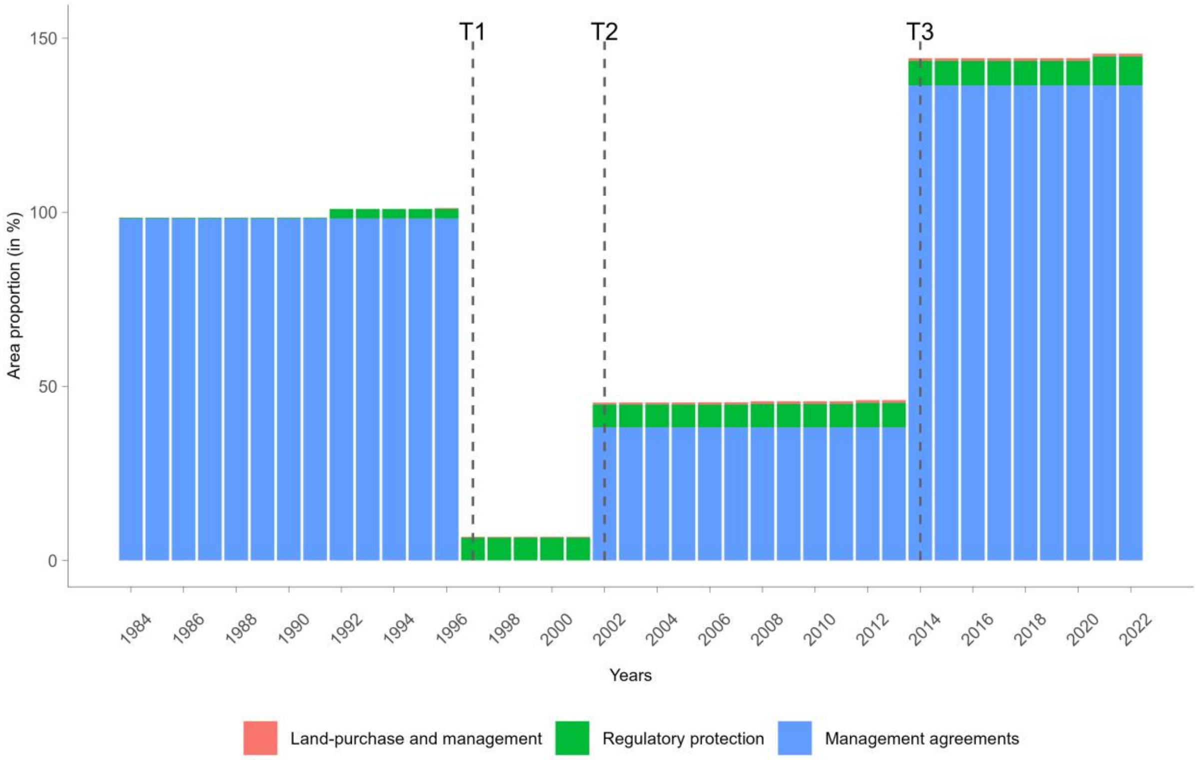

Figure 5.2.2 : Change in the cumulative annual surface area of protected areas represented by type of protected area in the Marais Poitevin between 1984 and 2022. The proportion of surface area may exceed 100% due to the overlapping of protected areas in the Marais Poitevin. T1: Loss of the Regional Nature Park label in 1997, T2: Creation of the Natura 2000 site in 2002, T3: Rehabilitation of the Regional Nature Park label. Source: Protected Planet (UNEP-WCMC and IUCN, 2024).

In parallel, three types of agri-environmental measures have been implemented: (i) the MAE (Mesures Agro-Environnementales) and MAET (Mesures Agro-Environnementales Territorialisées), which are financial incentives for farmers resulting from the 1992 reform of the European Common Agricultural Policy (CAP). These measures include the adoption of practices that are less harmful to the environment, such as reducing fertiliser inputs, crop rotation and the conservation of some threatened habitats (Souchère et al., 2003; Uthes and Matzdorf, 2013); (ii) the CTE (Contrats de Transition Ecologique; Ecological Transition Contracts), which are a non-financial public policy instrument designed to facilitate the implementation of ecological transition measures (Rodier, 2023); (iii) the CAD (Contrat d'Agriculture Durable), which took over from the CTE in 2004, is a voluntary contract between a farmer and the State to preserve the environment and production quality in return for payment.

5.2.2. Dataset generation

5.2.2.1. Annual maps of natural grassland and cropland

The grassland and crop maps were generated annually at 30 m spatial resolution over the period 1984 and 2022 by applying a Continuous Change Detection and Classification (CCDC) based on a time series of Landsat satellite images (Demarquet et al., 2024b). The images were classified according to the European Nature Information System typology (Davies et al., 2004), in which grasslands and crops are labelled as 'E: Grasslands and lands dominated by forbs, mosses or lichens' and 'I: Regularly or recently cultivated agricultural, horticultural and domestic habitats' respectively. The accuracy of the classification estimated on the basis of in situ observations is high for both grasslands and crops, with F1-scores of 0.85 and 0.89 (Appendix P). These continuous monitoring maps make it possible to detect changes that are not visible using the Corine Land Cover (CLC) product (Appendix Q**)**.

Two examples of temporal profiles classified for a plot under a MAE contract and a plot in a protected area are shown in Figure 5.2.3.

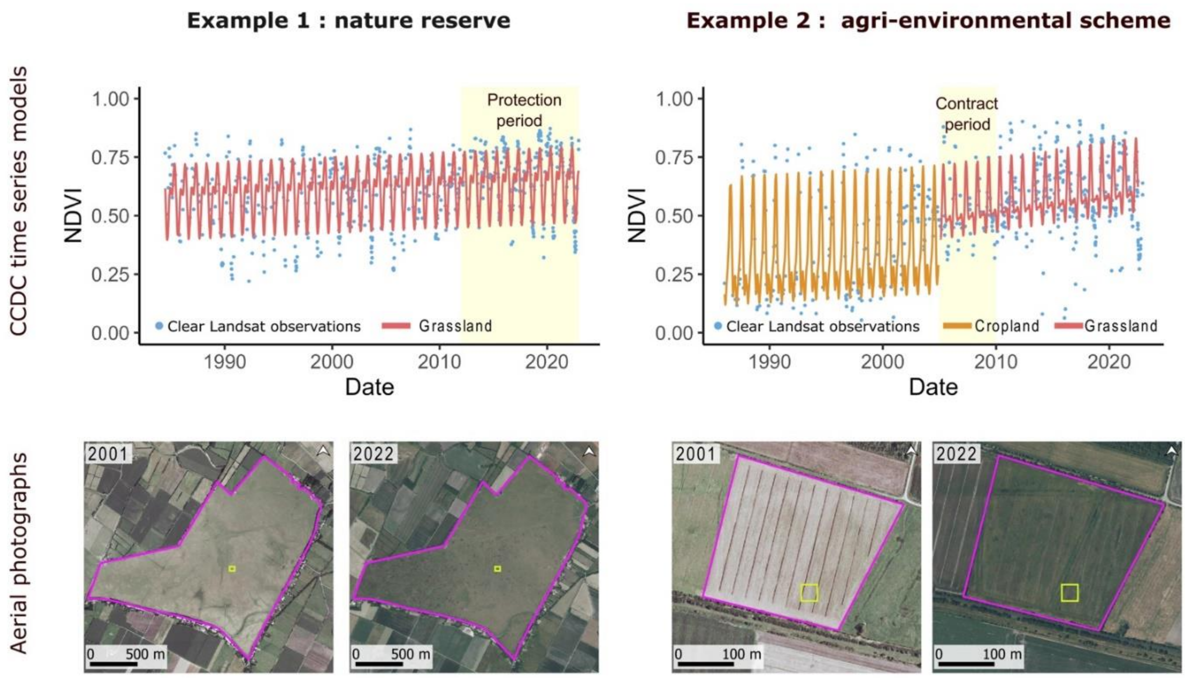

Figure 5.2.3. Examples of continuous change detection and classification (CCDC) of two Landsat pixels (top) located on the Poiré-sur-Velluire nature reserve (46.41° N, 0.93° W) created in 2012 (left) and on an agricultural plot (46.44° N, 1.07° W) subject to an agri-environmental measure between 2005 and 2010 (right). The outlines of the nature reserve and the agricultural plot (purple) and the extent of the two pixels (green squares) are shown on the aerial photographs (IGN ®) (bottom).

5.2.2.2. Selection of conservation areas

The numerous conservation areas implemented on the Marais Poitevin site include PAs and MAEs (UNEP-WCMC and IUCN, 2024). To meet the objective of this study, the PAs and MAEs were selected according to two criteria: (i) the area covered by the PAs and MAEs had to be strictly included within the study site, (ii) the dates on which the PAs were created and the periods during which the MAEs were set up had to be included in the period 1989 - 2017 in order to observe changes in the areas under grassland and crops (available between 1984 and 2022) a minimum of 5 years before and after the MAEs were set up and the PAs created. The conservation areas selected are detailed in Table 5.2.1 and geolocated in Figure 5.2.1.

Table 5.2.1. Summary of selected conservation areas

Conservation areas	Type	IUCN category	Territoire	Creation date	Area (ha)	Source
Natura 2000	PAs - Management agreements	IV	Marais Poitevin	2002	53 100	Protected Planet (UNEP-WCMC and IUCN, 2024)
Regional Nature Reserve	PAs - Regulatory protection	IV	Marais de la Vacherie	2008	166	
			Marais communal de Poiré-sur-Veilluire	2012	245	
			Ferme de Choisy	2012	78	
Land owned by Coastal and Lakeshore Protection Agency (perimeters)	PAs - Land purchase and management	IV	Marais Poitevin	1996	1832	French National Geographic Institute [1]
			Les Prés Cornut	2003	143	
			Marais des Magnils Reigniers	2008	445	
			Estuaire de la Sèvre Niortaise	2010	226	
Land owned by Natural Area Conservation Societies (perimeters)			Marais de Saint-Georges-de-Rex - Amure	1996	245	Local managers
			Marais de la Garette	2006	376	
Agri-environmental measures	Financial incitative	Non applicable	Parcelles agricoles conventionnées (n = 404)	2000-2014	1260	

[1] https://geoservices.ign.fr/services-web-experts-environnement

5.2.2.3. *Identification of Policy Key events*

Four events linked to public policies likely to have impacted on grassland conservation throughout the Marais Poitevin were identified between 1992 and 2014: (i) the CAP reform in 1992 (T1), which caused a significant change in the way funding was provided to farmers, with the implementation of financial incentives for grassland conservation and, conversely, the cessation of drainage subsidies (Guyomard et al.,

2022) ; (ii) the loss of the Regional Nature Park label in 1997 (T2) due to non-compliance with grassland conservation objectives; (iii) the introduction in 2002 of a government plan (T3) to improve grassland conservation following the condemnation of the French state by the European Commission for inadequate protection of birds in the Marais Poitevin (Sands et al., 1999); (iv) the recovery of the Regional Nature Park label in 2014 (T4).

5.2.3. Geospatial statistical analysis

At the scale of the Marais Poitevin site, statistical analysis was performed to assess the impact of the four events linked to public policy on changes in grassland and crops. To this end, annual trends in grassland and crops were defined for each of the five periods (1984 - 1992, 1992 - 1997, 1997 - 2002, 2002 - 2014, and 2014 - 2022) on the basis of annual grassland and crops maps derived from the Landsat image time series. For each pair of periods, a linear regression model was applied per EUNIS habitat (i.e., E and I) in order to analyse changes in habitat area as a function of time (continuous variable) and periods (factor). The trends (slopes) derived from the linear regression models were then calculated for each period and compared using a pairwise comparison test (Lenth, 2016). The proportions of grassland and crops within each conservation area were also calculated annually over the period 1984 - 2022.

All of these analyses were carried out using R software (R. Core Team, 2019) with the support of the *terra* (Hijmans, 2024) and *lsmeans* (Lenth, 2016) packages.

5.3. Results

5.3.1. Spatiotemporal dynamics of grasslands and crops at site scale

At the scale of the site, the areas under grassland and crops show two very contrasting trends over the entire 1984-2022 period (Figure 5.3.1). The area under grassland decreased significantly until around 1992, before gradually reducing and remaining almost stable until 2022. In total, a net loss of 5.6% of grassland area (around 5,000 ha) has been observed since 1984. In contrast, crop area increased sharply between 1984 and 1992, then stabilised over the last 20 years. Between 1984 and 2022, the net gain in crop area is estimated at 10.7% (9,800 hectares)

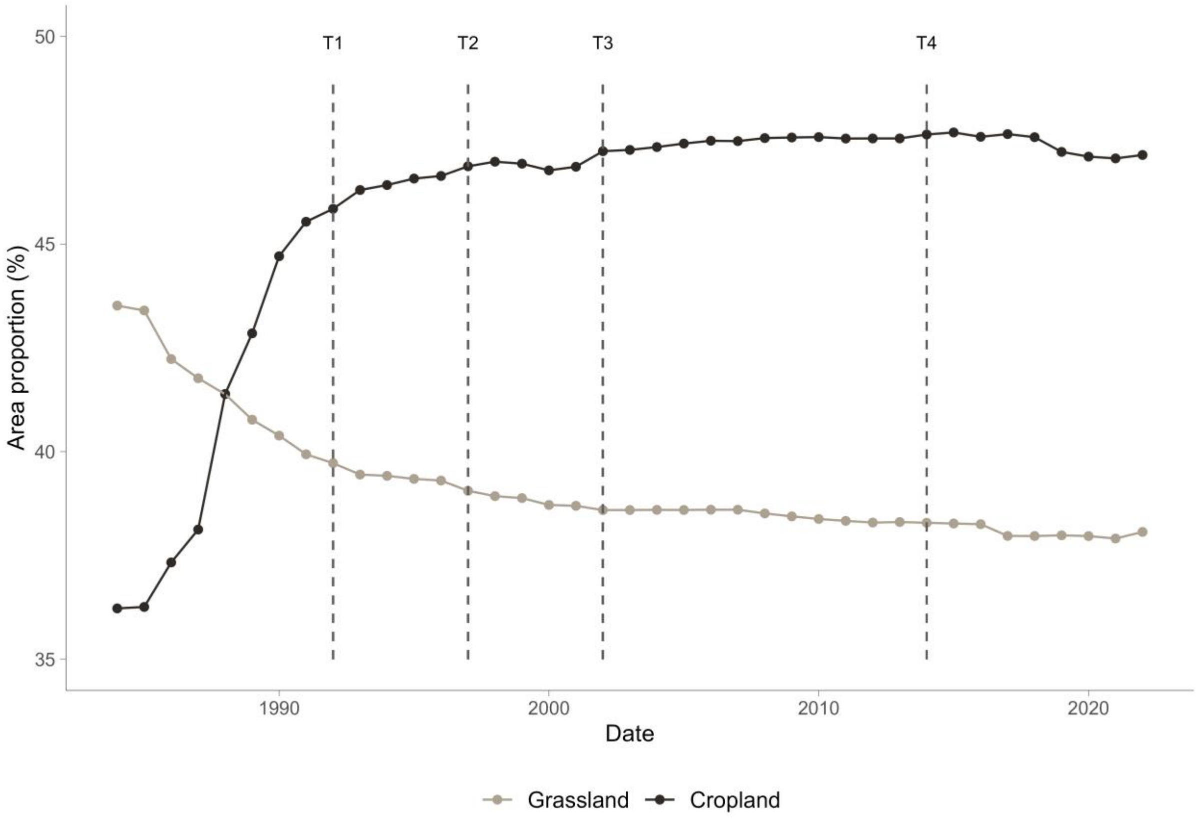

Figure 5.3.1. Changes in grassland and cropland areas (expressed as a percentage of the site's surface area). The dotted lines indicate four events linked to public policies implemented on the site (T1: 1992 - CAP reform; T2: 1997 - Loss of the NRP label; T3: 2002 - Government plan; T4: 2014 - Renewal of the NRP label).

Analysis by period shows that the reduction in grassland area slowed significantly following the CAP reform in 1992 and to a lesser extent following the government plan in 2002 (Table 5.3.1). Conversely, the increase in cropland area slowed significantly as a result of the CAP reform. A change of direction was observed in 2014 following the recovery of the NRP label, with a reduction in the cropland area.

*Table 5.3.1. Difference in annual trends of grassland and cropland areas before and after key events calculated using linear regression models before and after each key event and their corresponding statistical pairwise comparison test (using 0.05 as the critical significance level). Significance level is shown in superscript: *** < 0.001, ** < 0.01, * < 0.05, ns non-significant*

	Period 1		**Period 2**		
	Timespan	Trend per year	Timespan	Trend per year	Difference in trends
Grassland	1984 – 1992	-0.50%	1992 – 1997	-0.10%	+0.40% ***
	1992 – 1997	-0.10%	1997 – 2002	-0.09%	+0.01% ns
	1997 – 2002	-0.09%	2002 – 2014	-0.03%	+0.06% ***
	2002 – 2014	-0.03%	2014 – 2022	-0.04%	-0.01% ns
Cropland	1984 – 1992	+1.43%	1992 – 1997	+0.18%	-1.25% ***
	1992 – 1997	+0.18%	1997 – 2002	+0.04%	-0.14% ns
	1997 – 2002	+0.04%	2002 – 2014	+0.03%	-0.01% ns
	2002 – 2014	+0.03%	2014 – 2022	-0.10%	-0.13% ***

5.3.2. Spatiotemporal dynamics of grasslands and crops at conservation area scale

5.3.2.1. Natura 2000 site

Changes in grassland area vary according to location (Figure 5.3.2). Within the Natura 2000 site, grassland represents more than half the surface area of the site and its annual rate of change is stable both before and after the creation of the protected area in 2002. Outside the Natura 2000 site, grassland accounts for less than 25% of the total area and its annual rate of change is negative, particularly until the late 1990s. Cropland area is poorly and heavily represented both inside and outside the Natura 2000 site, with a positive annual rate of change both inside and outside the Natura 2000 site, particularly before 1992. However, a decrease in cropland has been observed within the Natura 2000 site since 2014.

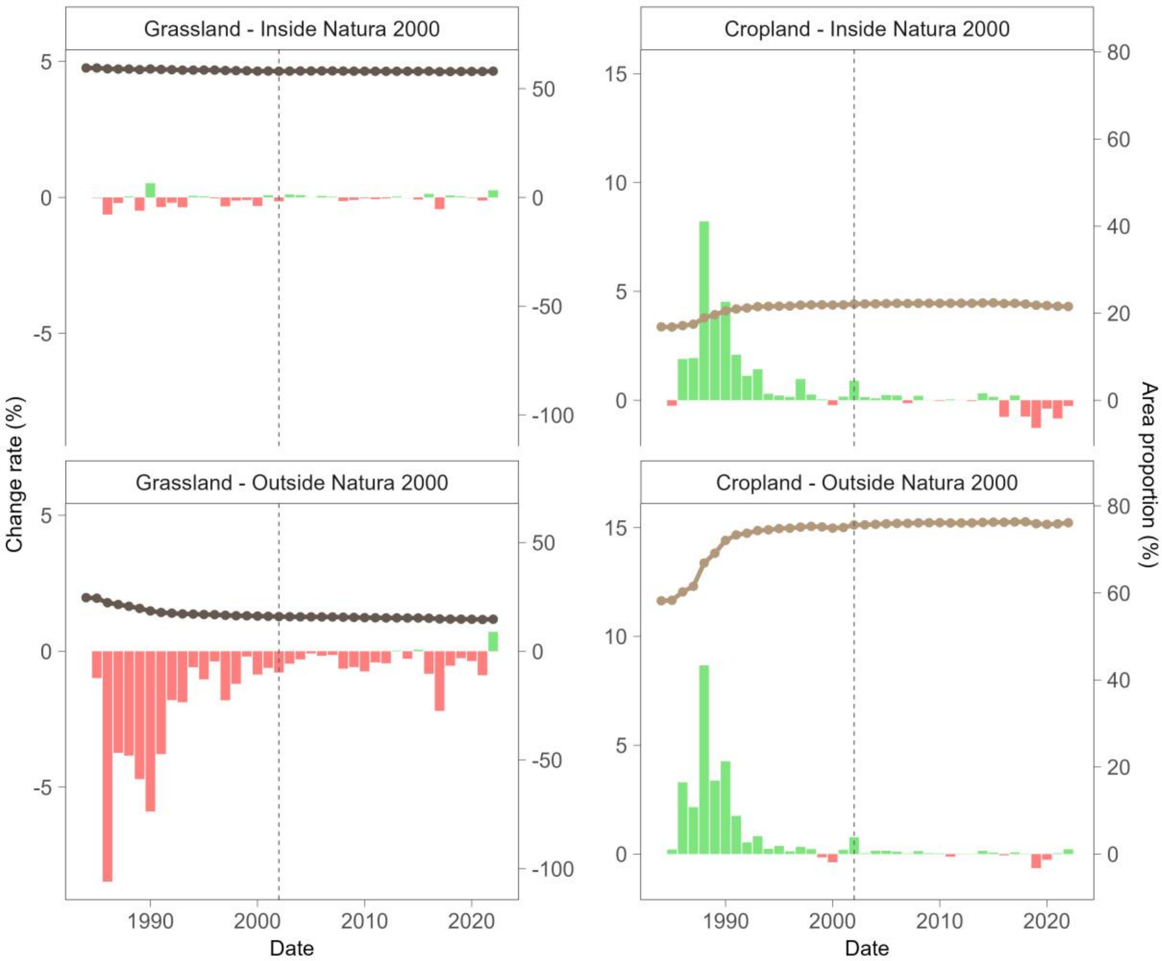

Figure 5.3.2: Annual change rate (colored bars; left y axis) and area proportion (colored lines; right y axis) of grassland (left) and cropland (right) inside (up) and outside (down) the Natura 2000 area. The dashed vertical line indicates the year 2002 when the Natura 2000 site was created.

5.3.2.2. *Agri-environmental measures*

The grassland area has increased overall on the agricultural plots on which agri-environmental measures have been applied (Figure 5.3.3). During the period in which the MAEs were contracted (2000 - 2014), the grassland area increased by 10% and 5% respectively inside and outside the Natura 2000 site. Following the end of the MAE contract in 2014, a decrease in the grassland area can be observed both inside and outside the Natura 2000 site. The cropland area decreased substantially during the MAE contract period, especially within the Natura 2000 site. After the end of the MAE contract in 2014, the cropland area increased again within the Natura 2000 site, while it remained stable outside the Natura 2000 site.

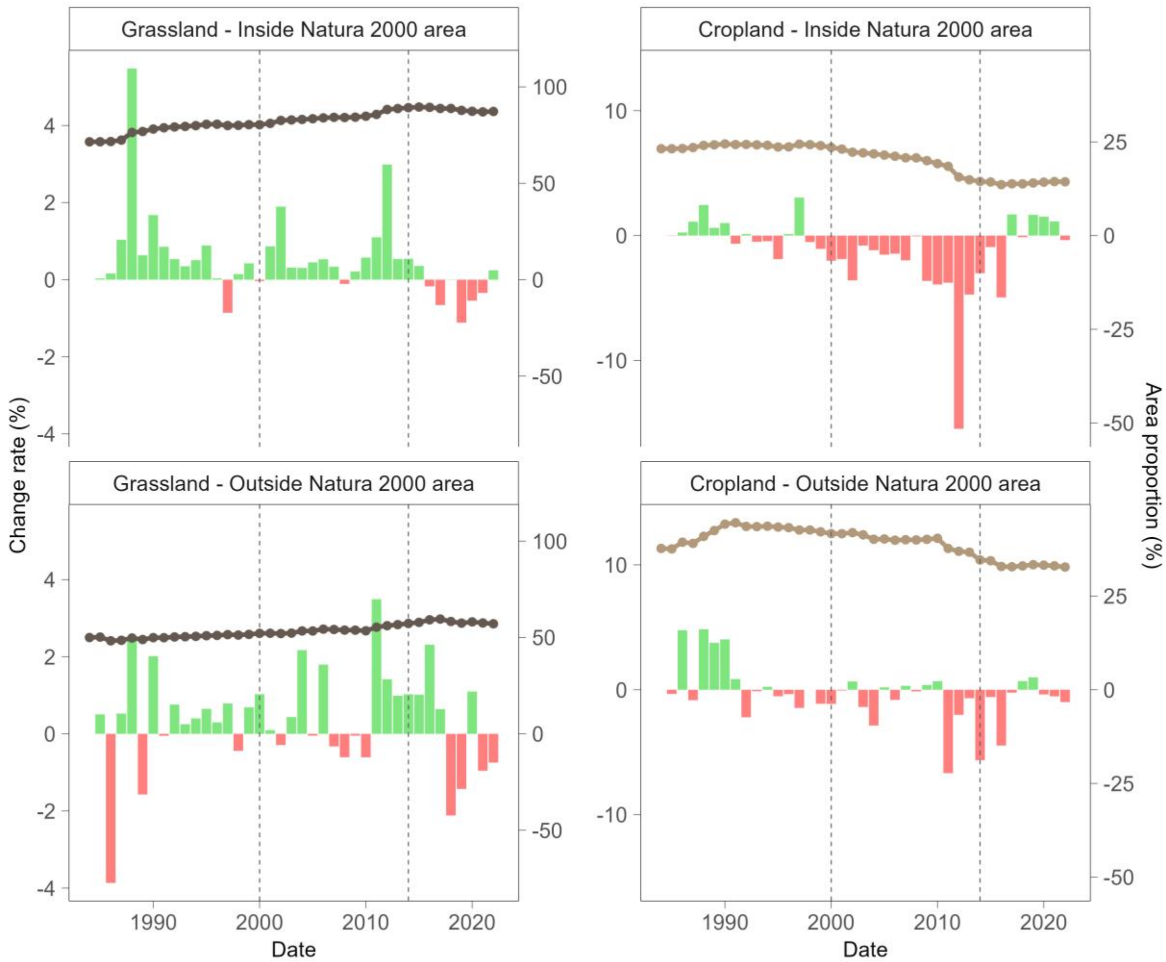

Figure 5.3.3: Changes in the annual rate of change (coloured bars; left y axis) and proportions (coloured lines; right y axis) of grassland areas (left) and cropland areas (right) on plots with at least one MAE, depending on whether they are located in the Natura 2000 site (top) or not (bottom). The two vertical dotted lines indicate the period when the MAE agreements were put in place on the plots concerned between 2000 and 2014.

5.3.2.3. *Nature reserves*

Grasslands, which account for a very high proportion (90 - 97%) of the areas within the perimeters of the three nature reserves, have remained stable over the entire 1984 - 2022 period, showing a very low rate of change (< 3%) (Figure 5.3.4). Conversely, crops account for a very small proportion of the surface area of the perimeters of the three nature reserves (0 - 4%) and have remained stable overall over the 1984 - 2022 period. However, the few cropland areas gradually declined in the 1980s on the Ferme de Choisy reserve and, to a lesser extent, on the communal marsh of Poiré-sur-Velluire, before disappearing in the early 1990s.

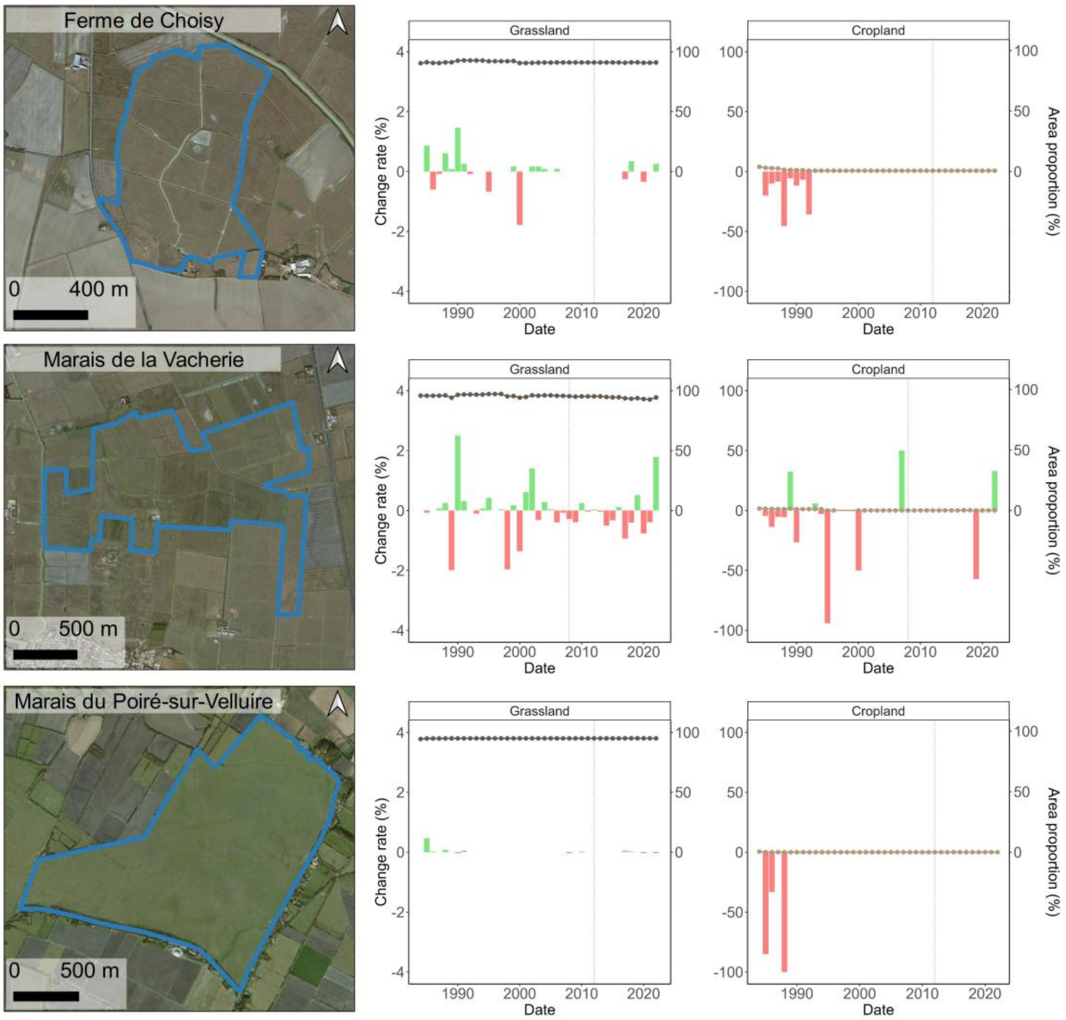

Figure 5.3.4. Location of the three nature reserves (blue line), background: ESRI imagery ® (left); annual rate of change (coloured bars; left y axis) and proportion of surface area (coloured lines; right y axis) in grassland (middle) and cropland (right) within each nature reserve. The vertical dotted lines on the graphs indicate the year in which the reserves were created.

5.3.2.4. *Land-purchased areas*

All sites have a higher proportion of grassland than cropland, except for the Prés Cornut site where grassland and cropland are relatively similar (Figure 5.3.5). Crops are absent from the Marais Poitevin and Marais de la Garette perimeters. Changes in grassland and cropland areas vary from site to site. Grassland areas have remained stable in the Saint-Georges-de-Rex - Amure marshes, the Magnils Reigniers marshes, the Marais Poitevin and the Prés Cornut marshes, although a noticeable decrease has been observed since the end of the 2000s in the case of the latter site. There has been an increase in the grassland area at the Marais de la Garette and, to a lesser extent, at the Sèvre Niortaise Estuary. Cropland increased until 1996 on the Saint-Georges-de-Rex - Amure marsh and until the end of the 1980s on the Prés Cornut site, after which it stabilised. Conversely, there has been a steady decline in the cropland area in the Magnils Reigniers marsh and the Sèvre Niortaise Estuary.

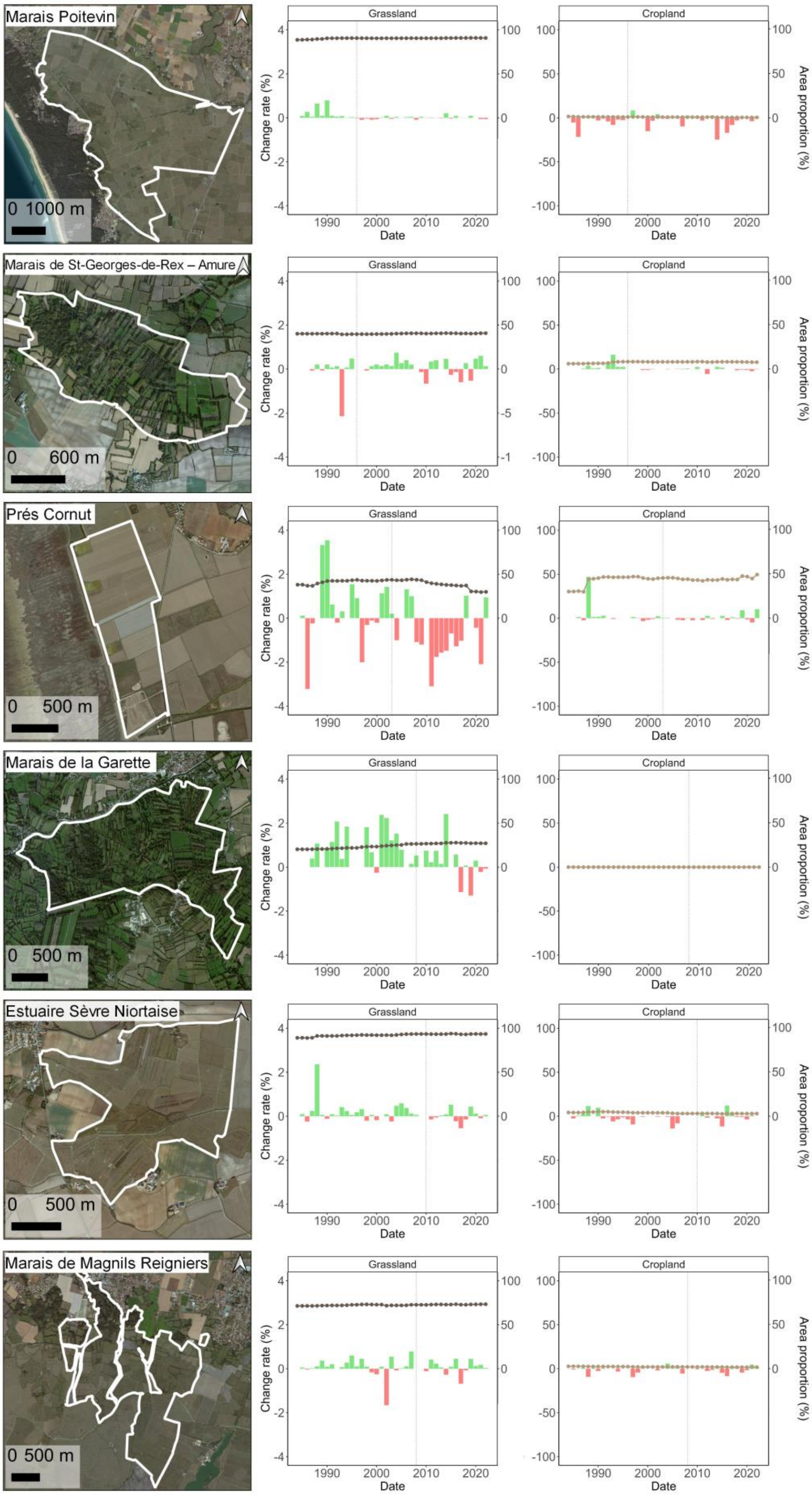
Marais Poitevin
0 1000 m
Marais de St-Georges-de-Rex – Amure
0 600 m
Prés Cornut
0 500 m
Marais de la Garette
0 500 m
Estuaire Sèvre Niortaise
0 500 m
Marais de Magnils Reigniers
0 500 m
Grassland
Cropland
Change rate (%)
Area proportion (%)
Date

Figure 5.3.5 : Location of the six land acquisition areas (white line), background: ESRI imagery ® (left); Annual net change (colored bars; left y axis) and area proportion (colored lines; right y axis) of grassland (middle) and cropland (right) inside land acquisition areas. Vertical dashed lines on the graphs indicate the implementation of the pre-emption perimeter.

5.4. Discussion

5.4.1. Contribution of long-term continuous monitoring

This study provides new insight into the effectiveness of agri-environmental policies and protected areas on grassland conservation using natural habitat maps derived from the Landsat archive that combine high spatial resolution (30 m), high update frequency (annual), and a long monitoring period (38 years). The high spatial resolution of these maps has enabled us to monitor the dynamics of small patches of grassland that are dominant in the fragmented landscape of the Poitevin marsh (Rapinel et al., 2015). The high spatial resolution combined with the long monitoring period has also made it possible, for the first time to our knowledge, to study the long-term effectiveness of conservation policies on plots subject to MAE or land acquisition perimeters. This long period of temporal monitoring is interesting because it offers a perspective of more than ten years on the dynamics of grassland and cropland areas before and after the implementation of these conservation policies: for example, the effect of the creation of the Natura 2000 site in 2002 on the dynamics of grassland areas could be observed with a perspective of 18 years. In addition, continuous monitoring on an annual time scale has made it possible, on the one hand, to compare precisely (i.e., without any time lag) trends in the area of grassland and cropland with key events, and, on the other hand, to highlight breaks or, conversely, stabilisation in trends in the area of grassland and crops. For example, the acceleration in the conversion of grassland to cropland between 1980 and 1990, followed by a slowdown between 1990 and 1995 in connection with the CAP reform previously observed in the Poitevin marsh (Duncan et al., 1999), has been clarified in our study: the acceleration was observed between 1987 and 1990 and the slowdown between 1991 and 1993. It should be kept in mind, however, that even though the accuracy of the classification of grassland and cropland is very high (F1-scores > 0.85), some confusion exists and may have been wrongly interpreted as changes of low amplitude.

In this study, we used annual maps of the main natural habitat types as an indicator of ecosystem structure. The use of other indicators derived from satellite time series and characterising ecosystem functions (Demarquet et al., 2024a; Rivarola et al., 2022) or floristic diversity (Purdon et al., 2022), would be an asset for better assessing the effectiveness of conservation policies (Martínez-López et al., 2021). In this context, a standardised methodological framework for using satellite data to evaluate conservation policies remains to be developed (Geldmann et al., 2021; Gohr et al., 2022).

5.4.2. Effect of protected areas policies

The aim of AP policies in the Marais Poitevin was to stop the decline in grassland areas observed in the Marais Poitevin since the 1950s (Godet and Thomas, 2013). This study shows that this objective has been achieved, since the area of grassland within the RAPs is relatively stable, whereas it is declining outside the RAPs. This confirms the effectiveness of APs in limiting anthropogenic pressures (He and Wei, 2023). On a European scale, these results support the effectiveness of the Natura 2000 network, in which a stable grassland area was observed between 2000 and 2018 in 86% of the sites evaluated (Cheţan and Dornik, 2021).

The effectiveness of PA policies in the Marais Poitevin can be explained by two factors: (i) the geographical superposition of PAs (nature reserves, land protection sites, Natura 2000 sites and regional nature parks), which combine the management and conservation measures implemented (Martorell et al., 2023), and (ii) the location of PAs on sites subject to less anthropogenic pressure due to biophysical conditions unfavourable to economic activities (i.e. presence of soils that are long saturated with water and difficult to drain), as has been highlighted in Spain (Rodríguez-Rodríguez and Martínez-Vega, 2018), Denmark (Levin et al., 2018) and more widely throughout Europe (Hermoso et al., 2018). Nevertheless, due to the geographical overlap of PAs, the respective effectiveness of each is difficult to assess (Rodríguez-Rodríguez and Martínez-Vega, 2018). In addition, we can note that, contrary to what we expected following the conclusions of the study by Duncan et al. (1999), the cessation in 1997 and then the resumption in 2014 of the PNR had no effect on the dynamics of areas under grassland or crops. This can be explained by the low level of protection afforded by this type of protected area (UNEP-WCMC and IUCN, 2024) and by its purpose, which is above all aimed at the sustainable development of an area.

5.4.3. Effects of agri-environmental policies

This study is the first, to our knowledge, to highlight the effect of the first reform of the CAP in 1992 on annual changes in grassland area at plot level. More specifically, a very clear anticipatory effect of the reform can be observed at the end of the 1980s, with a significant increase in the conversion of grassland to cropland, linked to the end of drainage subsidies (Duncan et al., 1999). Conversely, a strong decline in these conversions was observed from the application of the CAP reform in 1992, which marked an environmental turning point in its policy of financial incentives. The same anticipatory effect was observed later on at other sites in Europe for the following reforms, in 2003 in Denmark (Levin et al., 2018) and in 2013 in Bavaria (Haensel et al., 2023). In the Poitevin marsh, these reforms do not seem to have had any impact on the development of grassland and cropland outside protected areas. This can be explained by the fact that most of the grassland located on sites suitable for intensive agriculture had already been converted by the end of the 1980s.

This study also highlighted the positive effect of the MAEs on the Poitevin marsh, since the area under grassland increased during the contractual period (2000 - 2014) and remained stable overall for several years afterwards. This success can be explained not only by the fact that the majority of farmers in the Poitevin marsh have a good perception of grassland (Petit et al., 2022), but also by the fact that most of them are located within the Natura 2000 site, where economic pressures are lowest (Rouveyrol and Prima, 2024). However, as has been observed in Bavaria (Haensel et al., 2023), the effectiveness of the MAEs in conserving grassland is lower outside the Natura 2000 site, where the pressures are greatest. These results are a reminder of the importance of using financial leverage with farmers to conserve grassland (Tindale et al., 2024), despite the fact that the total surface area of the 404 plots contracted under MAEs over the period 2000-2014 represents less than 2% of the total surface area of the Poitevin marsh.

5.5. Conclusion

Continuous monitoring of the structure of the grassland ecosystem over the long term (1984-2022) and at high spatial resolution provides new insights into the effectiveness of agri-environmental policies and protected areas in a coastal marsh that has been under agricultural pressure since the introduction of the CAP in the 1960s. This study shows that although agri-environmental and protected area policies have different objectives and methods of application, they are complementary in terms of grassland conservation. As far as agri-environmental policies are concerned, the continuous monitoring of the main habitat types over time has allowed us not only to highlight the anticipatory effect of the first CAP reform, with an acceleration in the conversion of grassland to arable land at the end of the 1980s, but also to identify the turning point in this trend in 1992. The monitoring of the agricultural areas contracted under the MAE showed that they were effective in maintaining grasslands, as their area increased and then remained stable overall at the end of the contract period. The effect of the protected area policy has most likely contributed to the stabilisation of grassland areas, although long-term analysis has shown that protected areas have been established in areas with low agricultural pressure due to unfavorable biophysical conditions. This continuous monitoring of the spatiotemporal dynamics of grassland ecosystem structure provides policy makers with a tool to assess the effectiveness of conservation policies implemented over several decades. Future research will focus on applying this approach to larger areas, integrating indicators of ecosystem functioning with socio-economic indicators, and taking into account anthropogenic and climatic pressures on grasslands.

Conclusion to Chapter 5

In this chapter, we have shown that the continuous annual monitoring of the structure of grassland ecosystems using the Landsat archive over a period of nearly forty years with the CCDC can be used to assess the effect of conservation policies. More specifically, we have described the long-term evolution of grassland and cropland in the Marais Poitevin, highlighting the effect of protected areas on the maintenance of grassland areas and the effect of agri-environmental measures on the restoration of grassland in the Marais Poitevin. These results will enable managers to assess the effects of conservation policies on their areas and will help them to prepare future management plans.

More generally, these results, along with those described in the previous chapters, have highlighted the value of analysing the Landsat archive using a continuous change detection method. The strengths and limitations of this method as applied to wetland monitoring and characterisation will be discussed in the final part of this thesis.

GENERAL CONCLUSION & PERSPECTIVES

The main objective of this thesis was to assess the contribution of Landsat archives to the long-term monitoring and characterisation of Ramsar Wetlands of International Importance through the application of a continuous image time series analysis method. To answer this question, we explored four axes:

i. A literature review on the use of Landsat archive for wetland monitoring, to guide the choice of the time series analysis method used in the thesis;
ii. The application of the Continuous Change Detection and Classification (CCDC) method by deriving indicators of wetland structure and function, and by analysing the sensitivity and accuracy of this method on several Ramsar sites;
iii. The description and assessment of agricultural pressures on a Ramsar site (Marais Poitevin) based on wetland structure maps (natural habitats) obtained previously by applying the CCDC;
iv. A study of the value of the annual maps of natural habitats produced with the CCDC for assessing the effectiveness of public conservation policies.

We answered the main objective of the thesis, by showing the interest of using the CCDC to study the evolution of the structure and functioning of wetlands over the long term and by raising a certain number of questions and limitations. These are summarised in this chapter, which is structured around the methodological, thematic, and operational contributions of this thesis, and the perspectives envisaged.

Methodological contributions

We have shown the value of continuous analysis of the Landsat archive for monitoring and characterising wetlands over the long term. The literature review presented in Chapter 2 highlighted the limited use of continuous time series analysis methods, including CCDC, to process Landsat data, with authors often preferring traditional diachronic approaches using a few cloud-free Landsat images. However, CCDC enables continuous analysis, *i.e.*, using all the images in the Landsat archive, including those covered by clouds. This method has two particularly interesting advantages: (i) the classification of temporal segments, which enables changes in the structure of wetlands (natural habitats) to be detected with precision, and (ii) the production of synthetic images, which enables functional indicators to be derived.

We used the CCDC to generate an indicator of net annual primary productivity on a continuous basis in order to characterise changes in the functional status of wetlands. We have also shown that the accuracy of this indicator is stable over time, whatever the bioclimatic context. The production of synthetic images by the CCDC has already been used to monitor the phenology of wetland vegetation (Fu et al., 2022) but, for the first time to our knowledge, we have analysed the sensitivity of this method with respect to the number of clear Landsat observations used and the types of LULC. The results presented in Chapter 4 on four Ramsar sites around the world showed that the method was more sensitive to the type of land cover than to the number of clear observations available.

Indicators of wetland structure and area were generated continuously with the CCDC by classifying temporal segments. Compared with conventional methods, the CCDC has the advantage of using all the images contained in the Landsat archives during the study period, including those with high cloud cover and/or showing SLC-Off strips from the ETM+ sensor, which makes it possible to monitor the spatio-temporal dynamics of wetlands in greater detail. The indicators of wetland structure and area that we have derived from the CCDC cover a wide time span (around forty years) with a high update frequency (annual). These characteristics explain the interest raised by the CCDC, particularly for monitoring forest ecosystems (Chen et al., 2021) or wetlands (Yang et al., 2022). In addition, we have highlighted the advantages of CCDC compared with the traditional diachronic method, which is still widely used, as the change detection maps produced by CCDC have shown better accuracy.

In any case, the quality of classifications depends heavily on the availability of quality reference data (Friedl et al., 2022). Access to this data, which is essential for training and validating classification models, is often challenging, especially before the year 2000. The CCDC algorithm has the advantage of being asynchronous between the year of the reference data and that of the indicator produced by the classification of time segments. In this way, it overcomes the constraint of the availability of « historical » reference data (prior to the 2000s), which has enabled us to detect changes in the natural habitats of the Poitevin Marsh since 1984. The classification quality of the CCDC also depends on its parameterisation, which has so far been little studied and described in the literature. In a few studies, the CCDC was parameterised either by hyper-tuning (e.g. Yang et al., 2022) or by adjusting parameters according to expert opinion (e.g. Awty-Carroll et al., 2019b). The second option was applied in this thesis, by modifying the default value of certain parameters proposed in the API (Arévalo et al., 2020). Thus, to date, there is no consensus on how to optimally parameterise the

CCDC. It has been described that the detection of breaks is highly dependent on several parameters such as the *ChiSquareProbability* or the minimum number of consecutive observations *minObs*: it is thus possible to make the CCDC more or less sensitive to the detection of change (Pasquarella et al., 2022).

The application of the CCDC to the Landsat time series requires a high level of computing power (Zhu and Woodcock, 2014a) and also access to the hundreds of images contained in the archives, which requires a great deal of computing resources. Its recent implementation in cloud-computing via an API developed by Arévalo et al. (2020) and the deposit of the Landsat archive on the GEE platform make it possible to overcome these constraints. For the purposes of this thesis, the API source code was modified by adding two functionalities: (i) the integration of images from the new Landsat 9 satellite, and (ii) the possibility of selecting a study area by directly importing a GIS layer into GEE (the full scripts are available in Appendix E and Appendix F).

This thesis also highlights the contribution of the CCDC and Landsat archives to the production of essential biodiversity variables (EBVs) (Pereira et al., 2013; Skidmore et al., 2021b). The maps of natural habitats and net annual primary productivity generated correspond to the 'ecosystem distribution' and 'primary productivity' EBVs respectively. This mapping work was presented at an international conference (Demarquet et al., 2023b).

Thematic and operational contributions

From a thematic point of view, the results described in this thesis provide two new elements. Firstly, we have described and highlighted trends and changes in wetlands on a continuous basis. Compared with the changes observed using traditional diachronic approaches, the wetland dynamics highlighted using a continuous approach provide new light thanks to the high frequency of updating (decadal and annual) of the indicators produced. Secondly, the production of a functional indicator (annual net primary productivity) over the long term and at high spatial resolution, which until now has been limited in terms of spatial resolution and/or monitoring period, makes it possible to better assess the conservation status of wetlands. We have also identified three limitations to wetland monitoring with CCDC using images from Landsat archives. Two limitations are due to the characteristics of the Landsat images: (i) the spatial resolution of the Landsat images does not allow us to distinguish linear habitats or habitats distributed in small patches, (ii) the spectral resolution of the images (the Landsat 5/7 satellites being limited to 6 bands compared with 8 for the Landsat 8/9 satellites) does not allow us to distinguish habitats with a similar physiognomy. A third limitation is due to the way the CCDC works, which is better suited to detecting abrupt habitat changes (e.g., turning a meadow into arable land) than subtle changes (e.g., the gradual opening up of a meadow).

We have also shown that the continuous description of the characteristics of wetlands over time can be used to assess the effectiveness of public conservation policies, based on the example of the Marais Poitevin. From a temporal point of view, long-term monitoring provides an interesting insight into the dynamics of wetlands before and after the implementation of a public policy. From a spatial point of view, the high spatial resolution (30 m) of the indicators has made it possible, for example, to compare the inside and outside of protected areas. However, this would not have been possible with a diachronic approach, which is still used in the majority of scientific literature (e.g. Huang et al., 2019; Jia et al., 2016; Leberger et al., 2020).

More generally, this thesis highlights the fact that although agri-environmental and protected area policies have different objectives and methods of application, they are complementary when it comes to conserving grassland. The implementation of the first CAP reform in 1992 led to a significant decline in the conversion of grassland to crops in the Poitevin marshes. The MAEs offered to farmers in the 2000s enabled grassland areas to be reclaimed, even at the end of the contractual periods. As for the protected areas, their creation has helped to stabilise grassland areas. The main limitation of this analysis is that it does not establish a direct causal link between the implementation of a given public policy and its effect on grassland conservation. Indeed, the spatiotemporal dynamics of an ecosystem are linked to a set of socio-demographic and economic factors at several scales, requiring the acquisition of data and further analyses.

Despite these limitations, the use of the CCDC algorithm combined with the Landsat archive allows standardised monitoring (i.e., same data source, same method, same spatio-temporal resolution, and exhaustive coverage) of wetland structure and functions, which is essential for understanding trends (Skidmore et al., 2021b). For managers, this continuous monitoring approach is useful for assessing the effects of their management plans in relation to anthropogenic and climatic pressures (Lu and Xiao, 2024; Salimi et al., 2021). Standardised monitoring can also contribute to the reporting of international conventions, such as the Ramsar Convention or the European Habitats-Fauna-Flora Directive, for which the signatory states must provide information on the evolution of ecosystems at regular intervals, in order to assess the effectiveness of the conservation measures taken (Davidson et al., 2019; Delbosc et al., 2021). Although field approaches are essential for such monitoring, the differences induced by the use of different types of data and methodologies make spatiotemporal comparison challenging. The approach used in our work can help to bridge this gap, thanks in particular to its availability on GEE. The API developed by Arévalo et al. (2020) is intuitive to use thanks to its graphical interface, combined with open access to the Landsat archive in a standardised, pre-processed format. In this sense, this approach can be used by managers and decision-makers, regardless of the computing resources they possess.

Perspectives

The research work carried out during this thesis has enabled us to identify several perspectives for research and applications. From a methodological point of view, the first one would be to add other image sources to the CDDC. For example, the addition of Landsat MSS images would make it possible to go back even further into the past (1972), which would be very interesting in view of the strong agricultural pressures that affected wetlands in the 1970s. In addition, the addition of images from the SPOT World Heritage open archive (Nosavan et al., 2018) which contains SPOT images acquired between 1986 and 2015 at a spatial resolution of 20 m, would significantly increase the number of clear observations and thus improve the quality of the temporal interpolation carried out by the CCDC. However, the addition of these Landsat MSS or SPOT images, which have different spatial and spectral characteristics to the other Landsat sensors, requires a prior harmonisation stage. A second methodological perspective would be to improve the cloud mask applied to each image in the CCDC to retain only the clear pixels. The cloud detection method implemented in the CCDC tends to wrongly mask water surfaces (Foga et al., 2017; Zhu and Woodcock, 2014b) which have a spectral response similar to that of cast shadows. A third methodological perspective would be to compare the CCDC with alternative methods that notably improve the detection of more subtle changes. For example, the Detection and Characterisation of Coastal Tidal Wetland Change (DECODE) method has been developed to take better account of changes occurring in coastal wetlands, and in particular takes account of tides (Yang et al., 2022). Ye et al. (2023) have developed the OB-COLD algorithm for Object-Based Continuous Monitoring of Land Disturbance, which adds a spatial segmentation component to recognise disturbances. Other solutions have been developed for the continuous analysis of satellite time series, such as deep learning approaches (e.g. Ji et al., 2024). However, to our knowledge, there are still no graphical applications that make them easy to use on cloud computing platforms, limiting their use to researchers with solid programming skills and significant computing resources.

From a thematic point of view, a more in-depth assessment of the effectiveness of each conservation policy could be obtained by combining indicators derived from remote sensing data and field observations. While the monitoring of grassland areas derived from the analysis of remote sensing data is very useful for assessing the effectiveness of protected areas, other indicators derived from *in situ* observations (surveys of invasive species, breeding bird counts) or socio-economic diagnoses (interviews with stakeholders, etc.) are as relevant. In addition, efforts are needed to transfer the approach developed in this thesis to managers and political decision-makers (Pettorelli et al., 2014) to improve and manage wetlands more effectively.

REFERENCES

Ablat, X., Liu, G., Liu, Q., Huang, C., 2019. Application of Landsat derived indices and hydrological alteration matrices to quantify the response of floodplain wetlands to river hydrology in arid regions based on different dam operation strategies. *Science of The Total Environment* 688, 1389–1404. https://doi.org/10.1016/j.scitotenv.2019.06.232

Alademomi, A.S., Okolie, C.J., Daramola, O.E., Agboola, R.O., Salami, T.J., 2020. Assessing the relationship of LST, NDVI and EVI with land cover changes in the Lagos Lagoon environment. *Quaestiones Geographicae* 39, 87–109.

Alcaraz, D., Paruelo, J., Cabello, J., 2006. Identification of current ecosystem functional types in the Iberian Peninsula. *Global Ecology and Biogeography* 15, 200–212. https://doi.org/10.1111/j.1466-822X.2006.00215.x

Aljahdali, M.O., Munawar, S., Khan, W.R., 2021. Monitoring mangrove forest degradation and regeneration: Landsat time series analysis of moisture and vegetation indices at Rabigh Lagoon, Red Sea. *Forests* 12, 52.

Almahasheer, H., Aljowair, A., Duarte, C.M., Irigoien, X., 2016. Decadal stability of Red Sea mangroves. *Estuarine, Coastal and Shelf Science* 169, 164–172. https://doi.org/10.1016/j.ecss.2015.11.027

Amani, M., Mahdavi, S., Kakooei, M., Ghorbanian, A., Brisco, B., DeLancey, E.R., Toure, S., Reyes, E.L., 2021. Wetland Change Analysis in Alberta, Canada Using Four Decades of Landsat Imagery. *IEEE Journal of Selected Topics in Applied Earth Observations and Remote Sensing* 14, 10314–10335.

Anderson, M.J., 2014. Permutational multivariate analysis of variance (PERMANOVA). *Wiley StatsRef: Statistics Reference Online* 1–15.

Anzoategui, L.V., Gil-Leguizamón, P.A., Sanabria-Marin, R., 2023. Agricultural frontier and multi-temporality of vegetation cover in moorland of the Cortadera Regional Natural Park (Boyacá, Colombia). *Revista Bosque* 44, 159–170.

Arévalo, P., Baccini, A., Woodcock, C.E., Olofsson, P., Walker, W.S., 2023. Continuous mapping of aboveground biomass using Landsat time series. *Remote Sensing of Environment* 288, 113483. https://doi.org/10.1016/j.rse.2023.113483

Arévalo, P., Bullock, E.L., Woodcock, C.E., Olofsson, P., 2020. A Suite of Tools for Continuous Land Change Monitoring in Google Earth Engine. *Frontiers in Climate* 2. https://doi.org/10.3389/fclim.2020.576740

Asbridge, E., Lucas, R., Ticehurst, C., Bunting, P., 2016. Mangrove response to environmental change in Australia's Gulf of Carpentaria. *Ecology and Evolution* 6, 3523–3539. https://doi.org/10.1002/ece3.2140

Ashournejad, Q., Amiraslani, F., Moghadam, M.K., Toomanian, A., 2019. Assessing the changes of mangrove ecosystem services value in the Pars Special Economic Energy Zone. *Ocean & Coastal Management* 179, 104838. https://doi.org/10.1016/j.ocecoaman.2019.104838

Avtar, R., Navia, M., Sassen, J., Fujii, M., 2021. Impacts of changes in mangrove ecosystems in the Ba and Rewa deltas, Fiji using multi-temporal Landsat data and social survey. *Coastal Engineering Journal* 63, 386–407. https://doi.org/10.1080/21664250.2021.1932332

Awty-Carroll, K., Bunting, P., Hardy, A., Bell, G., 2019a. An evaluation and comparison of four dense time series change detection methods using simulated data. *Remote Sensing* 11, 2779.

Awty-Carroll, K., Bunting, P., Hardy, A., Bell, G., 2019b. Using Continuous Change Detection and Classification of Landsat Data to Investigate Long-Term Mangrove Dynamics in the Sundarbans Region. *Remote Sensing* 11, 2833. https://doi.org/10.3390/rs11232833

Banerjee, B.P., Raval, S., Timms, W., 2016. Evaluation of rainfall and wetland water area variability at Thirlmere Lakes using Landsat time-series data. *Int. J. Environ. Sci. Technol.* 13, 1781–1792. https://doi.org/10.1007/s13762-016-1018-z

Bansal, S., Creed, I.F., Tangen, B.A., Bridgham, S.D., Desai, A.R., Krauss, K.W., Neubauer, S.C., Noe, G.B., Rosenberry, D.O., Trettin, C., 2023. Practical guide to measuring wetland carbon pools and fluxes. *Wetlands* 43, 105.

Batáry, P., Dicks, L.V., Kleijn, D., Sutherland, W.J., 2015. The role of agri-environment schemes in conservation and environmental management. *Conservation Biology* 29, 1006–1016. https://doi.org/10.1111/cobi.12536

Behling, R., Milewski, R., Chabrillat, S., 2018. Spatiotemporal shoreline dynamics of Namibian coastal lagoons derived by a dense remote sensing time series approach. *International Journal of Applied Earth Observation and Geoinformation* 68, 262–271. https://doi.org/10.1016/j.jag.2018.01.009

Belgiu, M., Drăguţ, L., 2016. Random forest in remote sensing: A review of applications and future directions. *ISPRS Journal of Photogrammetry and Remote Sensing* 114, 24–31. https://doi.org/10.1016/j.isprsjprs.2016.01.011

Bengtsson, J., Bullock, J.M., Egoh, B., Everson, C., Everson, T., O'connor, T., O'farrell, P.J., Smith, H.G., Lindborg, R., 2019. Grasslands—more important for ecosystem services than you might think. Ecosphere 10: e02582. DOI.

Berhane, T., Lane, C., Mengistu, S., Christensen, J., Golden, H., Qiu, S., Zhu, Z., Wu, Q., 2020. Land-Cover Changes to Surface-Water Buffers in the Midwestern USA: 25 Years of Landsat Data Analyses (1993–2017). *Remote Sensing* 12, 754. https://doi.org/10.3390/rs12050754

Betbeder, J., Rapinel, S., Corgne, S., Pottier, E., Hubert-Moy, L., 2015. TerraSAR-X dual-pol time-series for mapping of wetland vegetation. *ISPRS Journal of Photogrammetry and Remote Sensing*, Multitemporal remote sensing data analysis 107, 90–98. https://doi.org/10.1016/j.isprsjprs.2015.05.001

Bioret, F., Gaudillat, V., Royer, J.S., 2013. The Prodrome of French vegetation: a national synsystem for phytosociological knowledge and management issues. *Plant Sociology* 50, 17–21.

Bishop-Taylor, R., Tulbure, M.G., Broich, M., 2017. Surface-water dynamics and land use influence landscape connectivity across a major dryland region. *Ecol Appl* 27, 1124–1137. https://doi.org/10.1002/eap.1507

Blanchette, M., Rousseau, A.N., Poulin, M., 2018. Mapping wetlands and land cover change with landsat archives: The added value of geomorphologic data: Cartographie de la dynamique spatio-temporelle des milieux humides à partir d'archives Landsat: La valeur ajoutée de données géomorphologiques. *Canadian Journal of Remote Sensing* 44, 337–356.

Bojinski, S., Verstraete, M., Peterson, T.C., Richter, C., Simmons, A., Zemp, M., 2014. The Concept of Essential Climate Variables in Support of Climate Research, Applications, and Policy. *Bulletin of the American Meteorological Society* 95, 1431–1443. https://doi.org/10.1175/BAMS-D-13-00047.1

Bonis, A., Bouzillé, J. aB, 2012. The project VegFrance: Towards a national vegetation database for France. *Plant Sociology* 49, 97–99.

Borro, M., Morandeira, N., Salvia, M., Minotti, P., Perna, P., Kandus, P., 2014. Mapping shallow lakes in a large South American floodplain: A frequency approach on multitemporal Landsat TM/ETM data. *Journal of Hydrology* 512, 39–52. https://doi.org/10.1016/j.jhydrol.2014.02.057

Breiman, L., 2001. Random Forests. *Machine Learning* 45, 5–32. https://doi.org/10.1023/A:1010933404324

Bridgewater, P., Kim, R.E., 2021. The Ramsar Convention on Wetlands at 50. *Nat Ecol Evol* 5, 268–270. https://doi.org/10.1038/s41559-021-01392-5

Brinson, M.M., 1993. A hydrogeomorphic classification for wetlands. US Army Corps of Engineers, Vicksburg, MS, USA.

Broich, M., Tulbure, M.G., Verbesselt, J., Xin, Q., Wearne, J., 2018. Quantifying Australia's dryland vegetation response to flooding and drought at sub-continental scale. *Remote Sensing of Environment* 212, 60–78. https://doi.org/10.1016/j.rse.2018.04.032

Buck, O., Haub, C., Woditsch, S., Lindemann, M., Kleinwillinghöfer, L., Hazeu, G., Kosztra, B., Kleeschulte, S., Arnold, S., Hölzl, M., 2015. Analysis of the LUCAS nomenclature and proposal for adaptation of the nomenclature in view of its use by the Copernicus land monitoring services.: EEA/EFTAS. Contract No

3436/B2015/RO-COPERNICUS/EEA. 56195. EEA-European Environment Agency.

Bullock, E.L., Nolte, C., Reboredo Segovia, A.L., Woodcock, C.E., 2020. Ongoing forest disturbance in Guatemala's protected areas. *Remote Sensing in Ecology and Conservation* 6, 141–152. https://doi.org/10.1002/rse2.130

Cabello, J., Fernández, N., Alcaraz-Segura, D., Oyonarte, C., Pineiro, G., Altesor, A., Delibes, M., Paruelo, J.M., 2012. The ecosystem functioning dimension in conservation: insights from remote sensing. *Biodiversity and Conservation* 21, 3287–3305.

Cai, X., Haile, A.T., Magidi, J., Mapedza, E., Nhamo, L., 2017. Living with floods – Household perception and satellite observations in the Barotse floodplain, Zambia. *Physics and Chemistry of the Earth, Parts A/B/C*, Infrastructural Planning for Water Security in Eastern and Southern Africa 100, 278–286. https://doi.org/10.1016/j.pce.2016.10.011

Cai, Y., Zhang, H., Zheng, P., Pan, W., 2016. Quantifying the Impact of Land use/Land Cover Changes on the Urban Heat Island: A Case Study of the Natural Wetlands Distribution Area of Fuzhou City, China. *Wetlands* 36, 285–298. https://doi.org/10.1007/s13157-016-0738-7

Campbell, T., Lantz, T., Fraser, R., 2018. Impacts of Climate Change and Intensive Lesser Snow Goose (Chen caerulescens caerulescens) Activity on Surface Water in High Arctic Pond Complexes. *Remote Sensing* 10, 1892. https://doi.org/10.3390/rs10121892

Carle, M.V., Sasser, C.E., 2016. Productivity and Resilience: Long-Term Trends and Storm-Driven Fluctuations in the Plant Community of the Accreting Wax Lake Delta. *Estuaries and coasts*.

Carney, J., Gillespie, T.W., Rosomoff, R., 2014. Assessing forest change in a priority West African mangrove ecosystem: 1986–2010. *Geoforum* 53, 126–135. https://doi.org/10.1016/j.geoforum.2014.02.013

Cavanaugh, K.C., Osland, M.J., Bardou, R., Hinojosa-Arango, G., López-Vivas, J.M., Parker, J.D., Rovai, A.S., Morueta-Holme, N., 2018. Sensitivity of mangrove range limits to climate variability. *Global Ecol Biogeogr* 27, 925–935. https://doi.org/10.1111/geb.12751

CBD Secretariat, 2010. The strategic plan for biodiversity 2011–2020 and the Aichi biodiversity targets. In Secretariat of the Convention on Biological Diversity. Nagoya, Japan.

Cetin, M., 2009. A satellite based assessment of the impact of urban expansion around a lagoon. *International Journal of Environmental Science and Technology* 4, 579–590. https://doi.org/10.1007/BF03326098

Chandra, A., Idrisova, A., 2011. Convention on Biological Diversity: a review of national challenges and opportunities for implementation. *Biodivers Conserv* 20, 3295–3316. https://doi.org/10.1007/s10531-011-0141-x

Charters, L.J., Aplin, P., Marston, C.G., Padfield, R., Rengasamy, N., Bin Dahalan, M.P., Evers, S., 2019. Peat swamp forest conservation withstands pervasive land conversion to oil palm plantation in North Selangor, Malaysia. *International Journal of Remote Sensing* 40, 7409–7438. https://doi.org/10.1080/01431161.2019.1574996

Chen, C., Ma, Y., Yu, D., Hu, Y., Ren, L., 2024. Tracking annual dynamics of carbon storage of salt marsh plants in the Yellow River Delta national nature reserve of china based on sentinel-2 imagery during 2017–2022. *International Journal of Applied Earth Observation and Geoinformation* 130, 103880. https://doi.org/10.1016/j.jag.2024.103880

Chen, C.-F., Son, N.-T., Chang, N.-B., Chen, C.-R., Chang, L.-Y., Valdez, M., Centeno, G., Thompson, C.A., Aceituno, J.L., 2013. Multi-Decadal Mangrove Forest Change Detection and Prediction in Honduras, Central America, with Landsat Imagery and a Markov Chain Model. *Remote Sensing* 5, 6408–6426. https://doi.org/10.3390/rs5126408

Chen, L., Ding, R., Zhu, E., Wu, H., Feng, D., 2024. How do coastal wetlands respond to the impact of sea level rise? *Ocean & Coastal Management* 255, 107229. https://doi.org/10.1016/j.ocecoaman.2024.107229

Chen, S., Woodcock, C.E., Bullock, E.L., Arévalo, P., Torchinava, P., Peng, S., Olofsson, P., 2021. Monitoring temperate forest degradation on Google Earth Engine using Landsat time series analysis. *Remote Sensing of Environment* 265, 112648. https://doi.org/10.1016/j.rse.2021.112648

Cherrington, E.A., Griffin, R.E., Anderson, E.R., Hernandez Sandoval, B.E., Flores-Anderson, A.I., Muench, R.E., Markert, K.N., Adams, E.C., Limaye, A.S., Irwin, D.E., 2020. Use of public Earth observation data for tracking progress in sustainable management of coastal forest ecosystems in Belize, Central America. *Remote Sensing of Environment* 245, 111798. https://doi.org/10.1016/j.rse.2020.111798

Cheţan, M.A., Dornik, A., 2021. 20 years of landscape dynamics within the world's largest multinational network of protected areas. *Journal of Environmental Management* 280, 111712.

Chouari, W., 2021. Wetland land cover change detection using multitemporal Landsat data: a case study of the Al-Asfar wetland, Kingdom of Saudi Arabia. *Arab J Geosci* 14, 523. https://doi.org/10.1007/s12517-021-06815-y

Chytrý, M., Tichý, L., Hennekens, S.M., Knollová, I., Janssen, J.A.M., Rodwell, J.S., Peterka, T., Marcenò, C., Landucci, F., Danihelka, J., Hájek, M., Dengler, J., Novák, P., Zukal, D., Jiménez-Alfaro, B., Mucina, L., Abdulhak, S., Aćić, S., Agrillo, E., Attorre, F., Bergmeier, E., Biurrun, I., Boch, S., Bölöni, J., Bonari, G., Braslavskaya, T., Bruelheide, H., Campos, J.A., Čarni, A., Casella, L., Ćuk, M., Ćušterevska, R., De Bie, E., Delbosc, P., Demina, O., Didukh, Y., Dítě, D., Dziuba, T., Ewald, J., Gavilán, R.G., Gégout, J.-C., Giusso del Galdo, G.P., Golub, V., Goncharova, N., Goral, F., Graf, U., Indreica, A., Isermann, M., Jandt, U., Jansen, F., Jansen, J., Jašková, A., Jiroušek, M., Kącki, Z., Kalníková, V., Kavgacı, A., Khanina, L., Yu. Korolyuk, A., Kozhevnikova, M., Kuzemko, A., Küzmič, F., Kuznetsov, O.L., Laiviņš, M., Lavrinenko, I., Lavrinenko, O., Lebedeva, M., Lososová, Z., Lysenko, T., Maciejewski, L., Mardari, C., Marinšek, A., Napreenko, M.G., Onyshchenko, V., Pérez-Haase, A., Pielech, R., Prokhorov, V., Rašomavičius, V., Rodríguez Rojo, M.P., Rūsiņa, S., Schrautzer, J., Šibík, J., Šilc, U., Škvorc, Ž., Smagin, V.A., Stančić, Z., Stanisci, A., Tikhonova, E., Tonteri, T., Uogintas, D., Valachovič, M., Vassilev, K., Vynokurov, D., Willner, W., Yamalov, S., Evans, D., Palitzsch Lund, M., Spyropoulou, R., Tryfon, E., Schaminée, J.H.J., 2020. EUNIS Habitat Classification: Expert system, characteristic species combinations and distribution maps of European habitats. *Applied Vegetation Science* 23, 648–675. https://doi.org/10.1111/avsc.12519

Clair, M., Gaudillat, V., Michez, N., Poncet, Laurent, Poncet, L., 2017. HABREF v3. 1, référentiel des typologies d’habitats et de végétation pour la France. Guide méthodologique. Service du Patrimoine Naturel, Museum National d’Histoire Naturelle, Paris, France.

Continuous Change Detection and Classification CCDC [WWW Document], 2024. . *openMRV*. URL https://www.openmrv.org/web/guest/w/modules/mrv/modules_2/continuous-change-detection-and-classification-ccdc (accessed 8.23.24).

Corbane, C., Lang, S., Pipkins, K., Alleaume, S., Deshayes, M., García Millán, V.E., Strasser, T., Vanden Borre, J., Toon, S., Michael, F., 2015. Remote sensing for mapping natural habitats and their conservation status – New opportunities and challenges. *International Journal of Applied Earth Observation and Geoinformation*, Special Issue on Earth observation for habitat mapping and biodiversity monitoring 37, 7–16. https://doi.org/10.1016/j.jag.2014.11.005

Correa, D.B., Alcântara, E., Libonati, R., Massi, K.G., Park, E., 2022. Increased burned area in the Pantanal over the past two decades. *Science of The Total Environment* 835, 155386. https://doi.org/10.1016/j.scitotenv.2022.155386

Costa, H., 2022. _mapaccuracy: Unbiased Thematic Map Accuracy and Area_.

Courouble, M., Davidson, N., Dinesen, L., Fennessy, S., Galewski, T., Guelmami, A., Kumar, R., McInnes, R., Perennou, C., Rebelo, L.-M., Robertson, H., Segura-Champagnon, L., Simpson, M., Stroud, D.A., 2021. Global Wetland Outlook: Special Edition 2021. Ramsar Convention Secretariat, Gland, Switzerland.

Crawford, C.J., Roy, D.P., Arab, S., Barnes, C., Vermote, E., Hulley, G., Gerace, A., Choate, M., Engebretson, C., Micijevic, E., Schmidt, G., Anderson, C., Anderson, M., Bouchard, M., Cook, B., Dittmeier, R., Howard, D., Jenkerson, C., Kim, M., Kleyians, T., Maiersperger, T., Mueller, C., Neigh, C., Owen, L., Page, B., Pahlevan, N., Rengarajan, R., Roger, J.-C., Sayler, K., Scaramuzza, P., Skakun, S., Yan, L., Zhang, H.K., Zhu, Z., Zahn, S., 2023. The 50-year Landsat collection 2 archive. *Science of Remote Sensing* 8, 100103. https://doi.org/10.1016/j.srs.2023.100103

Crist, E.P., 1985. A TM tasseled cap equivalent transformation for reflectance factor data. *Remote sensing of Environment* 17, 301–306.

Dąbrowska-Zielińska, K., Misiura, K., Malińska, A., Gurdak, R., Grzybowski, P., Bartold, M., Kluczek, M., 2022. Spatiotemporal estimation of gross primary production for terrestrial wetlands using satellite and field data. *Remote Sensing Applications: Society and Environment* 27, 100786.

Dahl, T.E., 2004. Remote sensing as a tool for monitoring wetland habitat change, in: *US Fish and Wildlife Service, Branch of Habitat Assessment, Fish and Wildlife Resource Centre*, Proceedings RMRS-P-42CD. Presented at the Monitoring Science and Technology Symposium: Unifying Knowledge for Sustainability in the Western Hemisphere, Denver, CO, p. 990.

Dang, A.T., Kumar, L., Reid, M., Nguyen, H., 2021. Remote sensing approach for monitoring coastal wetland in the Mekong Delta, Vietnam: Change trends and their driving forces. *Remote Sensing* 13, 3359.

Dangles, O., Rabatel, A., Kraemer, M., Zeballos, G., Soruco, A., Jacobsen, D., Anthelme, F., 2017. Ecosystem sentinels for climate change? Evidence of wetland cover changes over the last 30 years in the tropical Andes. *PLoS ONE* 12, e0175814. https://doi.org/10.1371/journal.pone.0175814

Darmawan, S., Sari, D.K., Wikantika, K., Tridawati, A., Hernawati, R., Sedu, M.K., 2020. Identification before-after Forest Fire and Prediction of Mangrove Forest Based on Markov-Cellular Automata in Part of Sembilang National Park, Banyuasin, South Sumatra, Indonesia. *Remote Sensing* 12, 3700. https://doi.org/10.3390/rs12223700

Davidson, N.C., 2014. How much wetland has the world lost? Long-term and recent trends in global wetland area. *Australian Journal of Marine and Freshwater Research* 65, 934–941. https://doi.org/10.1071/MF14173

Davidson, N.C., Dinesen, L., Fennessy, S., Finlayson, C.M., Grillas, P., Grobicki, A., McInnes, R.J., Stroud, D.A., 2020. Trends in the ecological character of the world's wetlands. *Mar. Freshwater Res.* 71, 127. https://doi.org/10.1071/MF18329

Davidson, N.C., Dinesen, L., Fennessy, S., Finlayson, C.M., Grillas, P., Grobicki, A., McInnes, R.J., Stroud, D.A., 2019. A review of the adequacy of reporting to the

Ramsar Convention on change in the ecological character of wetlands. *Mar. Freshwater Res.* 71, 117–126. https://doi.org/10.1071/MF18328

Davidson, N.C., Finlayson, C.M., 2018. Extent, regional distribution and changes in area of different classes of wetland. *Mar. Freshwater Res.* 69, 1525–1533. https://doi.org/10.1071/MF17377

Davies, C.E., Moss, D., Hill, M.O., 2004. EUNIS Habitat Classification. European Environment Agency, Copenhagen.

Davis, J.A., Froend, R., 1999. Loss and degradation of wetlands in southwestern Australia: underlying causes, consequences and solutions. *Wetlands Ecology and Management* 7, 13–23. https://doi.org/10.1023/A:1008400404021

de Souza Miranda, C., Cândido, A.K.A.A., Mioto, C.L., da Silva, N.M., Paranhos Filho, A.C., Pott, A., 2017. Geotechnology as support for the management of conservation units in Brazil's Pantanal. *Boletim do Museu Paraense Emílio Goeldi-Ciências Naturais* 12, 255–264.

Dearborn, K.D., Baltzer, J.L., 2021. Unexpected greening in a boreal permafrost peatland undergoing forest loss is partially attributable to tree species turnover. *Glob Change Biol* 27, 2867–2882. https://doi.org/10.1111/gcb.15608

DeLancey, E.R., Simms, J.F., Mahdianpari, M., Brisco, B., Mahoney, C., Kariyeva, J., 2020. Comparing Deep Learning and Shallow Learning for Large-Scale Wetland Classification in Alberta, Canada. *Remote Sensing* 12, 2. https://doi.org/10.3390/rs12010002

Delassus, L., Magnanon, S., Colasse, V., Glemarec, E., Guitton, H., Laurent, E., Thomassin, G., Bioret, F., Catteau, E., Clément, B., Diquelou, S., Felzines, J., De Foucault, B., Gauberville, C., Gaudillat, V., Guillevic, Y., Haury, J., Royer, J., Vallet, J., Geslin, J., Goret, M., Hardegen, M., Lacroix, P., Reimringer, K., Sellin, V., Waymel, J., Zambettakis, C., 2014. Classification physionomique et phytosociologique des végétations de Basse-Normandie, Bretagne et Pays de la Loire. Conservatoire Botanique National de Brest, Brest, France.

Delbosc, P., Lagrange, I., Rozo, C., Bensettiti, F., Bouzillé, J.-B., Evans, D., Lalanne, A., Rapinel, S., Bioret, F., 2021. Assessing the conservation status of coastal habitats under Article 17 of the EU Habitats Directive. *Biological Conservation* 254, 108935.

Demarquet, Q., Rapinel, S., Arvor, D., Corgne, S., Hubert-Moy, L., 2024a. Satellite Long-Term Monitoring of Wetland Ecosystem Functioning in Ramsar Sites for Their Sustainable Management. *Sustainability* 16, 6301.

Demarquet, Q., Rapinel, S., Dufour, S., Hubert-Moy, L., 2023a. Long-Term Wetland Monitoring Using the Landsat Archive: A Review. *Remote Sensing* 15, 820. https://doi.org/10.3390/rs15030820

Demarquet, Q., Rapinel, S., Dufour, S., Hubert-Moy, L., 2023b. Review of Long-term Wetland Monitoring Using the Landsat Archive: Focus on Opportunities for Essential Variables Derivation, in: *BioClim Wetlands 2023*. Unpublished.

Demarquet, Q., Rapinel, S., Gore, O., Dufour, S., Hubert-Moy, L., 2024b. Continuous change detection outperforms traditional post-classification change detection for long-term monitoring of wetlands. *International Journal of Applied Earth Observation and Geoinformation* 133, 104142. https://doi.org/10.1016/j.jag.2024.104142

Dervisoglu, A., Musaoğlu, N., Tanik, A., Şeker, D., Kaya, Ş., 2017. Satellite-based temporal assessment of a dried lake: case study of Akgol wetland. *FRESENIUS ENVIRONMENTAL BULLETIN* 26.

Devillers, P., Devillers-Terschuren, J., Ledant, J., 1991. CORINE biotopes manual. *Habitats of the European Community. Office for Official Publications of the European Communities, Luxembourg*.

Dewidar, K.M., 2011. Monitoring temporal changes of the surface water area of the Burullus and Manzala lagoons using automatic techniques applied to a Landsat satellite data series of the Nile Delta coast. *Mediterranean Marine Science* 12, 462–478. https://doi.org/10.12681/mms.45

Díaz-Delgado, R., Aragonés, D., Afán, I., Bustamante, J., 2016. Long-Term Monitoring of the Flooding Regime and Hydroperiod of Doñana Marshes with Landsat Time Series (1974–2014). *Remote Sensing* 8, 775. https://doi.org/10.3390/rs8090775

Ding, X., Shan, X., Chen, Y., Li, M., Li, J., Jin, X., 2020. Variations in fish habitat fragmentation caused by marine reclamation activities in the Bohai coastal region, China. *Ocean & Coastal Management* 184, 105038.

Dingle Robertson, L., King, D.J., Davies, C., 2015. Assessing Land Cover Change and Anthropogenic Disturbance in Wetlands Using Vegetation Fractions Derived from Landsat 5 TM Imagery (1984–2010). *Wetlands* 35, 1077–1091. https://doi.org/10.1007/s13157-015-0696-5

Diniz, C., Cortinhas, L., Nerino, G., Rodrigues, J., Sadeck, L., Adami, M., Souza-Filho, P., 2019. Brazilian Mangrove Status: Three Decades of Satellite Data Analysis. *Remote Sensing* 11, 808. https://doi.org/10.3390/rs11070808

Dipson, P.T., Chithra, S.V., Amarnath, A., Smitha, S.V., Harindranathan Nair, M.V., Shahin, A., 2015. Spatial changes of estuary in Ernakulam district, Southern India for last seven decades, using multi-temporal satellite data. *Journal of Environmental Management*, Land Cover/Land Use Change (LC/LUC) and Environmental Impacts in South Asia 148, 134–142. https://doi.org/10.1016/j.jenvman.2014.02.021

Dong, X., Chen, Z., 2021. Digital Examination of Vegetation Changes in River Floodplain Wetlands Based on Remote Sensing Images: A Case Study Based on the Downstream Section of Hailar River. *Forests* 12, 1206.

Dou, P., Cui, B., 2014. Dynamics and integrity of wetland network in estuary. *Ecological Informatics* 24, 1–10. https://doi.org/10.1016/j.ecoinf.2014.06.002

Doughty, C.L., Ambrose, R.F., Okin, G.S., Cavanaugh, K.C., 2021. Characterizing spatial variability in coastal wetland biomass across multiple scales using UAV and satellite imagery. *Remote Sensing in Ecology and Conservation* 7, 411–429. https://doi.org/10.1002/rse2.198

Dudley, N., Stolton, S., Shadie, P., 2013. Guidelines for applying protected area management categories including IUCN WCPA best practice guidance on recognising protected areas and assigning management categories and governance types. IUCN.

Duncan, C., Böhm, M., Turvey, S.T., 2021. Identifying the possibilities and pitfalls of conducting IUCN Red List assessments from remotely sensed habitat information based on insights from poorly known Cuban mammals. *Conservation Biology* 35, 1598–1614. https://doi.org/10.1111/cobi.13715

Duncan, P., Hewison, A.J.M., Houte, S., Rosoux, R., Tournebize, T., Dubs, F., Burel, F., Bretagnolle, V., 1999. Long-term changes in agricultural practices and wildfowling in an internationally important wetland, and their effects on the guild of wintering ducks. *Journal of applied ecology* 36, 11–23.

Dwyer, J.L., Roy, D.P., Sauer, B., Jenkerson, C.B., Zhang, H.K., Lymburner, L., 2018. Analysis Ready Data: Enabling Analysis of the Landsat Archive. *Remote Sensing* 10, 1363. https://doi.org/10.3390/rs10091363

Eddy, S., Iskandar, I., Ridho, M.R., Mulyana, A., 2017. Land cover changes in the Air Telang Protected Forest, South Sumatra, Indonesia (1989-2013). *Biodiversitas Journal of Biological Diversity* 18, 1538–1545. https://doi.org/10.13057/biodiv/d180431

EEA, 2014. Crosswalk between EUNIS habitats classification and Corine land cover [WWW Document]. *European Environmental Agency*. URL https://www.eea.europa.eu/data-and-maps/data/eunis-habitat-classification-1/documentation/eunis-clc.pdf (accessed 5.25.24).

Ehsani, A.H., Shakeryari, M., 2021. Monitoring of wetland changes affected by drought using four Landsat satellite data and Fuzzy ARTMAP classification method (case study Hamoun wetland, Iran). *Arab J Geosci* 14, 1363. https://doi.org/10.1007/s12517-020-06320-8

Ekumah, B., Armah, F.A., Afrifa, E.K.A., Aheto, D.W., Odoi, J.O., Afitiri, A.-R., 2020. Geospatial assessment of ecosystem health of coastal urban wetlands in Ghana.

Ocean & Coastal Management 193, 105226. https://doi.org/10.1016/j.ocecoaman.2020.105226

Elliott, J., Tindale, S., Outhwaite, S., Nicholson, F., Newell-Price, P., Sari, N.H., Hunter, E., Sánchez-Zamora, P., Jin, S., Gallardo-Cobos, R., 2024. European permanent grasslands: A systematic review of economic drivers of change, including a detailed analysis of the Czech Republic, Spain, Sweden, and UK. *Land* 13, 116.

Erwin, K.L., 2009. Wetlands and global climate change: the role of wetland restoration in a changing world. *Wetlands Ecol Manage* 17, 71–84. https://doi.org/10.1007/s11273-008-9119-1

Esbah, H., Deniz, B., Kara, B., Kesgin, B., 2010. Analyzing landscape changes in the Bafa Lake Nature Park of Turkey using remote sensing and landscape structure metrics. *Environ Monit Assess* 165, 617–632. https://doi.org/10.1007/s10661-009-0973-y

Eslami-Andargoli, L., Dale, P.E.R., Sipe, N., Chaseling, J., 2010. Local and landscape effects on spatial patterns of mangrove forest during wetter and drier periods: Moreton Bay, Southeast Queensland, Australia. *Estuarine, Coastal and Shelf Science* 89, 53–61. https://doi.org/10.1016/j.ecss.2010.05.011

European Court of Auditors, 2016. The Land Parcel Identification System: a useful tool to determine the eligibility of agricultural land – but its management could be further improved. Special report No 25, 2016. Publications Office.

Farr, T.G., Rosen, P.A., Caro, E., Crippen, R., Duren, R., Hensley, S., Kobrick, M., Paller, M., Rodriguez, E., Roth, L., Seal, D., Shaffer, S., Shimada, J., Umland, J., Werner, M., Oskin, M., Burbank, D., Alsdorf, D., 2007. The Shuttle Radar Topography Mission. *Reviews of Geophysics* 45. https://doi.org/10.1029/2005RG000183

Fernandez-Carrillo, A., Sanchez-Rodriguez, E., Rodriguez-Galiano, V.F., 2019. Characterising marshland temporal dynamics using remote sensing: The case of Bolboschoenetum maritimi in Doñana national park. *Applied Geography* 112, 102094. https://doi.org/10.1016/j.apgeog.2019.102094

Ferrarini, A., Gustin, M., Celada, C., 2021. Twenty-three years of land-use changes induced considerable threats to the main wetlands of Sardinia and Sicily (Italy) along the Mediterranean bird flyways. *Diversity* 13, 240.

Fickas, K.C., Cohen, W.B., Yang, Z., 2016. Landsat-based monitoring of annual wetland change in the Willamette Valley of Oregon, USA from 1972 to 2012. *Wetlands Ecol Manage* 24, 73–92. https://doi.org/10.1007/s11273-015-9452-0

Finlayson, C.M., Gardner, R.C., 2020. Ten key issues from the Global Wetland Outlook for decision makers. *Marine and Freshwater Research* 72, 301–310.

Finlayson, C.M., Milton, G.R., Prentice, R.C., 2018. Wetland types and distribution, in: Finlayson, C.M., Milton, G.R., Prentice, R.C., Davidson, N.C. (Eds.), *The Wetland*

Book II. Springer, Netherlands, pp. 19–35. https://doi.org/10.1007/978-94-007-4001-3_186

Fitoka, E., Tompoulidou, M., Hatziiordanou, L., Apostolakis, A., Höfer, R., Weise, K., Ververis, C., 2020. Water-related ecosystems' mapping and assessment based on remote sensing techniques and geospatial analysis: The SWOS national service case of the Greek Ramsar sites and their catchments. *Remote Sensing of Environment* 245, 111795. https://doi.org/10.1016/j.rse.2020.111795

Fluet-Chouinard, E., Stocker, B.D., Zhang, Z., Malhotra, A., Melton, J.R., Poulter, B., Kaplan, J.O., Goldewijk, K.K., Siebert, S., Minayeva, T., Hugelius, G., Joosten, H., Barthelmes, A., Prigent, C., Aires, F., Hoyt, A.M., Davidson, N., Finlayson, C.M., Lehner, B., Jackson, R.B., McIntyre, P.B., 2023. Extensive global wetland loss over the past three centuries. *Nature* 614, 281–286. https://doi.org/10.1038/s41586-022-05572-6

Foga, S., Scaramuzza, P.L., Guo, S., Zhu, Z., Dilley, R.D., Beckmann, T., Schmidt, G.L., Dwyer, J.L., Joseph Hughes, M., Laue, B., 2017. Cloud detection algorithm comparison and validation for operational Landsat data products. *Remote Sensing of Environment* 194, 379–390. https://doi.org/10.1016/j.rse.2017.03.026

Friedl, M.A., Woodcock, C.E., Olofsson, P., Zhu, Z., Loveland, T., Stanimirova, R., Arevalo, P., Bullock, E., Hu, K.-T., Zhang, Y., 2022. Medium Spatial Resolution Mapping of Global Land Cover and Land Cover Change Across Multiple Decades From Landsat. *Frontiers in Remote Sensing* 3.

Fritz, S., See, L., Perger, C., McCallum, I., Schill, C., Schepaschenko, D., Duerauer, M., Karner, M., Dresel, C., Laso-Bayas, J.-C., Lesiv, M., Moorthy, I., Salk, C.F., Danylo, O., Sturn, T., Albrecht, F., You, L., Kraxner, F., Obersteiner, M., 2017. A global dataset of crowdsourced land cover and land use reference data. *Sci Data* 4, 170075. https://doi.org/10.1038/sdata.2017.75

Frota, A.V.B. da, Ikeda-Castrillon, S.K., Kantek, D.L.Z., Silva, C.J. da, 2017. Macrohabitats of the Taiamã Ecological Station, in the context of the Pantanal wetland, Brazil. *Boletim do Museu Paraense Emílio Goeldi, Ciências Naturais* 12, 239–254.

Fu, B., Deng, L., Sun, W., He, H., Li, H., Wang, Yong, Wang, Yeqiao, 2024. Quantifying vegetation species functional traits along hydrologic gradients in karst wetland based on 3D mapping with UAV hyperspectral point cloud. *Remote Sensing of Environment* 307, 114160. https://doi.org/10.1016/j.rse.2024.114160

Fu, B., Lan, F., Yao, H., Qin, J., He, H., Liu, L., Huang, L., Fan, D., Gao, E., 2022. Spatio-temporal monitoring of marsh vegetation phenology and its response to hydro-meteorological factors using CCDC algorithm with optical and SAR images: In case of Honghe National Nature Reserve, China. *Science of The Total Environment* 843, 156990. https://doi.org/10.1016/j.scitotenv.2022.156990

Fuller, R.M., Smith, G.M., Devereux, B.J., 2003. The characterisation and measurement of land cover change through remote sensing: problems in operational applications? *International Journal of Applied Earth Observation and Geoinformation* 4, 243–253. https://doi.org/10.1016/S0303-2434(03)00004-7

Gallant, A.L., 2015. The Challenges of Remote Monitoring of Wetlands. *Remote Sensing* 7, 10938–10950. https://doi.org/10.3390/rs70810938

Gallego, J., Delincé, J., 2010. The European Land Use and Cover Area-Frame Statistical Survey, in: Benedetti, R., Bee, M., Espa, G., Piersimoni, F. (Eds.), *Agricultural Survey Methods*. John Wiley & Sons, Ltd, Chichester, UK, pp. 149–168. https://doi.org/10.1002/9780470665480.ch10

Gao, Z., Guo, H., Li, S., Wang, J., Ye, H., Han, S., Cao, W., 2022. Remote sensing of wetland evolution in predicting shallow groundwater arsenic distribution in two typical inland basins. *Science of The Total Environment* 806, 150496.

Gardner, R.C., Davidson, N.C., 2011. The Ramsar Convention, in: LePage, B.A. (Ed.), *Wetlands: Integrating Multidisciplinary Concepts*. Springer Netherlands, Dordrecht, pp. 189–203. https://doi.org/10.1007/978-94-007-0551-7_11

Gayol, M.P., Morandeira, N.S., Kandus, P., 2019. Dynamics of shallow lake cover types in relation to Paraná River flood pulses: assessment with multitemporal Landsat data. *Hydrobiologia* 833, 9–24.

GBIF, 2022. GBIF: The Global Biodiversity Information Facility (year) What is GBIF? [WWW Document]. URL https://www.gbif.org/what-is-gbif (accessed 3.15.22).

GCOS, 2010. Implementation plan for the global observing system climate in support of UNFCCC (2010 update). (GCOS Rep. 138). GCOS.

Geijzendorffer, I.R., Beltrame, C., Chazee, L., Gaget, E., Galewski, T., Guelmami, A., Perennou, C., Popoff, N., Guerra, C.A., Leberger, R., Jalbert, J., Grillas, P., 2019. A More Effective Ramsar Convention for the Conservation of Mediterranean Wetlands. *Front. Ecol. Evol.* 7. https://doi.org/10.3389/fevo.2019.00021

Geldmann, J., Deguignet, M., Balmford, A., Burgess, N.D., Dudley, N., Hockings, M., Kingston, N., Klimmek, H., Lewis, A.H., Rahbek, C., Stolton, S., Vincent, C., Wells, S., Woodley, S., Watson, J.E.M., 2021. Essential indicators for measuring site-based conservation effectiveness in the post-2020 global biodiversity framework. *Conservation Letters* 14, e12792. https://doi.org/10.1111/conl.12792

Ghoddousi, A., Loos, J., Kuemmerle, T., 2022. An Outcome-Oriented, Social–Ecological Framework for Assessing Protected Area Effectiveness. *BioScience* 72, 201–212. https://doi.org/10.1093/biosci/biab114

Ghosh, M., Kumar, L., Roy, C., 2017. Climate Variability and Mangrove Cover Dynamics at Species Level in the Sundarbans, Bangladesh. *Sustainability* 9, 805. https://doi.org/10.3390/su9050805

Ghosh, M.K., Kumar, L., Roy, C., 2016. Mapping Long-Term Changes in Mangrove Species Composition and Distribution in the Sundarbans. *Forests* 7, 305. https://doi.org/10.3390/f7120305

Giannetti, F., Pecchi, M., Travaglini, D., Francini, S., D'Amico, G., Vangi, E., Cocozza, C., Chirici, G., 2021. Estimating VAIA Windstorm Damaged Forest Area in Italy Using Time Series Sentinel-2 Imagery and Continuous Change Detection Algorithms. *Forests* 12, 680. https://doi.org/10.3390/f12060680

Gibbes, C., Southworth, J., Keys, E., 2009. Wetland conservation: Change and fragmentation in Trinidad's protected areas. *Geoforum*, Themed Issue: Postcoloniality, Responsibility and Care 40, 91–104. https://doi.org/10.1016/j.geoforum.2008.05.005

Gilani, H., Naz, H.I., Arshad, M., Nazim, K., Akram, U., Abrar, A., Asif, M., 2021. Evaluating mangrove conservation and sustainability through spatiotemporal (1990–2020) mangrove cover change analysis in Pakistan. *Estuarine, Coastal and Shelf Science* 249, 107128. https://doi.org/10.1016/j.ecss.2020.107128

Gillespie, T.W., Willis, K.S., Ostermann-Kelm, S., 2015. Spaceborne remote sensing of the world's protected areas. *Progress in Physical Geography: Earth and Environment* 39, 388–404. https://doi.org/10.1177/0309133314561648

Godet, L., Thomas, A., 2013. Three centuries of land cover changes in the largest French Atlantic wetland provide new insights for wetland conservation. *Applied Geography* 42, 133–139. https://doi.org/10.1016/j.apgeog.2013.05.011

Gohr, C., von Wehrden, H., May, F., Ibisch, P.L., 2022. Remotely sensed effectiveness assessments of protected areas lack a common framework: A review. *Ecosphere* 13, e4053. https://doi.org/10.1002/ecs2.4053

Gómez, C., White, J.C., Wulder, M.A., 2016. Optical remotely sensed time series data for land cover classification: A review. *ISPRS Journal of Photogrammetry and Remote Sensing* 116, 55–72. https://doi.org/10.1016/j.isprsjprs.2016.03.008

Gong, Z., Li, H., Zhao, W., Gong, H., 2013. Driving forces analysis of reservoir wetland evolution in Beijing during 1984–2010. *J. Geogr. Sci.* 23, 753–768. https://doi.org/10.1007/s11442-013-1042-6

Gopalakrishnan, L., Satyanarayana, B., Chen, D., Wolswijk, G., Amir, A.A., Vandegehuchte, M.B., Muslim, A.B., Koedam, N., Dahdouh-Guebas, F., 2021. Using historical archives and landsat imagery to explore changes in the mangrove cover of Peninsular Malaysia between 1853 and 2018. *Remote Sensing* 13, 3403.

Gorelick, N., Hancher, M., Dixon, M., Ilyushchenko, S., Thau, D., Moore, R., 2017. Google Earth Engine: Planetary-scale geospatial analysis for everyone. *Remote Sensing of Environment*, Big Remotely Sensed Data: tools, applications and experiences 202, 18–27. https://doi.org/10.1016/j.rse.2017.06.031

Gridded Climate: NOAA Physical Sciences Laboratory [WWW Document], 2024. URL https://psl.noaa.gov/data/gridded/ (accessed 8.20.24).

Guyomard, H., Pinto-Correia, T., Rouet-Leduc, J., 2022. Why and how to support the supply of non-provisioning ecosystem services by European grasslands through the Common Agricultural Policy?

Haensel, M., Scheinpflug, L., Riebl, R., Lohse, E.J., Röder, N., Koellner, T., 2023. Policy instruments and their success in preserving temperate grassland: Evidence from 16 years of implementation. *Land Use Policy* 132, 106766. https://doi.org/10.1016/j.landusepol.2023.106766

Hák, T., Janoušková, S., Moldan, B., 2016. Sustainable Development Goals: A need for relevant indicators. *Ecological Indicators* 60, 565–573. https://doi.org/10.1016/j.ecolind.2015.08.003

Hamandawana, H., Atyosi, Y., Bornman, T.G., 2020. Multi-temporal reconstruction of long-term changes in land cover in and around the Swartkops River Estuary, Eastern Cape, South Africa. *Environ Monit Assess* 192, 173. https://doi.org/10.1007/s10661-020-8136-2

Han, X., Chen, X., Feng, L., 2015. Four decades of winter wetland changes in Poyang Lake based on Landsat observations between 1973 and 2013. *Remote Sensing of Environment* 156, 426–437. https://doi.org/10.1016/j.rse.2014.10.003

Hartman, B.D., Bookhagen, B., Chadwick, O.A., 2016. The effects of check dams and other erosion control structures on the restoration of Andean bofedal ecosystems. *Restoration Ecology* 24, 761–772. https://doi.org/10.1111/rec.12402

Hason, M.M., Abbood, I.S., Odaa, S. aldeen, 2020. Land cover reflectance of Iraqi marshlands based on visible spectral multiband of satellite imagery. *Results in Engineering* 8, 100167. https://doi.org/10.1016/j.rineng.2020.100167

He, T., Fu, Y., Ding, H., Zheng, W., Huang, X., Li, R., Wu, S., 2022. Evaluation of Mangrove Wetlands Protection Patterns in the Guangdong–Hong Kong–Macao Greater Bay Area Using Time-Series Landsat Imageries. *Remote Sensing* 14, 6026. https://doi.org/10.3390/rs14236026

He, X., Wei, H., 2023. Biodiversity conservation and ecological value of protected areas: a review of current situation and future prospects. *Front. Ecol. Evol.* 11. https://doi.org/10.3389/fevo.2023.1261265

Hemati, M., Hasanlou, M., Mahdianpari, M., Mohammadimanesh, F., 2021. A Systematic Review of Landsat Data for Change Detection Applications: 50 Years of Monitoring the Earth. *Remote Sensing* 13, 2869. https://doi.org/10.3390/rs13152869

Hermoso, V., Morán-Ordóñez, A., Brotons, L., 2018. Assessing the role of Natura 2000 at maintaining dynamic landscapes in Europe over the last two decades:

implications for conservation. *Landscape Ecol* 33, 1447–1460. https://doi.org/10.1007/s10980-018-0683-3

Hiernaux, P., Turner, M.D., Eggen, M., Marie, J., Haywood, M., 2021. Resilience of wetland vegetation to recurrent drought in the Inland Niger Delta of Mali from 1982 to 2014. *Wetlands Ecol Manage* 29, 945–967. https://doi.org/10.1007/s11273-021-09822-8

Hijmans, R., 2022. terra: Spatial Data Anaysis. R package.

Hijmans, R.J., 2024. terra: Spatial Data Analysis.

Ho, J.C., Stumpf, R.P., Bridgeman, T.B., Michalak, A.M., 2017. Using Landsat to extend the historical record of lacustrine phytoplankton blooms: A Lake Erie case study. *Remote Sensing of Environment* 191, 273–285. https://doi.org/10.1016/j.rse.2016.12.013

Hoffmann, S., 2022. Challenges and opportunities of area-based conservation in reaching biodiversity and sustainability goals. *Biodiversity and Conservation* 31, 325–352.

Hong, H.T.C., Avtar, R., Fujii, M., 2019. Monitoring changes in land use and distribution of mangroves in the southeastern part of the Mekong River Delta, Vietnam. *Trop Ecol* 60, 552–565. https://doi.org/10.1007/s42965-020-00053-1

Hotaiba, A.M., Salem, B.B., Halmy, M.W.A., 2024. Assessment of Wetland Ecosystem's Health Using Remote Sensing – Case Study: Burullus Wetland – Ramsar Site. *Estuaries and Coasts* 47, 201–215. https://doi.org/10.1007/s12237-023-01274-y

Hu, L., Li, W., Xu, B., 2018. Monitoring mangrove forest change in China from 1990 to 2015 using Landsat-derived spectral-temporal variability metrics. *International Journal of Applied Earth Observation and Geoinformation* 73, 88–98. https://doi.org/10.1016/j.jag.2018.04.001

Hu, S., Niu, Z., Chen, Y., Li, L., Zhang, H., 2017. Global wetlands: Potential distribution, wetland loss, and status. *Science of The Total Environment* 586, 319–327. https://doi.org/10.1016/j.scitotenv.2017.02.001

Huang, D., Xu, L., Zou, S., Liu, B., Li, H., Pu, L., Chi, H., 2024. Mapping Paddy Rice in Rice–Wetland Coexistence Zone by Integrating Sentinel-1 and Sentinel-2 Data. *Agriculture* 14, 345. https://doi.org/10.3390/agriculture14030345

Huang, L., Shao, Q., Liu, J., 2019. Assessing the conservation effects of nature reserve networks under climate variability over the northeastern Tibetan plateau. *Ecological Indicators* 96, 163–173. https://doi.org/10.1016/j.ecolind.2018.08.034

Huang, Y., Peng, J., Sun, W., Chen, N., Du, Q., Ning, Y., Su, H., 2022. Two-Branch Attention Adversarial Domain Adaptation Network for Hyperspectral Image Classification. *IEEE Transactions on Geoscience and Remote Sensing* 60, 1–13. https://doi.org/10.1109/TGRS.2022.3215677

Huete, A., Didan, K., Miura, T., Rodriguez, E.P., Gao, X., Ferreira, L.G., 2002. Overview of the radiometric and biophysical performance of the MODIS vegetation indices. *Remote Sensing of Environment*, The Moderate Resolution Imaging Spectroradiometer (MODIS): a new generation of Land Surface Monitoring 83, 195–213. https://doi.org/10.1016/S0034-4257(02)00096-2

Huo, H., Guo, J., Li, Z.-L., Jiang, X., 2017. Remote Sensing of Spatiotemporal Changes in Wetland Geomorphology Based on Type 2 Fuzzy Sets: A Case Study of Beidagang Wetland from 1975 to 2015. *Remote Sensing* 9, 683. https://doi.org/10.3390/rs9070683

Husson, F., Le, S., Pagès, J., 2017. Exploratory Multivariate Analysis by Example Using R. CRC Press.

IGN, SHOM, 2009. Trait de côte Histolitt – v2.0, Descriptif technique. Institut Géographique National.

Islam, Md.M., Borgqvist, H., Kumar, L., 2019. Monitoring Mangrove forest landcover changes in the coastline of Bangladesh from 1976 to 2015. *Geocarto International* 34, 1458–1476. https://doi.org/10.1080/10106049.2018.1489423

Ivory, S.J., McGlue, M.M., Spera, S., Silva, A., Bergier, I., 2019. Vegetation, rainfall, and pulsing hydrology in the Pantanal, the world's largest tropical wetland. *Environ. Res. Lett.* 14, 124017. https://doi.org/10.1088/1748-9326/ab4ffe

Jackson, K.R., Ramakrishnan, L., Muriki, K., Canon, S., Cholia, S., Shalf, J., Wasserman, H.J., Wright, N.J., 2010. Performance Analysis of High Performance Computing Applications on the Amazon Web Services Cloud, in: *2010 IEEE Second International Conference on Cloud Computing Technology and Science*. Presented at the 2010 IEEE Second International Conference on Cloud Computing Technology and Science, pp. 159–168. https://doi.org/10.1109/CloudCom.2010.69

Jafarzadeh, H., Mahdianpari, M., Gill, E.W., Brisco, B., Mohammadimanesh, F., 2022. Remote Sensing and Machine Learning Tools to Support Wetland Monitoring: A Meta-Analysis of Three Decades of Research. *Remote Sensing* 14, 6104. https://doi.org/10.3390/rs14236104

Jayanthi, M., Thirumurthy, S., Muralidhar, M., Ravichandran, P., 2018. Impact of shrimp aquaculture development on important ecosystems in India. *Global Environmental Change* 52, 10–21. https://doi.org/10.1016/j.gloenvcha.2018.05.005

Ji, Y., Sun, W., Wang, Y., Lv, Z., Yang, G., Zhan, Y., Li, C., 2024. Domain Adaptive and Interactive Differential Attention Network for Remote Sensing Image Change Detection. *IEEE Transactions on Geoscience and Remote Sensing* 62, 1–16. https://doi.org/10.1109/TGRS.2024.3382116

Jia, M., Liu, M., Wang, Z., Mao, D., Ren, C., Cui, H., 2016. Evaluating the Effectiveness of Conservation on Mangroves: A Remote Sensing-Based Comparison for Two

Adjacent Protected Areas in Shenzhen and Hong Kong, China. *Remote Sensing* 8, 627. https://doi.org/10.3390/rs8080627

Jia, P., Zhang, Y., Xu, W., Xia, Z., Zhong, C., Yin, Y., 2018. Spatio-temporal evolution of coastlines of sand-barrier lagoons over 26 years through historic Landsat imagery in Lingshui County, Hainan Province, China. *J Coast Conserv* 23, 817–827. https://doi.org/10.1007/s11852-018-0664-3

Jiang, Z., Huete, A.R., Didan, K., Miura, T., 2008. Development of a two-band enhanced vegetation index without a blue band. *Remote Sensing of Environment* 112, 3833–3845. https://doi.org/10.1016/j.rse.2008.06.006

Jie, L., Wang, J., 2024. Research on the extraction method of coastal wetlands based on sentinel-2 data. *Marine Environmental Research* 106429. https://doi.org/10.1016/j.marenvres.2024.106429

Jones, K., Lanthier, Y., van der Voet, P., van Valkengoed, E., Taylor, D., Fernandez-Prieto, D., 2009. Monitoring and assessment of wetlands using Earth Observation: The GlobWetland project. *Journal of Environmental Management* 90, 2154–2169. https://doi.org/doi: DOI: 10.1016/j.jenvman.2007.07.037

Jordan, Y.C., Ghulam, A., Herrmann, R.B., 2012. Floodplain ecosystem response to climate variability and land-cover and land-use change in Lower Missouri River basin. *Landscape Ecol* 27, 843–857. https://doi.org/10.1007/s10980-012-9748-x

Ju, J., Masek, J.G., 2016. The vegetation greenness trend in Canada and US Alaska from 1984–2012 Landsat data. *Remote Sensing of Environment* 176, 1–16. https://doi.org/10.1016/j.rse.2016.01.001

Kabiri, S., Allen, M., Okuonzia, J.T., Akello, B., Ssabaganzi, R., Mubiru, D., 2020. Detecting level of wetland encroachment for urban agriculture in Uganda using hyper-temporal remote sensing. https://doi.org/10.12688/aasopenres.13040.1

Karim, M., Maanan, Mehdi, Maanan, Mohamed, Rhinane, H., Rueff, H., Baidder, L., 2019. Assessment of water body change and sedimentation rate in Moulay Bousselham wetland, Morocco, using geospatial technologies. *International journal of sediment research* 34, 65–72.

Kawser, U., Hoque, A., Nath, B., 2021. Observing the impacts of 1950s great Assam earthquake in the tectono-geomorphological deformations at the Young Meghna Estuarine Floodplain of Bangladesh: evidence from Noakhali Coastal Region. *Arab J Geosci* 14, 306. https://doi.org/10.1007/s12517-020-06427-y

Kennedy, R.E., Yang, Z., Cohen, W.B., 2010. Detecting trends in forest disturbance and recovery using yearly Landsat time series: 1. LandTrendr — Temporal segmentation algorithms. *Remote Sensing of Environment* 114, 2897–2910. https://doi.org/10.1016/j.rse.2010.07.008

Kennedy, R.E., Yang, Z., Gorelick, N., Braaten, J., Cavalcante, L., Cohen, W.B., Healey, S., 2018. Implementation of the LandTrendr Algorithm on Google Earth Engine. *Remote Sensing* 10, 691. https://doi.org/10.3390/rs10050691

Key, C., Benson, N., 2006. Landscape Assessment: Ground measure of severity, the Composite Burn Index; and Remote sensing of severity, the Normalized Burn Ratio., in: *FIREMON: Fire Effects Monitoring and Inventory System*, General Technical Report. Ogden, UT, p. LA 1-51.

Kingsford, R.T., Bino, G., Finlayson, C.M., Falster, D., Fitzsimons, J.A., Gawlik, D.E., Murray, N.J., Grillas, P., Gardner, R.C., Regan, T.J., Roux, D.J., Thomas, R.F., 2021. Ramsar Wetlands of International Importance–Improving Conservation Outcomes. *Front. Environ. Sci.* 9. https://doi.org/10.3389/fenvs.2021.643367

Kleijn, D., Sutherland, W.J., 2003. How effective are European agri-environment schemes in conserving and promoting biodiversity? *Journal of Applied Ecology* 40, 947–969. https://doi.org/10.1111/j.1365-2664.2003.00868.x

Kolari, T.H., Sallinen, A., Wolff, F., Kumpula, T., Tolonen, K., Tahvanainen, T., 2021. Ongoing fen–bog transition in a boreal aapa mire inferred from repeated field sampling, aerial images, and Landsat data. *Ecosystems* 1–23.

Koshale, J.P., Mahato, A., 2020. Spatio-Temporal Change Detection and Its Impact on the Waterbodies by Monitoring LU/LC Dynamics-A Case Study from Holy City of Ratanpur, Chhattisgarh, India. *Nature Environment & Pollution Technology* 19.

Krapu, C., Kumar, M., Borsuk, M., 2018. Identifying Wetland Consolidation Using Remote Sensing in the North Dakota Prairie Pothole Region. *Water Resour. Res.* 54, 7478–7494. https://doi.org/10.1029/2018WR023338

Kubacka, M., Smaga, Ł., 2019. Effectiveness of Natura 2000 areas for environmental protection in 21 European countries. *Regional Environmental Change* 19, 2079–2088.

Kubacka, M., Żywica, P., Vila Subirós, J., Bródka, S., Macias, A., 2022. How do the surrounding areas of national parks work in the context of landscape fragmentation? A case study of 159 protected areas selected in 11 EU countries. *Land Use Policy* 113, 105910. https://doi.org/10.1016/j.landusepol.2021.105910

Kuleli, T., Guneroglu, A., Karsli, F., Dihkan, M., 2011. Automatic detection of shoreline change on coastal Ramsar wetlands of Turkey. *Ocean Engineering* 38, 1141–1149. https://doi.org/10.1016/j.oceaneng.2011.05.006

Laengner, M.L., Siteur, K., van der Wal, D., 2019. Trends in the Seaward Extent of Saltmarshes across Europe from Long-Term Satellite Data. *Remote Sensing* 11, 1653. https://doi.org/10.3390/rs11141653

Landsberg, H., Pinna, M., 1978. L’atmosfera e il clima. *UTET, Torino (I)*.

Lap, Q.K., Luong, V.N., Hong, X.T., Tu, T.T., Thanh, K.T.P., 2021. Evaluation of Mangrove Rehabilitation After Being Destroyed by Chemical Warfare Using Remote Sensing Technology: A Case Study in Can Gio Mangrove Forest in Mekong Delta, Southern Vietnam. *APPLIED ECOLOGY AND ENVIRONMENTAL RESEARCH* 19, 3897–3930.

Lautier, T., Meurisse, D., 2003. Tome 1 du Document d'objectifs Natura 2000 du site FR2300122 "Marais Vernier Risle Maritime" (Dir. Habitats) et du site FR2310044 "Estuaire et Marais de la Basse Seine" (dir. Oiseaux) sur sa partie recoupant le site Habitats. Parc Naturel Régional des Boucles de la Seine Normande.

Lê, S., Josse, J., Husson, F., 2008. FactoMineR: A Package for Multivariate Analysis. *Journal of Statistical Software* 25, 1–18. https://doi.org/10.18637/jss.v025.i01

Leberger, R., Rosa, I.M.D., Guerra, C.A., Wolf, F., Pereira, H.M., 2020. Global patterns of forest loss across IUCN categories of protected areas. *Biological Conservation* 241, 108299. https://doi.org/10.1016/j.biocon.2019.108299

Lehner, B., Döll, P., 2004. Development and validation of a global database of lakes, reservoirs and wetlands. *Journal of Hydrology* 296, 1–22. https://doi.org/10.1016/j.jhydrol.2004.03.028

Lenth, R.V., 2016. Least-Squares Means: The R Package lsmeans. *Journal of Statistical Software* 69, 1–33. https://doi.org/10.18637/jss.v069.i01

Levin, G., Frederiksen, P., Nainggolan, D., 2018. Land-use trends related to Natura2000 sites in Denmark. *Land Use Policy* 76, 432–441. https://doi.org/10.1016/j.landusepol.2018.02.018

Li, M.S., Mao, L.J., Shen, W.J., Liu, S.Q., Wei, A.S., 2013. Change and fragmentation trends of Zhanjiang mangrove forests in southern China using multi-temporal Landsat imagery (1977–2010). *Estuarine, Coastal and Shelf Science*, Pressures, Stresses, Shocks and Trends in Estuarine Ecosystems 130, 111–120. https://doi.org/10.1016/j.ecss.2013.03.023

Li, S., Xu, L., Jing, Y., Yin, H., Li, X., Guan, X., 2021. High-quality vegetation index product generation: A review of NDVI time series reconstruction techniques. *International Journal of Applied Earth Observation and Geoinformation* 105, 102640.

Liang, K., Li, Y., 2019. Changes in Lake Area in Response to Climatic Forcing in the Endorheic Hongjian Lake Basin, China. *Remote Sensing* 11, 3046. https://doi.org/10.3390/rs11243046

Liao, Z., Liu, X., van Dijk, A., Yue, C., He, B., 2022. Continuous woody vegetation biomass estimation based on temporal modeling of Landsat data. *International Journal of Applied Earth Observation and Geoinformation* 110, 102811. https://doi.org/10.1016/j.jag.2022.102811

Liljedahl, A.K., Boike, J., Daanen, R.P., Fedorov, A.N., Frost, G.V., Grosse, G., Hinzman, L.D., Iijma, Y., Jorgenson, J.C., Matveyeva, N., Necsoiu, M., Raynolds, M.K., Romanovsky, V.E., Schulla, J., Tape, K.D., Walker, D.A., Wilson, C.J., Yabuki, H., Zona, D., 2016. Pan-Arctic ice-wedge degradation in warming permafrost and its influence on tundra hydrology. *Nature Geosci* 9, 312–318. https://doi.org/10.1038/ngeo2674

Lin, Y., Yu, J., Cai, J., Sneeuw, N., Li, F., 2018. Spatio-Temporal Analysis of Wetland Changes Using a Kernel Extreme Learning Machine Approach. *Remote Sensing* 10, 1129. https://doi.org/10.3390/rs10071129

Lipp-Nissinen, K.H., de Sá Piñeiro, B., Miranda, L.S., de Paula Alves, A., 2018. Temporal dynamics of land use and cover in Paurá Lagoon region, Middle Coast of Rio Grande do Sul (RS), Brazil. *Journal of Integrated Coastal Zone Management* 18, 25–39.

Liu, K., Sun, W., Shao, Y., Liu, W., Yang, G., Meng, X., Peng, J., Mao, D., Ren, K., 2022. Mapping Coastal Wetlands Using Transformer in Transformer Deep Network on China ZY1-02D Hyperspectral Satellite Images. *IEEE Journal of Selected Topics in Applied Earth Observations and Remote Sensing* 15, 3891–3903. https://doi.org/10.1109/JSTARS.2022.3173349

Liu, M., Hu, D., 2019. Response of Wetland Evapotranspiration to Land Use/Cover Change and Climate Change in Liaohe River Delta, China. *Water* 11, 955. https://doi.org/10.3390/w11050955

Liu, M., Liu, S., Ning, Y., Zhu, Y., Valbuena, R., Guo, R., Li, Y., Tang, W., Mo, D., Rosa, I.M.D., Kutia, M., Hu, W., 2020. Co-Evolution of Emerging Multi-Cities: Rates, Patterns and Driving Policies Revealed by Continuous Change Detection and Classification of Landsat Data. *Remote Sensing* 12, 2905. https://doi.org/10.3390/rs12182905

Liu, N., Ma, Z., 2024. Ecological restoration of coastal wetlands in China: Current status and suggestions. *Biological Conservation* 291, 110513. https://doi.org/10.1016/j.biocon.2024.110513

Liu, Q., Zhang, Y., Liu, L., Wang, Z., Nie, Y., Rai, M.K., 2021. A novel Landsat-based automated mapping of marsh wetland in the headwaters of the Brahmaputra, Ganges and Indus Rivers, southwestern Tibetan Plateau. *International Journal of Applied Earth Observation and Geoinformation* 103, 102481. https://doi.org/10.1016/j.jag.2021.102481

Liu, Y., Liu, Yongxue, Li, J., Sun, C., Xu, W., Zhao, B., 2020. Trajectory of coastal wetland vegetation in Xiangshan Bay, China, from image time series. *Marine Pollution Bulletin* 160, 111697. https://doi.org/10.1016/j.marpolbul.2020.111697

Lock, M.C., Skidmore, A.K., van Duren, I., Mücher, C.A., 2021. Evidence-based alignment of conservation policies with remote sensing-enabled essential biodiversity variables. *Ecological Indicators* 132, 108272. https://doi.org/10.1016/j.ecolind.2021.108272

Long, C., Dai, Z., Zhou, X., Mei, X., Mai Van, C., 2021. Mapping mangrove forests in the Red River Delta, Vietnam. *Forest Ecology and Management* 483, 118910. https://doi.org/10.1016/j.foreco.2020.118910

Long, K., Chen, Z., Zhang, H., Zhang, M., 2024. Spatiotemporal disturbances and attribution analysis of mangrove in southern China from 1986 to 2020 based on time-series Landsat imagery. *Science of The Total Environment* 912, 169157. https://doi.org/10.1016/j.scitotenv.2023.169157

Lopes, C.L., Mendes, R., Caçador, I., Dias, J.M., 2019. Evaluation of long-term estuarine vegetation changes through Landsat imagery. *Science of The Total Environment* 653, 512–522. https://doi.org/10.1016/j.scitotenv.2018.10.381

Lopes, M., Fauvel, M., Girard, S., Sheeren, D., 2017. Object-based classification of grasslands from high resolution satellite image time series using Gaussian mean map kernels. *Remote Sensing* 9, 688.

Lu, M., Xiao, Z., 2024. Wetland ecology and climate change: Addressing global challenges with countermeasures. *Advances in Resources Research* 4, 67–88. https://doi.org/10.50908/arr.4.1_67

Lubke, M., Rengarajan, R., Choate, M., 2021. Preliminary assessment of the geometric improvements to the Landsat Collection-2 archive, in: *Earth Observing Systems XXVI*. SPIE, pp. 125–137.

Lucas, R., Van De Kerchove, R., Otero, V., Lagomasino, D., Fatoyinbo, L., Omar, H., Satyanarayana, B., Dahdouh-Guebas, F., 2020. Structural characterisation of mangrove forests achieved through combining multiple sources of remote sensing data. *Remote Sensing of Environment* 237, 111543. https://doi.org/10.1016/j.rse.2019.111543

Lukacz, P.M., 2024. Imaginaries of democratization and the value of open environmental data: Analysis of Microsoft's planetary computer. *Big Data & Society* 11, 20539517241242448. https://doi.org/10.1177/20539517241242448

Luo, J., Li, X., Ma, R., Li, F., Duan, H., Hu, W., Qin, B., Huang, W., 2016. Applying remote sensing techniques to monitoring seasonal and interannual changes of aquatic vegetation in Taihu Lake, China. *Ecological Indicators* 60, 503–513. https://doi.org/10.1016/j.ecolind.2015.07.029

Lv, J., Jiang, W., Wang, W., Wu, Z., Liu, Y., Wang, X., Li, Z., 2019. Wetland Loss Identification and Evaluation Based on Landscape and Remote Sensing Indices in Xiong'an New Area. *Remote Sensing* 11, 2834. https://doi.org/10.3390/rs11232834

Lymburner, L., Bunting, P., Lucas, R., Scarth, P., Alam, I., Phillips, C., Ticehurst, C., Held, A., 2020. Mapping the multi-decadal mangrove dynamics of the Australian coastline. *Remote Sensing of Environment* 238, 111185. https://doi.org/10.1016/j.rse.2019.05.004

Mabwoga, S.O., Thukral, A.K., 2014. Characterization of change in the Harike wetland, a Ramsar site in India, using landsat satellite data. *SpringerPlus* 3, 576. https://doi.org/10.1186/2193-1801-3-576

MacKay, H., Finlayson, C.M., Fernandez-Prieto, D., Davidson, N., Pritchard, D., Rebelo, L.-M., 2009. The role of Earth Observation (EO) technologies in supporting implementation of the Ramsar Convention on Wetlands. *Journal of Environmental Management* 90, 2234–2242. https://doi.org/doi: DOI: 10.1016/j.jenvman.2008.01.019

Mahdavi, S., Salehi, B., Granger, J., Amani, M., Brisco, B., Huang, W., 2018. Remote sensing for wetland classification: A comprehensive review. *GIScience & Remote Sensing* 55, 623–658.

Mahdianpari, Masoud, Granger, J.E., Mohammadimanesh, F., Salehi, B., Brisco, B., Homayouni, S., Gill, E., Huberty, B., Lang, M., 2020. Meta-Analysis of Wetland Classification Using Remote Sensing: A Systematic Review of a 40-Year Trend in North America. *Remote Sensing* 12, 1882. https://doi.org/10.3390/rs12111882

Mahdianpari, M., Jafarzadeh, H., Granger, J.E., Mohammadimanesh, F., Brisco, B., Salehi, B., Homayouni, S., Weng, Q., 2020. A large-scale change monitoring of wetlands using time series Landsat imagery on Google Earth Engine: a case study in Newfoundland. *GIScience & Remote Sensing* 57, 1102–1124. https://doi.org/10.1080/15481603.2020.1846948

Maltby, E., 2018. Functional Assessment of Wetlands, in: Finlayson, C.M., Everard, M., Irvine, K., McInnes, R.J., Middleton, B.A., van Dam, A.A., Davidson, N.C. (Eds.), *The Wetland Book: I: Structure and Function, Management, and Methods*. Springer Netherlands, Dordrecht, pp. 1729–1739. https://doi.org/10.1007/978-90-481-9659-3_293

Maltby, E., Barker, T., 2009. The Wetlands Handbook, Wiley-Blackwell. ed. Oxford.

Mao, D., Tian, Y., Wang, Z., Jia, M., Du, J., Song, C., 2021. Wetland changes in the Amur River Basin: Differing trends and proximate causes on the Chinese and Russian sides. *Journal of Environmental Management* 280, 111670. https://doi.org/10.1016/j.jenvman.2020.111670

Mao, L., Li, M., Shen, W., 2020. Remote Sensing Applications for Monitoring Terrestrial Protected Areas: Progress in the Last Decade. *Sustainability* 12, 5016. https://doi.org/10.3390/su12125016

Marais poitevin | Ramsar Sites Information Service [WWW Document], 2024. URL https://rsis.ramsar.org/ris/2531?language=en (accessed 8.19.24).

Martínez-López, J., Bertzky, B., Willcock, S., Robuchon, M., Almagro, M., Delli, G., Dubois, G., 2021. Remote sensing methods for the biophysical characterization of protected areas globally: challenges and opportunities. *ISPRS International Journal of Geo-Information* 10, 384.

Martorell, G., Rodríguez-Rodríguez, D., Millán, V.G., 2023. Long-term assessment of the effectiveness of coastal protection regulations in conserving natural habitats in Spain. *Ocean & Coastal Management* 239, 106601.

Marzvan, S., Moravej, K., Felegari, S., Sharifi, A., Askari, M.S., 2021. Risk Assessment of Alien Azolla filiculoides Lam in Anzali Lagoon Using Remote Sensing Imagery. *Journal of the Indian Society of Remote Sensing* 49, 1801–1809.

Masek, J.G., Wulder, M.A., Markham, B., McCorkel, J., Crawford, C.J., Storey, J., Jenstrom, D.T., 2020. Landsat 9: Empowering open science and applications through continuity. *Remote Sensing of Environment* 248, 111968. https://doi.org/10.1016/j.rse.2020.111968

Masria, A., El-Adawy, A.A., Sarhan, T., 2020. A holistic evaluation of human-induced LULCC and shoreline dynamics of El-Burullus Lagoon through remote sensing techniques. *Innov. Infrastruct. Solut.* 5, 83. https://doi.org/10.1007/s41062-020-00331-w

Mazzarino, M., Finn, J.T., 2016. An NDVI analysis of vegetation trends in an Andean watershed. *Wetlands Ecol Manage* 24, 623–640. https://doi.org/10.1007/s11273-016-9492-0

McInnes, R.J., Everard, M., 2017. Rapid Assessment of Wetland Ecosystem Services (RAWES): An example from Colombo, Sri Lanka. *Ecosystem Services* 25, 89–105. https://doi.org/10.1016/j.ecoser.2017.03.024

Mcowen, C.J., Weatherdon, L.V., Bochove, J.-W.V., Sullivan, E., Blyth, S., Zockler, C., Stanwell-Smith, D., Kingston, N., Martin, C.S., Spalding, M., Fletcher, S., 2017. A global map of saltmarshes. *Biodivers Data J* e11764. https://doi.org/10.3897/BDJ.5.e11764

MedWet [WWW Document], 2024. URL https://medwet.org/ (accessed 8.20.24).

Menne, M.J., Durre, I., Vose, R.S., Gleason, B.E., Houston, T.G., 2012. An Overview of the Global Historical Climatology Network-Daily Database. *Journal of Atmospheric and Oceanic Technology* 29, 897–910. https://doi.org/10.1175/JTECH-D-11-00103.1

Mexicano, L., Glenn, E.P., Hinojosa-Huerta, O., Garcia-Hernandez, J., Flessa, K., Hinojosa-Corona, A., 2013. Long-term sustainability of the hydrology and vegetation of Cienega de Santa Clara, an anthropogenic wetland created by disposal of agricultural drain water in the delta of the Colorado River, Mexico. *Ecological Engineering*, Colorado Delta Wetlands 59, 111–120. https://doi.org/10.1016/j.ecoleng.2012.12.096

Mialhe, F., Gunnell, Y., Navratil, O., Choi, D., Sovann, C., Lejot, J., Gaudou, B., Se, B., Landon, N., 2019. Spatial growth of Phnom Penh, Cambodia (1973–2015): Patterns, rates, and socio-ecological consequences. *Land Use Policy* 87, 104061. https://doi.org/10.1016/j.landusepol.2019.104061

Millennium Ecosystem Assessment, 2005. Ecosystems and Human Well-Being: Wetlands and Water. World Resources Institute, Washington D.C., USA.

Minotti, P.G., Rajngewerc, M., Alí Santoro, V., Grimson, R., 2021. Evaluation of SAR C-band interferometric coherence time-series for coastal wetland hydropattern mapping. *Journal of South American Earth Sciences* 106, 102976. https://doi.org/10.1016/j.jsames.2020.102976

Misra, A., R., M.M., P., V., 2015. Assessment of the land use/land cover (LU/LC) and mangrove changes along the Mandovi–Zuari estuarine complex of Goa, India. *Arab J Geosci* 8, 267–279. https://doi.org/10.1007/s12517-013-1220-y

Mitsch, W.J., Bernal, B., Nahlik, A.M., Mander, Ü., Zhang, L., Anderson, C.J., Jørgensen, S.E., Brix, H., 2013. Wetlands, carbon, and climate change. *Landscape Ecol* 28, 583–597. https://doi.org/10.1007/s10980-012-9758-8

Mitsch, W.J., Gosselink, J.G., 2015. Wetlands (5th Edition), John Wiley&Sons. ed.

Mo, Y., Kearney, M.S., Turner, R.E., 2020. The resilience of coastal marshes to hurricanes: The potential impact of excess nutrients. *Environment International* 138, 105409. https://doi.org/10.1016/j.envint.2019.105409

Moberg, T., Harrison, I., Dudley, N., Bastin, L., 2022. Post-2020 Global Biodiversity Framework: Support and a Pathway for Inland Water Ecosystems in the '30 by 30' Target, Monitoring Framework and Implementation.

Moher, D., Liberati, A., Tetzlaff, J., Altman, D.G., Group*, P., 2009. Preferred reporting items for systematic reviews and meta-analyses: the PRISMA statement. *Annals of internal medicine* 151, 264–269.

Mondal, D., Pal, S., 2016. Monitoring dual-season hydrological dynamics of seasonally flooded wetlands in the lower reach of Mayurakshi River, Eastern India. *Geocarto International* 33, 225–239. https://doi.org/10.1080/10106049.2016.1240720

Moomaw, W.R., Chmura, G.L., Davies, G.T., Finlayson, C.M., Middleton, B.A., Natali, S.M., Perry, J.E., Roulet, N., Sutton-Grier, A.E., 2018a. Wetlands In a Changing Climate: Science, Policy and Management. *Wetlands* 38, 183–205. https://doi.org/10.1007/s13157-018-1023-8

Moomaw, W.R., Chmura, G.L., Davies, G.T., Finlayson, C.M., Middleton, B.A., Natali, S.M., Perry, J.E., Roulet, N., Sutton-Grier, A.E., 2018b. Wetlands In a Changing Climate: Science, Policy and Management. *Wetlands* 38, 183–205. https://doi.org/10.1007/s13157-018-1023-8

Mozumder, C., Tripathi, N.K., Tipdecho, T., 2014. Ecosystem evaluation (1989–2012) of Ramsar wetland Deepor Beel using satellite-derived indices. *Environ Monit Assess* 186, 7909–7927. https://doi.org/10.1007/s10661-014-3976-2

Mutanga, O., Kumar, L., 2019. Google earth engine applications, Remote sensing. MDPI.

Myneni, R.B., Hall, F.G., Sellers, P.J., Marshak, A.L., 1995. The interpretation of spectral vegetation indexes. *IEEE Transactions on Geoscience and Remote Sensing* 33, 481–486. https://doi.org/10.1109/TGRS.1995.8746029

Ndayisaba, F., Nahayo, L., Guo, H., Bao, A., Kayiranga, A., Karamage, F., Nyesheja, E., 2017. Mapping and Monitoring the Akagera Wetland in Rwanda. *Sustainability* 9, 174. https://doi.org/10.3390/su9020174

Nemani, R., 2012. NASA Earth Exchange: Next Generation Earth Science Collaborative, in: *The International Archives of the Photogrammetry, Remote Sensing and Spatial Information Sciences*. Presented at the WG VIII/6, VIII/8
ISPRS Bhopal 2011 Workshop Earth Observation for Terrestrial Ecosystem (Volume XXXVIII-8/W20) - 8 November, Bhopal, India, Copernicus GmbH, pp. 17–17. https://doi.org/10.5194/isprsarchives-XXXVIII-8-W20-17-2011

Nguyen, H.-H., McAlpine, C., Pullar, D., Johansen, K., Duke, N.C., 2013. The relationship of spatial–temporal changes in fringe mangrove extent and adjacent land-use: Case study of Kien Giang coast, Vietnam. *Ocean & Coastal Management* 76, 12–22. https://doi.org/10.1016/j.ocecoaman.2013.01.003

NOAA, n.d. Gridded Climate: NOAA Physical Sciences Laboratory [WWW Document]. URL https://psl.noaa.gov/data/gridded/ (accessed 8.30.23).

Nosavan, J., Moreau, A., Henry, P., 2018. Spot world heritage: exploring the past, in: *Sensors, Systems, and Next-Generation Satellites XXII*. SPIE, pp. 124–129.

Oasis de Ouled Saïd | Ramsar Sites Information Service [WWW Document], 2023. URL https://rsis.ramsar.org/ris/1060 (accessed 3.9.23).

O'Donnell, J.P.R., Schalles, J.F., 2016. Examination of Abiotic Drivers and Their Influence on Spartina alterniflora Biomass over a Twenty-Eight Year Period Using Landsat 5 TM Satellite Imagery of the Central Georgia Coast. *Remote Sensing* 8, 477. https://doi.org/10.3390/rs8060477

Ojima, D.S., DeFries, R.S., Goward, S.N., Hansen, A., Hansen, M.C., Loveland, T., Skole, D., Vogeler, J., 2022. Landsat@50. *Frontiers in Ecology and the Environment* 20, 340–342. https://doi.org/10.1002/fee.2541

Olofsson, P., Foody, G.M., Herold, M., Stehman, S.V., Woodcock, C.E., Wulder, M.A., 2014. Good practices for estimating area and assessing accuracy of land change. *Remote Sensing of Environment* 148, 42–57. https://doi.org/10.1016/j.rse.2014.02.015

Olofsson, P., Foody, G.M., Stehman, S.V., Woodcock, C.E., 2013. Making better use of accuracy data in land change studies: Estimating accuracy and area and quantifying uncertainty using stratified estimation. *Remote Sensing of Environment* 129, 122–131. https://doi.org/10.1016/j.rse.2012.10.031

Otero, V., Van De Kerchove, R., Satyanarayana, B., Mohd-Lokman, H., Lucas, R., Dahdouh-Guebas, F., 2019. An Analysis of the Early Regeneration of Mangrove Forests using Landsat Time Series in the Matang Mangrove Forest Reserve, Peninsular Malaysia. *Remote Sensing* 11, 774. https://doi.org/10.3390/rs11070774

Ouisse, T., Barnier, F., 2021. Observatoire du patrimoine naturel du Marais poitevin : bilan et préconisations. UMS PatriNat - OFB / CNRS / MNHN, Paris, France.

Ouyang, Z., Becker, R., Shaver, W., Chen, J., 2014. Evaluating the sensitivity of wetlands to climate change with remote sensing techniques. *Hydrological Processes* 28, 1703–1712. https://doi.org/10.1002/hyp.9685

Palmieri, A., 2016. Integrating statistical and geographical information: LUCAS survey, a case study for land monitoring in European Union, in: *UNECE Conference of European Statisticians Workshop on Statistical Data Collection*.

Pan, F., Xie, J., Lin, J., Zhao, T., Ji, Y., Hu, Q., Pan, X., Wang, C., Xi, X., 2018. Evaluation of Climate Change Impacts on Wetland Vegetation in the Dunhuang Yangguan National Nature Reserve in Northwest China Using Landsat Derived NDVI. *Remote Sensing* 10, 735. https://doi.org/10.3390/rs10050735

Parihar, S.M., Sarkar, S., Dutta, A., Sharma, S., Dutta, T., 2013. Characterizing wetland dynamics: a post-classification change detection analysis of the East Kolkata Wetlands using open source satellite data. *Geocarto International* 28, 273–287. https://doi.org/10.1080/10106049.2012.705337

Parracciani, C., Gigante, D., Mutanga, O., Bonafoni, S., Vizzari, M., 2024. Land cover changes in grassland landscapes: Combining enhanced Landsat data composition, LandTrendr, and machine learning classification in google earth engine with MLP-ANN scenario forecasting. *GIScience & Remote Sensing* 61, 2302221.

Pasquarella, V.J., Arévalo, P., Bratley, K.H., Bullock, E.L., Gorelick, N., Yang, Z., Kennedy, R.E., 2022. Demystifying LandTrendr and CCDC temporal segmentation. *International Journal of Applied Earth Observation and Geoinformation* 110, 102806. https://doi.org/10.1016/j.jag.2022.102806

Paul, S., Pal, S., 2020. Exploring wetland transformations in moribund deltaic parts of India. *Geocarto International* 35, 1873–1894.

Pedreros-Guarda, M., Abarca-del-Río, R., Escalona, K., García, I., Parra, Ó., 2021. A Google Earth Engine Application to Retrieve Long-Term Surface Temperature for Small Lakes. Case: San Pedro Lagoons, Chile. *Remote Sensing* 13, 4544.

Peng, J., Liu, S., Lu, W., Liu, M., Feng, S., Cong, P., 2021. Continuous Change Mapping to Understand Wetland Quantity and Quality Evolution and Driving Forces: A Case Study in the Liao River Estuary from 1986 to 2018. *Remote Sensing* 13, 4900. https://doi.org/10.3390/rs13234900

Pereira, H.M., Ferrier, S., Walters, M., Geller, G.N., Jongman, R.H.G., Scholes, R.J., Bruford, M.W., Brummitt, N., Butchart, S.H.M., Cardoso, A.C., Coops, N.C., Dulloo, E., Faith, D.P., Freyhof, J., Gregory, R.D., Heip, C., Höft, R., Hurtt, G., Jetz, W., Karp, D.S., McGeoch, M.A., Obura, D., Onoda, Y., Pettorelli, N., Reyers, B., Sayre, R., Scharlemann, J.P.W., Stuart, S.N., Turak, E., Walpole, M., Wegmann, M., 2013. Essential Biodiversity Variables. *Science* 339, 277–278. https://doi.org/10.1126/science.1229931

Petit, T., Sigwalt, A., Martel, G., Couvreur, S., 2022. The Place of Grasslands in Cattle Farmers' Perceptions of Forage Production: Useful Insights of 10 Years of Empirical Research on Grasslands. *Sustainability* 14, 12309. https://doi.org/10.3390/su141912309

Pettorelli, N., Laurance, W.F., O'Brien, T.G., Wegmann, M., Nagendra, H., Turner, W., 2014. Satellite remote sensing for applied ecologists: opportunities and challenges. *Journal of Applied Ecology* 51, 839–848.

Pettorelli, N., Vik, J.O., Mysterud, A., Gaillard, J.-M., Tucker, C.J., Stenseth, N.Chr., 2005. Using the satellite-derived NDVI to assess ecological responses to environmental change. *Trends in Ecology & Evolution* 20, 503–510. https://doi.org/10.1016/j.tree.2005.05.011

Piao, S., Wang, X., Park, T., Chen, C., Lian, X., He, Y., Bjerke, J.W., Chen, A., Ciais, P., Tømmervik, H., Nemani, R.R., Myneni, R.B., 2020. Characteristics, drivers and feedbacks of global greening. *Nat Rev Earth Environ* 1, 14–27. https://doi.org/10.1038/s43017-019-0001-x

Pirali Zefrehei Ahmad Reza, Aliakba, H., Saeid, P., Omid, B.K., Rasoul, G., 2020. Detection and Prediction of Water Body and Aquatic Plants Cover Changes of Choghakhor International Wetland, Using Landsat Imagery and the Cellular Automata–Markov Model. *Contemp. Probl. Ecol.* 13, 545–555. https://doi.org/10.1134/S1995425520050091

Pirttimysvuoma | Ramsar Sites Information Service [WWW Document], n.d. URL https://rsis.ramsar.org/ris/2177?language=en (accessed 3.9.23).

Potapov, P., Li, X., Hernandez-Serna, A., Tyukavina, A., Hansen, M.C., Kommareddy, A., Pickens, A., Turubanova, S., Tang, H., Silva, C.E., Armston, J., Dubayah, R., Blair, J.B., Hofton, M., 2021. Mapping global forest canopy height through integration of GEDI and Landsat data. *Remote Sensing of Environment* 253, 112165. https://doi.org/10.1016/j.rse.2020.112165

Potapov, P.V., Turubanova, S.A., Hansen, M.C., Adusei, B., Broich, M., Altstatt, A., Mane, L., Justice, C.O., 2012. Quantifying forest cover loss in Democratic Republic of the Congo, 2000–2010, with Landsat ETM + data. *Remote Sensing of Environment*, Landsat Legacy Special Issue 122, 106–116. https://doi.org/10.1016/j.rse.2011.08.027

Pouzet, P., Creach, A., Godet, L., 2015. Dynamique de la démographie et du bâti dans l'ouest du Marais poitevin depuis 1705. *Norois. Environnement, aménagement, société* 83–96. https://doi.org/10.4000/norois.5589

Purdon, A., Mole, M.A., Selier, J., Kruger, J., Mafumo, H., Olivier, P.I., 2022. Using the Rao's Q diversity index as an indicator of protected area effectiveness in conserving biodiversity. *Ecological Informatics* 72, 101920.

QGIS Development Team, 2018. QGIS Version 2.18.22.

Qiu, P., Wu, N., Luo, P., Wang, Z., Li, M., 2009. Analysis of dynamics and driving factors of wetland landscape in Zoige, Eastern Qinghai-Tibetan Plateau. *J. Mt. Sci.* 6, 42–55. https://doi.org/10.1007/s11629-009-0230-4

Qiu, S., Zhu, Z., He, B., 2019. Fmask 4.0: Improved cloud and cloud shadow detection in Landsats 4–8 and Sentinel-2 imagery. *Remote Sensing of Environment* 231, 111205. https://doi.org/10.1016/j.rse.2019.05.024

R Core Team, 2022. R: A language and environment for statistical computing.

R. Core Team, 2019. A language and environment for statistical computing. Vienna, Austria: R Foundation for Statistical Computing; 2012. *URL https://www. R-project. org*.

Radeloff, V.C., Dubinin, M., Coops, N.C., Allen, A.M., Brooks, T.M., Clayton, M.K., Costa, G.C., Graham, C.H., Helmers, D.P., Ives, A.R., 2019. The dynamic habitat indices (dhis) from modis and global biodiversity. *Remote sensing of environment* 222, 204–214.

Rakotomavo, A., Fromard, F., 2010. Dynamics of mangrove forests in the Mangoky River delta, Madagascar, under the influence of natural and human factors. *Forest Ecology and Management* 259, 1161–1169. https://doi.org/10.1016/j.foreco.2010.01.002

Ramsar Convention on Wetlands, 2015. Scaling Up Wetland Conservation, Wise Use and Restoration to Achieve the Sustainable Developmenct Goals 2018 [WWW Document]. URL https://ramsar.org/sites/default/files/documents/library/cop12_res02_strategic_plan_e_0.pdf

Ramsar Convention Secretariat, 2024. The List of Wetlands of International Importance. Published 5 June 2024. Ramsar Convention Secretariat.

Ramsar Convention Secretariat, 2018. Global Wetland Outlook: State of the World's Wetlands and their Services to People. Ramsar Convention Secretariat, Gland, Switzerland.

Ramsar Convention Secretariat, 2016. The Fourth Ramsar Strategic Plan 2016-2024. (Ramsar handbooks for the wise use of wetlands, 5th edition, vol. 2). Ramsar Convention Secretariat, Gland, Switzerland.

Ramsar Convention Secretariat, 2006a. The Ramsar Convention manual: a guide to the Convention on Wetlands (Ramsar, Iran, 1971) (No. 4th Edition). Ramsar Convention Secretariat, Gland, Switzerland.

Ramsar Convention Secretariat, 2006b. The Ramsar Convention manual: a guide to the Convention on Wetlands (Ramsar, Iran, 1971) (No. 4th Edition). Ramsar Convention Secretariat, Gland, Switzerland.

Rapinel, S., Bouzillé, J.-B., Oszwald, J., Bonis, A., 2015. Use of bi-Seasonal Landsat-8 Imagery for Mapping Marshland Plant Community Combinations at the Regional Scale. *Wetlands* 35, 1043–1054. https://doi.org/10.1007/s13157-015-0693-8

Rapinel, S., Clément, B., Dufour, S., Hubert-Moy, L., 2018. Fine-Scale Monitoring of Long-term Wetland Loss Using LiDAR Data and Historical Aerial Photographs: the Example of the Couesnon Floodplain, France. *Wetlands* 38, 423–435. https://doi.org/10.1007/s13157-017-0985-2

Rapinel, S., Fabre, E., Dufour, S., Arvor, D., Mony, C., Hubert-Moy, L., 2019. Mapping potential, existing and efficient wetlands using free remote sensing data. *Journal of Environmental Management* 247, 829–839. https://doi.org/10.1016/j.jenvman.2019.06.098

Raynolds, M.K., Walker, D.A., 2016. Increased wetness confounds Landsat-derived NDVI trends in the central Alaska North Slope region, 1985–2011. *Environ. Res. Lett.* 11, 085004. https://doi.org/10.1088/1748-9326/11/8/085004

Rebelo, A.J., Scheunders, P., Esler, K.J., Meire, P., 2017. Detecting, mapping and classifying wetland fragments at a landscape scale. *Remote Sensing Applications: Society and Environment* 8, 212–223. https://doi.org/10.1016/j.rsase.2017.09.005

Rebelo, L.-M., Finlayson, C.M., Strauch, A., Rosenqvist, A., Perennou, C., Tottrup, C., Hilarides, L., Paganini, M., Wielaard, N., Siegert, F., 2018. The use of Earth Observation for wetland inventory, assessment and monitoring. *Ramsar Technical Report*.

Regnauld, H., Costa, S., Musereau, J., 2015. Spits on the French Atlantic and Channel Coasts: Morphological Behaviour and Present Management Policies, in: Randazzo, G., Jackson, D.W.T., Cooper, J.A.G. (Eds.), *Sand and Gravel Spits*. Springer International Publishing, Cham, pp. 247–258. https://doi.org/10.1007/978-3-319-13716-2_13

Reynaert, M., Souza-Rodrigues, E., van Benthem, A.A., 2024. The environmental impacts of protected area policy. *Regional Science and Urban Economics*, Urban Economics and the Environment 107, 103968. https://doi.org/10.1016/j.regsciurbeco.2023.103968

Richardson, J.T.E., 2011. Eta squared and partial eta squared as measures of effect size in educational research. *Educational Research Review* 6, 135–147. https://doi.org/10.1016/j.edurev.2010.12.001

Rivarola, M.D., Dein, J., Simberloff, D., Herrero, H.V., 2022. Assessing Protected Area Zoning Effectiveness With Remote Sensing Data: The Case of Nahuel Huapi National Park, Argentina. *Frontiers in Remote Sensing* 3, 901463.

Robert, S., Brosseau, O., 2022. Principaux types de données mis à disposition du public sur le site de l'Inventaire national du patrimoine naturel (INPN) : V2. (No. mnhn-04148916). PatriNat (OFB-CNRS-MNHN).

Rodier, F., 2023. Fabriquer la transition écologique et solidaire entre Etat et projets de territoire : étude de trois Contrats de Transition Ecologique (CTE) en territoire de montagne (phdthesis). Université Grenoble Alpes [2020-....].

Rodríguez-Rodríguez, D., Martínez-Vega, J., 2018. Effect of legal protection and management of protected areas at preventing land development: a Spanish case study. *Regional Environmental Change* 18, 2483–2494.

Rodríguez-Rodríguez, D., Martínez-Vega, J., Echavarría, P., 2019. A twenty year GIS-based assessment of environmental sustainability of land use changes in and around protected areas of a fast developing country: Spain. *International Journal of Applied Earth Observation and Geoinformation* 74, 169–179.

Rodríguez-Rodríguez, D., Sinoga, J.D., 2022. Moderate effectiveness of multiple-use protected areas as a policy tool for land conservation in Atlantic Spain in the past 30 years. *Land Use Policy* 112, 105801.

Rossi, R.E., Archer, S.K., Giri, C., Layman, C.A., 2020. The role of multiple stressors in a dwarf red mangrove (Rhizophora mangle) dieback. *Estuarine, Coastal and Shelf Science* 237, 106660. https://doi.org/10.1016/j.ecss.2020.106660

Rossiter, D.G., 2016. Digital Soil Resource Inventories: Status and Prospects in 2015, in: Zhang, G.-L., Brus, D., Liu, F., Song, X.-D., Lagacherie, P. (Eds.), *Digital Soil Mapping Across Paradigms, Scales and Boundaries*, Springer Environmental Science and Engineering. Springer, Singapore, pp. 275–286. https://doi.org/10.1007/978-981-10-0415-5_22

Rouveyrol, P., Prima, M.-C., 2024. Do agri-environmental schemes target effectively species, habitats and pressures in French Natura 2000 network? *Agriculture, Ecosystems & Environment* 373, 109114. https://doi.org/10.1016/j.agee.2024.109114

Salimi, S., Almuktar, S.A.A.A.N., Scholz, M., 2021. Impact of climate change on wetland ecosystems: A critical review of experimental wetlands. *Journal of Environmental Management* 286, 112160. https://doi.org/10.1016/j.jenvman.2021.112160

Sands, P., Lefevere, J., McDorman, T.L., Dommen, C., Tarasofsky, R., 1999. XI. Reports from International Courts and Tribunals. *Yearbook of International Environmental Law* 10, 621–652. https://doi.org/10.1093/yiel/10.1.621

Sarma, P.K., Lahkar, B.P., Ghosh, S., Rabha, A., Das, J.P., Nath, N.K., Dey, S., Brahma, N., 2008. Land-use and land-cover change and future implication analysis in Manas National Park, India using multi-temporal satellite data. *Current science* 223–227.

Sayre, R., Karagulle, D., Frye, C., Boucher, T., Wolff, N.H., Breyer, S., Wright, D., Martin, M., Butler, K., Van Graafeiland, K., Touval, J., Sotomayor, L., McGowan, J., Game, E.T., Possingham, H., 2020. An assessment of the representation of ecosystems in global protected areas using new maps of World Climate Regions and World Ecosystems. *Global Ecology and Conservation* 21, e00860. https://doi.org/10.1016/j.gecco.2019.e00860

Schaffer-Smith, D., Swenson, J.J., Barbaree, B., Reiter, M.E., 2017. Three decades of Landsat-derived spring surface water dynamics in an agricultural wetland mosaic; Implications for migratory shorebirds. *Remote Sensing of Environment* 193, 180–192. https://doi.org/10.1016/j.rse.2017.02.016

Schwatke, C., Scherer, D., Dettmering, D., 2019. Automated Extraction of Consistent Time-Variable Water Surfaces of Lakes and Reservoirs Based on Landsat and Sentinel-2. *Remote Sensing* 11, 1010. https://doi.org/10.3390/rs11091010

Shaeri Karimi, S., Saintilan, N., Wen, L., Cox, J., 2021. Spatio-temporal effects of inundation and climate on vegetation greenness dynamics in dryland floodplains. *Ecohydrology* e2378.

Shi, S., Chang, Y., Li, Y., Hu, Y., Liu, M., Ma, J., Xiong, Z., Wen, D., Li, B., Zhang, T., 2021. Using Time Series Optical and SAR Data to Assess the Impact of Historical Wetland Change on Current Wetland in Zhenlai County, Jilin Province, China. *Remote Sensing* 13, 4514.

Skidmore, A.K., Coops, N.C., Neinavaz, E., Ali, A., Schaepman, M.E., Paganini, M., Kissling, W.D., Vihervaara, P., Darvishzadeh, R., Feilhauer, H., Fernandez, M., Fernández, N., Gorelick, N., Geijzendorffer, I., Heiden, U., Heurich, M., Hobern, D., Holzwarth, S., Muller-Karger, F.E., Van De Kerchove, R., Lausch, A., Leitão, P.J., Lock, M.C., Mücher, C.A., O'Connor, B., Rocchini, D., Roeoesli, C., Turner, W., Vis, J.K., Wang, T., Wegmann, M., Wingate, V., 2021a. Priority list of biodiversity metrics to observe from space. *Nat Ecol Evol* 5, 896–906. https://doi.org/10.1038/s41559-021-01451-x

Skidmore, A.K., Coops, N.C., Neinavaz, E., Ali, A., Schaepman, M.E., Paganini, M., Kissling, W.D., Vihervaara, P., Darvishzadeh, R., Feilhauer, H., Fernandez, M., Fernández, N., Gorelick, N., Geijzendorffer, I., Heiden, U., Heurich, M., Hobern, D., Holzwarth, S., Muller-Karger, F.E., Van De Kerchove, R., Lausch, A., Leitão, P.J., Lock, M.C., Mücher, C.A., O'Connor, B., Rocchini, D., Roeoesli, C., Turner, W., Vis, J.K., Wang, T., Wegmann, M., Wingate, V., 2021b. Priority list of biodiversity metrics to observe from space. *Nat Ecol Evol* 5, 896–906. https://doi.org/10.1038/s41559-021-01451-x

Soliman, G.A.A., Soussa, H., 2011. Wetland change detection in Nile swamps of southern Sudan using multitemporal satellite imagery. *JARS* 5, 053517. https://doi.org/10.1117/1.3571009

Son, N.T., Thanh, B.X., Da, C.T., 2016. Monitoring Mangrove Forest Changes from Multi-temporal Landsat Data in Can Gio Biosphere Reserve, Vietnam. *Wetlands* 36, 565–576. https://doi.org/10.1007/s13157-016-0767-2

Souchère, V., King, C., Dubreuil, N., Lecomte-Morel, V., Le Bissonnais, Y., Chalat, M., 2003. Grassland and crop trends: role of the European Union Common Agricultural Policy and consequences for runoff and soil erosion. *Environmental Science & Policy*, Socio-economic Factors in Soil Erosion and Conservation 6, 7–16. https://doi.org/10.1016/S1462-9011(02)00121-1

Souza Jr, C.M., Roberts, D.A., Cochrane, M.A., 2005. Combining spectral and spatial information to map canopy damage from selective logging and forest fires. *Remote Sensing of Environment* 98, 329–343.

Stehman, S.V., Foody, G.M., 2019. Key issues in rigorous accuracy assessment of land cover products. *Remote Sensing of Environment* 231, 111199. https://doi.org/10.1016/j.rse.2019.05.018

Strauch, A., Bunting, P., Campbell, J., Cornish, N., Eberle, J., Fatoyinbo, T., Franke, J., Hentze, K., Lagomasino, D., Lucas, R., Paganini, M., Rebelo, L.-M., Riffler, M., Rosenqvist, A., Steinbach, S., Thonfeld, F., Tottrup, C., 2022a. The Fate of Wetlands: Can the View From Space Help Us to Stop and Reverse Their Global Decline?, in: *Earth Observation Applications and Global Policy Frameworks*. American Geophysical Union (AGU), pp. 85–104. https://doi.org/10.1002/9781119536789.ch5

Strauch, A., Bunting, P., Campbell, J., Cornish, N., Eberle, J., Fatoyinbo, T., Franke, J., Hentze, K., Lagomasino, D., Lucas, R., Paganini, M., Rebelo, L.-M., Riffler, M., Rosenqvist, A., Steinbach, S., Thonfeld, F., Tottrup, C., 2022b. The Fate of Wetlands, in: *Earth Observation Applications and Global Policy Frameworks*. American Geophysical Union (AGU), pp. 85–104. https://doi.org/10.1002/9781119536789.ch5

Street, J.O., Carroll, R.J., Ruppert, D., 1988. A Note on Computing Robust Regression Estimates via Iteratively Reweighted Least Squares. *The American Statistician* 42, 152–154. https://doi.org/10.1080/00031305.1988.10475548

Stroud, D.A., Davidson, N.C., 2021. Fifty years of criteria development for selecting wetlands of international importance. *Mar. Freshwater Res.* 73, 1134–1148. https://doi.org/10.1071/MF21190

Sun, C., Fagherazzi, S., Liu, Y., 2018. Classification mapping of salt marsh vegetation by flexible monthly NDVI time-series using Landsat imagery. *Estuarine, Coastal and Shelf Science* 213, 61–80. https://doi.org/10.1016/j.ecss.2018.08.007

Sun, W., Liu, K., Ren, G., Liu, W., Yang, G., Meng, X., Peng, J., 2021. A simple and effective spectral-spatial method for mapping large-scale coastal wetlands using China ZY1-02D satellite hyperspectral images. *International Journal of Applied Earth Observation and Geoinformation* 104, 102572. https://doi.org/10.1016/j.jag.2021.102572

Tahsin, S., Medeiros, S.C., Singh, A., 2019. Wetland Dynamics Inferred from Spectral Analyses of Hydro-Meteorological Signals and Landsat Derived Vegetation Indices. *Remote Sensing* 12, 12. https://doi.org/10.3390/rs12010012

Talukdar, G., Sarma, A.K., Bhattacharjya, R.K., 2020. Mapping agricultural activities and their temporal variations in the riverine ecosystem of the Brahmaputra River using geospatial techniques. *Remote Sensing Applications: Society and Environment* 20, 100423. https://doi.org/10.1016/j.rsase.2020.100423

Tang, Z., Li, Y., Gu, Y., Jiang, W., Xue, Y., Hu, Q., LaGrange, T., Bishop, A., Drahota, J., Li, R., 2016. Assessing Nebraska playa wetland inundation status during 1985–2015 using Landsat data and Google Earth Engine. *Environ Monit Assess* 188, 654. https://doi.org/10.1007/s10661-016-5664-x

Taravat, A., Rajaei, M., Emadodin, I., Hasheminejad, H., Mousavian, R., Biniyaz, E., 2016. A Spaceborne Multisensory, Multitemporal Approach to Monitor Water Level and Storage Variations of Lakes. *Water* 8, 478. https://doi.org/10.3390/w8110478

The Ramsar Convention on Wetlands [WWW Document], 2024. URL https://www.ramsar.org/ (accessed 8.20.24).

Thomas, R.F., Kingsford, R.T., Lu, Y., Hunter, S.J., 2011. Landsat mapping of annual inundation (1979–2006) of the Macquarie Marshes in semi-arid Australia. *International Journal of Remote Sensing* 32, 4545–4569. https://doi.org/10.1080/01431161.2010.489064

Tian, Y., Luo, L., Mao, D., Wang, Z., Li, L., Liang, J., 2017. Using Landsat images to quantify different human threats to the Shuangtai Estuary Ramsar site, China. *Ocean & Coastal Management* 135, 56–64. https://doi.org/10.1016/j.ocecoaman.2016.11.011

Tibshirani, R., 1996. Regression Shrinkage and Selection Via the Lasso. *Journal of the Royal Statistical Society: Series B (Methodological)* 58, 267–288. https://doi.org/10.1111/j.2517-6161.1996.tb02080.x

Tin, H.C., Ni, T.N.K., Tuan, L.V., Saizen, I., Catherman, R., 2019. Spatial and temporal variability of mangrove ecosystems in the Cu Lao Cham-Hoi An Biosphere

Reserve, Vietnam. *Regional Studies in Marine Science* 27, 100550. https://doi.org/10.1016/j.rsma.2019.100550

Tindale, S., Cao, Y., Jin, S., Green, O., Burd, M., Vicario-Modrono, V., Alonso, N., Clingo, S., Gallardo-Cobos, R., Sanchez-Zamora, P., 2024. Tipping points and farmer decision-making in European permanent grassland (PG) agricultural systems. *Journal of Rural Studies* 110, 103364.

Tiné, M., Perez, L., Molowny-Horas, R., Darveau, M., 2019. Hybrid spatiotemporal simulation of future changes in open wetlands: A study of the Abitibi-Témiscamingue region, Québec, Canada. *International Journal of Applied Earth Observation and Geoinformation* 74, 302–313. https://doi.org/10.1016/j.jag.2018.10.001

Tootchi, A., Jost, A., Ducharne, A., 2018. Multi-source global wetland maps combining surface water imagery and groundwater constraints. *Sorbonne Université, Paris, France*. https://doi.org/10.1594/PANGAEA.892657

Tope-Ajayi, O.O., Adedeji, O.H., Adeofun, C.O., Awokola, S.O., 2016. Land use change assessment, prediction using remote sensing, and gis aided markov chain modelling at eleyele wetland area, Nigeria. *Journal of Settlements and Spatial Planning* 7, 51–63.

Tortini, R., Noujdina, N., Yeo, S., Ricko, M., Birkett, C.M., Khandelwal, A., Kumar, V., Marlier, M.E., Lettenmaier, D.P., 2020. Satellite-based remote sensing data set of global surface water storage change from 1992 to 2018. *Earth System Science Data* 12, 1141–1151. https://doi.org/10.5194/essd-12-1141-2020

Tran Thi, V., Tien Thi Xuan, A., Phan Nguyen, H., Dahdouh-Guebas, F., Koedam, N., 2014. Application of remote sensing and GIS for detection of long-term mangrove shoreline changes in Mui Ca Mau, Vietnam. *Biogeosciences* 11, 3781–3795. https://doi.org/10.5194/bg-11-3781-2014

Tuholske, C., Tane, Z., López-Carr, D., Roberts, D., Cassels, S., 2017. Thirty years of land use/cover change in the Caribbean: Assessing the relationship between urbanization and mangrove loss in Roatán, Honduras. *Applied Geography* 88, 84–93. https://doi.org/10.1016/j.apgeog.2017.08.018

Umarhadi, D.A., Widyatmanti, W., Kumar, P., Yunus, A.P., Khedher, K.M., Kharrazi, A., Avtar, R., 2022. Tropical peat subsidence rates are related to decadal LULC changes: Insights from InSAR analysis. *Science of The Total Environment* 816, 151561. https://doi.org/10.1016/j.scitotenv.2021.151561

UNEP-WCMC, IUCN, 2024. Protected Planet: The World Database on Protected Areas (WDPA) and World Database on Other Effective Area-based Conservation Measures (WD-OECM). URL www.protectedplanet.net (accessed 5.5.24).

United Nations, 2015. Transforming our World: The 2030 Agenda for Sustainable Development. Outcome Document for the UN Summit to Adopt the Post-2015 Development Agenda. New York, NY, USA.

Ursu, A., Stoleriu, C.C., Ion, C., Jitariu, V., Enea, A., 2020. Romanian natura 2000 network: Evaluation of the threats and pressures through the Corine land cover dataset. *Remote Sensing* 12, 2075.

USGS, 2021. Landsat collection 2 (Report No. 2021–3002), Fact Sheet. Reston, VA. https://doi.org/10.3133/fs20213002

Uthes, S., Matzdorf, B., 2013. Studies on Agri-environmental Measures: A Survey of the Literature. *Environmental Management* 51, 251–266. https://doi.org/10.1007/s00267-012-9959-6

Uuemaa, E., Ahi, S., Montibeller, B., Muru, M., Kmoch, A., 2020. Vertical Accuracy of Freely Available Global Digital Elevation Models (ASTER, AW3D30, MERIT, TanDEM-X, SRTM, and NASADEM). *Remote Sensing* 12, 3482. https://doi.org/10.3390/rs12213482

Van Alphen, R., Rains, K.C., Rodgers, M., Malservisi, R., Dixon, T.H., 2024. UAV-Based Wetland Monitoring: Multispectral and Lidar Fusion with Random Forest Classification. *Drones* 8, 113. https://doi.org/10.3390/drones8030113

Vanden Borre, J., Paelinckx, D., Mücher, C.A., Kooistra, L., Haest, B., De Blust, G., Schmidt, A.M., 2011. Integrating remote sensing in Natura 2000 habitat monitoring: Prospects on the way forward. *Journal for Nature Conservation* 19, 116–125. https://doi.org/10.1016/j.jnc.2010.07.003

Vanderhoof, M.K., Lane, C.R., McManus, M.G., Alexander, L.C., Christensen, J.R., 2018. Wetlands inform how climate extremes influence surface water expansion and contraction. *Hydrol. Earth Syst. Sci.* 22, 1851–1873. https://doi.org/10.5194/hess-22-1851-2018

Vannoppen, A., Degerickx, J., Souverijns, N., Gobin, A., 2023. Spatio-Temporal Dynamics in Grasslands Using the Landsat Archive. *Land* 12, 934. https://doi.org/10.3390/land12040934

Veettil, B.K., Florêncio de Souza, S., Simões, J.C., Ruiz Pereira, S.F., 2017. Decadal evolution of glaciers and glacial lakes in the Apolobamba–Carabaya region, tropical Andes (Bolivia–Peru). *Geografiska Annaler: Series A, Physical Geography* 99, 193–206. https://doi.org/10.1080/04353676.2017.1299577

Verbesselt, J., Hyndman, R., Newnham, G., Culvenor, D., 2010. Detecting trend and seasonal changes in satellite image time series. *Remote Sensing of Environment* 114, 106–115. https://doi.org/10.1016/j.rse.2009.08.014

Villate Daza, D.A., Sánchez Moreno, H., Portz, L., Portantiolo Manzolli, R., Bolívar-Anillo, H.J., Anfuso, G., 2020. Mangrove Forests Evolution and Threats in the Caribbean Sea of Colombia. *Water* 12, 1113. https://doi.org/10.3390/w12041113

Viñuales, J.E., 2016. The Paris Agreement on Climate Change. *German YB Int'l L.* 59, 11.

Wang, H., Zhou, Y., Wu, J., Wang, C., Zhang, R., Xiong, X., Xu, C., 2023. Human activities dominate a staged degradation pattern of coastal tidal wetlands in Jiangsu province, China. *Ecological Indicators* 154, 110579. https://doi.org/10.1016/j.ecolind.2023.110579

Wang, P., Numbere, A.O., Camilo, G.R., 2016. Long-Term Changes in Mangrove Landscape of the Niger River Delta, Nigeria. *American Journal of Environmental Sciences* 12, 248–259. https://doi.org/10.3844/ajessp.2016.248.259

Wang, X., Xiao, X., Xu, X., Zou, Z., Chen, B., Qin, Y., Zhang, X., Dong, J., Liu, D., Pan, L., Li, B., 2021. Rebound in China's coastal wetlands following conservation and restoration. *Nat Sustain* 4, 1076–1083. https://doi.org/10.1038/s41893-021-00793-5

Weise, K., Höfer, R., Franke, J., Guelmami, A., Simonson, W., Muro, J., O'Connor, B., Strauch, A., Flink, S., Eberle, J., Mino, E., Thulin, S., Philipson, P., van Valkengoed, E., Truckenbrodt, J., Zander, F., Sánchez, A., Schröder, C., Thonfeld, F., Fitoka, E., Scott, E., Ling, M., Schwarz, M., Kunz, I., Thürmer, G., Plasmeijer, A., Hilarides, L., 2020. Wetland extent tools for SDG 6.6.1 reporting from the Satellite-based Wetland Observation Service (SWOS). *Remote Sensing of Environment* 247, 111892. https://doi.org/10.1016/j.rse.2020.111892

Wells, A.F., Frost, G.V., Macander, M.J., Jorgenson, M.T., Roth, J.E., Davis, W.A., Pullman, E.R., 2021. Integrated terrain unit mapping on the Beaufort Coastal Plain, North Slope, Alaska, USA. *Landscape Ecol* 36, 549–579. https://doi.org/10.1007/s10980-020-01154-x

Wen, L., Mason, T.J., Ryan, S., Ling, J.E., Saintilan, N., Rodriguez, J., 2023. Monitoring long-term vegetation condition dynamics in persistent semi-arid wetland communities using time series of Landsat data. *Science of The Total Environment* 905, 167212. https://doi.org/10.1016/j.scitotenv.2023.167212

Wheeler, B., Torchiano, M., Torchiano, M.M., 2016. Package 'lmPerm.' *R package version* 1.1-2.

Wilson, N.R., Norman, L.M., 2018. Analysis of vegetation recovery surrounding a restored wetland using the normalized difference infrared index (NDII) and normalized difference vegetation index (NDVI). *International Journal of Remote Sensing* 39, 3243–3274.

Woodcock, C.E., Allen, R., Anderson, M., Belward, A., Bindschadler, R., Cohen, W., Gao, F., Goward, S.N., Helder, D., Helmer, E., Nemani, R., Oreopoulos, L., Schott, J., Thenkabail, P.S., Vermote, E.F., Vogelmann, J., Wulder, M.A., Wynne, R., 2008. Free Access to Landsat Imagery. *Science* 320, 1011–1011. https://doi.org/10.1126/science.320.5879.1011a

Wu, W., Zhao, Z., Mao, Y., 2015. A comparative study on the dynamics and geologic conditions of wetlands in Shangri-La County and Lijiang City in northwestern Yunnan plateau. *International Journal of Sustainable Development & World Ecology* 22, 151–155. https://doi.org/10.1080/13504509.2014.925520

Wu, Y., Xiao, X., Chen, B., Ma, J., Wang, X., Zhang, Y., Zhao, B., Li, B., 2018. Tracking the phenology and expansion of Spartina alterniflora coastal wetland by time series MODIS and Landsat images. *Multimed Tools Appl* 79, 5175–5195. https://doi.org/10.1007/s11042-018-6314-9

Wuepper, D., Wiebecke, I., Meier, L., Vogelsanger, S., Bramato, S., Fürholz, A., Finger, R., 2024. Agri-environmental policies from 1960 to 2022. *Nat Food* 5, 323–331. https://doi.org/10.1038/s43016-024-00945-8

Wulder, M.A., Li, Z., Campbell, E.M., White, J.C., Hobart, G., Hermosilla, T., Coops, N.C., 2018. A national assessment of wetland status and trends for Canada's forested ecosystems using 33 years of earth observation satellite data. *Remote Sensing* 10, 1623.

Wulder, M.A., Loveland, T.R., Roy, D.P., Crawford, C.J., Masek, J.G., Woodcock, C.E., Allen, R.G., Anderson, M.C., Belward, A.S., Cohen, W.B., Dwyer, J., Erb, A., Gao, F., Griffiths, P., Helder, D., Hermosilla, T., Hipple, J.D., Hostert, P., Hughes, M.J., Huntington, J., Johnson, D.M., Kennedy, R., Kilic, A., Li, Z., Lymburner, L., McCorkel, J., Pahlevan, N., Scambos, T.A., Schaaf, C., Schott, J.R., Sheng, Y., Storey, J., Vermote, E., Vogelmann, J., White, J.C., Wynne, R.H., Zhu, Z., 2019. Current status of Landsat program, science, and applications. *Remote Sensing of Environment* 225, 127–147. https://doi.org/10.1016/j.rse.2019.02.015

Wulder, M.A., Masek, J.G., Cohen, W.B., Loveland, T.R., Woodcock, C.E., 2012. Opening the archive: How free data has enabled the science and monitoring promise of Landsat. *Remote Sensing of Environment*, Landsat Legacy Special Issue 122, 2–10. https://doi.org/10.1016/j.rse.2012.01.010

Wulder, M.A., Roy, D.P., Radeloff, V.C., Loveland, T.R., Anderson, M.C., Johnson, D.M., Healey, S., Zhu, Z., Scambos, T.A., Pahlevan, N., Hansen, M., Gorelick, N., Crawford, C.J., Masek, J.G., Hermosilla, T., White, J.C., Belward, A.S., Schaaf, C., Woodcock, C.E., Huntington, J.L., Lymburner, L., Hostert, P., Gao, F., Lyapustin, A., Pekel, J.-F., Strobl, P., Cook, B.D., 2022. Fifty years of Landsat science and impacts. *Remote Sensing of Environment* 280, 113195. https://doi.org/10.1016/j.rse.2022.113195

Wulder, M.A., White, J.C., Loveland, T.R., Woodcock, C.E., Belward, A.S., Cohen, W.B., Fosnight, E.A., Shaw, J., Masek, J.G., Roy, D.P., 2016. The global Landsat archive: Status, consolidation, and direction. *Remote Sensing of Environment*, Landsat 8 Science Results 185, 271–283. https://doi.org/10.1016/j.rse.2015.11.032

Xian, G.Z., Smith, K., Wellington, D., Horton, J., Zhou, Q., Li, C., Auch, R., Brown, J.F., Zhu, Z., Reker, R.R., 2022. Implementation of the CCDC algorithm to produce the LCMAP Collection 1.0 annual land surface change product. *Earth System Science Data* 14, 143–162. https://doi.org/10.5194/essd-14-143-2022

Xie, C., Huang, X., Mu, H., Yin, W., 2017. Impacts of Land-Use Changes on the Lakes across the Yangtze Floodplain in China. *Environ. Sci. Technol.* 51, 3669–3677. https://doi.org/10.1021/acs.est.6b04260

Xie, S., Liu, L., Zhang, X., Yang, J., 2022. Mapping the annual dynamics of land cover in Beijing from 2001 to 2020 using Landsat dense time series stack. *ISPRS Journal of Photogrammetry and Remote Sensing* 185, 201–218. https://doi.org/10.1016/j.isprsjprs.2022.01.014

Xie, Z., Liu, J., Ma, Z., Duan, X., Cui, Y., 2012. Effect of surrounding land-use change on the wetland landscape pattern of a natural protected area in Tianjin, China. *International Journal of Sustainable Development & World Ecology* 19, 16–24. https://doi.org/10.1080/13504509.2011.583697

Xu, J., Morris, P.J., Liu, J., Holden, J., 2018. PEATMAP: Refining estimates of global peatland distribution based on a meta-analysis. *CATENA* 160, 134–140. https://doi.org/10.1016/j.catena.2017.09.010

Xu, X., Chen, M., Yang, G., Jiang, B., Zhang, J., 2020. Wetland ecosystem services research: A critical review. *Global Ecology and Conservation* 22, e01027. https://doi.org/10.1016/j.gecco.2020.e01027

Yan, D., Li, J., Yao, X., Luan, Z., 2021. Quantifying the Long-Term Expansion and Dieback of Spartina Alterniflora Using Google Earth Engine and Object-Based Hierarchical Random Forest Classification. *IEEE Journal of Selected Topics in Applied Earth Observations and Remote Sensing* 14, 9781–9793.

Yang, L., Wang, Lunche, Yu, D., Yao, R., Li, C., He, Q., Wang, S., Wang, Lizhe, 2020. Four decades of wetland changes in Dongting Lake using Landsat observations during 1978–2018. *Journal of Hydrology* 587, 124954. https://doi.org/10.1016/j.jhydrol.2020.124954

Yang, R., Chen, Y., Qiu, Y., Lu, K., Wang, X., Sun, G., Liang, Q., Song, H., Liu, S., 2023. Assessing the Landscape Ecological Health (LEH) of Wetlands: Research Content and Evaluation Methods (2000–2022). *Water* 15, 2410. https://doi.org/10.3390/w15132410

Yang, X., Zhu, Zhe, Qiu, S., Kroeger, K.D., Zhu, Zhiliang, Covington, S., 2022. Detection and characterization of coastal tidal wetland change in the northeastern US using Landsat time series. *Remote Sensing of Environment* 276, 113047. https://doi.org/10.1016/j.rse.2022.113047

Ye, S., Zhu, Z., Cao, G., 2023. Object-based continuous monitoring of land disturbances from dense Landsat time series. *Remote Sensing of Environment* 287, 113462. https://doi.org/10.1016/j.rse.2023.113462

Yi, Q., Huixin, G., Yaomin, Z., Jinlian, S., Xingyu, Z., Huize, Y., Jiaxin, W., Zhenguo, N., Liping, L., Shudong, W., Tianjie, Z., Yue, C., Zongming, W., Dehua, M., Mingming, J., Ke, G., Peng, G., Guofa, C., Xiankai, H., 2024. Global conservation priorities for wetlands and setting post-2025 targets. *Commun Earth Environ* 5, 1–11. https://doi.org/10.1038/s43247-023-01195-5

Yushanjiang, A., Zhang, F., Kung, H., Li, Z., 2018. Spatial–temporal variation of ecosystem service values in Ebinur Lake Wetland National Natural Reserve from 1972 to 2016, Xinjiang, arid region of China. *Environ Earth Sci* 77, 586. https://doi.org/10.1007/s12665-018-7764-0

Zanaga, D., Van De Kerchove, R., Daems, D., De Keersmaecker, W., Brockmann, C., Kirches, G., Wevers, J., Cartus, O., Santoro, M., Fritz, S., Lesiv, M., Herold, M., Tsendbazar, N.-E., Xu, P., Ramoino, F., Arino, O., 2022. ESA WorldCover 10 m 2021 v200. https://doi.org/10.5281/zenodo.7254221

Zefrehei, A.R.P., Fallah, M., Hedayati, A., 2021. Applying remote sensing techniques to changes of water body and aquatic plants in Anzali International Wetland (1985-2018). *Theoretical and Applied Ecology* 65–72.

Zefrehei, A.R.P., Hedayati, A., Pourmanafi, S., Kashkooli, O.B., Ghorbani, R., 2020. Monitoring spatiotemporal variability of water quality parameters Using Landsat imagery in Choghakhor International Wetland during the last 32 years. *Ann. Limnol. - Int. J. Lim.* 56, 6. https://doi.org/10.1051/limn/2020004

Zelelew, S.A., Abebe, W.B., Amsalu, T., 2021. Land-use cover change impact on Cranes nesting space in the Lake Tana Biosphere Reserve area, Blue Nile Basin. *Wetlands Ecol Manage* 29, 495–505. https://doi.org/10.1007/s11273-021-09796-7

Zhang, C., Xiao, X., Wang, X., Qin, Y., Doughty, R., Yang, X., Meng, C., Yao, Y., Dong, J., 2024. Mapping wetlands in Northeast China by using knowledge-based algorithms and microwave (PALSAR-2, Sentinel-1), optical (Sentinel-2, Landsat), and thermal (MODIS) images. *Journal of Environmental Management* 349, 119618. https://doi.org/10.1016/j.jenvman.2023.119618

Zhang, K., Thapa, B., Ross, M., Gann, D., 2016. Remote sensing of seasonal changes and disturbances in mangrove forest: a case study from South Florida. *Ecosphere* 7, e01366. https://doi.org/10.1002/ecs2.1366

Zhang, L., Wu, Z., Chen, J., Liu, D., Chen, P., 2022. Spatiotemporal patterns and drivers of net primary production in the terrestrial ecosystem of the Dajiuhu Basin, China, between 1990 and 2018. *Ecological Informatics* 72, 101839. https://doi.org/10.1016/j.ecoinf.2022.101839

Zhang, S., Na, X., Kong, B., Wang, Z., Jiang, H., Yu, H., Zhao, Z., Li, X., Liu, C., Dale, P., 2009. Identifying wetland change in China's Sanjiang Plain using remote sensing. *Wetlands* 29, 302. https://doi.org/10.1672/08-04.1

Zhang, Y., Woodcock, C., Olofsson, P., Tang, X., Stanimirova, R., Bullock, E.L., 2022. A Global Analysis of the Spatial and Temporal Variability of Usable Landsat Observations at the Pixel Scale. *Remote Sensing, Section on Remote Sensing Time Series Analysis*.

Zhao, G., Ye, S., Li, G., Yu, X., McClellan, S.A., 2017. Soil Organic Carbon Storage Changes in Coastal Wetlands of the Liaohe Delta, China, Based on Landscape Patterns. *Estuaries and Coasts* 40, 967–976. https://doi.org/10.1007/s12237-016-0194-x

Zheng, L., Xu, J., Tan, Z., Xu, G., Xu, L., Wang, X., 2020. A thirty-year Landsat study reveals changes to a river-lake junction ecosystem after implementation of the three Gorges dam. *Journal of Hydrology* 589, 125185. https://doi.org/10.1016/j.jhydrol.2020.125185

Zhu, Z., 2017. Change detection using landsat time series: A review of frequencies, preprocessing, algorithms, and applications. *ISPRS Journal of Photogrammetry and Remote Sensing* 130, 370–384. https://doi.org/10.1016/j.isprsjprs.2017.06.013

Zhu, Z., Woodcock, C.E., 2014a. Continuous change detection and classification of land cover using all available Landsat data. *Remote Sensing of Environment* 144, 152–171. https://doi.org/10.1016/j.rse.2014.01.011

Zhu, Z., Woodcock, C.E., 2014b. Automated cloud, cloud shadow, and snow detection in multitemporal Landsat data: An algorithm designed specifically for monitoring land cover change. *Remote Sensing of Environment* 152, 217–234. https://doi.org/10.1016/j.rse.2014.06.012

Zhu, Z., Woodcock, C.E., 2012. Object-based cloud and cloud shadow detection in Landsat imagery. *Remote Sensing of Environment* 118, 83–94. https://doi.org/10.1016/j.rse.2011.10.028

Zhu, Z., Woodcock, C.E., Holden, C., Yang, Z., 2015. Generating synthetic Landsat images based on all available Landsat data: Predicting Landsat surface reflectance at any given time. *Remote Sensing of Environment* 162, 67–83. https://doi.org/10.1016/j.rse.2015.02.009

1

LIST OF FIGURES

LIST OF TABLES

APPENDIX

Appendix A. Keywords selected per topic for the literature search. An asterisk (*) was used to retrieve variations of a term.

	Topics		
	Landsat	**Monitoring**	**Wetlands**
	---------------- AND ----------------		
	Landsat*	Change	Marsh*
	L4 TM	Long term	Wet*
	L5 TM	Monitor*	Lagoon*
	L7 ETM+	Decadal	Moor*
	L8 OLI	Century	Bog*
	L1 MSS	Historical	Floodplain*
	L8 TIRS	Trajector*	Swamp*
	Thematic Mapper	Trend*	Mire*
	Operational Land Imager	Decade	Fen*
	Thermal Infrared Sensor	Long-term	Palustrine*
OR	Multispectral Scanner	197* - 199*	Lacustrine*
		197* - 200*	Riverine*
		197* - 201*	Reedbed*
		197* - 202*	Saltmarsh*
		198* - 200*	Peatland*
		198* - 201*	Wetland*
		198* - 202*	RAMSAR
		199* - 201*	Mangrove*
		199* - 202*	
		200* - 202*	

Appendix B. Full list of reviewed studies

Abdul Aziz, A., Phinn, S., Dargusch, P., Omar, H., Arjasakusuma, S., 2015. Assessing the potential applications of Landsat image archive in the ecological monitoring and management of a production mangrove forest in Malaysia. Wetlands Ecol Manage 23, 1049–1066. https://doi.org/10.1007/s11273-015-9443-1

Ablat, X., Liu, G., Liu, Q., Huang, C., 2019. Application of Landsat derived indices and hydrological alteration matrices to quantify the response of floodplain wetlands to river hydrology in arid regions based on different dam operation strategies. Science of The Total Environment 688, 1389–1404. https://doi.org/10.1016/j.scitotenv.2019.06.232

Ahmed, M.H., El Leithy, B.M., Thompson, J.R., Flower, R.J., Ramdani, M., Ayache, F., Hassan, S.M., 2009. Application of remote sensing to site characterisation and environmental change analysis of North African coastal lagoons. Hydrobiologia 622, 147–171. https://doi.org/10.1007/s10750-008-9682-8

Alademomi, A.S., Okolie, C.J., Daramola, O.E., Agboola, R.O., Salami, T.J., 2020. Assessing the relationship of LST, NDVI and EVI with land cover changes in the Lagos Lagoon environment. Quaestiones Geographicae 39, 87–109.

Albhaisi, M., Brendonck, L., Batelaan, O., 2013. Predicted impacts of land use change on groundwater recharge of the upper Berg catchment, South Africa. Water SA 39, 211–220. https://doi.org/10.4314/wsa.v39i2.4

Aljahdali, M.O., Munawar, S., Khan, W.R., 2021. Monitoring mangrove forest degradation and regeneration: Landsat time series analysis of moisture and vegetation indices at Rabigh Lagoon, Red Sea. Forests 12, 52.

Allen, Y.C., Couvillion, B.R., Barras, J.A., 2012. Using Multitemporal Remote Sensing Imagery and Inundation Measures to Improve Land Change Estimates in Coastal Wetlands. Estuaries and Coasts 35, 190–200. https://doi.org/10.1007/s12237-011-9437-z

Almahasheer, H., Aljowair, A., Duarte, C.M., Irigoien, X., 2016. Decadal stability of Red Sea mangroves. Estuarine, Coastal and Shelf Science 169, 164–172. https://doi.org/10.1016/j.ecss.2015.11.027

Alphan, H., 2012. Classifying land cover conversions in coastal wetlands in the Mediterranean: Pairwise comparisons of landsat images. Land Degradation & Development 23, 278–292. https://doi.org/10.1002/ldr.1080

Alphan, H., 2011. Comparing the utility of image algebra operations for characterizing landscape changes: The case of the Mediterranean coast. Journal of Environmental Management 92, 2961–2971. https://doi.org/10.1016/j.jenvman.2011.07.009

Amani, M., Mahdavi, S., Kakooei, M., Ghorbanian, A., Brisco, B., DeLancey, E.R., Toure, S., Reyes, E.L., 2021. Wetland Change Analysis in Alberta, Canada Using Four Decades of Landsat Imagery. IEEE Journal of Selected Topics in Applied Earth Observations and Remote Sensing 14, 10314–10335.

Andrieu, J., 2018. Land cover changes on the West-African coastline from the Saloum Delta (Senegal) to Rio Geba (Guinea-Bissau) between 1979 and 2015. European Journal of Remote Sensing 51, 314–325. https://doi.org/10.1080/22797254.2018.1432295

Anwar, Md.S., Takewaka, S., 2014. Analyses on phenological and morphological variations of mangrove forests along the southwest coast of Bangladesh. J Coast Conserv 18, 339–357. https://doi.org/10.1007/s11852-014-0321-4

Asbridge, E., Lucas, R., Rogers, K., Accad, A., 2018. The extent of mangrove change and potential for recovery following severe Tropical Cyclone Yasi, Hinchinbrook Island, Queensland, Australia. Ecol Evol 8, 10416–10434. https://doi.org/10.1002/ece3.4485

Asbridge, E., Lucas, R., Ticehurst, C., Bunting, P., 2016. Mangrove response to environmental change in Australia's Gulf of Carpentaria. Ecology and Evolution 6, 3523–3539. https://doi.org/10.1002/ece3.2140

Asbridge, E., Lucas, R.M., 2016. Mangrove Response to Environmental Change in Kakadu National Park. IEEE Journal of Selected Topics in Applied Earth Observations and Remote Sensing 9, 5612–5620. https://doi.org/10.1109/JSTARS.2016.2616449

Ashok, A., Rani, H.P., Jayakumar, K.V., 2021. Monitoring of dynamic wetland changes using NDVI and NDWI based landsat imagery. Remote Sensing Applications: Society and Environment 23, 100547. https://doi.org/10.1016/j.rsase.2021.100547

Ashournejad, Q., Amiraslani, F., Moghadam, M.K., Toomanian, A., 2019. Assessing the changes of mangrove ecosystem services value in the Pars Special Economic Energy Zone. Ocean & Coastal Management 179, 104838. https://doi.org/10.1016/j.ocecoaman.2019.104838

Avtar, R., Navia, M., Sassen, J., Fujii, M., 2021. Impacts of changes in mangrove ecosystems in the Ba and Rewa deltas, Fiji using multi-temporal Landsat data and social survey. Coastal Engineering Journal 63, 386–407. https://doi.org/10.1080/21664250.2021.1932332

Bacani, V.M., Sakamoto, A.Y., Quénol, H., Vannier, C., Corgne, S., 2016. Markov chains–cellular automata modeling and multicriteria analysis of land cover change in the Lower Nhecolândia subregion of the Brazilian Pantanal wetland. JARS 10, 016004. https://doi.org/10.1117/1.JRS.10.016004

Banerjee, B.P., Raval, S., Timms, W., 2016. Evaluation of rainfall and wetland water area variability at Thirlmere Lakes using Landsat time-series data. Int. J. Environ. Sci. Technol. 13, 1781–1792. https://doi.org/10.1007/s13762-016-1018-z

Barik, K.K., Mitra, D., Annadurai, R., Tripathy, J.K., Nanda, S., 2016. Geospatial analysis of coastal environment: A case study on Bhitarkanika Mangroves, East coast of India. IJMS Vol.45(04) [April 2016].

Basumatary, H., Sah, R.K., Das, A.K., 2019. Analyzing Area Dynamics on a Protected Floodplain Using Long-Term Sequential Data: The Case of Kaziranga National Park. J Indian Soc Remote Sens 47, 1557–1566. https://doi.org/10.1007/s12524-019-01000-x

Behling, R., Milewski, R., Chabrillat, S., 2018. Spatiotemporal shoreline dynamics of Namibian coastal lagoons derived by a dense remote sensing time series approach. International Journal of

Applied Earth Observation and Geoinformation 68, 262–271. https://doi.org/10.1016/j.jag.2018.01.009

Berberoğlu, S., Akin, A., Atkinson, P.M., Curran, P.J., 2010. Utilizing image texture to detect land-cover change in Mediterranean coastal wetlands. International Journal of Remote Sensing 31, 2793–2815. https://doi.org/10.1080/01431160903111077

Berhane, T., Lane, C., Mengistu, S., Christensen, J., Golden, H., Qiu, S., Zhu, Z., Wu, Q., 2020. Land-Cover Changes to Surface-Water Buffers in the Midwestern USA: 25 Years of Landsat Data Analyses (1993–2017). Remote Sensing 12, 754. https://doi.org/10.3390/rs12050754

Bhattacharjee, S., Islam, M.T., Kabir, M.E., Kabir, M.M., 2021. Land-Use and Land-Cover Change Detection in a North-Eastern Wetland Ecosystem of Bangladesh Using Remote Sensing and GIS Techniques. Earth Syst Environ 5, 319–340. https://doi.org/10.1007/s41748-021-00228-3

Bianchi, L.O., Rivera, J.A., Rojas, F., Britos Navarro, M., Villalba, R., 2017. A regional water balance indicator inferred from satellite images of an Andean endorheic basin in central-western Argentina. Hydrological Sciences Journal 62, 533–545. https://doi.org/10.1080/02626667.2016.1247210

Bishop-Taylor, R., Tulbure, M.G., Broich, M., 2017. Surface-water dynamics and land use influence landscape connectivity across a major dryland region. Ecol Appl 27, 1124–1137. https://doi.org/10.1002/eap.1507

Blanchette, M., Rousseau, A.N., Poulin, M., 2018. Mapping wetlands and land cover change with landsat archives: The added value of geomorphologic data: Cartographie de la dynamique spatio-temporelle des milieux humides à partir d'archives Landsat: La valeur ajoutée de données géomorphologiques. Canadian Journal of Remote Sensing 44, 337–356.

Borro, M., Morandeira, N., Salvia, M., Minotti, P., Perna, P., Kandus, P., 2014. Mapping shallow lakes in a large South American floodplain: A frequency approach on multitemporal Landsat TM/ETM data. Journal of Hydrology 512, 39–52. https://doi.org/10.1016/j.jhydrol.2014.02.057

Brasil, M.C.O., de Magalhães Filho, R., do Espírito-Santo, M.M., Leite, M.E., Veloso, M. das D.M., Falcão, L.A.D., 2021. Land-cover changes and drivers of palm swamp degradation in southeastern Brazil from 1984 to 2018. Applied Geography 137, 102604.

Broich, M., Tulbure, M.G., Verbesselt, J., Xin, Q., Wearne, J., 2018. Quantifying Australia's dryland vegetation response to flooding and drought at sub-continental scale. Remote Sensing of Environment 212, 60–78. https://doi.org/10.1016/j.rse.2018.04.032

Brooke, B., Lymburner, L., Lewis, A., 2017. Coastal dynamics of Northern Australia – Insights from the Landsat Data Cube. Remote Sensing Applications: Society and Environment 8, 94–98. https://doi.org/10.1016/j.rsase.2017.08.003

Buitre, M., Zhang, H., Lin, H., 2019. The Mangrove Forests Change and Impacts from Tropical Cyclones in the Philippines Using Time Series Satellite Imagery. Remote Sensing 11, 688. https://doi.org/10.3390/rs11060688

Cai, X., Haile, A.T., Magidi, J., Mapedza, E., Nhamo, L., 2017. Living with floods – Household perception and satellite observations in the Barotse floodplain, Zambia. Physics and Chemistry of the Earth, Parts A/B/C, Infrastructural Planning for Water Security in Eastern and Southern Africa 100, 278–286. https://doi.org/10.1016/j.pce.2016.10.011

Cai, Y., Zhang, H., Pan, W., Chen, Y., Wang, X., 2012. Urban expansion and its influencing factors in Natural Wetland Distribution Area in Fuzhou City, China. Chin. Geogr. Sci. 22, 568–577. https://doi.org/10.1007/s11769-012-0564-7

Cai, Y., Zhang, H., Zheng, P., Pan, W., 2016. Quantifying the Impact of Land use/Land Cover Changes on the Urban Heat Island: A Case Study of the Natural Wetlands Distribution Area of Fuzhou City, China. Wetlands 36, 285–298. https://doi.org/10.1007/s13157-016-0738-7

Cai, Y.-B., Zhang, H., Pan, W.-B., Chen, Y.-H., Wang, X.-R., 2013. Land use pattern, socio-economic development, and assessment of their impacts on ecosystem service value: study on natural wetlands distribution area (NWDA) in Fuzhou city, southeastern China. Environ Monit Assess 185, 5111–5123. https://doi.org/10.1007/s10661-012-2929-x

Camilleri, S., De Giglio, M., Stecchi, F., Pérez-Hurtado, A., 2017. Land use and land cover change analysis in predominantly man-made coastal wetlands: towards a methodological framework. Wetlands Ecol Manage 25, 23–43. https://doi.org/10.1007/s11273-016-9500-4

Campbell, T., Lantz, T., Fraser, R., 2018. Impacts of Climate Change and Intensive Lesser Snow Goose (Chen caerulescens caerulescens) Activity on Surface Water in High Arctic Pond Complexes. Remote Sensing 10, 1892. https://doi.org/10.3390/rs10121892

Carle, M.V., Sasser, C.E., 2016. Productivity and Resilience: Long-Term Trends and Storm-Driven Fluctuations in the Plant Community of the Accreting Wax Lake Delta. Estuaries and coasts.

Carney, J., Gillespie, T.W., Rosomoff, R., 2014. Assessing forest change in a priority West African mangrove ecosystem: 1986–2010. Geoforum 53, 126–135. https://doi.org/10.1016/j.geoforum.2014.02.013

Castillo, Y.B., Kim, K., Kim, H.S., 2021. Thirty-two years of mangrove forest land cover change in Parita Bay, Panama. Forest Science and Technology 1–13. https://doi.org/10.1080/21580103.2021.1922512

Cavanaugh, K.C., Osland, M.J., Bardou, R., Hinojosa-Arango, G., López-Vivas, J.M., Parker, J.D., Rovai, A.S., Morueta-Holme, N., 2018. Sensitivity of mangrove range limits to climate variability. Global Ecol Biogeogr 27, 925–935. https://doi.org/10.1111/geb.12751

Cetin, M., 2009. A satellite based assessment of the impact of urban expansion around a lagoon. International Journal of Environmental Science and Technology 4, 579–590. https://doi.org/10.1007/BF03326098

Charters, L.J., Aplin, P., Marston, C.G., Padfield, R., Rengasamy, N., Bin Dahalan, M.P., Evers, S., 2019. Peat swamp forest conservation withstands pervasive land conversion to oil palm plantation in North Selangor, Malaysia. International Journal of Remote Sensing 40, 7409–7438. https://doi.org/10.1080/01431161.2019.1574996

Chen, C.-F., Son, N.-T., Chang, N.-B., Chen, C.-R., Chang, L.-Y., Valdez, M., Centeno, G., Thompson, C.A., Aceituno, J.L., 2013. Multi-Decadal Mangrove Forest Change Detection and Prediction in

Honduras, Central America, with Landsat Imagery and a Markov Chain Model. Remote Sensing 5, 6408–6426. https://doi.org/10.3390/rs5126408

Chen, Y., Dong, J., Xiao, X., Ma, Z., Tan, K., Melville, D., Li, B., Lu, H., Liu, J., Liu, F., 2019. Effects of reclamation and natural changes on coastal wetlands bordering China's Yellow Sea from 1984 to 2015. Land Degrad Dev 30, 1533–1544. https://doi.org/10.1002/ldr.3322

Cherrington, E.A., Griffin, R.E., Anderson, E.R., Hernandez Sandoval, B.E., Flores-Anderson, A.I., Muench, R.E., Markert, K.N., Adams, E.C., Limaye, A.S., Irwin, D.E., 2020. Use of public Earth observation data for tracking progress in sustainable management of coastal forest ecosystems in Belize, Central America. Remote Sensing of Environment 245, 111798. https://doi.org/10.1016/j.rse.2020.111798

Chouari, W., 2021. Wetland land cover change detection using multitemporal Landsat data: a case study of the Al-Asfar wetland, Kingdom of Saudi Arabia. Arab J Geosci 14, 523. https://doi.org/10.1007/s12517-021-06815-y

Cissell, J.R., Steinberg, M.K., 2018. Mapping forty years of mangrove cover trends and their implications for flats fisheries in Ciénaga de Zapata, Cuba. Environmental Biology of Fishes 102, 417–427.

Collados-Lara, A.-J., Pardo-Igúzquiza, E., Pulido-Velazquez, D., Baena-Ruiz, L., 2021. Estimation of the Monthly Dynamics of Surface Water in Wetlands from Satellite and Secondary Hydro-Climatological Data. Remote Sensing 13, 2380. https://doi.org/10.3390/rs13122380

Cong, P., Chen, K., Qu, L., Han, J., 2019. Dynamic Changes in the Wetland Landscape Pattern of the Yellow River Delta from 1976 to 2016 Based on Satellite Data. Chin. Geogr. Sci. 29, 372–381. https://doi.org/10.1007/s11769-019-1039-x

Constance, A., Haverkamp, P.J., Bunbury, N., Schaepman-Strub, G., 2021. Extent change of protected mangrove forest and its relation to wave power exposure on Aldabra Atoll. Global Ecology and Conservation 27, e01564. https://doi.org/10.1016/j.gecco.2021.e01564

Conti, L.A., Sampaio de Araujo, C.A., Cunha-Lignon, M. [UNESP, 2016. Spatial database modeling for mangrove forests mapping; example of two estuarine systems in Brazil. Modeling Earth Systems And Environment 12. https://doi.org/10.1007/s40808-016-0129-3

Dang, A.T., Kumar, L., Reid, M., Nguyen, H., 2021. Remote sensing approach for monitoring coastal wetland in the Mekong Delta, Vietnam: Change trends and their driving forces. Remote Sensing 13, 3359.

Dangles, O., Rabatel, A., Kraemer, M., Zeballos, G., Soruco, A., Jacobsen, D., Anthelme, F., 2017. Ecosystem sentinels for climate change? Evidence of wetland cover changes over the last 30 years in the tropical Andes. PLoS ONE 12, e0175814. https://doi.org/10.1371/journal.pone.0175814

Darmawan, S., Sari, D.K., Wikantika, K., Tridawati, A., Hernawati, R., Sedu, M.K., 2020. Identification before-after Forest Fire and Prediction of Mangrove Forest Based on Markov-Cellular Automata in Part of Sembilang National Park, Banyuasin, South Sumatra, Indonesia. Remote Sensing 12, 3700. https://doi.org/10.3390/rs12223700

Das, R.T., Pal, S., 2017. Exploring geospatial changes of wetland in different hydrological paradigms using water presence frequency approach in Barind Tract of West Bengal. Spat. Inf. Res. 25, 467–479. https://doi.org/10.1007/s41324-017-0114-6

Datta, D., Deb, S., 2012. Analysis of coastal land use/land cover changes in the Indian Sunderbans using remotely sensed data. Geo-spatial Information Science 15, 241–250. https://doi.org/10.1080/10095020.2012.714104

Dawson, S.K., Fisher, A., Lucas, R., Hutchinson, D.K., Berney, P., Keith, D., Catford, J.A., Kingsford, R.T., 2016. Remote Sensing Measures Restoration Successes, but Canopy Heights Lag in Restoring Floodplain Vegetation. Remote Sensing 8, 542. https://doi.org/10.3390/rs8070542

de la Fuente, A., Meruane, C., Suárez, F., 2021. Long-term spatiotemporal variability in high Andean wetlands in northern Chile. Science of The Total Environment 756, 143830. https://doi.org/10.1016/j.scitotenv.2020.143830

Dearborn, K.D., Baltzer, J.L., 2021. Unexpected greening in a boreal permafrost peatland undergoing forest loss is partially attributable to tree species turnover. Glob Change Biol 27, 2867–2882. https://doi.org/10.1111/gcb.15608

Dervisoglu, A., 2021. Analysis of the Temporal Changes of Inland Ramsar Sites in Turkey Using Google Earth Engine. IJGI 10, 521. https://doi.org/10.3390/ijgi10080521

Dervisoglu, A., Musaoğlu, N., Tanik, A., Şeker, D., Kaya, Ş., 2017. Satellite-based temporal assessment of a dried lake: case study of Akgol wetland. FRESENIUS ENVIRONMENTAL BULLETIN 26.

Dewidar, K.M., 2011. Monitoring temporal changes of the surface water area of the Burullus and Manzala lagoons using automatic techniques applied to a Landsat satellite data series of the Nile Delta coast. Mediterranean Marine Science 12, 462–478. https://doi.org/10.12681/mms.45

Díaz-Delgado, R., Aragonés, D., Afán, I., Bustamante, J., 2016. Long-Term Monitoring of the Flooding Regime and Hydroperiod of Doñana Marshes with Landsat Time Series (1974–2014). Remote Sensing 8, 775. https://doi.org/10.3390/rs8090775

Ding, X., Shan, X., Chen, Y., Li, M., Li, J., Jin, X., 2020. Variations in fish habitat fragmentation caused by marine reclamation activities in the Bohai coastal region, China. Ocean & Coastal Management 184, 105038.

Dingle Robertson, L., King, D.J., Davies, C., 2015. Assessing Land Cover Change and Anthropogenic Disturbance in Wetlands Using Vegetation Fractions Derived from Landsat 5 TM Imagery (1984–2010). Wetlands 35, 1077–1091. https://doi.org/10.1007/s13157-015-0696-5

Diniz, C., Cortinhas, L., Nerino, G., Rodrigues, J., Sadeck, L., Adami, M., Souza-Filho, P., 2019. Brazilian Mangrove Status: Three Decades of Satellite Data Analysis. Remote Sensing 11, 808. https://doi.org/10.3390/rs11070808

Dipson, P.T., Chithra, S.V., Amarnath, A., Smitha, S.V., Harindranathan Nair, M.V., Shahin, A., 2015. Spatial changes of estuary in Ernakulam district, Southern India for last seven decades, using multi-temporal satellite data. Journal of Environmental Management, Land Cover/Land Use Change (LC/LUC) and Environmental Impacts in South Asia 148, 134–142. https://doi.org/10.1016/j.jenvman.2014.02.021

Disperati, L., Virdis, S.G.P., 2015. Assessment of land-use and land-cover changes from 1965 to 2014 in Tam Giang-Cau Hai Lagoon, central Vietnam. Applied Geography 58, 48–64. https://doi.org/10.1016/j.apgeog.2014.12.012

Dong, X., Chen, Z., 2021. Digital Examination of Vegetation Changes in River Floodplain Wetlands Based on Remote Sensing Images: A Case Study Based on the Downstream Section of Hailar River. Forests 12, 1206.

Dou, P., Cui, B., 2014. Dynamics and integrity of wetland network in estuary. Ecological Informatics 24, 1–10. https://doi.org/10.1016/j.ecoinf.2014.06.002

Douglas, S.H., Bernier, J.C., Smith, K.E.L., 2018. Analysis of multi-decadal wetland changes, and cumulative impact of multiple storms 1984 to 2017. Wetlands Ecol Manage 26, 1121–1142. https://doi.org/10.1007/s11273-018-9635-6

Doyle, C., Beach, T., Luzzadder-Beach, S., 2021. Tropical Forest and Wetland Losses and the Role of Protected Areas in Northwestern Belize, Revealed from Landsat and Machine Learning. Remote Sensing 13, 379. https://doi.org/10.3390/rs13030379

Duku, E., Mattah, P.A.D., Angnuureng, D.B., 2021. Assessment of Land Use/Land Cover Change and Morphometric Parameters in the Keta Lagoon Complex Ramsar Site, Ghana. Water 13, 2537.

Duncan, C., Böhm, M., Turvey, S.T., 2021. Identifying the possibilities and pitfalls of conducting IUCN Red List assessments from remotely sensed habitat information based on insights from poorly known Cuban mammals. Conservation Biology 35, 1598–1614. https://doi.org/10.1111/cobi.13715

Eddy, S., Iskandar, I., Ridho, M.R., Mulyana, A., 2017. Land cover changes in the Air Telang Protected Forest, South Sumatra, Indonesia (1989-2013). Biodiversitas Journal of Biological Diversity 18, 1538–1545. https://doi.org/10.13057/biodiv/d180431

Eddy, S., Milantara, N., Sasmito, S.D., Kajita, T., Basyuni, M., 2021. Anthropogenic Drivers of Mangrove Loss and Associated Carbon Emissions in South Sumatra, Indonesia. Forests 12, 187. https://doi.org/10.3390/f12020187

Ehsani, A.H., Shakeryari, M., 2021. Monitoring of wetland changes affected by drought using four Landsat satellite data and Fuzzy ARTMAP classification method (case study Hamoun wetland, Iran). Arab J Geosci 14, 1363. https://doi.org/10.1007/s12517-020-06320-8

Ekumah, B., Armah, F.A., Afrifa, E.K.A., Aheto, D.W., Odoi, J.O., Afitiri, A.-R., 2020. Geospatial assessment of ecosystem health of coastal urban wetlands in Ghana. Ocean & Coastal Management 193, 105226. https://doi.org/10.1016/j.ocecoaman.2020.105226

Eslami-Andargoli, L., Dale, P.E.R., Sipe, N., Chaseling, J., 2010. Local and landscape effects on spatial patterns of mangrove forest during wetter and drier periods: Moreton Bay, Southeast Queensland, Australia. Estuarine, Coastal and Shelf Science 89, 53–61. https://doi.org/10.1016/j.ecss.2010.05.011

Fazelpoor, K., Yousefi, S., Martínez-Fernández, V., García de Jalón, D., 2021. Geomorphological evolution along international riverine borders: The flow of the Aras River through Iran, Azerbaijan, and Armenia. Journal of Environmental Management 290, 112599. https://doi.org/10.1016/j.jenvman.2021.112599

Feng, L., Han, X., Hu, C., Chen, X., 2016. Four decades of wetland changes of the largest freshwater lake in China: Possible linkage to the Three Gorges Dam? Remote Sensing of Environment 176, 43–55. https://doi.org/10.1016/j.rse.2016.01.011

Feng, Z., Tan, G., Xia, J., Shu, C., Chen, P., Wu, M., Wu, X., 2020. Dynamics of mangrove forests in Shenzhen Bay in response to natural and anthropogenic factors from 1988 to 2017. Journal of Hydrology 591, 125271. https://doi.org/10.1016/j.jhydrol.2020.125271

Fickas, K.C., Cohen, W.B., Yang, Z., 2016. Landsat-based monitoring of annual wetland change in the Willamette Valley of Oregon, USA from 1972 to 2012. Wetlands Ecol Manage 24, 73–92. https://doi.org/10.1007/s11273-015-9452-0

Fitoka, E., Tompoulidou, M., Hatziiordanou, L., Apostolakis, A., Höfer, R., Weise, K., Ververis, C., 2020. Water-related ecosystems' mapping and assessment based on remote sensing techniques and geospatial analysis: The SWOS national service case of the Greek Ramsar sites and their catchments. Remote Sensing of Environment 245, 111795. https://doi.org/10.1016/j.rse.2020.111795

Fragal, E.H., Silva, T.S.F., Novo, E.M.L. de M., 2016. Reconstructing historical forest cover change in the Lower Amazon floodplains using the LandTrendr algorithm. Acta Amaz. 46, 13–24. https://doi.org/10.1590/1809-4392201500835

Gao, W., Wan, L.H., Du, Y.X., Zhu, D.Y., 2019. The effect of landscape pattern in response to ecological environment and climate change in Xiaoxing'Anling, Heilongjiang province, China. APPLIED ECOLOGY AND ENVIRONMENTAL RESEARCH 17, 15419–15429.

Gao, Z., Guo, H., Li, S., Wang, J., Ye, H., Han, S., Cao, W., 2022. Remote sensing of wetland evolution in predicting shallow groundwater arsenic distribution in two typical inland basins. Science of The Total Environment 806, 150496.

Gayol, M.P., Morandeira, N.S., Kandus, P., 2019. Dynamics of shallow lake cover types in relation to Paraná River flood pulses: assessment with multitemporal Landsat data. Hydrobiologia 833, 9–24.

Geng, M., Li, F., Gao, Y., Li, Z., Chen, X., Deng, Z., Zou, Y., Xie, Y., Wang, Z., 2021. Wetland Area Change from 1986-2016 in the Dongting Lake Watershed at the Sub-Watershed Scale. Polish Journal of Environmental Studies 30.

Gholami, D.M., Baharlouii, M., 2019. Monitoring long-term mangrove shoreline changes along the northern coasts of the Persian Gulf and the Oman Sea. Emerging Science Journal 3, 88–100.

Ghosh, M., Kumar, L., Roy, C., 2017. Climate Variability and Mangrove Cover Dynamics at Species Level in the Sundarbans, Bangladesh. Sustainability 9, 805. https://doi.org/10.3390/su9050805

Ghosh, M.K., Kumar, L., Roy, C., 2016. Mapping Long-Term Changes in Mangrove Species Composition and Distribution in the Sundarbans. Forests 7, 305. https://doi.org/10.3390/f7120305

Gilani, H., Naz, H.I., Arshad, M., Nazim, K., Akram, U., Abrar, A., Asif, M., 2021. Evaluating mangrove conservation and sustainability through spatiotemporal (1990–2020) mangrove cover change analysis in Pakistan. Estuarine, Coastal and Shelf Science 249, 107128. https://doi.org/10.1016/j.ecss.2020.107128

Giri, C., Long, J., 2016. Is the Geographic Range of Mangrove Forests in the Conterminous United States Really Expanding? Sensors 16, 2010. https://doi.org/10.3390/s16122010

Godoy, M.D.P., de Lacerda, L.D., 2014. River-Island Morphological Response to Basin Land-Use Change within the Jaguaribe River Estuary, NE Brazil. Journal of Coastal Research 30, 399–410. https://doi.org/10.2112/JCOASTRES-D-13-00059.1

Gong, Z., Li, H., Zhao, W., Gong, H., 2013. Driving forces analysis of reservoir wetland evolution in Beijing during 1984–2010. J. Geogr. Sci. 23, 753–768. https://doi.org/10.1007/s11442-013-1042-6

Gopalakrishnan, L., Satyanarayana, B., Chen, D., Wolswijk, G., Amir, A.A., Vandegehuchte, M.B., Muslim, A.B., Koedam, N., Dahdouh-Guebas, F., 2021. Using historical archives and landsat imagery to explore changes in the mangrove cover of Peninsular Malaysia between 1853 and 2018. Remote Sensing 13, 3403.

Guo, H., Cai, Y., Yang, Z., Zhu, Z., Ouyang, Y., 2021. Dynamic simulation of coastal wetlands for Guangdong-Hong Kong-Macao Greater Bay area based on multi-temporal Landsat images and FLUS model. Ecological Indicators 125, 107559. https://doi.org/10.1016/j.ecolind.2021.107559

Halabisky, M., Moskal, L.M., Gillespie, A., Hannam, M., 2016. Reconstructing semi-arid wetland surface water dynamics through spectral mixture analysis of a time series of Landsat satellite images (1984–2011). Remote Sensing of Environment 177, 171–183. https://doi.org/10.1016/j.rse.2016.02.040

Halder, S., Samanta, K., Das, S., Pathak, D., 2021. Monitoring the inter-decade spatial–temporal dynamics of the Sundarban mangrove forest of India from 1990 to 2019. Regional Studies in Marine Science 44, 101718. https://doi.org/10.1016/j.rsma.2021.101718

Hamandawana, H., Atyosi, Y., Bornman, T.G., 2020. Multi-temporal reconstruction of long-term changes in land cover in and around the Swartkops River Estuary, Eastern Cape, South Africa. Environ Monit Assess 192, 173. https://doi.org/10.1007/s10661-020-8136-2

Han, X., Chen, X., Feng, L., 2015. Four decades of winter wetland changes in Poyang Lake based on Landsat observations between 1973 and 2013. Remote Sensing of Environment 156, 426–437. https://doi.org/10.1016/j.rse.2014.10.003

Han, X., Feng, L., Hu, C., Kramer, P., 2018. Hurricane-induced changes in the Everglades National Park mangrove forest: Landsat observations between 1985 and 2017. Journal of Geophysical Research: Biogeosciences 123, 3470–3488.

Haque, Md.I., Basak, R., 2017. Land cover change detection using GIS and remote sensing techniques: A spatio-temporal study on Tanguar Haor, Sunamganj, Bangladesh. The Egyptian Journal of Remote Sensing and Space Science 20, 251–263. https://doi.org/10.1016/j.ejrs.2016.12.003

Harezlak, V., Geerling, G.W., Rogers, C.K., Penning, W.E., Augustijn, D.C.M., Hulscher, S.J.M.H., 2020. Revealing 35 years of landcover dynamics in floodplains of trained lowland rivers using satellite data. River Res Applic 36, 1213–1221. https://doi.org/10.1002/rra.3633

Hartman, B.D., Bookhagen, B., Chadwick, O.A., 2016. The effects of check dams and other erosion control structures on the restoration of Andean bofedal ecosystems. Restoration Ecology 24, 761–772. https://doi.org/10.1111/rec.12402

Hashim, B.M., Sultan, M.A., Attyia, M.N., Al Maliki, A.A., Al-Ansari, N., 2019. Change Detection and Impact of Climate Changes to Iraqi Southern Marshes Using Landsat 2 MSS, Landsat 8 OLI and Sentinel 2 MSI Data and GIS Applications. Applied Sciences 9, 2016. https://doi.org/10.3390/app9102016

Hason, M.M., Abbood, I.S., Odaa, S. aldeen, 2020. Land cover reflectance of Iraqi marshlands based on visible spectral multiband of satellite imagery. Results in Engineering 8, 100167. https://doi.org/10.1016/j.rineng.2020.100167

Hempattarasuwan, N., Christakos, G., Wu, J., 2019. Changes of Wiang Nong Lom and Nong Luang Wetlands in Chiang Saen Valley (Chiang Rai Province, Thailand) During the Period 1988–2017. IEEE J. Sel. Top. Appl. Earth Observations Remote Sensing 12, 4224–4238. https://doi.org/10.1109/JSTARS.2019.2937949

Hiernaux, P., Turner, M.D., Eggen, M., Marie, J., Haywood, M., 2021. Resilience of wetland vegetation to recurrent drought in the Inland Niger Delta of Mali from 1982 to 2014. Wetlands Ecol Manage 29, 945–967. https://doi.org/10.1007/s11273-021-09822-8

Ho, J.C., Stumpf, R.P., Bridgeman, T.B., Michalak, A.M., 2017. Using Landsat to extend the historical record of lacustrine phytoplankton blooms: A Lake Erie case study. Remote Sensing of Environment 191, 273–285. https://doi.org/10.1016/j.rse.2016.12.013

Hong, H.T.C., Avtar, R., Fujii, M., 2019. Monitoring changes in land use and distribution of mangroves in the southeastern part of the Mekong River Delta, Vietnam. Trop Ecol 60, 552–565. https://doi.org/10.1007/s42965-020-00053-1

Hopkinson, C., Fuoco, B., Grant, T., Bayley, S.E., Brisco, B., MacDonald, R., 2020. Wetland Hydroperiod Change Along the Upper Columbia River Floodplain, Canada, 1984 to 2019. Remote Sensing 12, 4084. https://doi.org/10.3390/rs12244084

Htwe, T.N., Kywe, M., Buerkert, A., Brinkmann, K., 2015. Transformation processes in farming systems and surrounding areas of Inle Lake, Myanmar, during the last 40 years. Journal of Land Use Science 10, 205–223. https://doi.org/10.1080/1747423X.2013.878764

Hu, L., Li, W., Xu, B., 2018. Monitoring mangrove forest change in China from 1990 to 2015 using Landsat-derived spectral-temporal variability metrics. International Journal of Applied Earth Observation and Geoinformation 73, 88–98. https://doi.org/10.1016/j.jag.2018.04.001

Huo, H., Guo, J., Li, Z.-L., Jiang, X., 2017. Remote Sensing of Spatiotemporal Changes in Wetland Geomorphology Based on Type 2 Fuzzy Sets: A Case Study of Beidagang Wetland from 1975 to 2015. Remote Sensing 9, 683. https://doi.org/10.3390/rs9070683

Hussien, K., Demissie, B., Meaza, H., 2018. Spatiotemporal wetland changes and their threats in North Central Ethiopian Highlands: Kassaye Hussien, Biadgilgn Demissie and Hailemariam Meaza. Singapore Journal of Tropical Geography 39, 332–350. https://doi.org/10.1111/sjtg.12242

Ibitoye, M.O., Komolafe, A.A., Adegboyega, A.-A.S., Adebola, A.O., Oladeji, O.D., 2019. Analysis of vulnerable urban properties within river Ala floodplain in Akure, Southwestern Nigeria. Spat. Inf. Res. 28, 431–445. https://doi.org/10.1007/s41324-019-00298-6

Ibrahim, T., Geremew, B., Tesfay, F., 2021. Spatio-temporal dynamic of land use and land cover in andit tid watershed, wet frost/afro-alpine highland of ethiopia. Edelweiss Applied Science and Technology 5, 33–38.

İrdemez, Ş., Eymirli, E.B., 2021. Determination of spatiotemporal changes in Erzurum plain wetland system using remote sensing techniques. Environmental Monitoring and Assessment 193, 1–13.

Islam, H., Abbasi, H., Karam, A., Chughtai, A.H., Ahmed Jiskani, M., 2021. Geospatial analysis of wetlands based on land use/land cover dynamics using remote sensing and GIS in Sindh, Pakistan. Science Progress 104, 00368504211026143.

Islam, Md.M., Borgqvist, H., Kumar, L., 2019. Monitoring Mangrove forest landcover changes in the coastline of Bangladesh from 1976 to 2015. Geocarto International 34, 1458–1476. https://doi.org/10.1080/10106049.2018.1489423

Jacintha, T., Rajasree, S.R., Kumar, J.D., Sriganesh, J., 2019. Assessment of wetland change dynamics of Chennai coast, Tamil Nadu, India, using satellite remote sensing.

Jacob, A.L., Bonnell, T.R., Dowhaniuk, N., Hartter, J., 2014. Topographic and spectral data resolve land cover misclassification to distinguish and monitor wetlands in western Uganda. ISPRS Journal of Photogrammetry and Remote Sensing 94, 114–126. https://doi.org/10.1016/j.isprsjprs.2014.05.001

Jamali, A.A., Naeeni, M.A.M., Zarei, G., 2020. Assessing the expansion of saline lands through vegetation and wetland loss using remote sensing and GIS. Remote Sensing Applications: Society and Environment 20, 100428.

Jayanthi, M., Thirumurthy, S., Muralidhar, M., Ravichandran, P., 2018a. Impact of shrimp aquaculture development on important ecosystems in India. Global Environmental Change 52, 10–21. https://doi.org/10.1016/j.gloenvcha.2018.05.005

Jayanthi, M., Thirumurthy, S., Nagaraj, G., Muralidhar, M., Ravichandran, P., 2018b. Spatial and temporal changes in mangrove cover across the protected and unprotected forests of India. Estuarine, Coastal and Shelf Science 213, 81–91. https://doi.org/10.1016/j.ecss.2018.08.016

Jia, M., Liu, M., Wang, Z., Mao, D., Ren, C., Cui, H., 2016. Evaluating the Effectiveness of Conservation on Mangroves: A Remote Sensing-Based Comparison for Two Adjacent Protected Areas in Shenzhen and Hong Kong, China. Remote Sensing 8, 627. https://doi.org/10.3390/rs8080627

Jia, M., Wang, Z., Liu, D., Ren, C., Tang, X., Dong, Z., 2015a. Monitoring Loss and Recovery of Salt Marshes in the Liao River Delta, China. Journal of Coastal Research 31, 371–377. https://doi.org/10.2112/JCOASTRES-D-13-00056.1

Jia, M., Wang, Z., Zhang, Y., Mao, D., Wang, C., 2018. Monitoring loss and recovery of mangrove forests during 42 years: The achievements of mangrove conservation in China. International Journal of Applied Earth Observation and Geoinformation 73, 535–545. https://doi.org/10.1016/j.jag.2018.07.025

Jia, M., Wang, Z., Zhang, Y., Ren, C., Song, K., 2015b. Landsat-Based Estimation of Mangrove Forest Loss and Restoration in Guangxi Province, China, Influenced by Human and Natural Factors.

IEEE Journal of Selected Topics in Applied Earth Observations and Remote Sensing 8, 311–323. https://doi.org/10.1109/JSTARS.2014.2333527

Jia, P., Zhang, Y., Xu, W., Xia, Z., Zhong, C., Yin, Y., 2018. Spatio-temporal evolution of coastlines of sand-barrier lagoons over 26 years through historic Landsat imagery in Lingshui County, Hainan Province, China. J Coast Conserv 23, 817–827. https://doi.org/10.1007/s11852-018-0664-3

Jiang, W., Wang, W., Chen, Y., Liu, J., Tang, H., Hou, P., Yang, Y., 2012. Quantifying driving forces of urban wetlands change in Beijing City. J. Geogr. Sci. 22, 301–314. https://doi.org/10.1007/s11442-012-0928-z

Jin, H., Huang, C., Lang, M.W., Yeo, I.-Y., Stehman, S.V., 2017. Monitoring of wetland inundation dynamics in the Delmarva Peninsula using Landsat time-series imagery from 1985 to 2011. Remote Sensing of Environment 190, 26–41. https://doi.org/10.1016/j.rse.2016.12.001

John, S., C, R., Muraleedharan, K.R., B, S., G, S., Azeez S, A., 2020. Current asymmetry and its implications for morphological changes in Vembanad Lake, the second largest wetland ecosystem in India. Estuarine, Coastal and Shelf Science 246, 107013. https://doi.org/10.1016/j.ecss.2020.107013

Jordan, Y.C., Ghulam, A., Herrmann, R.B., 2012. Floodplain ecosystem response to climate variability and land-cover and land-use change in Lower Missouri River basin. Landscape Ecol 27, 843–857. https://doi.org/10.1007/s10980-012-9748-x

Jouma, N., Dadaser-Celik, F., 2021. Landscape transformation after irrigation development in and around a semi-arid wetland ecosystem. Landscape and Ecological Engineering 17, 439–457.

Ju, J., Masek, J.G., 2016. The vegetation greenness trend in Canada and US Alaska from 1984–2012 Landsat data. Remote Sensing of Environment 176, 1–16. https://doi.org/10.1016/j.rse.2016.01.001

Kabiri, S., Allen, M., Okuonzia, J.T., Akello, B., Ssabaganzi, R., Mubiru, D., 2020. Detecting level of wetland encroachment for urban agriculture in Uganda using hyper-temporal remote sensing. https://doi.org/10.12688/aasopenres.13040.1

Kanniah, K.D., Sheikhi, A., Cracknell, A.P., Goh, H.C., Tan, K.P., Ho, C.S., Rasli, F.N., 2015. Satellite Images for Monitoring Mangrove Cover Changes in a Fast Growing Economic Region in Southern Peninsular Malaysia. Remote Sensing 7, 14360–14385. https://doi.org/10.3390/rs71114360

Karim, M., Maanan, Mehdi, Maanan, Mohamed, Rhinane, H., Rueff, H., Baidder, L., 2019. Assessment of water body change and sedimentation rate in Moulay Bousselham wetland, Morocco, using geospatial technologies. International journal of sediment research 34, 65–72.

Kawser, U., Hoque, A., Nath, B., 2021. Observing the impacts of 1950s great Assam earthquake in the tectono-geomorphological deformations at the Young Meghna Estuarine Floodplain of Bangladesh: evidence from Noakhali Coastal Region. Arab J Geosci 14, 306. https://doi.org/10.1007/s12517-020-06427-y

Kayastha, N., Thomas, V., Galbraith, J., Banskota, A., 2012. Monitoring Wetland Change Using Inter-Annual Landsat Time-Series Data. Wetlands 32, 1149–1162. https://doi.org/10.1007/s13157-012-0345-1

Kearney, M.S., Riter, J.C.A., Turner, R.E., 2011. Freshwater river diversions for marsh restoration in Louisiana: Twenty-six years of changing vegetative cover and marsh area. Geophysical Research Letters 38. https://doi.org/10.1029/2011GL047847

Kharazmi, R., Tavili, A., Rahdari, M.R., Chaban, L., Panidi, E., Rodrigo-Comino, J., 2018. Monitoring and assessment of seasonal land cover changes using remote sensing: a 30-year (1987–2016) case study of Hamoun Wetland, Iran. Environ Monit Assess 190, 356. https://doi.org/10.1007/s10661-018-6726-z

Kirui, K.B., Kairo, J.G., Bosire, J., Viergever, K.M., Rudra, S., Huxham, M., Briers, R.A., 2013. Mapping of mangrove forest land cover change along the Kenya coastline using Landsat imagery. Ocean & Coastal Management 83, 19–24. https://doi.org/10.1016/j.ocecoaman.2011.12.004

Kolari, T.H., Sallinen, A., Wolff, F., Kumpula, T., Tolonen, K., Tahvanainen, T., 2021. Ongoing fen–bog transition in a boreal aapa mire inferred from repeated field sampling, aerial images, and Landsat data. Ecosystems 1–23.

Koshale, J.P., Mahato, A., 2020. Spatio-Temporal Change Detection and Its Impact on the Waterbodies by Monitoring LU/LC Dynamics-A Case Study from Holy City of Ratanpur, Chhattisgarh, India. Nature Environment & Pollution Technology 19.

Krapu, C., Kumar, M., Borsuk, M., 2018. Identifying Wetland Consolidation Using Remote Sensing in the North Dakota Prairie Pothole Region. Water Resour. Res. 54, 7478–7494. https://doi.org/10.1029/2018WR023338

Kubo, S., Naga Kumar, K.Ch.V., Demudu, G., Hema Malini, B., Nageswara Rao, K., Agrawal, R., Ramakrishnan, R., Rajawat, A.S., 2017. Monitoring of Eco-Restoration of Mangrove Wetlands through Time Series Satellite Images: A Study on Krishna-Godavari Delta Region, East Coast of India. Geog. Rev. Japan B 90, 66–75. https://doi.org/10.4157/geogrevjapanb.90.66

Kuleli, T., Guneroglu, A., Karsli, F., Dihkan, M., 2011. Automatic detection of shoreline change on coastal Ramsar wetlands of Turkey. Ocean Engineering 38, 1141–1149. https://doi.org/10.1016/j.oceaneng.2011.05.006

Kumar, M., Mondal, I., Pham, Q.B., 2021. Monitoring forest landcover changes in the Eastern Sundarban of Bangladesh from 1989 to 2019. Acta Geophys. 69, 561–577. https://doi.org/10.1007/s11600-021-00551-3

Laengner, M.L., Siteur, K., van der Wal, D., 2019. Trends in the Seaward Extent of Saltmarshes across Europe from Long-Term Satellite Data. Remote Sensing 11, 1653. https://doi.org/10.3390/rs11141653

Lamsal, P., Atreya, K., Ghosh, M.K., Pant, K.P., 2019. Effects of population, land cover change, and climatic variability on wetland resource degradation in a Ramsar listed Ghodaghodi Lake Complex, Nepal. Environ Monit Assess 191, 415. https://doi.org/10.1007/s10661-019-7514-0

Lap, Q.K., Luong, V.N., Hong, X.T., Tu, T.T., Thanh, K.T.P., 2021. Evaluation of Mangrove Rehabilitation After Being Destroyed by Chemical Warfare Using Remote Sensing Technology: A Case Study in Can Gio Mangrove Forest in Mekong Delta, Southern Vietnam. APPLIED ECOLOGY AND ENVIRONMENTAL RESEARCH 19, 3897–3930.

Li, D., Lu, D., Wu, M., Shao, X., Wei, J., 2017. Examining Land Cover and Greenness Dynamics in Hangzhou Bay in 1985–2016 Using Landsat Time-Series Data. Remote Sensing 10, 32. https://doi.org/10.3390/rs10010032

Li, J., Hu, J., Wei, D., Sheng-li, H., Hai-feng, J., Chun-ling, Z., Huai-xiu, L., 2013. Revealing storage-area relationship of open water in ungauged subalpine wetland - Napahai in Northwest Yunnan, China. IMHE OpenIR 10. https://doi.org/10.1007/s11629-013-2596-6

Li, M.S., Mao, L.J., Shen, W.J., Liu, S.Q., Wei, A.S., 2013. Change and fragmentation trends of Zhanjiang mangrove forests in southern China using multi-temporal Landsat imagery (1977–2010). Estuarine, Coastal and Shelf Science, Pressures, Stresses, Shocks and Trends in Estuarine Ecosystems 130, 111–120. https://doi.org/10.1016/j.ecss.2013.03.023

Li, X., Mitra, C., Marzen, L., Yang, Q., 2016. Spatial and Temporal Patterns of Wetland Cover Changes in East Kolkata Wetlands, India from 1972 to 2011. IJAGR 7, 1–13. https://doi.org/10.4018/ijagr.2016040101

Li, Y., Mao, D., Wang, Z., Wang, X., Tan, X., Jia, M., Ren, C., 2021. Identifying variable changes in wetlands and their anthropogenic threats bordering the Yellow Sea for water bird conservation. Global Ecology and Conservation 27, e01613. https://doi.org/10.1016/j.gecco.2021.e01613

Li, Z., Gong, Z., Guan, H., Zhang, Q., 2018. Dynamic estimating of wetland vegetation cover based on linear spectral mixture and time phase transformation models. International Journal of Remote Sensing 39, 9294–9311. https://doi.org/10.1080/01431161.2018.1531318

Li, Z., Liu, M., Hu, Y., Xue, Z., Sui, J., 2020. The spatiotemporal changes of marshland and the driving forces in the Sanjiang Plain, Northeast China from 1980 to 2016. Ecol Process 9, 24. https://doi.org/10.1186/s13717-020-00226-9

Liang, K., Li, Y., 2019. Changes in Lake Area in Response to Climatic Forcing in the Endorheic Hongjian Lake Basin, China. Remote Sensing 11, 3046. https://doi.org/10.3390/rs11243046

Liao, H., Li, G., Cui, L., Ouyang, N., Zhang, Y., Wang, S., 2014. Study on Evolution Features and Spatial Distribution Patterns of Coastal Wetlands in North Jiangsu Province, China. Wetlands 34, 877–891. https://doi.org/10.1007/s13157-014-0550-1

Liao, J., Zhen, J., Zhang, L., Metternicht, G., 2019. Understanding Dynamics of Mangrove Forest on Protected Areas of Hainan Island, China: 30 Years of Evidence from Remote Sensing. Sustainability 11, 5356. https://doi.org/10.3390/su11195356

Lin, W., Cen, J., Xu, D., Du, S., Gao, J., 2018. Wetland landscape pattern changes over a period of rapid development (1985–2015) in the ZhouShan Islands of Zhejiang province, China. Estuarine, Coastal and Shelf Science 213, 148–159.

Lin, Y., Yu, J., Cai, J., Sneeuw, N., Li, F., 2018. Spatio-Temporal Analysis of Wetland Changes Using a Kernel Extreme Learning Machine Approach. Remote Sensing 10, 1129. https://doi.org/10.3390/rs10071129

Lipp-Nissinen, K.H., de Sá Piñeiro, B., Miranda, L.S., de Paula Alves, A., 2018. Temporal dynamics of land use and cover in Paurá Lagoon region, Middle Coast of Rio Grande do Sul (RS), Brazil. Journal of Integrated Coastal Zone Management 18, 25–39.

Liu, D., Chen, W., Menz, G., Dubovyk, O., 2020. Development of integrated wetland change detection approach: In case of Erdos Larus Relictus National Nature Reserve, China. Science of The Total Environment 731, 139166. https://doi.org/10.1016/j.scitotenv.2020.139166

Liu, M., Hu, D., 2019. Response of Wetland Evapotranspiration to Land Use/Cover Change and Climate Change in Liaohe River Delta, China. Water 11, 955. https://doi.org/10.3390/w11050955

Liu, Y., Liu, Yongxue, Li, J., Sun, C., Xu, W., Zhao, B., 2020. Trajectory of coastal wetland vegetation in Xiangshan Bay, China, from image time series. Marine Pollution Bulletin 160, 111697. https://doi.org/10.1016/j.marpolbul.2020.111697

Long, C., Dai, Z., Zhou, X., Mei, X., Mai Van, C., 2021. Mapping mangrove forests in the Red River Delta, Vietnam. Forest Ecology and Management 483, 118910. https://doi.org/10.1016/j.foreco.2020.118910

Lopes, C.L., Mendes, R., Caçador, I., Dias, J.M., 2020. Assessing salt marsh extent and condition changes with 35 years of Landsat imagery: Tagus Estuary case study. Remote Sensing of Environment 247, 111939. https://doi.org/10.1016/j.rse.2020.111939

Lopes, C.L., Mendes, R., Caçador, I., Dias, J.M., 2019. Evaluation of long-term estuarine vegetation changes through Landsat imagery. Science of The Total Environment 653, 512–522. https://doi.org/10.1016/j.scitotenv.2018.10.381

López, N., Márquez Romance, A., Guevara Pérez, E., 2020. Change dynamics of land-use and land-cover for tropical wetland management. Water Practice and Technology 15, 632–644. https://doi.org/10.2166/wpt.2020.049

Louzada, R.O., Bergier, I., Assine, M.L., 2020. Landscape changes in avulsive river systems: Case study of Taquari River on Brazilian Pantanal wetlands. Science of The Total Environment 723, 138067. https://doi.org/10.1016/j.scitotenv.2020.138067

Lucas, R., Van De Kerchove, R., Otero, V., Lagomasino, D., Fatoyinbo, L., Omar, H., Satyanarayana, B., Dahdouh-Guebas, F., 2020. Structural characterisation of mangrove forests achieved through combining multiple sources of remote sensing data. Remote Sensing of Environment 237, 111543. https://doi.org/10.1016/j.rse.2019.111543

Luo, J., Li, X., Ma, R., Li, F., Duan, H., Hu, W., Qin, B., Huang, W., 2016. Applying remote sensing techniques to monitoring seasonal and interannual changes of aquatic vegetation in Taihu Lake, China. Ecological Indicators 60, 503–513. https://doi.org/10.1016/j.ecolind.2015.07.029

Lv, J., Jiang, W., Wang, W., Wu, Z., Liu, Y., Wang, X., Li, Z., 2019. Wetland Loss Identification and Evaluation Based on Landscape and Remote Sensing Indices in Xiong'an New Area. Remote Sensing 11, 2834. https://doi.org/10.3390/rs11232834

Lymburner, L., Bunting, P., Lucas, R., Scarth, P., Alam, I., Phillips, C., Ticehurst, C., Held, A., 2020. Mapping the multi-decadal mangrove dynamics of the Australian coastline. Remote Sensing of Environment 238, 111185. https://doi.org/10.1016/j.rse.2019.05.004

Ma, C., Ai, B., Zhao, J., Xu, X., Huang, W., 2019. Change Detection of Mangrove Forests in Coastal Guangdong during the Past Three Decades Based on Remote Sensing Data. Remote Sensing 11, 921. https://doi.org/10.3390/rs11080921

Mabwoga, S.O., Thukral, A.K., 2014. Characterization of change in the Harike wetland, a Ramsar site in India, using landsat satellite data. SpringerPlus 3, 576. https://doi.org/10.1186/2193-1801-3-576

Mahdianpari, M., Jafarzadeh, H., Granger, J.E., Mohammadimanesh, F., Brisco, B., Salehi, B., Homayouni, S., Weng, Q., 2020. A large-scale change monitoring of wetlands using time series Landsat imagery on Google Earth Engine: a case study in Newfoundland. GIScience & Remote Sensing 57, 1102–1124. https://doi.org/10.1080/15481603.2020.1846948

Maleki, S., Koupaei, S.S., Soffianian, A., Saatchi, S., Pourmanafi, S., Rahdari, V., 2019. Human and Climate Effects on the Hamoun Wetlands. Weather, Climate, and Society 11, 609–622. https://doi.org/10.1175/WCAS-D-18-0070.1

Mandal, M.S.H., Hosaka, T., 2020. Assessing cyclone disturbances (1988–2016) in the Sundarbans mangrove forests using Landsat and Google Earth Engine. Nat Hazards 102, 133–150. https://doi.org/10.1007/s11069-020-03914-z

Mao, D., Tian, Y., Wang, Z., Jia, M., Du, J., Song, C., 2021. Wetland changes in the Amur River Basin: Differing trends and proximate causes on the Chinese and Russian sides. Journal of Environmental Management 280, 111670. https://doi.org/10.1016/j.jenvman.2020.111670

Martínez-López, J., Carreño, M.F., Palazón-Ferrando, J.A., Martínez-Fernández, J., Esteve, M.A., 2014. Free advanced modeling and remote-sensing techniques for wetland watershed delineation and monitoring. International Journal of Geographical Information Science 28, 1610–1625. https://doi.org/10.1080/13658816.2013.852677

Marzvan, S., Moravej, K., Felegari, S., Sharifi, A., Askari, M.S., 2021. Risk Assessment of Alien Azolla filiculoides Lam in Anzali Lagoon Using Remote Sensing Imagery. Journal of the Indian Society of Remote Sensing 49, 1801–1809.

Masria, A., El-Adawy, A.A., Sarhan, T., 2020. A holistic evaluation of human-induced LULCC and shoreline dynamics of El-Burullus Lagoon through remote sensing techniques. Innov. Infrastruct. Solut. 5, 83. https://doi.org/10.1007/s41062-020-00331-w

Mazzarino, M., Finn, J.T., 2016. An NDVI analysis of vegetation trends in an Andean watershed. Wetlands Ecol Manage 24, 623–640. https://doi.org/10.1007/s11273-016-9492-0

Medjani, F., Hamdaoui, O., Djidel, M., Ducrot, D., 2015. Diachronic evolution of wetlands in a desert arid climate of the basin of Ouargla (southeastern Algeria) between 1987 and 2009 by remote sensing. Arab J Geosci 8, 10181–10192. https://doi.org/10.1007/s12517-015-1958-5

Meng, W., Hu, B., He, M., Liu, B., Mo, X., Li, H., Wang, Z., Zhang, Y., 2017. Temporal-spatial variations and driving factors analysis of coastal reclamation in China. Estuarine, Coastal and Shelf Science 191, 39–49. https://doi.org/10.1016/j.ecss.2017.04.008

Mexicano, L., Glenn, E.P., Hinojosa-Huerta, O., Garcia-Hernandez, J., Flessa, K., Hinojosa-Corona, A., 2013. Long-term sustainability of the hydrology and vegetation of Cienega de Santa Clara, an anthropogenic wetland created by disposal of agricultural drain water in the delta of the Colorado River, Mexico. Ecological Engineering, Colorado Delta Wetlands 59, 111–120. https://doi.org/10.1016/j.ecoleng.2012.12.096

Mialhe, F., Gunnell, Y., Navratil, O., Choi, D., Sovann, C., Lejot, J., Gaudou, B., Se, B., Landon, N., 2019. Spatial growth of Phnom Penh, Cambodia (1973–2015): Patterns, rates, and socio-ecological consequences. Land Use Policy 87, 104061. https://doi.org/10.1016/j.landusepol.2019.104061

Miranda, I.M., Toldo Jr, E.E., da Fontoura Klein, A.H., da Silva, G.V., 2019. Shoreline evolution of lagoon sandy spits and adjacent beaches, Lagoa dos Patos, Brazil. Journal of Coastal Research 35, 1010–1023.

Misra, A., R., M.M., P., V., 2015. Assessment of the land use/land cover (LU/LC) and mangrove changes along the Mandovi–Zuari estuarine complex of Goa, India. Arab J Geosci 8, 267–279. https://doi.org/10.1007/s12517-013-1220-y

Mo, Y., Kearney, M.S., Turner, R.E., 2020. The resilience of coastal marshes to hurricanes: The potential impact of excess nutrients. Environment International 138, 105409. https://doi.org/10.1016/j.envint.2019.105409

Mohanty, P.C., Shetty, S., Mahendra, R.S., Nayak, R.K., Sharma, L.K., Rama Rao, E.P., 2021. Spatio-temporal changes of mangrove cover and its impact on bio-carbon flux along the West Bengal coast, Northeast coast of India. European Journal of Remote Sensing 54, 525–537.

Mondal, D., Pal, S., 2016. Monitoring dual-season hydrological dynamics of seasonally flooded wetlands in the lower reach of Mayurakshi River, Eastern India. Geocarto International 33, 225–239. https://doi.org/10.1080/10106049.2016.1240720

Mozumder, C., Tripathi, N.K., Tipdecho, T., 2014. Ecosystem evaluation (1989–2012) of Ramsar wetland Deepor Beel using satellite-derived indices. Environ Monit Assess 186, 7909–7927. https://doi.org/10.1007/s10661-014-3976-2

Mu, S., Li, B., Yao, J., Yang, G., Wan, R., Xu, X., 2020. Monitoring the spatio-temporal dynamics of the wetland vegetation in Poyang Lake by Landsat and MODIS observations. Science of The Total Environment 725, 138096. https://doi.org/10.1016/j.scitotenv.2020.138096

Mukherjee, K., Pal, S., Mukhopadhyay, M., 2018. Impact of flood and seasonality on wetland changing trends in the Diara region of West Bengal, India. Spat. Inf. Res. 26, 357–367. https://doi.org/10.1007/s41324-018-0177-z

Munishi, S., Jewitt, G., 2019. Degradation of Kilombero Valley Ramsar wetlands in Tanzania. Physics and Chemistry of the Earth, Parts A/B/C 112, 216–227. https://doi.org/10.1016/j.pce.2019.03.008

Murray-Hudson, M., Wolski, P., Cassidy, L., Brown, M.T., Thito, K., Kashe, K., Mosimanyana, E., 2015. Remote Sensing-derived hydroperiod as a predictor of floodplain vegetation composition. Wetlands Ecol Manage 23, 603–616. https://doi.org/10.1007/s11273-014-9340-z

Nababa, I., Symeonakis, E., Koukoulas, S., Higginbottom, T., Cavan, G., Marsden, S., 2020. Land Cover Dynamics and Mangrove Degradation in the Niger Delta Region. Remote Sensing 12, 3619. https://doi.org/10.3390/rs12213619

Nagel, G.W., de Moraes Novo, E.M.L., Martins, V.S., Campos-Silva, J.V., Barbosa, C.C.F., Bonnet, M.P., 2022. Impacts of meander migration on the Amazon riverine communities using Landsat time series and cloud computing. Science of The Total Environment 806, 150449.

Naik, R., Sharma, L., 2021. Spatio-temporal modelling for the evaluation of an altered Indian saline Ramsar site and its drivers for ecosystem management and restoration. PloS one 16, e0248543.

Nannawo, A.S., Lohani, T.K., Eshete, A.A., 2021. Exemplifying the effects using WetSpass model depicting the landscape modifications on long-term surface and subsurface hydrological water balance in bilate basin, Ethiopia. Advances in Civil Engineering 2021.

Nasab, F.Q., Rahnama, M.B., 2019. Developing restoration strategies in Jazmurian wetland by remote sensing. Int. J. Environ. Sci. Technol. 17, 2767–2782. https://doi.org/10.1007/s13762-019-02568-0

Näschen, K., Diekkrüger, B., Leemhuis, C., Steinbach, S., Seregina, L., Thonfeld, F., van der Linden, R., 2018. Hydrological Modeling in Data-Scarce Catchments: The Kilombero Floodplain in Tanzania. Water 10, 599. https://doi.org/10.3390/w10050599

Nasser Mohamed Eid, A., Olatubara, C.O., Ewemoje, T.A., Farouk, H., El-Hennawy, M.T., 2020. Coastal wetland vegetation features and digital Change Detection Mapping based on remotely sensed imagery: El-Burullus Lake, Egypt. International Soil and Water Conservation Research 8, 66–79. https://doi.org/10.1016/j.iswcr.2020.01.004

Ndayisaba, F., Nahayo, L., Guo, H., Bao, A., Kayiranga, A., Karamage, F., Nyesheja, E., 2017. Mapping and Monitoring the Akagera Wetland in Rwanda. Sustainability 9, 174. https://doi.org/10.3390/su9020174

Nguyen, H.-H., McAlpine, C., Pullar, D., Johansen, K., Duke, N.C., 2013. The relationship of spatial–temporal changes in fringe mangrove extent and adjacent land-use: Case study of Kien Giang coast, Vietnam. Ocean & Coastal Management 76, 12–22. https://doi.org/10.1016/j.ocecoaman.2013.01.003

Nguyen, H.T.T., Hardy, G.E.S., Le, T.V., Nguyen, H.Q., Nguyen, H.H., Nguyen, T.V., Dell, B., 2021. Mangrove Forest Landcover Changes in Coastal Vietnam: A Case Study from 1973 to 2020 in Thanh Hoa and Nghe An Provinces. Forests 12, 637. https://doi.org/10.3390/f12050637

Nurwanda, A., Honjo, T., 2020. The prediction of city expansion and land surface temperature in Bogor City, Indonesia. Sustainable Cities and Society 52, 101772. https://doi.org/10.1016/j.scs.2019.101772

Obiefuna, J.N., Nwilo, P.C., Atagbaza, A.O., Okolie, C.J., 2013. Land Cover Dynamics Associated with the Spatial Changes in the Wetlands of Lagos/Lekki Lagoon System of Lagos, Nigeria. Journal of Coastal Research 29, 671–679. https://doi.org/10.2112/JCOASTRES-D-12-00038.1

O'Donnell, J.P.R., Schalles, J.F., 2016. Examination of Abiotic Drivers and Their Influence on Spartina alterniflora Biomass over a Twenty-Eight Year Period Using Landsat 5 TM Satellite Imagery of the Central Georgia Coast. Remote Sensing 8, 477. https://doi.org/10.3390/rs8060477

Orimoloye, I.R., Kalumba, A.M., Mazinyo, S.P., Nel, W., 2020. Geospatial analysis of wetland dynamics: wetland depletion and biodiversity conservation of Isimangaliso Wetland, South Africa. Journal of King Saud University-Science 32, 90–96.

Orimoloye, I.R., Mazinyo, S.P., Kalumba, A.M., Nel, W., Adigun, A.I., Ololade, O.O., 2019. Wetland shift monitoring using remote sensing and GIS techniques: landscape dynamics and its implications on Isimangaliso Wetland Park, South Africa. Earth Sci Inform 12, 553–563. https://doi.org/10.1007/s12145-019-00400-4

Otero, V., Lucas, R., Van De Kerchove, R., Satyanarayana, B., Mohd-Lokman, H., Dahdouh-Guebas, F., 2020. Spatial analysis of early mangrove regeneration in the Matang Mangrove Forest Reserve, Peninsular Malaysia, using geomatics. Forest Ecology and Management 472, 118213. https://doi.org/10.1016/j.foreco.2020.118213

Otero, V., Van De Kerchove, R., Satyanarayana, B., Mohd-Lokman, H., Lucas, R., Dahdouh-Guebas, F., 2019. An Analysis of the Early Regeneration of Mangrove Forests using Landsat Time Series in the Matang Mangrove Forest Reserve, Peninsular Malaysia. Remote Sensing 11, 774. https://doi.org/10.3390/rs11070774

Ouyang, Z., Becker, R., Shaver, W., Chen, J., 2014. Evaluating the sensitivity of wetlands to climate change with remote sensing techniques. Hydrological Processes 28, 1703–1712. https://doi.org/10.1002/hyp.9685

Ozturk, D., Sesli, F.A., 2015. Shoreline change analysis of the Kizilirmak Lagoon Series. Ocean & Coastal Management, Special Issue: Third International Symposium on Integrated Coastal Zone Management (ICZM): Towards Sustainable Coasts - "Recent developments and advancements" 118, 290–308. https://doi.org/10.1016/j.ocecoaman.2015.03.009

Özyavuz, M., 2011. Determination of Temporal Changes in Lakes Mert and Erikli Using Remote Sensing and Geographic Information Systems. Journal of Coastal Research 27, 174–181. https://doi.org/10.2112/JCOASTRES-D-10-00107.1

Pal, R., Biswas, S.S., Pramanik, M.K., Mondal, B., 2016. Bank vulnerability and avulsion modeling of the Bhagirathi-Hugli river between Ajay and Jalangi confluences in lower Ganga Plain, India. Modeling Earth Systems and Environment 2, 1–10. https://doi.org/10.1007/s40808-016-0125-7

Pal, S., Paul, S., 2021. Stability consistency and trend mapping of seasonally inundated wetlands in Moribund deltaic part of India. Environ Dev Sustain 23, 12925–12953. https://doi.org/10.1007/s10668-020-01193-z

Pan, F., Xie, J., Lin, J., Zhao, T., Ji, Y., Hu, Q., Pan, X., Wang, C., Xi, X., 2018. Evaluation of Climate Change Impacts on Wetland Vegetation in the Dunhuang Yangguan National Nature Reserve in Northwest China Using Landsat Derived NDVI. Remote Sensing 10, 735. https://doi.org/10.3390/rs10050735

Parihar, S.M., Sarkar, S., Dutta, A., Sharma, S., Dutta, T., 2013. Characterizing wetland dynamics: a post-classification change detection analysis of the East Kolkata Wetlands using open source satellite data. Geocarto International 28, 273–287. https://doi.org/10.1080/10106049.2012.705337

Pattanaik, C., Narendra Prasad, S., 2011. Assessment of aquaculture impact on mangroves of Mahanadi delta (Orissa), East coast of India using remote sensing and GIS. Ocean & Coastal Management 54, 789–795. https://doi.org/10.1016/j.ocecoaman.2011.07.013

Paul, S., Pal, S., 2020a. Exploring wetland transformations in moribund deltaic parts of India. Geocarto International 35, 1873–1894.

Paul, S., Pal, S., 2020b. Predicting wetland area and water depth of Ganges moribund deltaic parts of India. Remote Sensing Applications: Society and Environment 19, 100338. https://doi.org/10.1016/j.rsase.2020.100338

Pedreros-Guarda, M., Abarca-del-Río, R., Escalona, K., García, I., Parra, Ó., 2021. A Google Earth Engine Application to Retrieve Long-Term Surface Temperature for Small Lakes. Case: San Pedro Lagoons, Chile. Remote Sensing 13, 4544.

Peneva-Reed, E.I., Krauss, K.W., Bullock, E.L., Zhu, Z., Woltz, V.L., Drexler, J.Z., Conrad, J.R., Stehman, S.V., 2021. Carbon stock losses and recovery observed for a mangrove ecosystem following a major hurricane in Southwest Florida. Estuarine, Coastal and Shelf Science 248, 106750.

Pereira, G., Ramos, R. de C., Rocha, L.C., Brunsell, N.A., Merino, E.R., Mataveli, G.A.V., Cardozo, F. da S., 2021. Rainfall patterns and geomorphological controls driving inundation frequency in tropical wetlands: How does the Pantanal flood? Progress in Physical Geography: Earth and Environment 45, 669–686. https://doi.org/10.1177/0309133320987719

Pimple, U., Simonetti, D., Hinks, I., Oszwald, J., Berger, U., Pungkul, S., Leadprathom, K., Pravinvongvuthi, T., Maprasoap, P., Gond, V., 2020. A history of the rehabilitation of mangroves and an assessment of their diversity and structure using Landsat annual composites (1987–2019) and transect plot inventories. Forest Ecology and Management 462, 118007. https://doi.org/10.1016/j.foreco.2020.118007

Pirasteh, S., Zenner, E.K., Mafi-Gholami, D., Jaafari, A., Nouri Kamari, A., Liu, G., Zhu, Q., Li, J., 2021. Modeling mangrove responses to multi-decadal climate change and anthropogenic impacts using a long-term time series of satellite imagery. International Journal of Applied Earth Observation and Geoinformation 102, 102390. https://doi.org/10.1016/j.jag.2021.102390

Potter, C., Amer, R., 2020. Mapping 30 years of change in the marshlands of Breton Sound basin (southeastern Louisiana, USA): Coastal land area and vegetation green cover. Journal of Coastal Research 36, 437–450.

Pujiono, E., Kwak, D.-A., Lee, W.-K., Sulistyanto, Kim, S.-R., Lee, J.Y., Lee, S.-H., Park, T., Kim, M.-I., 2013. RGB-NDVI color composites for monitoring the change in mangrove area at the Maubesi Nature Reserve, Indonesia. Forest Science and Technology 9, 171–179. https://doi.org/10.1080/21580103.2013.842327

Qiu, P., Wu, N., Luo, P., Wang, Z., Li, M., 2009. Analysis of dynamics and driving factors of wetland landscape in Zoige, Eastern Qinghai-Tibetan Plateau. J. Mt. Sci. 6, 42–55. https://doi.org/10.1007/s11629-009-0230-4

Quader, M.A., Agrawal, S., Kervyn, M., 2017. Multi-decadal land cover evolution in the Sundarban, the largest mangrove forest in the world. Ocean & Coastal Management 139, 113–124. https://doi.org/10.1016/j.ocecoaman.2017.02.008

Quang, N.H., Quinn, C.H., Stringer, L.C., Carrie, R., Hackney, C.R., Van Hue, L.T., Van Tan, D., Nga, P.T.T., 2020. Multi-Decadal Changes in Mangrove Extent, Age and Species in the Red River Estuaries of Viet Nam. Remote Sensing 12, 2289. https://doi.org/10.3390/rs12142289

Rakotomavo, A., Fromard, F., 2010. Dynamics of mangrove forests in the Mangoky River delta, Madagascar, under the influence of natural and human factors. Forest Ecology and Management 259, 1161–1169. https://doi.org/10.1016/j.foreco.2010.01.002

Raynolds, M.K., Walker, D.A., 2016. Increased wetness confounds Landsat-derived NDVI trends in the central Alaska North Slope region, 1985–2011. Environ. Res. Lett. 11, 085004. https://doi.org/10.1088/1748-9326/11/8/085004

Reddy, C.S., Pasha, S.V., Jha, C.S., 2016. Spatio-temporal changes associated with natural and anthropogenic factors in wetlands of Great Rann of Kachchh, India. J Coast Conserv 20, 145–155. https://doi.org/10.1007/s11852-016-0425-0

Renó, V.F., Novo, E.M.L.M., Suemitsu, C., Rennó, C.D., Silva, T.S.F., 2011. Assessment of deforestation in the Lower Amazon floodplain using historical Landsat MSS/TM imagery. Remote Sensing of Environment 115, 3446–3456. https://doi.org/10.1016/j.rse.2011.08.008

Rosen, T., Xu, Y.J., 2015. Estimation of sedimentation rates in the distributary basin of the Mississippi River, the Atchafalaya River Basin, USA. Hydrology Research 46, 244–257. https://doi.org/10.2166/nh.2013.181

Rossi, R.E., Archer, S.K., Giri, C., Layman, C.A., 2020. The role of multiple stressors in a dwarf red mangrove (Rhizophora mangle) dieback. Estuarine, Coastal and Shelf Science 237, 106660. https://doi.org/10.1016/j.ecss.2020.106660

Samuel, K.J., Atobatele, R.E., 2019. Change in administrative status, urban growth, and land use/cover in a medium-sized African city. Human Geographies 13, 5–22.

Schaffer-Smith, D., Swenson, J.J., Barbaree, B., Reiter, M.E., 2017. Three decades of Landsat-derived spring surface water dynamics in an agricultural wetland mosaic; Implications for migratory shorebirds. Remote Sensing of Environment 193, 180–192. https://doi.org/10.1016/j.rse.2017.02.016

Schwatke, C., Scherer, D., Dettmering, D., 2019. Automated Extraction of Consistent Time-Variable Water Surfaces of Lakes and Reservoirs Based on Landsat and Sentinel-2. Remote Sensing 11, 1010. https://doi.org/10.3390/rs11091010

Shaeri Karimi, S., Saintilan, N., Wen, L., Cox, J., 2021. Spatio-temporal effects of inundation and climate on vegetation greenness dynamics in dryland floodplains. Ecohydrology e2378.

Sharma, G., Patnaik, K.V.K.R.K., 2020. Assessment of Coringa Mangrove shoreline migration using geospatial techniques. Journal of Operational Oceanography 1–10. https://doi.org/10.1080/1755876X.2020.1840245

Shewit, G., Minwyelet, M., Tesfaye, M., Lewoye, T., Ferehiwot, M., 2017. Land use change and its drivers in Kurt Bahir wetland, north-western Ethiopia. African Journal of Aquatic Science 42, 45–54. https://doi.org/10.2989/16085914.2017.1292178

Shi, S., Chang, Y., Li, Y., Hu, Y., Liu, M., Ma, J., Xiong, Z., Wen, D., Li, B., Zhang, T., 2021. Using Time Series Optical and SAR Data to Assess the Impact of Historical Wetland Change on Current Wetland in Zhenlai County, Jilin Province, China. Remote Sensing 13, 4514.

Shi, S., Chang, Y., Wang, G., Li, Z., Hu, Y., Liu, M., Li, Y., Li, B., Zong, M., Huang, W., 2020. Planning for the wetland restoration potential based on the viability of the seed bank and the land-use change trajectory in the Sanjiang Plain of China. Science of The Total Environment 733, 139208. https://doi.org/10.1016/j.scitotenv.2020.139208

Sibanda, S., Ahmed, F., 2020. Modelling historic and future land use/land cover changes and their impact on wetland area in Shashe sub-catchment, Zimbabwe. Model. Earth Syst. Environ. 7, 57–70. https://doi.org/10.1007/s40808-020-00963-y

Silio-Calzada, A., Barquín, J., Huszar, V.L.M., Mazzeo, N., Méndez, F., Álvarez-Martínez, J.M., 2017. Long-term dynamics of a floodplain shallow lake in the Pantanal wetland: Is it all about climate? Science of The Total Environment 605–606, 527–540. https://doi.org/10.1016/j.scitotenv.2017.06.183

Sohel, Md.S.I., Hore, S.K., Salam, M.A., Hoque, M.A., Ahmed, N., Rahman, M.M., Khan, H.M., Rahman, S., 2021. Analysis of erosion–accretion dynamics of major rivers of world's largest mangrove forest using geospatial techniques. Regional Studies in Marine Science 46, 101901. https://doi.org/10.1016/j.rsma.2021.101901

Soliman, G.A.A., Soussa, H., 2011. Wetland change detection in Nile swamps of southern Sudan using multitemporal satellite imagery. JARS 5, 053517. https://doi.org/10.1117/1.3571009

Son, N.-T., Chen, C.-F., Chang, N.-B., Chen, C.-R., Chang, L.-Y., Thanh, B.-X., 2015. Mangrove Mapping and Change Detection in Ca Mau Peninsula, Vietnam, Using Landsat Data and Object-Based Image Analysis. IEEE Journal of Selected Topics in Applied Earth Observations and Remote Sensing 8, 503–510. https://doi.org/10.1109/JSTARS.2014.2360691

Son, N.T., Thanh, B.X., Da, C.T., 2016. Monitoring Mangrove Forest Changes from Multi-temporal Landsat Data in Can Gio Biosphere Reserve, Vietnam. Wetlands 36, 565–576. https://doi.org/10.1007/s13157-016-0767-2

Song, K., Wang, Z., Du, J., Liu, L., Zeng, L., Ren, C., 2014. Wetland Degradation: Its Driving Forces and Environmental Impacts in the Sanjiang Plain, China. Environmental Management 2, 255–271. https://doi.org/10.1007/s00267-014-0278-y

Song, K., Wang, Z., Li, L., Tedesco, L., Li, F., Jin, C., Du, J., 2012. Wetlands shrinkage, fragmentation and their links to agriculture in the Muleng–Xingkai Plain, China. Journal of Environmental Management 111, 120–132. https://doi.org/10.1016/j.jenvman.2012.06.038

Soto, J., Román-Figueroa, C., Paneque, M., 2019. A Model for Estimating the Vegetation Cover in the High-Altitude Wetlands of the Andes (HAWA). Land 8, 20. https://doi.org/10.3390/land8010020

Sullivan, D.G., White, J.G., Vepraskas, M., 2019. Assessing Carolina Bay Wetland Restoration Risks to Downstream Water Quality by Characterizing Land Use and Stream Proximity. Wetlands 39, 495–506. https://doi.org/10.1007/s13157-018-1095-5

Sun, C., Fagherazzi, S., Liu, Y., 2018. Classification mapping of salt marsh vegetation by flexible monthly NDVI time-series using Landsat imagery. Estuarine, Coastal and Shelf Science 213, 61–80. https://doi.org/10.1016/j.ecss.2018.08.007

Suyadi, Gao, J., Lundquist, C.J., Schwendenmann, L., 2019. Land-based and climatic stressors of mangrove cover change in the Auckland Region, New Zealand. Aquatic Conserv: Mar Freshw Ecosyst 29, 1466–1483. https://doi.org/10.1002/aqc.3146

Tahsin, S., Medeiros, S.C., Singh, A., 2019. Wetland Dynamics Inferred from Spectral Analyses of Hydro-Meteorological Signals and Landsat Derived Vegetation Indices. Remote Sensing 12, 12. https://doi.org/10.3390/rs12010012

Talukdar, G., Sarma, A.K., Bhattacharjya, R.K., 2020. Mapping agricultural activities and their temporal variations in the riverine ecosystem of the Brahmaputra River using geospatial techniques. Remote Sensing Applications: Society and Environment 20, 100423. https://doi.org/10.1016/j.rsase.2020.100423

Tang, Z., Li, Y., Gu, Y., Jiang, W., Xue, Y., Hu, Q., LaGrange, T., Bishop, A., Drahota, J., Li, R., 2016. Assessing Nebraska playa wetland inundation status during 1985–2015 using Landsat data and Google Earth Engine. Environ Monit Assess 188, 654. https://doi.org/10.1007/s10661-016-5664-x

Tania, A.H., Gazi, Md.Y., Mia, Md.B., 2021. Evaluation of water quantity–quality, floodplain landuse, and land surface temperature (LST) of Turag River in Bangladesh: an integrated approach of geospatial, field, and laboratory analyses. SN Appl. Sci. 3, 63. https://doi.org/10.1007/s42452-020-04011-3

Taravat, A., Rajaei, M., Emadodin, I., Hasheminejad, H., Mousavian, R., Biniyaz, E., 2016. A Spaceborne Multisensory, Multitemporal Approach to Monitor Water Level and Storage Variations of Lakes. Water 8, 478. https://doi.org/10.3390/w8110478

Teferi, E., Uhlenbrook, S., Bewket, W., Wenninger, J., Simane, B., 2010. The use of remote sensing to quantify wetland loss in the Choke Mountain range, Upper Blue Nile basin, Ethiopia. Hydrology and Earth System Sciences 14, 2415–2428. https://doi.org/10.5194/hess-14-2415-2010

ter Borg, R.N., Barron, J., 2021. Development of constructed wetlands in agricultural landscapes using remote sensing techniques. Acta Agriculturae Scandinavica, Section B—Soil & Plant Science 1–16.

Thakur, S., Mondal, I., Bar, S., Nandi, S., Ghosh, P.B., Das, P., De, T.K., 2021. Shoreline changes and its impact on the mangrove ecosystems of some islands of Indian Sundarbans, North-East coast of India. Journal of Cleaner Production 284, 124764.

Thomas, R.F., Kingsford, R.T., Lu, Y., Cox, S.J., Sims, N.C., Hunter, S.J., 2015. Mapping inundation in the heterogeneous floodplain wetlands of the Macquarie Marshes, using Landsat Thematic Mapper. Journal of Hydrology 524, 194–213. https://doi.org/10.1016/j.jhydrol.2015.02.029

Thomas, R.F., Kingsford, R.T., Lu, Y., Hunter, S.J., 2011. Landsat mapping of annual inundation (1979–2006) of the Macquarie Marshes in semi-arid Australia. International Journal of Remote Sensing 32, 4545–4569. https://doi.org/10.1080/01431161.2010.489064

Tian, B., Zhou, Y.-X., Thom, R.M., Diefenderfer, H.L., Yuan, Q., 2015. Detecting wetland changes in Shanghai, China using FORMOSAT and Landsat TM imagery. Journal of Hydrology 529, 1–10. https://doi.org/10.1016/j.jhydrol.2015.07.007

Tian, Y., Luo, L., Mao, D., Wang, Z., Li, L., Liang, J., 2017. Using Landsat images to quantify different human threats to the Shuangtai Estuary Ramsar site, China. Ocean & Coastal Management 135, 56–64. https://doi.org/10.1016/j.ocecoaman.2016.11.011

Tibebu Kassawmar, N., Ram Mohan Rao, K., Lemlem Abraha, G., 2011. An integrated approach for spatio-temporal variability analysis of wetlands: a case study of Abaya and Chamo lakes, Ethiopia. Environ Monit Assess 180, 313–324. https://doi.org/10.1007/s10661-010-1790-z

Tin, H.C., Ni, T.N.K., Tuan, L.V., Saizen, I., Catherman, R., 2019. Spatial and temporal variability of mangrove ecosystems in the Cu Lao Cham-Hoi An Biosphere Reserve, Vietnam. Regional Studies in Marine Science 27, 100550. https://doi.org/10.1016/j.rsma.2019.100550

Tiné, M., Perez, L., Molowny-Horas, R., Darveau, M., 2019. Hybrid spatiotemporal simulation of future changes in open wetlands: A study of the Abitibi-Témiscamingue region, Québec, Canada. International Journal of Applied Earth Observation and Geoinformation 74, 302–313. https://doi.org/10.1016/j.jag.2018.10.001

Toosi, N.B., Soffianian, A.R., Fakheran, S., Pourmanafi, S., Ginzler, C., Waser, L.T., 2019. Comparing different classification algorithms for monitoring mangrove cover changes in southern Iran. Global Ecology and Conservation 19, e00662. https://doi.org/10.1016/j.gecco.2019.e00662

Tope-Ajayi, O.O., Adedeji, O.H., Adeofun, C.O., Awokola, S.O., 2016. Land use change assessment, prediction using remote sensing, and gis aided markov chain modelling at eleyele wetland area, Nigeria. Journal of Settlements and Spatial Planning 7, 51–63.

Tran, H., Tran, T., Kervyn, M., 2015. Dynamics of Land Cover/Land Use Changes in the Mekong Delta, 1973–2011: A Remote Sensing Analysis of the Tran Van Thoi District, Ca Mau Province, Vietnam. Remote Sensing 7, 2899–2925. https://doi.org/10.3390/rs70302899

Tran Thi, V., Tien Thi Xuan, A., Phan Nguyen, H., Dahdouh-Guebas, F., Koedam, N., 2014. Application of remote sensing and GIS for detection of long-term mangrove shoreline changes in Mui Ca Mau, Vietnam. Biogeosciences 11, 3781–3795. https://doi.org/10.5194/bg-11-3781-2014

Tuholske, C., Tane, Z., López-Carr, D., Roberts, D., Cassels, S., 2017. Thirty years of land use/cover change in the Caribbean: Assessing the relationship between urbanization and mangrove loss in Roatán, Honduras. Applied Geography 88, 84–93. https://doi.org/10.1016/j.apgeog.2017.08.018

Umarhadi, D.A., Widyatmanti, W., Kumar, P., Yunus, A.P., Khedher, K.M., Kharrazi, A., Avtar, R., 2022. Tropical peat subsidence rates are related to decadal LULC changes: Insights from InSAR analysis. Science of The Total Environment 816, 151561. https://doi.org/10.1016/j.scitotenv.2021.151561

Utami, W., Wibowo, Y.A., Hadi, A.H., Permadi, F.B., 2021. The impact of mangrove damage on tidal flooding in the subdistrict of Tugu, Semarang, Central Java. Journal of Degraded and Mining Lands Management 9, 3093.

Valderrama-Landeros, L., Blanco y Correa, M., Flores-Verdugo, F., Álvarez-Sánchez, L.F., Flores-de-Santiago, F., 2020. Spatiotemporal shoreline dynamics of Marismas Nacionales, Pacific coast of Mexico, based on a remote sensing and GIS mapping approach. Environ Monit Assess 192, 123. https://doi.org/10.1007/s10661-020-8094-8

Vanderhoof, M.K., Lane, C.R., McManus, M.G., Alexander, L.C., Christensen, J.R., 2018. Wetlands inform how climate extremes influence surface water expansion and contraction. Hydrol. Earth Syst. Sci. 22, 1851–1873. https://doi.org/10.5194/hess-22-1851-2018

Veettil, B., Quang, N., 2019. Mangrove forests of Cambodia: Recent changes and future threats. Ocean & Coastal Management 181, 104895. https://doi.org/10.1016/j.ocecoaman.2019.104895

Veettil, B.K., Florêncio de Souza, S., Simões, J.C., Ruiz Pereira, S.F., 2017. Decadal evolution of glaciers and glacial lakes in the Apolobamba–Carabaya region, tropical Andes (Bolivia–Peru). Geografiska Annaler: Series A, Physical Geography 99, 193–206. https://doi.org/10.1080/04353676.2017.1299577

Veettil, B.K., Van, D.D., Quang, N.X., Hoai, P.N., 2020. Spatiotemporal dynamics of mangrove forests in the Andaman and Nicobar Islands (India). Regional Studies in Marine Science 39, 101455. https://doi.org/10.1016/j.rsma.2020.101455

Vijay, R., Dey, J., Sakhre, S., Kumar, R., 2020. Impact of urbanization on creeks of Mumbai, India: a geospatial assessment approach. J Coast Conserv 24, 4. https://doi.org/10.1007/s11852-019-00721-y

Villate Daza, D.A., Sánchez Moreno, H., Portz, L., Portantiolo Manzolli, R., Bolívar-Anillo, H.J., Anfuso, G., 2020. Mangrove Forests Evolution and Threats in the Caribbean Sea of Colombia. Water 12, 1113. https://doi.org/10.3390/w12041113

Waiyasusri, K., 2021. Monitoring the Land Cover Changes in Mangrove Areas and Urbanization using Normalized Difference Vegetation Index and Normalized Difference Built-up Index in Krabi Estuary Wetland, Krabi Province, Thailand. Applied Environmental Research 43, 1–16.

Wan, L., Zhang, Y., Zhang, X., Qi, S., Na, X., 2015. Comparison of land use/land cover change and landscape patterns in Honghe National Nature Reserve and the surrounding Jiansanjiang Region, China. Ecological Indicators, Environmental issues in China: Monitoring, assessment and management 51, 205–214. https://doi.org/10.1016/j.ecolind.2014.11.025

Wang, D., Gao, S., Zhao, Yangyang, Chatzipavlis, A., Chen, Y., Gao, J., Zhao, Yongqiang, 2021. An eco-parametric method to derive sedimentation rates for coastal saltmarshes. Science of The Total Environment 770, 144756. https://doi.org/10.1016/j.scitotenv.2020.144756

Wang, P., Numbere, A.O., Camilo, G.R., 2016. Long-Term Changes in Mangrove Landscape of the Niger River Delta, Nigeria. American Journal of Environmental Sciences 12, 248–259. https://doi.org/10.3844/ajessp.2016.248.259

Wang, S., Zhang, Lifu, Zhang, H., Han, X., Zhang, Linshan, 2020. Spatial–Temporal Wetland Landcover Changes of Poyang Lake Derived from Landsat and HJ-1A/B Data in the Dry Season from 1973–2019. Remote Sensing 12, 1595.

Wang, X., Xiao, X., Xu, X., Zou, Z., Chen, B., Qin, Y., Zhang, X., Dong, J., Liu, D., Pan, L., Li, B., 2021. Rebound in China's coastal wetlands following conservation and restoration. Nat Sustain 4, 1076–1083. https://doi.org/10.1038/s41893-021-00793-5

Ward, D.P., Petty, A., Setterfield, S.A., Douglas, M.M., Ferdinands, K., Hamilton, S.K., Phinn, S., 2014. Floodplain inundation and vegetation dynamics in the Alligator Rivers region (Kakadu) of northern Australia assessed using optical and radar remote sensing. Remote Sensing of Environment 147, 43–55. https://doi.org/10.1016/j.rse.2014.02.009

Watchorn, K.E., Goldsborough, G., Hudon, C., Taranu, Z.E., 2021. Emergent vegetation in Netley-Libau Marsh: Temporal changes (1990–2013) in cover in relation to Lake Winnipeg level and Red River flow. Journal of Great Lakes Research 47, 690–702.

Wei, Q., Shao, Y., Xie, C., Cui, B., Tian, B., Brisco, B., Li, K., Tang, W., 2021. Number and nest-site selection of breeding black-necked cranes over the past 40 years in the Longbao Wetland Nature Reserve, Qinghai, China. Big Earth Data 5, 217–236.

Wells, A.F., Frost, G.V., Macander, M.J., Jorgenson, M.T., Roth, J.E., Davis, W.A., Pullman, E.R., 2021. Integrated terrain unit mapping on the Beaufort Coastal Plain, North Slope, Alaska, USA. Landscape Ecol 36, 549–579. https://doi.org/10.1007/s10980-020-01154-x

Wen, C., Dong, W., Meng, Y., Li, C., Zhang, Q., 2019. Application of a loose coupling model for assessing the impact of land-cover changes on groundwater recharge in the Jinan spring area, China. Environ Earth Sci 78, 382. https://doi.org/10.1007/s12665-019-8388-8

Wilson, N.R., Norman, L.M., 2018. Analysis of vegetation recovery surrounding a restored wetland using the normalized difference infrared index (NDII) and normalized difference vegetation index (NDVI). International Journal of Remote Sensing 39, 3243–3274.

Wilson, N.R., Norman, L.M., Villarreal, M., Gass, L., Tiller, R., Salywon, A., 2016. Comparison of remote sensing indices for monitoring of desert cienegas. Arid Land Research and Management 30, 460–478. https://doi.org/10.1080/15324982.2016.1170076

Wu, W., Yang, Z., Tian, B., Huang, Y., Zhou, Y., Zhang, T., 2018. Impacts of coastal reclamation on wetlands: Loss, resilience, and sustainable management. Estuarine, Coastal and Shelf Science 210, 153–161. https://doi.org/10.1016/j.ecss.2018.06.013

Wu, W., Zhao, Z., Mao, Y., 2015. A comparative study on the dynamics and geologic conditions of wetlands in Shangri-La County and Lijiang City in northwestern Yunnan plateau. International Journal of Sustainable Development & World Ecology 22, 151–155. https://doi.org/10.1080/13504509.2014.925520

Wu, W., Zhou, Y., Tian, B., 2017. Coastal wetlands facing climate change and anthropogenic activities: A remote sensing analysis and modelling application. Ocean & Coastal Management 138, 1–10. https://doi.org/10.1016/j.ocecoaman.2017.01.005

Wu, Y., Xiao, X., Chen, B., Ma, J., Wang, X., Zhang, Y., Zhao, B., Li, B., 2018. Tracking the phenology and expansion of Spartina alterniflora coastal wetland by time series MODIS and Landsat images. Multimed Tools Appl 79, 5175–5195. https://doi.org/10.1007/s11042-018-6314-9

Wulder, M.A., Li, Z., Campbell, E.M., White, J.C., Hobart, G., Hermosilla, T., Coops, N.C., 2018. A national assessment of wetland status and trends for Canada’s forested ecosystems using 33 years of earth observation satellite data. Remote Sensing 10, 1623.

Xiao, H., Su, F., Fu, D., Wang, Q., Huang, C., 2020. Coastal Mangrove Response to Marine Erosion: Evaluating the Impacts of Spatial Distribution and Vegetation Growth in Bangkok Bay from 1987 to 2017. Remote Sensing 12, 220. https://doi.org/10.3390/rs12020220

Xie, C., Huang, X., Mu, H., Yin, W., 2017. Impacts of Land-Use Changes on the Lakes across the Yangtze Floodplain in China. Environ. Sci. Technol. 51, 3669–3677. https://doi.org/10.1021/acs.est.6b04260

Xie, Z., Huete, A., Ma, X., Restrepo-Coupe, N., Devadas, R., Clarke, K., Lewis, M., 2016. Landsat and GRACE observations of arid wetland dynamics in a dryland river system under multi-decadal hydroclimatic extremes. Journal of Hydrology 543, 818–831. https://doi.org/10.1016/j.jhydrol.2016.11.001

Xie, Z., Liu, J., Ma, Z., Duan, X., Cui, Y., 2012a. Effect of surrounding land-use change on the wetland landscape pattern of a natural protected area in Tianjin, China. International Journal of Sustainable Development & World Ecology 19, 16–24. https://doi.org/10.1080/13504509.2011.583697

Xie, Z., Xu, L., Duan, X., Xu, X., 2012b. Analysis of boundary adjustments and land use policy change – A case study of Tianjin Palaeocoast and Wetland National Natural Reserve, China. Ocean & Coastal Management 56, 56–63. https://doi.org/10.1016/j.ocecoaman.2011.06.010

Yan, D., Li, J., Yao, X., Luan, Z., 2021. Quantifying the Long-Term Expansion and Dieback of Spartina Alterniflora Using Google Earth Engine and Object-Based Hierarchical Random Forest Classification. IEEE Journal of Selected Topics in Applied Earth Observations and Remote Sensing 14, 9781–9793.

Yang, L., Wang, Lunche, Yu, D., Yao, R., Li, C., He, Q., Wang, S., Wang, Lizhe, 2020. Four decades of wetland changes in Dongting Lake using Landsat observations during 1978–2018. Journal of Hydrology 587, 124954. https://doi.org/10.1016/j.jhydrol.2020.124954

Yesquen, D.L.N., Ayala, K.K.L., Olivera, C.C., Nakayo, J.L.J., Flores, J.W.V., Farfan, E.R.E., 2021. Impact of Climate Variability on the Ecological Components of a Swamp: the Case of Pantanos De Villa, Peru. Chemical Engineering Transactions 86, 493–498.

You, H., Xu, L., Liu, G., Wang, X., Wu, Y., Jiang, J., 2015. Effects of Inter-Annual Water Level Fluctuations on Vegetation Evolution in Typical Wetlands of Poyang Lake, China. Wetlands 35, 931–943. https://doi.org/10.1007/s13157-015-0684-9

Yu, H., Zhang, F., Kung, H., Johnson, V.C., Bane, C.S., Wang, J., Ren, Y., Zhang, Y., 2017. Analysis of land cover and landscape change patterns in Ebinur Lake Wetland National Nature Reserve, China from 1972 to 2013. Wetlands Ecol Manage 25, 619–637. https://doi.org/10.1007/s11273-017-9541-3

Yushanjiang, A., Zhang, F., Kung, H., Li, Z., 2018. Spatial–temporal variation of ecosystem service values in Ebinur Lake Wetland National Natural Reserve from 1972 to 2016, Xinjiang, arid region of China. Environ Earth Sci 77, 586. https://doi.org/10.1007/s12665-018-7764-0

Zefrehei, A.R.P., Aliakba, H., Saeid, P., Omid, B.K., Rasoul, G., 2020a. Detection and Prediction of Water Body and Aquatic Plants Cover Changes of Choghakhor International Wetland, Using Landsat Imagery and the Cellular Automata–Markov Model. Contemp. Probl. Ecol. 13, 545–555. https://doi.org/10.1134/S1995425520050091

Zefrehei, A.R.P., Fallah, M., Hedayati, A., 2021a. Applying remote sensing techniques to changes of water body and aquatic plants in Anzali International Wetland (1985-2018). Theoretical and Applied Ecology 65–72.

Zefrehei, A.R.P., Hedayati, A., Fallah, M., 2021b. Mapping Changes of Water Quality Parameters Pattern in Anzali International Wetland Using Remote Sensing. Journal of Water and Environment Technology 19, 130–138.

Zefrehei, A.R.P., Hedayati, A., Pourmanafi, S., Kashkooli, O.B., Ghorbani, R., 2020b. Monitoring spatiotemporal variability of water quality parameters Using Landsat imagery in Choghakhor International Wetland during the last 32 years. Ann. Limnol. - Int. J. Lim. 56, 6. https://doi.org/10.1051/limn/2020004

Zelelew, S.A., Abebe, W.B., Amsalu, T., 2021. Land-use cover change impact on Cranes nesting space in the Lake Tana Biosphere Reserve area, Blue Nile Basin. Wetlands Ecol Manage 29, 495–505. https://doi.org/10.1007/s11273-021-09796-7

Zhang, B., Zhang, Q., Feng, C., Feng, Q., Zhang, S., 2017. Understanding Land Use and Land Cover Dynamics from 1976 to 2014 in Yellow River Delta. Land 6, 20. https://doi.org/10.3390/land6010020

Zhang, J., Zhang, Y., Lloyd, H., Zhang, Z., Li, D., 2021. Rapid reclamation and degradation of suaeda salsa saltmarsh along coastal china's northern yellow sea. Land 10, 835.

Zhang, K., Thapa, B., Ross, M., Gann, D., 2016. Remote sensing of seasonal changes and disturbances in mangrove forest: a case study from South Florida. Ecosphere 7, e01366. https://doi.org/10.1002/ecs2.1366

Zhang, S., Na, X., Kong, B., Wang, Z., Jiang, H., Yu, H., Zhao, Z., Li, X., Liu, C., Dale, P., 2009. Identifying wetland change in China's Sanjiang Plain using remote sensing. Wetlands 29, 302. https://doi.org/10.1672/08-04.1

Zhang, S., Zhang, W., Zhang, L., Qi, Q., Xu, F., Huang, W., 2019. Analysis of water area in caofeidian wetland in 1984~2013 based on remote sensing image data. Environmental Engineering and Management Journal 18, 1347–1355.

Zhang, X., Zhang, Y., Zhu, L., Chi, W., Yang, Z., Wang, B., Lv, K., Wang, H., Lu, Z., 2018. Spatial-temporal evolution of the eastern Nanhui mudflat in the Changjiang (Yangtze River) Estuary under intensified human activities. Geomorphology 309, 38–50.

Zhang, Z., Ke, C., 2016. Monitoring and analysis of changes in a wetland landscape in Xingzi county. Earth Sci Inform 9, 35–45. https://doi.org/10.1007/s12145-015-0232-4

Zhang, Z., Lei, L., He, Z., Su, Y., Li, L., Wang, X., Guo, X., 2020. Tracking Changing Evidences of Water in Wetland Using the Satellite Long-Term Observations from 1984 to 2017. Water 12, 1602. https://doi.org/10.3390/w12061602

Zhao, C., Gong, J., Zeng, Q., Yang, M., Wang, Y., 2021. Landscape Pattern Evolution Processes and the Driving Forces in the Wetlands of Lake Baiyangdian. Sustainability 13, 9747.

Zhao, G., Ye, S., Li, G., Yu, X., McClellan, S.A., 2017. Soil Organic Carbon Storage Changes in Coastal Wetlands of the Liaohe Delta, China, Based on Landscape Patterns. Estuaries and Coasts 40, 967–976. https://doi.org/10.1007/s12237-016-0194-x

Zhao, H., Wang, X., Cai, Y., Liu, W., 2016. Wetland Transitions and Protection under Rapid Urban Expansion: A Case Study of Pearl River Estuary, China. Sustainability 8, 471. https://doi.org/10.3390/su8050471

Zheng, L., Xu, J., Tan, Z., Xu, G., Xu, L., Wang, X., 2020. A thirty-year Landsat study reveals changes to a river-lake junction ecosystem after implementation of the three Gorges dam. Journal of Hydrology 589, 125185. https://doi.org/10.1016/j.jhydrol.2020.125185

Zheng, L., Xu, J., Wang, D., Xu, G., Tan, Z., Xu, L., Wang, X., 2021. Acceleration of vegetation dynamics in hydrologically connected wetlands caused by dam operation. Hydrological Processes 35. https://doi.org/10.1002/hyp.14026

Zheng, Z., Li, Y., Guo, Y., Xu, Y., Liu, G., Du, C., 2015. Landsat-Based Long-Term Monitoring of Total Suspended Matter Concentration Pattern Change in the Wet Season for Dongting Lake, China. Remote Sensing 7, 13975–13999. https://doi.org/10.3390/rs71013975

Zhu, B., Liao, J., Shen, G., 2021. Combining time series and land cover data for analyzing spatio-temporal changes in mangrove forests: A case study of Qinglangang Nature Reserve, Hainan, China. Ecological Indicators 131, 108135. https://doi.org/10.1016/j.ecolind.2021.108135

Zhu, C., Zhang, X., Huang, Q., 2018. Four Decades of Estuarine Wetland Changes in the Yellow River Delta Based on Landsat Observations Between 1973 and 2013. Water 10, 933. https://doi.org/10.3390/w10070933

Appendix C. Full description of the categories listed in Table 1.2.1

Topics	Attributes	Categories
A. Landsat data analysis	A1. Change detection	**Diachronic**: change detection by processing two images of different dates. **Multitemporal**: processing of more than two images for several different dates. **Time Series**: processing of all available images.
	A2. Methods	**Classification**: classification (supervised or unsupervised) of land cover/use applied on one to several images. **Regression**: regression of parameters retrieved from Landsat archive. **Profile analysis**: time series analysis such as any methodology applied to all available Landsat images studying one or several parameters through time.
	A3. Artificial intelligence	**Yes**: use of artificial intelligence methods for Landsat archive processing (*e.g.* machine learning, deep learning). **No**: use of non-artificial intelligence methods (e.g. spectral index interpretation).
	A4. Deep learning	**Yes**: use of deep learning methods for Landsat archive processing. **No**: no use of deep learning methods.
	A5. Supervised method	**Yes**: use of supervised methods for Landsat archive processing. **No**: use of unsupervised methods.
	A6. Validation	**Field data**: validation of results using field reference data. **Visual image interpretation**: validation of results using visual interpretation of other image sources than Landsat (e.g. very high resolution imagery such as Google Earth images). **Both**: combination of field reference data and visual image interpretation for validation. **None**: no explicit validation provided.
B. Wetland monitoring	B1. Wetlands type	Defined based on level 2 Ramsar classification (see Appendix C)
	B2. Spatial extent	**Local**: study sites covering less than 10 000 km² **Regional**: study sites covering more than 10 000 km² or at country level. **Continental**: studies covering several countries in a same

	continent. **Global**: global coverage or study sites spread over several continents.
B3. Topic	**LULC**: studies aiming to monitor and describe land cover and land use changes in wetland habitats. **Fragmentation and connectivity**: studies aiming to monitor and investigate wetland fragmentation and connectivity. **Biophysical parameters**: studies aiming to investigate wetland biophysical parameter variations (*e.g.*, water surface temperature, chlorophyll content, biomass, phenology). **Hazards**: studies aiming to describe and evaluate the impacts of natural hazards on wetlands (*e.g.*, hurricanes, storms, earthquakes). **Ecosystem services**: studies aiming to evaluate and monitor ecosystem services of wetlands, as well as their economic values. **Biodiversity**: studies aiming to investigate and monitor wetlands biodiversity (*e.g.*, species composition). **Hydrology**: studies aiming to investigate floods, water presence, and levels of water availability in wetlands.
B4. Drivers of change	**LULC changes**: land cover and land use changes. **Climate changes**: includes various phenomena related to climate change (*e.g.* warming temperature, sea level rise). **Invasive species**: installation and spread of invasive species in wetland ecosystems. **Restauration and/or conservation**: measures and policies of restoration and conservation applied to wetlands. **Combination**: the combination of several drivers of change previously described. **No drivers of change**: studies in which drivers of change were not explicitly described.
B5. Essential Biodiversity Variables	**Species population**: Spatial and temporal variability in the distribution and abundance of species' populations. **Species traits**: Within-species variation in trait measurements along the axis of taxonomic diversity. **Community composition**: Abundance and diversity of organisms making up ecosystems. **Ecosystem function**: Attributes related to the performance of

		ecosystems that result from the collective activities of organisms. **Ecosystem structure**: Spatial arrangement of ecosystem units collectively defined by organisms forming these units.
	B6. Remote Sensing – Enabled Biodiversity Variables	**Examples of different remote sensing products related to each RS-EBV (from Skidmore et al. 2021 supplementary information):** **Species phenology**: Green-up (start of season); Senescence (end of season); Peak season (max of season). **Species morphology**: Leaf dry matter content; Specific Leaf Area **Species physiology**: Gross primary production (GPP); Net primary production (NPP); LAI; Chlorophyll content. **Population structure by age/size class**: Population density; Forest species and age class. **Species distribution**: Species richness; Species diversity indices (e.g., Shannon index). **Species abundance**: Species abundance; Relative species abundance. **Community diversity**: Taxonomic diversity; Functional diversity. **Species composition**: Number or percentage of species occurring together. **Ecosystem phenology**: Land surface green-up (start of season); Land surface senescence (end of season); Land surface peak (max of season). **Ecosystem physiology**: Gross primary production (GPP); Net primary production (NPP); LAI; Specific Leaf Area; Evapotranspiration; FAPAR; Ecosystem soil moisture; Carbon cycle; Chlorophyll and foliar content. **Ecosystem disturbances (natural source)**: Biological effects of irregular inundations; Biological effects of fire disturbances. **Spatial configuration**: Ecosystem structural variance; Ecosystem fragmentation. **Habitat structure**: Land cover; Fraction of vegetation cover; Above-ground biomass; LAI; Urban habitat; Ice cover habitat; Vegetation height; Habitat structure.
	B7. Remote Sensing Essential Climate Variables	**Examples of products related to Essential Climate Variables:** **Lakes**: Lake water level; Water extent; Lake surface water temperature; Lake ice thickness; Lake ice cover; Lake color.

	Soil moisture: Surface soil moisture; Surface inundation; Freeze/thaw; Root-zone soil moisture. **River discharge**: River discharge; Water level; Flow velocity; Cross-section. **Groundwater**: Groundwater volume charge; Groundwater level; Groundwater recharge; Groundwater discharge; Wellhead level; Water quality. **Glaciers**: Glacier area; Glacier elevation change; Glacier mass change. **Ice sheet and shelves**: Surface elevation change; Ice velocity; Ice mass change; Grounding line location and thickness. **Snow cover**: Area covered by snow; Snow depth; Snow water equivalent. **Permafrost**: Thermal state of permafrost; Active layer thickness. **Albedo**: Maps of DHR albedo for adaptation and modelling; Maps of BHR albedo for adaptation and modelling. **Land cover**: Maps of land cover; Maps of high-resolution land cover; Maps of key IPCC land use; Related changes and land management types. **Above-ground biomass**: Maps of above-ground biomass **Land surface temperature**: Maps of land surface temperature. **Evapotranspiration**: Land heat flux; Sensible heat flux. **Fire**: Burnt areas; Active fire maps; Fire radiative power. **Leaf Area Index**: Maps of LAI for adaptation and modelling. **Soil carbon**: %Carbon in soil; Mineral soil bulk density to 30 cms and 1m; Peatlands total depth of profile, area and location. **FAPAR**: Maps of FAPAR for adaptation and modelling. **Anthropogenic greenhouse gas fluxes**: Emissions from fossil fuel use, industry, agriculture and waste sector; Emissions/removals by IPCC land categories; Estimated fluxes by inversions of observed atmospheric composition – continental; Estimated fluxes by inversions of observed atmospheric composition – national; Hi-res CO_2 column concentrations to monitor point sources. **Anthropogenic water use**: Volume of water per year
B8. Intra-annual observations	**Yes**: processing of intra-annual images **No**: processing of inter-annual images

	B9. Study period	20 to 30 years / 30 to 40 years / More than 40 years
C. Landsat products	C1. Satellite	Landsat 1-2-3 (MSS) / Landsat 4-5 (MSS-TM) / Landsat 7 (ETM+) / Landsat 8 (OLI-TIRS)
	C2. Spectral domain	**Visible**: use of visible spectral bands (*i.e.*, from blue to red). **Infrared**: use of near-infrared (NIR) and short-wave infrared (SWIR) spectral bands. **Thermal**: use of thermal bands. **Combination**: mix of previously described categories.
	C3. Pre-processing level	**Level 1**: use of first preprocessing level of Landsat archive, i.e., not corrected from atmospheric effects. Also comprising studies that applied geometric corrections. **Level 2**: use of second preprocessing level of Landsat archive, i.e., corrected from atmospheric disturbances, geometry; pixel data in surface reflectance and temperature. **Derived products**: use of products derived from Landsat archive (e.g. Global Surface Water, Landsat Foliage Projection Cover). **Composite**: use of cloudless image composite retrieved from Landsat archive processing.
D. Tools	D1. Cloud	**Yes**: use of cloud computing solutions for processing. **No**: use of local computing solutions for processing.
	D2. Open-source software	**Yes**: use of open-source software for processing (e.g., QGIS, R, Python). **No**: use of non-open-source software for processing (*e.g.*, ERDAS, ENVI, ArcGis).
E. Users	E1. Users	**Scientists**: studies aiming to develop new methods and techniques useful for scientific community and fundamental research. **Managers**: studies aiming to bring elements and results in order to help policymakers and managers to improve wetland conservation (applied research). **Both**: studies showing interest in both previous categories.
	E2. Journals discipline	Main disciplines of journals in which the reviewed studies were published.

Appendix D. Ramsar Classification System of wetlands (Ramsar Convention Secretariat, 2006b). Single asterisk (*) refers to inclusion of floodplain wetlands such as seasonally inundated grasslands (including natural wet meadows), shrublands,

woodlands or forests. Double asterisks (**) refers to inclusion of intensively managed or grazed wet meadows or pastures.

Level 1	Level 2	Description
Marine/ Coastal wetlands	A	Permanent shallow marine waters less than six meters deep at low tide; includes sea bays and straits
	B	Marine subtidal aquatic beds; includes kelp beds, sea-grass beds, tropical marine meadows
	C	Coral reefs
	D	Rocky marine shores; includes rocky offshore islands, sea cliffs
	E	Sand, shingle or pebble shores; includes sand bars, spits and sandy islets; includes dune systems
	F	Estuarine waters; permanent water of estuaries and estuarine systems of deltas
	G	Intertidal mud, sand or salt flats
	H	Intertidal marshes; includes salt marshes, salt meadows, saltings, raised salt marshes; includes tidal brackish and freshwater marshes
	I	Intertidal forested wetlands; includes mangrove swamps, nipah swamps and tidal freshwater swamp forests
	J	Coastal brackish/saline lagoons; brackish to saline lagoons with at least one relatively narrow connection to the sea
	K	Coastal freshwater lagoons; includes freshwater delta lagoons
Inland wetlands	L	Permanent inland deltas
	M	Permanent rivers/streams/creeks; includes waterfalls
	N	Seasonal/intermittent/irregular rivers/streams/creeks
	O	Permanent freshwater lakes (over 8 ha); includes large oxbow lakes
	P	Seasonal/intermittent freshwater lakes (over 8 ha); includes floodplain lakes
	Q	Permanent saline/brackish/alkaline lakes
	R	Seasonal/intermittent saline/brackish/alkaline lakes and flats*
	Sp	Permanent saline/brackish/alkaline marshes/pools
	Ss	Seasonal/intermittent saline/brackish/alkaline marshes/ pools*
	Tp	Permanent freshwater marshes/pools; ponds (below 8 ha), marshes and swamps on inorganic soils; with emergent vegetation water-logged for at least most of the growing season

	Ts	Seasonal/intermittent freshwater marshes/pools on inorganic soil; includes sloughs, potholes, seasonally flooded meadows, sedge marshes*
	U	Non-forested peatlands; includes shrub or open bogs, swamps, fens
	Va	Alpine wetlands; includes alpine meadows, temporary waters from snowmelt
	Vt	Tundra wetlands; includes tundra pools, temporary waters from snowmelt
	W	Shrub-dominated wetlands; Shrub swamps, shrub-dominated freshwater marsh, shrub carr, alder thicket; on inorganic soils*
	Xf	Freshwater, tree-dominated wetlands; includes freshwater swamp forest, seasonally flooded forest, wooded swamps; on inorganic soils*
	Xp	Forested peatlands; peatswamp forest*
	Y	Freshwater springs; oases
	Zg	Geothermal wetlands
	Zk	Subterranean karst and cave hydrological systems
Human-made wetlands	1	Aquaculture (*e.g.* fish/shrimp) ponds
	2	Ponds; includes farm ponds, stock ponds, small tanks; (generally below 8 ha)
	3	Irrigated land; includes irrigation channels and rice fields
	4	Seasonally flooded agricultural land**
	5	Salt exploitation sites; salt pans, salines, etc.
	6	Water storage areas; reservoirs/barrages/dams/impoundments; (generally over 8 ha)
	7	Excavations; gravel/brick/clay pits; borrow pits, mining pools
	8	Wastewater treatment areas; sewage farms, settling ponds, oxidation basins
	9	Canals and drainage channels, ditches

Appendix E. Javascript GEE API code for selection of Landsat time series for CCDC input, modified and based on Arévalo et al. (2020)

```
////////////////////////////////////////////////////////////////////
//
// Utility functions for getting inputs for CCDC
//
// Modified version of Arévalo et al. (2020)
//
///////////////////////////////////////////////////////////////////

var dateUtils = require('users/parevalo_bu/gee-ccdc-tools:ccdcUtilities/dates.js')
var ccdcUtils = require('users/parevalo_bu/gee-ccdc-tools:ccdcUtilities/ccdc.js')

/**
* Get Landsat images for a specific region
* Possible bands and indices: BLUE, GREEN, RED, NIR, SWIR1, SWIR2, NDVI, NBR,
* EVI, EVI2,BRIGHTNESS, GREENNESS, WETNESS
* @param {ee.Dict} options Parameter file containing the keys below
* @param {Number} collection Lansat collection to use (1 or 2)
* @param {String} start First date to filter images
* @param {String} end Last date to filter images
* @param {String} startDoy First day of year to filter images
* @param {String} endDoy Last day of year to filter images
* @param {ee.Geometry} region Region to filter the collection
* @param {list} targetBands Bands and indices to return
* @param {Bool} useMask Retrieve images after performing filtering of clouds,
* cloud shadows and removing other bad pixels (true), or retrieve
* entire collection false)
* @param {Dictionary} sensors Dictionary with sensors to retrieve
* @return {ee.ImageCollection} Landat image collection filtered wit the specified
* parameters
*/
function getLandsat(options) {
  var collection = (options && options.collection) || 2
  var start = (options && options.start) || '1984-04-12'
  var end = (options && options.end) || '1984-04-13'
  var startDoy = (options && options.startDOY) || 1
  var endDoy = (options && options.endDOY) || 366
  var region = (options && options.region) || region
  var targetBands = (options && options.targetBands) || ['BLUE','GREEN','RED',
      'NIR','SWIR1','SWIR2','TEMP', 'NBR','NDFI','NDVI','GV','NPV','Shade','Soil',
      'EVI', 'EVI2', 'BRIGHTNESS', 'GREENNESS', 'WETNESS']
  var useMask = (options && options.useMask) || true
  var sensors = (options && options.sensors) || {l4: true, l5: true, l7: true, l8: true, l9:
true}

  //if (useMask == 'No') {
    //useMask = false
  //}

  // Define collection to use and select band names and functions accordingly
  if (collection == 1){
    var collection8 = ee.ImageCollection('LANDSAT/LC08/C01/T1_SR')
        .filterDate(start, end)
    var collection7 = ee.ImageCollection('LANDSAT/LE07/C01/T1_SR')
        .filterDate(start, end)
    var collection5 = ee.ImageCollection('LANDSAT/LT05/C01/T1_SR')
        .filterDate(start, end)
    var collection4 = ee.ImageCollection('LANDSAT/LT04/C01/T1_SR')
        .filterDate(start, end)

    // Retrieve filtered images (clouds, shadows, etc) or raw time series
    if (useMask) {
      collection9 = collection9.map(prepare)
      collection8 = collection8.map(prepareL8)
      collection7 = collection7.map(prepareL7)
      collection5 = collection5.map(prepareL4L5)
      collection4 = collection4.map(prepareL4L5)

    } else {
      var bandListL89 = ['B2', 'B3', 'B4', 'B5', 'B6', 'B7', 'B10']
      var nameListL89 = ['BLUE', 'GREEN', 'RED', 'NIR', 'SWIR1', 'SWIR2', 'TEMP']
      var bandListL457 = ['B1', 'B2','B3','B4','B5','B6','B7']
      var nameListL457 = ['BLUE', 'GREEN', 'RED', 'NIR', 'SWIR1', 'SWIR2']
      collection9 = collection9.map(function(i) {
        return i.select(bandListL89).rename(nameListL89)})
      collection8 = collection8.map(function(i) {
```

```
          return i.select(bandListL89).rename(nameListL89)})
      collection7 = collection7.map(function(i) {
          return i.select(bandListL457).rename(nameListL457)})
      collection4 = collection4.map(function(i) {
          return i.select(bandListL457).rename(nameListL457)})
      collection5 = collection5.map(function(i) {
          return i.select(bandListL457).rename(nameListL457)})

    }

  } else if (collection == 2){
    var collection9 = ee.ImageCollection('LANDSAT/LC09/C02/T1_L2')
        .filterDate(start, end);
    var collection8 = ee.ImageCollection('LANDSAT/LC08/C02/T1_L2')
        .filterDate(start, end);
    var collection7 = ee.ImageCollection('LANDSAT/LE07/C02/T1_L2')
        .filterDate(start, end);
    var collection5 = ee.ImageCollection('LANDSAT/LT05/C02/T1_L2')
        .filterDate(start, end);
    var collection4 = ee.ImageCollection('LANDSAT/LT04/C02/T1_L2')
        .filterDate(start, end);


    if (useMask) {
      collection9 = collection9.map(prepareL8L9Col2)
      collection8 = collection8.map(prepareL8L9Col2)
      collection7 = collection7.map(prepareL4L5L7Col2)
      collection5 = collection5.map(prepareL4L5L7Col2)
      collection4 = collection4.map(prepareL4L5L7Col2)

    } else {
      var bandListL89 = ['SR_B2', 'SR_B3', 'SR_B4', 'SR_B5', 'SR_B6', 'SR_B7', 'ST_B10']
      var nameListL89 = ['BLUE', 'GREEN', 'RED', 'NIR', 'SWIR1', 'SWIR2', 'TEMP']
      var bandListL457 = ['SR_B1', 'SR_B2','SR_B3','SR_B4','SR_B5','SR_B7', 'ST_B6']
      var nameListL457 = ['BLUE', 'GREEN', 'RED', 'NIR', 'SWIR1', 'SWIR2', 'TEMP']
      collection9 = collection9.map(function(i) {
        return i.select(bandListL89).rename(nameListL89)})
      collection8 = collection8.map(function(i) {
          return i.select(bandListL89).rename(nameListL89)})
      collection7 = collection7.map(function(i) {
          return i.select(bandListL457).rename(nameListL457)})
      collection4 = collection4.map(function(i) {
          return i.select(bandListL457).rename(nameListL457)})
      collection5 = collection5.map(function(i) {
          return i.select(bandListL457).rename(nameListL457)})
    }
  }

  // Merge all collections, compute indices and filter if requested
  var col = collection4.merge(collection5)
                       .merge(collection7)
                       .merge(collection8)
                       .merge(collection9)
  if (region) {
    col = col.filterBounds(region)
  }

  var indices = doIndices(col).select(targetBands)

  if (!sensors.l5) {
    indices = indices.filterMetadata('SATELLITE','not_equals','LANDSAT_5')
  }
  if (!sensors.l4) {
    indices = indices.filterMetadata('SATELLITE','not_equals','LANDSAT_4')
  }
  if (!sensors.l7) {
    indices = indices.filterMetadata('SATELLITE','not_equals','LANDSAT_7')
  }
  if (!sensors.l8) {
    indices = indices.filterMetadata('SATELLITE','not_equals','LANDSAT_8')
  }
  if (!sensors.l9) {
    indices = indices.filterMetadata('SATELLITE','not_equals','LANDSAT_9')
  }
  var indices = indices.filter(ee.Filter.dayOfYear(startDoy, endDoy))

  return ee.ImageCollection(indices)
}

/**
* Calculate spectral indices for all bands in collection
```

```
* @param {ee.ImageCollection} collection Landsat image collection
* @returns {ee.ImageCollection} Landsat image with spectral indices
*/
function doIndices(collection) {
  return collection.map(function(image) {
    var NDVI =  calcNDVI(image)
    var NBR = calcNBR(image)
    var EVI = calcEVI(image)
    var EVI2 = calcEVI2(image)
    var TC = tcTrans(image)
    // NDFI function requires surface reflectance bands only
    var BANDS = ['BLUE','GREEN','RED','NIR','SWIR1','SWIR2']
    var NDFI = calcNDFI(image.select(BANDS))
    return image.addBands([NDVI, NBR, EVI, EVI2, TC, NDFI])
  })
}

/**
 * Get Sentinel-2 surface reflectance data.
 * Taken directly from GEE examples repo.
 *
 * @param {ee.Geometry} roi target study area to filter data
 *
 * @returns (ee.ImageCollection) Sentinel-2 SR and spectral indices
 */
function getS2(roi) {
  // Sentinel-2 Level 1C data.  Bands B7, B8, B8A and B10 from this
  // dataset are needed as input to CDI and the cloud mask function.
  var s2 = ee.ImageCollection('COPERNICUS/S2');
  // Cloud probability dataset.  The probability band is used in
  // the cloud mask function.
  var s2c = ee.ImageCollection('COPERNICUS/S2_CLOUD_PROBABILITY');
  // Sentinel-2 surface reflectance data for the composite.
  var s2Sr = ee.ImageCollection('COPERNICUS/S2_SR');

  // Dates over which to create a median composite.
  var start = ee.Date('2016-03-01');
  var end = ee.Date('2021-09-01');

  // S2 L1C for Cloud Displacement Index (CDI) bands.
  s2 = s2.filterDate(start, end)
      .select(['B7', 'B8', 'B8A', 'B10']);
  // S2Cloudless for the cloud probability band.
  s2c = s2c.filterDate(start, end)
  // S2 L2A for surface reflectance bands.
  s2Sr = s2Sr.filterDate(start, end)
      .select(['B2', 'B3', 'B4', 'B5','B8','B11','B12']);
  if (roi) {
    s2 = s2.filterBounds(roi)
    s2c = s2c.filterBounds(roi)
    s2Sr = s2Sr.filterBounds(roi)
  }
  // Join two collections on their 'system:index' property.
  // The propertyName parameter is the name of the property
  // that references the joined image.
  function indexJoin(collectionA, collectionB, propertyName) {
    var joined = ee.ImageCollection(ee.Join.saveFirst(propertyName).apply({
      primary: collectionA,
      secondary: collectionB,
      condition: ee.Filter.equals({
        leftField: 'system:index',
        rightField: 'system:index'})
    }));
    // Merge the bands of the joined image.
    return joined.map(function(image) {
      return image.addBands(ee.Image(image.get(propertyName)));
    });
  }

  // Aggressively mask clouds and shadows.
  function maskImage(image) {
    // Compute the cloud displacement index from the L1C bands.
    var cdi = ee.Algorithms.Sentinel2.CDI(image);
    var s2c = image.select('probability');
    var cirrus = image.select('B10').multiply(0.0001);

    // Assume low-to-mid atmospheric clouds to be pixels where probability
    // is greater than 65%, and CDI is less than -0.5. For higher atmosphere
    // cirrus clouds, assume the cirrus band is greater than 0.01.
    // The final cloud mask is one or both of these conditions.
    var isCloud = s2c.gt(65).and(cdi.lt(-0.5)).or(cirrus.gt(0.01));
```

```
    // Reproject is required to perform spatial operations at 20m scale.
    // 20m scale is for speed, and assumes clouds don't require 10m precision.
    isCloud = isCloud.focal_min(3).focal_max(16);
    isCloud = isCloud.reproject({crs: cdi.projection(), scale: 20});

    // Project shadows from clouds we found in the last step. This assumes we're working in
    // a UTM projection.
    var shadowAzimuth = ee.Number(90)
        .subtract(ee.Number(image.get('MEAN_SOLAR_AZIMUTH_ANGLE')));

    // With the following reproject, the shadows are projected 5km.
    isCloud = isCloud.directionalDistanceTransform(shadowAzimuth, 50);
    isCloud = isCloud.reproject({crs: cdi.projection(), scale: 100});

    isCloud = isCloud.select('distance').mask();
    return image.select('B2', 'B3', 'B4','B8','B11','B12')
      .rename(['BLUE','GREEN','RED','NIR','SWIR1','SWIR2'])
      .divide(10000).updateMask(isCloud.not())
      .set('system:time_start',ee.Image(image.get('l1c')).get('system:time_start'))
  }

  // Join the cloud probability dataset to surface reflectance.
  var withCloudProbability = indexJoin(s2Sr, s2c, 'cloud_probability');
  // Join the L1C data to get the bands needed for CDI.
  var withS2L1C = indexJoin(withCloudProbability, s2, 'l1c');

  // Map the cloud masking function over the joined collection.
  return doIndices(ee.ImageCollection(withS2L1C.map(maskImage)));
}

/**
* Calculate NDVI for an image
* @param {ee.Image} image  Landsat image with NIR and RED bands
* @returns {ee.Image} NDVI image
*/
function calcNDVI(image) {
   var ndvi = ee.Image(image).normalizedDifference(['NIR', 'RED']).rename('NDVI');
   return ndvi
};

/**
* Calculate NBR for an image
* @param {ee.Image} image  Landsat image with NIR and SWIR2 bands
* @returns {ee.Image} NBR image
*/
function calcNBR(image) {
  var nbr = ee.Image(image).normalizedDifference(['NIR', 'SWIR2']).rename('NBR');
  return nbr
};

/**
 * Calculate NDFI using endmembers from Souza et al., 2005
 * @param {ee.Image} Surface reflectance image with 6 bands (i.e. not thermal)
 * @returns {ee.Image} NDFI transform
 */
function calcNDFI(image) {
  /* Do spectral unmixing */
  var gv = [.0500, .0900, .0400, .6100, .3000, .1000]
  var shade = [0, 0, 0, 0, 0, 0]
  var npv = [.1400, .1700, .2200, .3000, .5500, .3000]
  var soil = [.2000, .3000, .3400, .5800, .6000, .5800]
  var cloud = [.9000, .9600, .8000, .7800, .7200, .6500]
  var cf = .1 // Not parameterized
  var cfThreshold = ee.Image.constant(cf)
  var unmixImage = ee.Image(image).unmix([gv, shade, npv, soil, cloud], true,true)
                .rename(['band_0', 'band_1', 'band_2','band_3','band_4'])
  var newImage = ee.Image(image).addBands(unmixImage)
  var mask = newImage.select('band_4').lt(cfThreshold)
  var ndfi = ee.Image(unmixImage).expression(
    '((GV / (1 - SHADE)) - (NPV + SOIL)) / ((GV / (1 - SHADE)) + NPV + SOIL)', {
      'GV': ee.Image(unmixImage).select('band_0'),
      'SHADE': ee.Image(unmixImage).select('band_1'),
      'NPV': ee.Image(unmixImage).select('band_2'),
      'SOIL': ee.Image(unmixImage).select('band_3')
    })

  return ee.Image(newImage)
        .addBands(ee.Image(ndfi).rename(['NDFI']))
        .select(['band_0','band_1','band_2','band_3','NDFI'])
        .rename(['GV','Shade','NPV','Soil','NDFI'])
```

```
        .updateMask(mask)
  }

/**
* Calculate EVI for an image
* @param {ee.Image} image Landsat image with NIR, RED, and BLUE bands
* @returns {ee.Image} EVI transform
*/
function calcEVI(image) {

  var evi = ee.Image(image).expression(
          'float(2.5*(((B4) - (B3)) / ((B4) + (6 * (B3)) - (7.5 * (B1)) + 1)))',
          {
              'B4': ee.Image(image).select(['NIR']),
              'B3': ee.Image(image).select(['RED']),
              'B1': ee.Image(image).select(['BLUE'])
          }).rename('EVI');

  return evi
};

/**
* Calculate EVI2 for an image
* @param {ee.Image} image  Landsat image with NIR and RED
* @returns {ee.Image} EVI2 transform
*/
function calcEVI2(image) {
  var evi2 = ee.Image(image).expression(
        'float(2.5*(((B4) - (B3)) / ((B4) + (2.4 * (B3)) + 1)))',
        {
            'B4': image.select('NIR'),
            'B3': image.select('RED')
        });
  return evi2.rename('EVI2')
};

/**
* Tassel Cap coefficients from Crist 1985
* @param {ee.Image} image Landsat image with BLUE, GREEN, RED, NIR, SWIR1, and SWIR2
* @returns {ee.Image} 3-band image with Brightness, Greenness, and Wetness
*/
function tcTrans(image) {

    // Calculate tasseled cap transformation
    var brightness = image.expression(
        '(L1 * B1) + (L2 * B2) + (L3 * B3) + (L4 * B4) + (L5 * B5) + (L6 * B6)',
        {
            'L1': image.select('BLUE'),
            'B1': 0.2043,
            'L2': image.select('GREEN'),
            'B2': 0.4158,
            'L3': image.select('RED'),
            'B3': 0.5524,
            'L4': image.select('NIR'),
            'B4': 0.5741,
            'L5': image.select('SWIR1'),
            'B5': 0.3124,
            'L6': image.select('SWIR2'),
            'B6': 0.2303
        });
    var greenness = image.expression(
        '(L1 * B1) + (L2 * B2) + (L3 * B3) + (L4 * B4) + (L5 * B5) + (L6 * B6)',
        {
            'L1': image.select('BLUE'),
            'B1': -0.1603,
            'L2': image.select('GREEN'),
            'B2': -0.2819,
            'L3': image.select('RED'),
            'B3': -0.4934,
            'L4': image.select('NIR'),
            'B4': 0.7940,
            'L5': image.select('SWIR1'),
            'B5': -0.0002,
            'L6': image.select('SWIR2'),
            'B6': -0.1446
        });
    var wetness = image.expression(
        '(L1 * B1) + (L2 * B2) + (L3 * B3) + (L4 * B4) + (L5 * B5) + (L6 * B6)',
        {
            'L1': image.select('BLUE'),
            'B1': 0.0315,
```

```
            'L2': image.select('GREEN'),
            'B2': 0.2021,
            'L3': image.select('RED'),
            'B3': 0.3102,
            'L4': image.select('NIR'),
            'B4': 0.1594,
            'L5': image.select('SWIR1'),
            'B5': -0.6806,
            'L6': image.select('SWIR2'),
            'B6': -0.6109
        });

    var bright =  ee.Image(brightness).rename('BRIGHTNESS');
    var green = ee.Image(greenness).rename('GREENNESS');
    var wet = ee.Image(wetness).rename('WETNESS');

    var tasseledCap = ee.Image([bright, green, wet])
    return tasseledCap
}

/**
 * Create a grid with features corresponding to latitudinal strips
 * @param {Dictionary} options parameter file
 * @param {Number} minY  minimum latititude coordinate
 * @param {Number} maxY  maximum latititude coordinate
 * @param {Number} minX  minimum longitude coordinate
 * @param {Number} minX  maximum longitude coordinate
 * @param {Number} size size of features in units of latitudinal degrees
 * @returns {ee.FeatureCollection} grid of features along latitudinal lines
*/
function makeLatGrid(minY, maxY, minX, maxX, size) {

  var ySeq = ee.List.sequence(minY, maxY, size)
  var numFeats = ySeq.length().subtract(2)
  var feats = ee.List.sequence(0, numFeats).map(function(num) {
    num = ee.Number(num)
    var num2 = num.add(1)
    var y1 = ee.Number(ySeq.get(num))
    var y2 = ee.Number(ySeq.get(num2))
    var feat = ee.Feature(ee.Geometry.Polygon([[maxX, y2], [minX, y2], [minX, y1], [maxX,
y1]]))
    return feat
  })
  return ee.FeatureCollection(feats)
}

/**
 * Create a grid with features corresponding to longitudinal strips
 * @param {Dictionary} options parameter file
 * @param {Number} minY minimum latititude coordinate
 * @param {Number} maxY maximum latititude coordinate
 * @param {Number} minX minimum longitude coordinate
 * @param {Number} minX maximum longitude coordinate
 * @param {Number} size size of features in units of latitudinal degrees
 * @returns {ee.FeatureCollection} grid of features along longitudinal lines
 */
function makeLonGrid(minY, maxY, minX, maxX, size) {

  var ySeq = ee.List.sequence(minX, maxX, size)
  var numFeats = ySeq.length().subtract(2)
  var feats = ee.List.sequence(0, numFeats).map(function(num) {
    num = ee.Number(num)
    var num2 = num.add(1)
    var x1 = ee.Number(ySeq.get(num))
    var x2 = ee.Number(ySeq.get(num2))
    var feat = ee.Feature(ee.Geometry.Polygon([[x2, maxY], [x1, maxY], [x1, minY], [x2,
minY]]))
    return feat
  })
  return ee.FeatureCollection(feats)
}

/**
 * Create a grid with features corresponding to longitudinal strips
 * @param {Number} minY minimum latititude coordinate
 * @param {Number} maxY maximum latititude coordinate
 * @param {Number} minX minimum longitude coordinate
 * @param {Number} minX maximum longitude coordinate
 * @param {Number} size size of features in units of latitudinal degrees
 * @returns {ee.FeatureCollection} grid of features along longitudinal lines
*/
```

```
function makeLonLatGrid(minY, maxY, minX, maxX, size) {

  var xSeq = ee.List.sequence(minX, maxX, size)
  var ySeq = ee.List.sequence(minY, maxY, size)

  var numFeatsY = ySeq.length().subtract(2)
  var numFeatsX = xSeq.length().subtract(2)

  var feats = ee.List.sequence(0, numFeatsY).map(function(y) {
    y = ee.Number(y)
    var y2 = y.add(1)
    var y1_val = ee.Number(ySeq.get(y))
    var y2_val = ee.Number(ySeq.get(y2))
    var feat = ee.List.sequence(0, numFeatsX).map(function(x) {
      x = ee.Number(x)
      var x2 = x.add(1)
      var x1_val = ee.Number(xSeq.get(x))
      var x2_val = ee.Number(xSeq.get(x2))
      return ee.Feature(ee.Geometry.Polygon([[x2_val, y2_val], [x1_val, y2_val], [x1_val,
y1_val], [x2_val, y1_val]]))
    })
    return feat

  })
  return ee.FeatureCollection(feats.flatten())
}

/**
* Create a grid with features overlaying the bounding box of a geometry
* @param {ee.Geometry} geo geometry to use as spec for grid
* @param {Number} size size of features in units of degrees
* @returns {ee.FeatureCollection} grid of features along
*/
function makeAutoGrid(geo, size) {
  var coordList = ee.List(geo.coordinates().get(0))

  var lonList = coordList.map(function (c) {
    return ee.List(c).flatten().get(0);
  })

  var latList = coordList.map(function (c) {
    return ee.List(c).flatten().get(1);
  })


  var minY = latList.reduce(ee.Reducer.min())
  var maxY = latList.reduce(ee.Reducer.max())


  var minX = lonList.reduce(ee.Reducer.min())
  var maxX = lonList.reduce(ee.Reducer.max())

  var xSeq = ee.List.sequence(minX, maxX, size)
  var ySeq = ee.List.sequence(minY, maxY, size)

  var numFeatsY = ySeq.length().subtract(2)
  var numFeatsX = xSeq.length().subtract(2)

  var feats = ee.List.sequence(0, numFeatsY).map(function(y) {
    y = ee.Number(y)
    var y2 = y.add(1)
    var y1_val = ee.Number(ySeq.get(y))
    var y2_val = ee.Number(ySeq.get(y2))
    var feat = ee.List.sequence(0, numFeatsX).map(function(x) {
      x = ee.Number(x)
      var x2 = x.add(1)
      var x1_val = ee.Number(xSeq.get(x))
      var x2_val = ee.Number(xSeq.get(x2))
      return ee.Feature(ee.Geometry.Polygon([[x2_val, y2_val], [x1_val, y2_val], [x1_val,
y1_val], [x2_val, y1_val]]))
    })
    return feat

  })
  return ee.FeatureCollection(feats.flatten())
}


/**
* Get ancillary data for trainning and classification.
* @returns {ee.Image} Multi-band image containing ancillary layers
```

```
*/
function getAncillary(){

  var srtm = ee.Image('USGS/SRTMGL1_003').rename('ELEVATION')
  var alos =  ee.Image("JAXA/ALOS/AW3D30/V2_2").select(0).rename('ELEVATION')
  var demImage = ee.ImageCollection([alos,srtm]).mosaic()

  var slope = ee.Terrain.slope(demImage).rename('DEM_SLOPE')
  var aspect = ee.Terrain.aspect(demImage).rename('ASPECT')
  var bio =
ee.Image('WORLDCLIM/V1/BIO').select(['bio01','bio12']).rename(['TEMPERATURE','RAINFALL'])
  var water = ee.Image('JRC/GSW1_1/GlobalSurfaceWater')
    .select('occurrence')
    .rename('WATER_OCCURRENCE')
  var pop = ee.ImageCollection("WorldPop/GP/100m/pop")
    .filterMetadata('year','equals',2000)
    .mosaic()
    .rename('POPULATION')

  var hansen = ee.Image("UMD/hansen/global_forest_change_2018_v1_6")
    .select('treecover2000')
    .rename('TREE_COVER')

  var nightLights = ee.ImageCollection("NOAA/VIIRS/DNB/MONTHLY_V1/VCMCFG")
                          .filter(ee.Filter.date('2019-01-01', '2019-12-31'))
                          .select('avg_rad')
                          .mosaic()
                          .rename('NIGHT_LIGHTS')

  // I can't get this to work without memory errors
  // var settlement = ee.Image("JRC/GHSL/P2016/SMOD_POP_GLOBE_V1/2000")
  // var distance = ee.Image(1).cumulativeCost(
  //   settlement.gt(1),
  //   100000)
  // .divide(100)
  // .int32()
  // .rename('DISTANCE_SETTLEMENT')

  return ee.Image.cat([demImage, slope, aspect, bio, pop, water, hansen,
nightLights]).unmask()

}

// /**
// * Get Sentinel-2 Data
// * From EE Examples Repo
// * @param {string} startDate beginning date in format 'YYYY-MM-DD'
// * @param {string} endDate end date in format 'YYYY-MM-DD'
// * @returns {ee.Image} masked median Sentinel-2 image
// */
// var getS2 = function(startDate, endDate) {
//   startDate = startDate || '2014-01-01'
//   endDate = endDate || '2021-12-31'

//   var maskS2clouds = function(image) {
//     var qa = image.select('QA60')

//     // Bits 10 and 11 are clouds and cirrus, respectively.
//     var cloudBitMask = 1 << 10;
//     var cirrusBitMask = 1 << 11;

//     // Both flags should be set to zero, indicating clear conditions.
//     var mask = qa.bitwiseAnd(cloudBitMask).eq(0).and(
//               qa.bitwiseAnd(cirrusBitMask).eq(0))

//     // Return the masked and scaled data, without the QA bands.
//     return image.updateMask(mask).divide(10000)
//         .select("B.*")
//         .copyProperties(image, ["system:time_start"])
//   }

//   // Map the function over one year of data and take the median.
//   // Load Sentinel-2 TOA reflectance data.
//   var collection = ee.ImageCollection('COPERNICUS/S2_SR')
//       // Pre-filter to get less cloudy granules.
//       .filter(ee.Filter.lt('CLOUDY_PIXEL_PERCENTAGE', 50))
//       .map(maskS2clouds)

//       //4 and 8
//   // Add NDVI
//   collection = collection.map(function(im) {
```

```
//     return im.addBands(ee.Image(im).normalizedDifference(['B8', 'B4']).rename('NDVI'));

//   })

//   return collection
// }



function prepare(orbit) {
  // Load the Sentinel-1 ImageCollection.
  return ee.ImageCollection('COPERNICUS/S1_GRD')
    .filter(ee.Filter.listContains('transmitterReceiverPolarisation', 'VV'))
    .filter(ee.Filter.listContains('transmitterReceiverPolarisation', 'VH'))
    .filter(ee.Filter.eq('instrumentMode', 'IW'))
    .filter(ee.Filter.eq('orbitProperties_pass', orbit))
}

/**
 * Get Sentinel 1 data
 * @param {string} [mode='ASCENDING'] orbital pass mode ('ASCENDING' or 'DESCENDING')
 * @param {number} [focalSize=3] window size for focal mean (1 means no averaging)
 * @return {ee.ImageCollection} Sentinel 1 collection with VH, VV, and ratio bands smoothed
with focal mean
 */
function getS1(focalSize, kernelType) {
  focalSize = focalSize || 3
  kernelType = kernelType || 'circle'
  var data = ee.ImageCollection('COPERNICUS/S1_GRD')
    .filter(ee.Filter.listContains('transmitterReceiverPolarisation', 'VV'))
    .filter(ee.Filter.listContains('transmitterReceiverPolarisation', 'VH'))
    .filter(ee.Filter.eq('instrumentMode', 'IW'))
    .select(['V.','angle'])
    .map(function(img) {
      var geom = img.geometry()
      var angle = img.select('angle')
      var edge = img.select('VV').lt(-30.0); //-30

      var fmean = img.select('V.').add(30).focal_mean(focalSize, kernelType)
      var ratio = fmean.select('VH').divide(fmean.select('VV')).rename('ratio').multiply(30)
      return
img.select().addBands(fmean).addBands(ratio).addBands(angle)//.clip(geom)//.set('angle',angle)
    })

    // .select(['V.','angle'])
    // .map(function(img) {
    //   var angle = img.select('angle').sample({numPixels: 1}).first().get('angle')
    //   var angleReversed = img.select('angle').multiply(-1).rename('angleReversed')
    //   var edge = img.select('VV').lt(-30.0); //-30

    //   var fmean = img.select('V.').add(30).focal_mean(focalSize, kernelType )
    //   var ratio =
fmean.select('VH').divide(fmean.select('VV')).rename('ratio').multiply(30)
    //   var smoothed = img.select('angle').addBands([fmean, ratio, angleReversed])
    //   return smoothed.updateMask(edge.not()).set('angle',angle)
    // })

  return data
  }

/**
 * Generate Landsat collection as created for the global CCDC algorithm
 * AKA Noel's filtering
 */


/**
* Prepare Landsat 4 and 5 with strict filtering of noisy pixels
* @param {ee.Image} image Landsat SR image with pixel_qa band
* @returns {ee.Image} Landsat image with masked noisy pixels
*/
function prepareL4L5(image){
  var bandList = ['B1', 'B2','B3','B4','B5','B7','B6']
  var nameList = ['BLUE', 'GREEN', 'RED', 'NIR', 'SWIR1', 'SWIR2', 'TEMP']
  var scaling = [10000, 10000, 10000, 10000, 10000, 10000, 1000]
  var scaled =
ee.Image(image).select(bandList).rename(nameList).divide(ee.Image.constant(scaling))

  var validQA = [66, 130, 68, 132]
  var mask1 = ee.Image(image).select(['pixel_qa']).remap(validQA, ee.List.repeat(1,
validQA.length), 0)
```

```
  // Gat valid data mask, for pixels without band saturation
  var mask2 = image.select('radsat_qa').eq(0)
  var mask3 = image.select(bandList).reduce(ee.Reducer.min()).gt(0)
  // Mask hazy pixels. Aggressively filters too many images in arid regions (e.g Egypt)
  // unless we force include 'nodata' values by unmasking
  var mask4 = image.select("sr_atmos_opacity").unmask().lt(300)
  return ee.Image(image).addBands(scaled).updateMask(mask1.and(mask2).and(mask3).and(mask4))
}

/**
* Prepare Landsat 7 with strict filtering of noisy pixels
* @param {ee.Image} image Landsat SR image with pixel_qa band
* @returns {ee.Image} Landsat image with masked noisy pixels
*/
function prepareL7(image){
  var bandList = ['B1', 'B2','B3','B4','B5','B7','B6']
  var nameList = ['BLUE', 'GREEN', 'RED', 'NIR', 'SWIR1', 'SWIR2', 'TEMP']
  var scaling = [10000, 10000, 10000, 10000, 10000, 10000, 1000]
  var scaled =
ee.Image(image).select(bandList).rename(nameList).divide(ee.Image.constant(scaling))

  var validQA = [66, 130, 68, 132]
  var mask1 = ee.Image(image).select(['pixel_qa']).remap(validQA, ee.List.repeat(1,
validQA.length), 0)
  // Gat valid data mask, for pixels without band saturation
  var mask2 = image.select('radsat_qa').eq(0)
  var mask3 = image.select(bandList).reduce(ee.Reducer.min()).gt(0)
  // Mask hazy pixels. Aggressively filters too many images in arid regions (e.g Egypt)
  // unless we force include 'nodata' values by unmasking
  var mask4 = image.select("sr_atmos_opacity").unmask().lt(300)
  // Slightly erode bands to get rid of artifacts due to scan lines
  var mask5 = ee.Image(image).mask().reduce(ee.Reducer.min()).focal_min(2.5)
  return
ee.Image(image).addBands(scaled).updateMask(mask1.and(mask2).and(mask3).and(mask4).and(mask5))
}

/**
* Prepare Landsat 8 with strict filtering of noisy pixels
* @param {ee.Image} image Landsat SR image with pixel_qa band
* @returns {ee.Image} Landsat image with masked noisy pixels
*/
function prepareL8(image){
  var bandList = ['B2', 'B3', 'B4', 'B5', 'B6', 'B7', 'B10']
  var nameList = ['BLUE', 'GREEN', 'RED', 'NIR', 'SWIR1', 'SWIR2', 'TEMP']
  var scaling = [10000, 10000, 10000, 10000, 10000, 10000, 1000]

  var validTOA = [66, 68, 72, 80, 96, 100, 130, 132, 136, 144, 160, 164]
  var validQA = [322, 386, 324, 388, 836, 900]

  var scaled =
ee.Image(image).select(bandList).rename(nameList).divide(ee.Image.constant(scaling))
  var mask1 = ee.Image(image).select(['pixel_qa']).remap(validQA, ee.List.repeat(1,
validQA.length), 0)
  var mask2 = image.select('radsat_qa').eq(0)
  var mask3 = image.select(bandList).reduce(ee.Reducer.min()).gt(0)
  var mask4 = ee.Image(image).select(['sr_aerosol']).remap(validTOA, ee.List.repeat(1,
validTOA.length), 0)
  return ee.Image(image).addBands(scaled).updateMask(mask1.and(mask2).and(mask3).and(mask4))
}

/**
* Prepare Collection 2 Landsat 4, 5, and 7 with strict filtering of noisy pixels
* @param {ee.Image} image Landsat SR image with pixel_qa band
* @returns {ee.Image} Landsat image with masked noisy pixels
*/
function prepareL4L5L7Col2(image){

  var bandList = ['SR_B1','SR_B2','SR_B3','SR_B4','SR_B5','SR_B7','ST_B6']
  var nameList = ['BLUE', 'GREEN', 'RED', 'NIR', 'SWIR1', 'SWIR2', 'TEMP']
  var subBand = ['BLUE', 'GREEN', 'RED', 'NIR', 'SWIR1', 'SWIR2']

  var opticalBands = image.select('SR_B.').multiply(0.0000275).add(-0.2);
  var thermalBand = image.select('ST_B6').multiply(0.00341802).add(149.0);
  var scaled = opticalBands.addBands(thermalBand, null, true).select(bandList)
      .rename(nameList);

  var validQA = [5440, 5504]  //5442, 5506

  var mask1 = ee.Image(image).select(['QA_PIXEL']).remap(
      validQA, ee.List.repeat(1, validQA.length), 0)
```

```
  // Gat valid data mask, for pixels without band saturation
  var mask2 = image.select('QA_RADSAT').eq(0)
  var mask3 = scaled.select(subBand).reduce(ee.Reducer.min()).gt(0)
  var mask4 = scaled.select(subBand).reduce(ee.Reducer.max()).lt(1)
  // Mask hazy pixels using AOD threshold
  var mask5 = (image.select("SR_ATMOS_OPACITY").unmask(-1)).lt(300)
  return ee.Image(image).addBands(scaled)
      .updateMask(mask1.and(mask2).and(mask3).and(mask4).and(mask5))
}

/**
* Prepare Collection 2 Landsat 8 with strict filtering of noisy pixels
* @param {ee.Image} image Landsat SR image with pixel_qa band
* @param {Boolean} switch between with/without mask
* @returns {ee.Image} Landsat image with masked noisy pixels
*/
function prepareL8L9Col2(image){

  var bandList = ['SR_B2', 'SR_B3', 'SR_B4', 'SR_B5', 'SR_B6', 'SR_B7', 'ST_B10']
  var nameList = ['BLUE', 'GREEN', 'RED', 'NIR', 'SWIR1', 'SWIR2', 'TEMP']
  var subBand = ['BLUE', 'GREEN', 'RED', 'NIR', 'SWIR1', 'SWIR2']

  var opticalBands = image.select('SR_B.').multiply(0.0000275).add(-0.2);
  var thermalBand = image.select('ST_B10').multiply(0.00341802).add(149.0);
  var scaled = opticalBands.addBands(thermalBand, null, true).select(bandList)
      .rename(nameList);

  var validTOA = [2, 4, 32, 66, 68, 96, 100, 130, 132, 160, 164]
  var validQA = [21824, 21888] // 21826, 21890

  var mask1 = ee.Image(image).select(['QA_PIXEL']).remap(
      validQA, ee.List.repeat(1, validQA.length), 0)
  var mask2 = image.select('QA_RADSAT').eq(0)
  // Assume that all saturated pixels equal to 20000
  var mask3 = scaled.select(subBand).reduce(ee.Reducer.min()).gt(0)
  var mask4 = scaled.select(subBand).reduce(ee.Reducer.max()).lt(1)
  var mask5 = ee.Image(image).select(['SR_QA_AEROSOL']).remap(
      validTOA, ee.List.repeat(1, validTOA.length), 0)

  return ee.Image(image).addBands(scaled)
      .updateMask(mask1.and(mask2).and(mask3).and(mask4).and(mask5))
}

/**
* Generate and combine filtered collections of Landsat 4, 5, 7 and 8
* Simpler and faster than getLandsat
* @param {ee.Image} geom Geometry used to filter the collection
* @param {String} startDate Initial date to filter the collection
* @param {String} endDate Final date to filter the collection
* @param {Integer} collection Landsat collection to use (1 or 2)
* @returns {ee.ImageCollection} Filtered Landsat collection
*/
function generateCollection(geom, startDate, endDate, collection){
  collection = collection || 1

  if (collection == 1){
    var filteredL8 = (ee.ImageCollection('LANDSAT/LC08/C01/T1_SR')
        .filter("WRS_ROW < 122")
        .filterBounds(geom)
        .map(prepareL8))

    var filteredL7 = (ee.ImageCollection('LANDSAT/LE07/C01/T1_SR')
        .filter("WRS_ROW < 122")
        .filterBounds(geom)
        .map(prepareL7))

    // Originally not included in Noel's run
    var filteredL4 = (ee.ImageCollection('LANDSAT/LT04/C01/T1_SR')
        .filter("WRS_ROW < 122")
        .filterBounds(geom)
        .map(prepareL4L5))
    var filteredL5 = (ee.ImageCollection('LANDSAT/LT05/C01/T1_SR')
        .filter("WRS_ROW < 122")
        .filterBounds(geom)
        .map(prepareL4L5))
  } else if (collection == 2){
    var filteredL8 = (ee.ImageCollection('LANDSAT/LC08/C02/T1_L2')
        .filter("WRS_ROW < 122")
        .filterBounds(geom)
        .map(prepareL8L9Col2))
```

```
    var filteredL7 = (ee.ImageCollection('LANDSAT/LE07/C02/T1_L2')
        .filter("WRS_ROW < 122")
        .filterBounds(geom)
        .map(prepareL4L5L7Col2))

    // Originally not included in Noel's run
    var filteredL4 = (ee.ImageCollection('LANDSAT/LT04/C02/T1_L2')
        .filter("WRS_ROW < 122")
        .filterBounds(geom)
              .map(prepareL4L5L7Col2))
    var filteredL5 = (ee.ImageCollection('LANDSAT/LT05/C02/T1_L2')
        .filter("WRS_ROW < 122")
        .filterBounds(geom)
                    .map(prepareL4L5L7Col2))
  }

  var mergedCollections = ee.ImageCollection(filteredL8).merge(filteredL7)
      .merge(filteredL5).merge(filteredL4).filterDate(startDate, endDate)
  return mergedCollections
}

/**
* Make a ccd image from the most recent known global run
* @param {String} metadataFilter Which ccdc run prefix to use
* @param {List} segs List with the segment names
* @param {Number} numberOfSegments Max number of segments to retrieve from the CCDC results
* @param {List} bandNames List with the band names to use
* @param {List} inputFeatures List with the CCDC features to extract
* @returns {ee.Image} Filtered CCDC results in 'long' format
*/
function makeCcdImage(metadataFilter, segs, numberOfSegments,bandNames,inputFeatures, version)
{
  metadataFilter = metadataFilter || 'z'
  numberOfSegments = numberOfSegments || 6
  bandNames = bandNames || ["BLUE","GREEN","RED","NIR","SWIR1","SWIR2","TEMP"]
  segs = segs || ['S1','S2','S3','S4','S5','S6']
  bandNames = bandNames || ["BLUE","GREEN","RED","NIR","SWIR1","SWIR2","TEMP"]
  inputFeatures = inputFeatures || ["INTP", "SLP","PHASE","AMPLITUDE","RMSE"]
  version = version || 'v2'

  var ccdcCollection = ee.ImageCollection("projects/CCDC/" + version)

  // Get CCDC coefficients
  var ccdcCollectionFiltered = ccdcCollection
    .filterMetadata('system:index', 'starts_with',metadataFilter)

  // CCDC mosaic image
  var ccdc = ccdcCollectionFiltered.mosaic()

  // Turn array image into image
  return ee.Image(ccdcUtils.buildCcdImage(ccdc, numberOfSegments, bandNames))

}

exports = {
  getLandsat: getLandsat,
  generateCollection: generateCollection,
  doIndices: doIndices,
  makeLatGrid: makeLatGrid,
  makeLonGrid: makeLonGrid,
  makeLonLatGrid: makeLonLatGrid,
  getAncillary: getAncillary,
  getS2: getS2,
  getS1: getS1,
  makeCcdImage: makeCcdImage,
  calcNDVI: calcNDVI,
  calcNBR: calcNBR,
  calcEVI: calcEVI,
  calcEVI2: calcEVI2,
  tcTrans: tcTrans,
  calcNDFI: calcNDFI,
  makeAutoGrid: makeAutoGrid,
}
```

Appendix F. Javascript GEE API code for submitting the CCDC in GEE, modified and based on Arévalo et al. (2020). Available online at https://code.earthengine.google.com/?accept_repo=users/demarquetquentin/CCDC_Poitevin

```
// -----------------------------------------------------------------------------------------
//
// Submission of CCDC in Google Earth Engine
//
// Most of the code directly come from Arévalo et al. (2020) API
// (Arévalo, P., Bullock, E.L., Woodcock, C.E., Olofsson, P., 2020.
// A Suite of Tools for Continuous Land Change Monitoring in Google Earth Engine.
// Front. Clim. 2. https://doi.org/10.3389/fclim.2020.576740)
//
// But some parts have been modified to meet the needs and
// objectives of the study
//
// Original codes from Arévalo et al. can be found in the following repository:
// https://code.earthengine.google.com/?accept_repo=users/parevalo_bu/gee-ccdc-tools
//
// -----------------------------------------------------------------------------------------

// This script requires some other code located in different files
// that have to be called
//
// Modified version of the original 'inputs.js' script that adds:
// - selection of Landsat 9 images
// - selection of Collection 2 images (Collection 1 was originally set by default)
var utils = require('users/demarquetquentin/CCDC_Poitevin:inputScript.js')

// Other libraries:
var ccdc_utils = require('users/parevalo_bu/gee-ccdc-tools:ccdcUtilities/ccdc.js')
var composite = require("users/google/toolkits:landcover/impl/composites.js").Composites

/**
 * Define visualization parameters.
 *
 * The first dictionary contains the parameters
 * for titles, the second contains the style for the 'Run CCDC' button.
 */
var visLabels = {
  fontWeight: 'bold',
  fontSize: '14px',
  width: '590px',
  padding: '4px 4px 4px 4px',
  border: '1px solid black',
  color: 'white',
  backgroundColor: 'black',
  textAlign: 'left'
  }

var runStyle = {
  fontWeight: 'bold',
  fontSize: '14px',
  width: '590px',
  padding: '4px 4px 4px 4px',
  border: '1px solid black',
  color: 'black',
  backgroundColor: 'white',
  textAlign: 'center'
  }

var sensor = 'landsat'

/**
 * Global GLANCE land grid.
 *
 * This feature collection contains the grid system
 * for all continents for areas that overlap with land.
 * More information on GLANCE and the grid can be found here:
 *  http://sites.bu.edu/measures/
 */
var grids =
ee.FeatureCollection('projects/GLANCE/GRIDS/GEOG_LAND/GLANCE_v01_GLOBAL_TILE_LAND')
```

```
/**
 * Panels to hold the ui.Widgets.
 *
 * There is a main panel that holds everything, and then a second panel called
 * geoPanel that holds the options for selecting the output extent.
 */
var mainPanel = ui.Panel({style: {width: '600px'}})
.add(ui.Label('Continuous Change Detection and Classification (CCDC)',visLabels))
.add(ui.Label('User interface for submitting CCDC'))
.add(ui.Label('Please see instructions'))
.add(ui.Label('Input Parameters',visLabels))

ui.root.add(mainPanel)

var geoPanel = ui.Panel()

/**
 * Define global variables.
 *
 * These make it easier for interacting between ui.Widgets.
 */
var outGeo, outGeos, outGeosSize, tool, drive, asset
var h = 0
var v = 0
var r = 0
var geoType = 0
var regionList = ['Select Method','Use shapefile geometry', 'Draw on Map','Single Tile','Tile
Intersecting Point','Multiple Tiles','Draw Multiple Tiles on Map']

/**
 * Use asset (shapefile) geometry for images selection on the Area of interest
 * (Not previously provided in the original version)
 */
function shpGeom () {
  geoPanel.add(shpGeomPanel)

  var showGeom = ui.Button('Load Shapefile Geometry', function(){
    var asset = shpGeomPanel.widgets().get(1).getValue()
    outGeo = ee.FeatureCollection(asset)
    runButton.widgets().get(0).setDisabled(false)
    runButton.widgets().get(0).style().set('backgroundColor','#5ab4ac')
    Map.addLayer(outGeo, {}, 'Input SHP geometry')
    Map.centerObject(outGeo)
  })
  geoPanel.add(showGeom)
}

/**
 * Draw a box on the map
 *
 * Written by Justin Braaten (I think): https://emapr.github.io/LT-GEE/
 * https://code.earthengine.google.com/82b08b69bd596ada4747cb4bb7ea9526
 *
 * This function allows you to click on the map and after 5 clicks, the
 * locations and joined, making a Polygon. This polygon can be used as the
 * geographic extent of the analysis.
 */
var DrawAreaTool = function() {
  var map = Map
  var drawingToolLayer = ui.Map.Layer({name: 'Area Selection Tool', visParams:
{palette:'#4A8BF4', color:'#4A8BF4' }});

  this.map = map;
  this.selection = null;
  this.active = false;
  this.points = [];
  this.area = null;

  this.listeners = [];

  var tool = this;

  this.initialize = function() {
    this.map.onClick(this.onMouseClick);
    map.layers().reset()
    map.layers().set(0, drawingToolLayer);
  };

  this.startDrawing = function() {
    this.active = true;
    this.points = [];
```

```
    this.map.style().set('cursor', 'crosshair');
    drawingToolLayer.setShown(true);
  };

  this.stopDrawing = function() {
    tool.active = false;
    tool.map.style().set('cursor', 'hand');

    if(tool.points.length < 2) {
      return;
    }

    var closedPoints = tool.points.slice(0,-1);
    tool.area = ee.Geometry.Polygon(closedPoints)///.bounds();

    var empty = ee.Image().byte();
    var test = empty.paint({
      featureCollection: ee.FeatureCollection(tool.area),
      color: 1,
      width: 4
    });

    drawingToolLayer.setEeObject(test);

    tool.listeners.map(function(listener) {
      listener(tool.area);
    });
    runButton.widgets().get(0).setDisabled(false)
    runButton.widgets().get(0).style().set('backgroundColor','#5ab4ac')

  };

  this.onMouseClick = function(coords) {
    if(!tool.active) {
      return;
    }

    tool.points.push([coords.lon, coords.lat]);

    var geom = tool.points.length > 1 ? ee.Geometry.LineString(tool.points) :
ee.Geometry.Point(tool.points[0]);
    drawingToolLayer.setEeObject(geom);

    if(tool.points.length > 4) {
      tool.stopDrawing();
    }
  };

  this.onFinished = function(listener) {
    tool.listeners.push(listener);
  };

  this.initialize();
};

/**
 * Helper function for drawing output extent.
 *
 * This function faciliates the drawing of the output extent using the
 * DrawAreaTool() function.
 */
function doAreaTool() {
  geoPanel.add(ui.Label('Slowly click five points on the map and the application will generate
a rectangle for the output extent geometry.'))
  tool = new DrawAreaTool();
  tool.startDrawing();
  tool.onFinished(function(geometry) {
    outGeo = ee.Feature(geometry);
  });

}

/**
 * Helper function for drawing output extent and finding overlapping tiles
 *
 * This function faciliates the drawing of the output extent using the
 * DrawAreaTool() function.
 */
function drawMultipleTiles() {
```

```
  geoPanel.add(ui.Label('Slowly click five points on the map and the application will generate
a rectangle for the output extent geometry.'))
  tool = new DrawAreaTool();
  tool.startDrawing();
  tool.onFinished(function(geometry) {
    var tempGeo = grids.filterBounds(geometry);

    tempGeo.size().evaluate(function(val) {
      if (val > 0) {
        outGeos = ee.FeatureCollection(tempGeo)
        Map.addLayer(outGeos, {},'Output Geometry')
        Map.centerObject(outGeos)
        runButton.widgets().get(0).setDisabled(false)
        runButton.widgets().get(0).style().set('backgroundColor','#5ab4ac')
        outGeosSize = val
      } else {
        print('No overlapping tiles found!')
      }
    })
  })

}

/**
 * Specify a single tile.
 *
 * This function filters the GLANCE global grid based on the users
 * input properties in the GUI.
 */
function doSingleTile() {
  geoPanel.add(singleTilePanel)

  var tempGeo
  var validateTile = ui.Button('Load Tile', function(){
    h = Number(singleTilePanel.widgets().get(3).getValue())
    v = Number(singleTilePanel.widgets().get(1).getValue())
    r = String(singleTilePanel.widgets().get(5).getValue())
    tempGeo = grids.filterMetadata('horizontal','equals',h)
      .filterMetadata('vertical','equals',v)
      .filterMetadata('zone','equals',r)

    tempGeo.size().evaluate(function(val) {
      if (val > 0) {
        outGeo = ee.Feature(tempGeo.first())
        runButton.widgets().get(0).setDisabled(false)
        runButton.widgets().get(0).style().set('backgroundColor','#5ab4ac')
        Map.addLayer(outGeo, {},'Output Geometry')
        Map.centerObject(outGeo)
      }
      else {
        print('No Tile Found!')
      }
    })
  })
  geoPanel.add(validateTile)
}

/**
 * Find a single tile by clicking on the map.
 *
 * This function filters the GLANCE global grid based on the intersection of
 * a point clicked on the map.
 */
function doPoint() {
  var hasClicked = false
  Map.style().set('cursor', 'crosshair');
  geoPanel.add(ui.Label('Click a location on the map to load the intersecting tile'))
  Map.onClick(function(coords) {
    Map.layers().reset()
    var latitude = coords.lat
    var longitude = coords.lon
    var point = ee.Geometry.Point([longitude, latitude])
    var tempGeo = grids.filterBounds(point)

    Map.layers().set(0, point)
    // Map.layers().set(1, outGeo)

    tempGeo.size().evaluate(function(val) {
      if (val > 0) {
        outGeo = ee.Feature(tempGeo.first())
        runButton.widgets().get(0).setDisabled(false)
```

```
        runButton.widgets().get(0).style().set('backgroundColor','#5ab4ac')
        Map.addLayer(outGeo, {},'Output Geometry')
        Map.centerObject(outGeo)
        Map.unlisten()
      }
   })

  })
}

/**
 * Specify a range of tiles.
 *
 * This function filters the GLANCE global grid based on a range of
 * the users input properties in the GUI.
 */
function doMultipleTiles() {
  geoPanel.add(multiplePanelStart)
  geoPanel.add(multiplePanelEnd)

  var tempGeo
  var validateTile = ui.Button('Load Tiles', function(){
    var h1 = Number(multiplePanelStart.widgets().get(3).getValue())
    var v1 = Number(multiplePanelStart.widgets().get(1).getValue())

    var h2 = Number(multiplePanelEnd.widgets().get(3).getValue())
    var v2 = Number(multiplePanelEnd.widgets().get(1).getValue())

    var r = String(multiplePanelStart.widgets().get(5).getValue())
    tempGeo = grids.filterMetadata('horizontal','greater_than',h1)
      .filterMetadata('horizontal','less_than',h2)
      .filterMetadata('vertical','greater_than',v1)
      .filterMetadata('vertical','less_than',v2)
      .filterMetadata('zone','equals',r)

    tempGeo.size().evaluate(function(val) {
      if (val > 0) {
        outGeos = ee.FeatureCollection(tempGeo)
        Map.addLayer(outGeos, {},'Output Geometry')
        Map.centerObject(outGeos)
        runButton.widgets().get(0).setDisabled(false)
        runButton.widgets().get(0).style().set('backgroundColor','#5ab4ac')
        outGeosSize = val
      } else if (val === 0) {
        print('No Tile Found!')
      }
    })
  })
  geoPanel.add(validateTile)
}


/**
 * Turn an array image into a band image
 *
 */
var arrayToImage = function(array, band) {
  var zeros = ee.Array(0).repeat(0, 1)
  var img = array.select(band).arrayCat(zeros, 0).float().arraySlice(0, 0, 1)
  return img.arrayFlatten([[band]])
}


/**
 * Run CCDC and save results.
 *
 * This function filters the GLANCE global grid based on a range of
 * the users input properties in the GUI.
 */
var doCcdc = function() {
  Map.layers().reset()

  var minDate = String(dates.widgets().get(1).getValue()).split('-')[0]
  var maxDate = String(dates.widgets().get(3).getValue()).split('-')[0]
  var years = maxDate - minDate

  if (sensor == 'landsat') {
    var landsatParams = {
      collection: Number(landsatCol.widgets().get(1).getValue()),
      start: String(dates.widgets().get(1).getValue()),
      end: String(dates.widgets().get(3).getValue()),
```

```
      region: outGeo.geometry(),
      startDOY: Number(doys.widgets().get(1).getValue()),
      endDOY: Number(doys.widgets().get(3).getValue()),
      sensors: {
        l4: landsats.widgets().get(1).getValue(),
        l5: landsats.widgets().get(2).getValue(),
        l7: landsats.widgets().get(3).getValue(),
        l8: landsats.widgets().get(4).getValue(),
        l9: landsats.widgets().get(5).getValue()
      }
    }
    var inputData = ee.ImageCollection(utils.getLandsat(landsatParams))
                    .filterBounds(outGeo.geometry())
    Map.addLayer(ee.ImageCollection(inputData).first(), {bands: ['RED', 'GREEN', 'BLUE']},
'First image collection')

  } else {
    var s1Data = ee.ImageCollection(utils.getS1()).filterBounds(outGeo.geometry())
    if (s1s.widgets().get(1).getValue()) {
      var inputData = s1Data.filterMetadata('orbitProperties_pass','equals','ASCENDING')
    } else if (s1s.widgets().get(2).getValue()) {
      var inputData = s1Data.filterMetadata('orbitProperties_pass','equals','DESCENDING')
    } else if (s1s.widgets().get(3).getValue()) {
      var inputData = s1Data.filterMetadata('orbitProperties_pass','equals','ASCENDING')
      inputData = composite.createTemporalComposites(
        inputData,
        ee.Date(String(dates.widgets().get(1).getValue()))
        , years*26, 2, 'week', ee.Reducer.mean())
        .filterDate(
          ee.Date(String(dates.widgets().get(1).getValue())),
          ee.Date(String(dates.widgets().get(3).getValue())))
    } else if (s1s.widgets().get(4).getValue()) {
      var inputData = s1Data.filterMetadata('orbitProperties_pass','equals','DESCENDING')
      inputData = composite.createTemporalComposites(
        inputData,
        ee.Date(String(dates.widgets().get(1).getValue()))
        , years*26, 2, 'week', ee.Reducer.mean())
    } else  {
      var inputData = composite.createTemporalComposites(
        s1Data,
        ee.Date(String(dates.widgets().get(1).getValue()))
        , years*26, 2, 'week', ee.Reducer.mean())
    }
  }
  inputData = inputData.filterDate(
          ee.Date(String(dates.widgets().get(1).getValue())),
          ee.Date(String(dates.widgets().get(3).getValue())))
  print('Number of input images from your selection:', inputData.size())

  var bpB = String(breakpointBands.widgets().get(1).getValue()).trim().split(/\s*,\s*/);

  if (tmaskBands.widgets().get(1).getValue()) {
    var tmB = String(tmaskBands.widgets().get(1).getValue()).trim().split(/\s*,\s*/);
  } else {
    var tmB = null
  }
  var ccdcParameters = {
    breakpointBands: bpB,
    tmaskBands: tmB,
    minObservations: Number(minObservations.widgets().get(1).getValue()),
    chiSquareProbability: Number(chiSquareProbability.widgets().get(1).getValue()),
    minNumOfYearsScaler: Number(minNumOfYearsScaler.widgets().get(1).getValue()),
    dateFormat: Number(dateFormat.widgets().get(1).getValue()),
    lambda: Number(lambda.widgets().get(1).getValue()),
    maxIterations: Number(maxIterations.widgets().get(1).getValue()),
    collection: inputData,
  }

  var outputParams = {
    start: String(dates.widgets().get(1).getValue()),
    end: String(dates.widgets().get(3).getValue()),
    startDOY: Number(doys.widgets().get(1).getValue()),
    endDOY: Number(doys.widgets().get(3).getValue()),
    sensor: sensor,
    breakpointBands: ccdcParameters.breakpointBands,
    tmaskBands: ccdcParameters.tmaskBands,
    minObservations: ccdcParameters.minObservations,
    chiSquareProbability:ccdcParameters.chiSquareProbability,
    minNumOfYearsScaler: ccdcParameters.minNumOfYearsScaler,
    dateFormat: ccdcParameters.dateFormat,
    lambda: ccdcParameters.lambda,
```

```
    maxIterations: ccdcParameters.maxIterations,
    user: ee.data.getAssetRoots()[0].id.split('/')[1]
  }

  var drive = outputFormat.widgets().get(1).getValue()
  var asset = outputFormat.widgets().get(2).getValue()

  var results = ee.Algorithms.TemporalSegmentation.Ccdc(ccdcParameters)

  var outFolder = String(outputFolder.widgets().get(1).getValue())
  var outAsset = 'CCDC_output'
  var outDesc = outAsset + '_asset'
  var exportBands = ['BLUE','GREEN', 'RED', 'NIR', 'SWIR1', 'SWIR2', 'TEMP', 'NDVI',
                     'EVI', 'EVI2', 'NBR', 'NDFI', 'GV', 'NPV', 'Shade', 'Soil', 'BRIGHTNESS',
'GREENNESS', 'WETNESS']
  var imageToExport = ee.Image(ccdc_utils.buildCcdImage(results, 10, exportBands))


  if (drive) {
    Export.image.toDrive({
      // 'Long' version of CCDC results, required when exporting to drive
      image: imageToExport,
      scale: 30,
      region: outGeo.geometry(),

    })
  }
  if (asset == true) {
    Export.image.toAsset({
      // Ensures we export the original CCDC array image
      image: results.setMulti(outputParams),
      description: outDesc,
      assetId: outFolder + outAsset,
      scale: 30,
      maxPixels: 1e12,
      region: outGeo.geometry(),
      pyramidingPolicy: {
        ".default": 'sample'
      }

    })
  }
}

/**
 * Panels containing ui.Widgets
 *
 * Each panel has atleast one widget to define how CCDC is run. Many
 * contain a label and a textbox (indices 0 and 1), while buttons and
 * checkboxes may not contain label widgets.
 */
var dates = ui.Panel(
  [
    ui.Label({value:'startDate:', style:{color:'black'}}),
    ui.Textbox({value:'1984-01-01', style:{stretch: 'horizontal'}}),
    ui.Label({value:'endDate:', style:{color:'black'}}),
    ui.Textbox({value:'2022-12-31', style:{stretch: 'horizontal'}})
  ],
  ui.Panel.Layout.Flow('horizontal'),
  {stretch: 'horizontal'}
);

var doys = ui.Panel(
  [
    ui.Label({value:'startDOY:', style:{color:'black'}}),
    ui.Textbox({value:'1', style:{stretch: 'horizontal'}}),
    ui.Label({value:'endDOY:', style:{color:'black'}}),
    ui.Textbox({value:'365', style:{stretch: 'horizontal'}})
  ],
  ui.Panel.Layout.Flow('horizontal'),
  {stretch: 'horizontal'}
);

var maskImage = ui.Panel(
  [
    ui.Label({value:'Mask Image?', style:{color:'black'}}),
    ui.Textbox({value:null, style:{stretch: 'horizontal'}}),
  ],
  ui.Panel.Layout.Flow('horizontal'),
  {stretch: 'horizontal'}
);
```

```
var switchBandsLandsat = function(check) {
  if (check) {
    breakpointBands.widgets().get(1).setValue(['GREEN', 'RED', 'NIR', 'SWIR1', 'SWIR2'])
    tmaskBands.widgets().get(1).setValue(['GREEN','SWIR2'])
    sensor = 'landsat'
  }
}

var landsats = ui.Panel(
  [
    ui.Label({value:'Landsats:', style:{color:'black'}}),
    ui.Checkbox({label:'L4', value: true, onChange: switchBandsLandsat, style:{stretch:
'horizontal'}}),
    ui.Checkbox({label:'L5', value: true, onChange: switchBandsLandsat, style:{stretch:
'horizontal'}}),
    ui.Checkbox({label:'L7', value: true, onChange: switchBandsLandsat, style:{stretch:
'horizontal'}}),
    ui.Checkbox({label:'L8', value: true, onChange: switchBandsLandsat, style:{stretch:
'horizontal'}}),
    ui.Checkbox({label:'L9', value: true, onChange: switchBandsLandsat, style:{stretch:
'horizontal'}})
  ],
  ui.Panel.Layout.Flow('horizontal'),
  {stretch: 'horizontal'}
);

var landsatCol = ui.Panel(
  [
    ui.Label({value:'Collection ?', style:{color:'black'}}),
    ui.Textbox({value: 2, style:{stretch: 'horizontal'}}),
  ],
  ui.Panel.Layout.Flow('horizontal'),
  {stretch: 'horizontal'}
);

var switchBandsS1 = function() {
  breakpointBands.widgets().get(1).setValue(['VV','VH','ratio'])
  tmaskBands.widgets().get(1).setValue(null)
  sensor = 's1'
}

var turnOffS1_1 = function(check) {
  if (check) {
    switchBandsS1()
    s1s.widgets().get(2).setValue(false)
    s1s.widgets().get(3).setValue(false)
    s1s.widgets().get(4).setValue(false)
    landsats.widgets().get(1).setDisabled(true)
    landsats.widgets().get(2).setDisabled(true)
    landsats.widgets().get(3).setDisabled(true)
    landsats.widgets().get(4).setDisabled(true)
    landsats.widgets().get(1).setValue(false)
    landsats.widgets().get(2).setValue(false)
    landsats.widgets().get(3).setValue(false)
    landsats.widgets().get(4).setValue(false)
  }  else {
    // switchBandsLandsat()
    landsats.widgets().get(1).setDisabled(false)
    landsats.widgets().get(2).setDisabled(false)
    landsats.widgets().get(3).setDisabled(false)
    landsats.widgets().get(4).setDisabled(false)
  }
}

var turnOffS1_2 = function(check) {
  if (check) {
    switchBandsS1()
    s1s.widgets().get(1).setValue(false)
    s1s.widgets().get(3).setValue(false)
    s1s.widgets().get(4).setValue(false)
    landsats.widgets().get(1).setDisabled(true)
    landsats.widgets().get(2).setDisabled(true)
    landsats.widgets().get(3).setDisabled(true)
    landsats.widgets().get(4).setDisabled(true)
    landsats.widgets().get(1).setValue(false)
    landsats.widgets().get(2).setValue(false)
    landsats.widgets().get(3).setValue(false)
    landsats.widgets().get(4).setValue(false)
  }  else {
    // switchBandsLandsat()
```

```
    landsats.widgets().get(1).setDisabled(false)
    landsats.widgets().get(2).setDisabled(false)
    landsats.widgets().get(3).setDisabled(false)
    landsats.widgets().get(4).setDisabled(false)
  }
}

var turnOffS1_3 = function(check) {
  if (check) {
    switchBandsS1()
    s1s.widgets().get(1).setValue(false)
    s1s.widgets().get(2).setValue(false)
    s1s.widgets().get(4).setValue(false)
    landsats.widgets().get(1).setDisabled(true)
    landsats.widgets().get(2).setDisabled(true)
    landsats.widgets().get(3).setDisabled(true)
    landsats.widgets().get(4).setDisabled(true)
    landsats.widgets().get(1).setValue(false)
    landsats.widgets().get(2).setValue(false)
    landsats.widgets().get(3).setValue(false)
    landsats.widgets().get(4).setValue(false)
  }  else {
    // switchBandsLandsat()
    landsats.widgets().get(1).setDisabled(false)
    landsats.widgets().get(2).setDisabled(false)
    landsats.widgets().get(3).setDisabled(false)
    landsats.widgets().get(4).setDisabled(false)
  }
}

var turnOffS1_4 = function(check) {
  if (check) {
    switchBandsS1()
    s1s.widgets().get(1).setValue(false)
    s1s.widgets().get(2).setValue(false)
    s1s.widgets().get(3).setValue(false)
    landsats.widgets().get(1).setDisabled(true)
    landsats.widgets().get(2).setDisabled(true)
    landsats.widgets().get(3).setDisabled(true)
    landsats.widgets().get(4).setDisabled(true)
    landsats.widgets().get(1).setValue(false)
    landsats.widgets().get(2).setValue(false)
    landsats.widgets().get(3).setValue(false)
    landsats.widgets().get(4).setValue(false)
  }  else {
    // switchBandsLandsat()
    landsats.widgets().get(1).setDisabled(false)
    landsats.widgets().get(2).setDisabled(false)
    landsats.widgets().get(3).setDisabled(false)
    landsats.widgets().get(4).setDisabled(false)
  }
}
var s1s = ui.Panel(
  [
    ui.Label({value:'Sentinel 1:', style:{color:'black'}}),
    ui.Checkbox({label:'GRD (Raw; Ascending)', value: false, onChange: turnOffS1_1,
style:{stretch: 'horizontal'}}),
    ui.Checkbox({label:'GRD (Raw; Descending)', value: false, onChange: turnOffS1_2,
style:{stretch: 'horizontal'}}),
    ui.Checkbox({label:'GRD (Composite; Ascending)', value: false, onChange: turnOffS1_3,
style:{stretch: 'horizontal'}}),
    ui.Checkbox({label:'GRD (Composite; Descending)', value: false, onChange: turnOffS1_4,
style:{stretch: 'horizontal'}}),
    ui.Checkbox({label:'GRD (Composite; Both)', value: false, onChange: turnOffS1_4,
style:{stretch: 'horizontal'}}),
  ],
  ui.Panel.Layout.Flow('horizontal'),
  {stretch: 'horizontal'}
);

var outputFormat = ui.Panel(
  [
    ui.Label({value:'Export format:', style:{color:'black'}}),
    ui.Checkbox({label:'GDrive', value: false, style:{stretch: 'horizontal'}}),
    ui.Checkbox({label:'Asset', value: true, style:{stretch: 'horizontal'}}),
  ],
  ui.Panel.Layout.Flow('horizontal'),
  {stretch: 'horizontal'}
);

var outputFolder = ui.Panel(
```

```
  [
    ui.Label({value:'Export folder:', style:{color:'black'}}),
    ui.Textbox({placeholder:'projects/ee-quen-dem/assets/', value: 'projects/ee-quen-
dem/assets/', style:{stretch: 'horizontal'}}),
  ],
  ui.Panel.Layout.Flow('horizontal'),
  {stretch: 'horizontal'}
);

var regions = ['Select Region','AF','AN','AS','EU','NA','OC','SA']
var singleTilePanel = ui.Panel(
  [
    ui.Label({value:'Vertical #:', style:{color:'black'}}),
    ui.Textbox({value:32, style:{stretch: 'horizontal'}}),
    ui.Label({value:'Horizontal #:', style:{color:'black'}}),
    ui.Textbox({value:61, style:{stretch: 'horizontal'}}) ,
    ui.Label({value:'Region', style:{color:'black'}}),
    ui.Select({items:regions,value: regions[5], style:{stretch: 'horizontal'}})
  ],
  ui.Panel.Layout.Flow('horizontal'),
  {stretch: 'horizontal'}
);

var multiplePanelStart = ui.Panel(
  [
    ui.Label({value:'Vertical # Min:', style:{color:'black'}}),
    ui.Textbox({value:30, style:{stretch: 'horizontal'}}),
    ui.Label({value:'Horizontal # Min:', style:{color:'black'}}),
    ui.Textbox({value:60, style:{stretch: 'horizontal'}}),
    ui.Label({value:'Region', style:{color:'black'}}),
    ui.Select({items:regions,value: regions[0], style:{stretch: 'horizontal'}})
  ],
  ui.Panel.Layout.Flow('horizontal'),
  {stretch: 'horizontal'}
);

var multiplePanelEnd = ui.Panel(
  [
    ui.Label({value:'Vertical # Max:', style:{color:'black'}}),
    ui.Textbox({value:35, style:{stretch: 'horizontal'}}),
    ui.Label({value:'Horizontal # End:', style:{color:'black'}}),
    ui.Textbox({value:65, style:{stretch: 'horizontal'}}),
  ],
  ui.Panel.Layout.Flow('horizontal'),
  {stretch: 'horizontal'}
);

var shpGeomPanel = ui.Panel(
  [
    ui.Label({value: 'Asset', style:{color:'black'}}),
    ui.Textbox({placeholder:'asset path', value: '', style:{stretch: 'horizontal'}}),
  ],
  ui.Panel.Layout.Flow('horizontal'),
  {stretch: 'horizontal'}
  );

var breakpointBands = ui.Panel(
  [
    ui.Label({value:'breakpointBands:', style:{color:'black'}}),
    ui.Textbox({value:['BLUE, GREEN, RED, NIR, SWIR1, SWIR2, TEMP, NDVI, EVI, EVI2, NBR, NDFI,
GV, NPV, Shade, Soil, BRIGHTNESS, GREENNESS, WETNESS'], style:{stretch: 'horizontal'}})
  ],
  ui.Panel.Layout.Flow('horizontal'),
  {stretch: 'horizontal'}
);
var tmaskBands = ui.Panel(
  [
    ui.Label({value:'tmaskBands:', style:{color:'black'}}),
    ui.Textbox({value:['GREEN, SWIR2'], style:{stretch: 'horizontal'}})
  ],
  ui.Panel.Layout.Flow('horizontal'),
  {stretch: 'horizontal'}
);

var minObservations = ui.Panel(
  [
    ui.Label({value:'minObservations:', style:{color:'black'}}),
    ui.Textbox({value:6, style:{stretch: 'horizontal'}})
  ],
  ui.Panel.Layout.Flow('horizontal'),
  {stretch: 'horizontal'}
```

```
);
var chiSquareProbability = ui.Panel(
  [
    ui.Label({value:'chiSquareProbability:', style:{color:'black'}}),
    ui.Textbox({value:0.99, style:{stretch: 'horizontal'}})
  ],
  ui.Panel.Layout.Flow('horizontal'),
  {stretch: 'horizontal'}
);
var minNumOfYearsScaler = ui.Panel(
  [
    ui.Label({value:'minNumOfYearsScaler:', style:{color:'black'}}),
    ui.Textbox({value:1.33, style:{stretch: 'horizontal'}})
  ],
  ui.Panel.Layout.Flow('horizontal'),
  {stretch: 'horizontal'}
);
var dateFormat = ui.Panel(
  [
    ui.Label({value:'dateFormat:', style:{color:'black'}}),
    ui.Textbox({value:1, style:{stretch: 'horizontal'}})
  ],
  ui.Panel.Layout.Flow('horizontal'),
  {stretch: 'horizontal'}
);
var lambda = ui.Panel(
  [
    ui.Label({value:'lambda:', style:{color:'black'}}),
    ui.Textbox({value:0.002, style:{stretch: 'horizontal'}})
  ],
  ui.Panel.Layout.Flow('horizontal'),
  {stretch: 'horizontal'}
);
var maxIterations = ui.Panel(
  [
    ui.Label({value:'maxIterations:', style:{color:'black'}}),
    ui.Textbox({value:10000, style:{stretch: 'horizontal'}})
  ],
  ui.Panel.Layout.Flow('horizontal'),
  {stretch: 'horizontal'}
);

var regionFuncs = [shpGeom, doAreaTool, doSingleTile, doPoint, doMultipleTiles,
drawMultipleTiles]
var selectRegion = ui.Panel(
  [
    ui.Label({value:'Define Study Region:', style:{color:'black'}}),
    ui.Select({
      value: 'Select Method',
      items: regionList,
      onChange: function(obj) {
        geoPanel.clear()
        Map.unlisten()
        Map.layers().reset()
        runButton.widgets().get(0).style().set('backgroundColor','white')
        runButton.widgets().get(0).setDisabled(true)

        var index = regionList.indexOf(obj) - 1
        geoType= index

        var regionFunc = regionFuncs[index]
        regionFunc(obj)
      }
    })
  ],
  ui.Panel.Layout.Flow('horizontal'),
  {stretch: 'horizontal'}
);

var runButton = ui.Panel(
  [
    ui.Button({label:'Run CCDC', style:runStyle, disabled: true}),
  ],
  ui.Panel.Layout.Flow('horizontal'),
  {stretch: 'horizontal'}
);


/**
 * Add individual panels to the main panel.
 */
```

```
mainPanel.add(dates)
mainPanel.add(doys)
mainPanel.add(maskImage)
mainPanel.add(landsats)
mainPanel.add(landsatCol)
mainPanel.add(s1s)

mainPanel.add(ui.Label('CCDC Parameters',visLabels))
mainPanel.add(breakpointBands)
mainPanel.add(tmaskBands)
mainPanel.add(minObservations)
mainPanel.add(chiSquareProbability)
mainPanel.add(minNumOfYearsScaler)
mainPanel.add(dateFormat)
mainPanel.add(lambda)
mainPanel.add(maxIterations)
mainPanel.add(ui.Label('Define Output Extent',visLabels))
mainPanel.add(selectRegion)
mainPanel.add(geoPanel)
mainPanel.add(ui.Label('Output Options',visLabels))
mainPanel.add(outputFormat)
mainPanel.add(outputFolder)
mainPanel.add(runButton)


/**
 * Run CCDC and save the results.
 *
 * When the 'Run CCDC' button is clicked, either submit
 * a single task via the doCcdc() function or a task
 * for each tile is multiple are defined.
 */
runButton.widgets().get(0).onClick(function() {
  // geoTypes indexed by 'Select Method' widget values
  // 0 is with shapefile geometry (from me)
  // 1 and 2 are single features
  // 3 is tile intersecting point
  // 4-5 are multiple tiles
  //
  print(geoType)
  if (geoType < 4) {
      doCcdc()
  } else if (geoType == 4) {
      var h_temp = outGeo.get('horizontal')
      var v_temp  = outGeo.get('vertical')
      var r_temp = outGeo.get('zone')
      var listToEvaluate = ee.List([h_temp, v_temp, r_temp])
      listToEvaluate.evaluate(function(obj) {
        h = obj[0]
        v = obj[1]
        r = obj[2]
        doCcdc()
      })
  } else {
    var outGeosList = outGeos.toList(100);

    for (var i =0; i< outGeosSize; i++) {
      outGeo = ee.Feature(outGeosList.get(i))
      var h_temp = outGeo.get('horizontal')
      var v_temp  = outGeo.get('vertical')
      var r_temp = outGeo.get('zone')
      var listToEvaluate = ee.List([h_temp, v_temp, r_temp, i])
      listToEvaluate.evaluate(function(obj) {
        h = obj[0]
        v = obj[1]
        r = obj[2]
        outGeo = ee.Feature(outGeosList.get(obj[3]))

        doCcdc()
      })
    }
  }
})
```

Appendix G. Summary of the number of available images per Landsat sensor and per tile for each study site for the 1984–2021 study period. ES: Ecological Station.

Sensor	Pirttimysvuoma				Marais Vernier			Ouled Saïd			Taiamã ES
	194/12	195/12	196/12	197/12	200/26	201/25	201/26	196/40	197/39	197/40	222/72
L4-5 TM	106	61	96	110	222	342	237	426	352	365	344
L7 ETM+	143	139	137	128	237	332	245	318	331	330	419
L8-9 OLI/TIRS	73	87	79	104	129	197	149	198	197	198	166

Appendix H. Number of clear Landsat observations available for the continuous change detection and classification algorithm from 1984-2022.

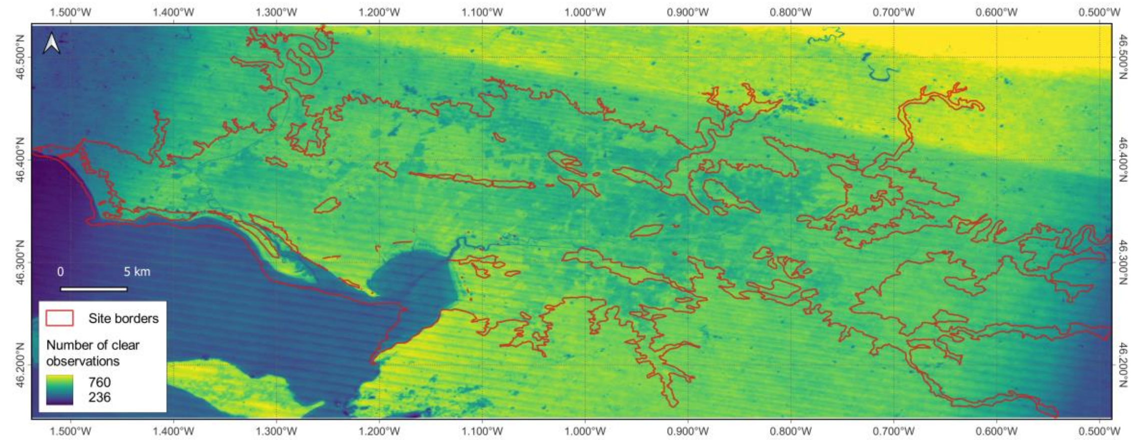

Appendix I. Confusion matrix for habitat types in 1984 derived from post-classification change detection (rows) and reference Dataset 1 (columns).

	Reference							
Classification	A	B	C1J5	C3	E	G	I	J
A	20	0	0	0	0	0	0	0
B	0	20	0	0	0	0	0	0
C1J5	0	0	20	0	0	0	0	0
C3	0	0	0	20	0	0	0	0
E	0	0	0	0	16	4	0	0
G	0	0	0	0	0	20	0	0
I	0	0	0	1	3	0	16	0
J	1	0	0	1	0	0	2	17
UA	1.00	1.00	1.00	1.00	0.80	1.00	0.80	0.81
PA	0.95	1.00	1.00	0.91	0.84	0.83	0.89	1.00

Appendix J. Confusion matrix for habitat types in 2022 derived from post-classification change detection (rows) and reference Dataset 1 (columns).

	Reference							
Classification	A	B	C1J5	C3	E	G	I	J
A	17	0	0	3	0	0	0	0
B	5	15	0	0	0	0	0	0
C1J5	0	0	19	1	0	0	0	0
C3	0	0	0	1	17	2	0	0
E	0	0	0	0	15	0	5	0
G	0	0	0	0	0	20	0	0
I	0	0	0	0	1	0	19	0
J	1	0	0	0	0	0	5	14
UA	0.85	0.75	0.95	0.05	0.75	1.00	0.95	0.70
PA	0.74	1.00	1.00	0.20	0.45	0.91	0.66	1.00

Appendix K. Confusion matrix for habitat types in 1984 derived from continuous change detection and classification (rows) and reference Dataset 1 (columns).

	Reference							
Classification	A	B	C1J5	C3	E	G	I	J
A	18	0	0	2	0	0	0	0
B	2	17	0	1	0	0	0	0
C1J5	0	0	20	0	0	0	0	0
D	0	0	0	8	0	0	0	0
E	0	0	0	4	19	0	3	0
G	0	1	0	3	1	20	0	0
I	0	0	0	2	0	0	15	0
J	0	2	0	0	0	0	2	20
UA	0.90	0.85	1.00	1.00	0.73	0.80	0.88	0.83
PA	0.90	0.85	1.00	0.40	0.95	1.00	0.75	1.00

Appendix L. Confusion matrix for habitat types in 2022 derived from continuous change detection and classification (rows) and reference Dataset 1 (columns).

	Reference							
Classification	A	B	C1J5	C3	E	G	I	J
A	19	0	0	0	0	0	0	0
B	0	20	0	0	0	0	0	0
C1J5	0	0	20	0	0	0	0	0
D	0	0	0	8	0	0	0	0
E	0	0	0	12	20	0	1	0
G	0	0	0	0	0	20	0	0
I	0	0	0	0	0	0	19	0
J	1	0	0	0	0	0	0	20
UA	1.00	1.00	1.00	1.00	0.61	1.00	1.00	0.95
PA	0.95	1.00	1.00	0.40	1.00	1.00	0.95	1.00

Appendix M. Confusion matrix for class of changes between 1984 and 2022 derived from continuous change detection and classification (rows) and reference Dataset 2 (columns).

	Reference			
Classification	Wetland loss	Wetland gain	Stable wetland	Stable damaged wetland
Wetland loss	50	0	0	4
Wetland gain	1	20	8	13
Stable wetland	12	2	93	5
Stable damaged wetland	9	0	3	106
UA	0.93±0.04	0.48±0.08	0.83±0.04	0.90±0.03
PA	0.56±0.05	0.62±0.08	0.96±0.01	0.90±0.02

Appendix N. Confusion matrix for class of changes between 1984 and 2022 derived from post-classification change detection (rows) and reference Dataset 2 (columns).

	Reference			
Classification	Wetland loss	Wetland gain	Stable wetland	Stable damaged wetland
Wetland loss	45	1	12	58
Wetland gain	2	6	10	10
Stable wetland	16	13	79	29
Stable damaged wetland	9	2	3	31
UA	0.39±0.05	0.21±0.08	0.58±0.04	0.69±0.07
PA	0.58±0.05	0.19±0.07	0.81±0.03	0.26±0.03

Appendix O. Conversion table between EUNIS level 1 habitats and the various nomenclatures used in Chapter 4.

EUNIS 2012	Regional classification of vegetation	CORINE Biotopes	EUNIS 2020	LPIS	LUCAS
A – Marine habitats	Agropyrion pungentis Géhu 1968	14 Mud flats and sand flats	MA22 Atlantic littoral biogenic habitat		
	Agropyro pungentis – Suaedetum verae Géhu 1976	15.1 Salt pioneer swards			
	Astero tripolii – Phragmitetum australis (Jeschke 1968) Succow 1974	15.2 Cordgrass swards			
	Beto maritimae – Atriplicetum laciniatae Tüxen (1950) 1967	15.3 Atlantic salt meadows			
	Brassico nigrae – Carduetum tenuiflori Bouzillé	Foucault & Lahondère 1984	15.52 Mediterranean short rush	Sedge	Barley and clover saltmarshes
	Euphorbio portlandicae – Helichrysion stoechadis Géhu & Tüxen ex Sissingh 1974	15.62 Atlantic salt scrubs			
	Halimionetum portulacoidis Kühnholtz-Lordat 1927				
	Laguro ovati – Brometum rigidi Géhu & Géhu-Franck 1985				
	Parapholido strigosae – Hordeetum marini Géhu & de Foucault 1978				
	Puccinellietum maritimae Christiansen 1927				
	Puccinellio maritimae – Salicornietum				

	fruticosae (Arènes 1933) Géhu (1975)			
	Salicornion dolichostachyo – fragilis Géhu & Rivas-Martínez ex Géhu 2004			
	Salicornion europaeo – ramosissimae Géhu & Géhu-Franck ex Rivas-Martínez 1990			
	Scirpetum compacti Van Langendonck 1931			
	Spartinetea glabrae Tüxen 1962			
	Spartinetum maritimae (Emberg. & Regn. 1926) Corillion 1953			
B – Coastal habitats	16.11 Unvegetated sand beaches	N11 Atlantic	Baltic and Arctic sand beach	
	16.21 Shifting dunes	N13 Atlantic and Baltic shifting coastal dune		
	16.22 Grey dunes	N15 Atlantic and Baltic coastal dune grassland (grey dune)		
	16.29 Wooded dunes			
	16.34 Dune-slack grasslands			
	17.2 Shingle beach drift lines			
C1 – Natural permanent surface waters and	22.1 Fresh waters	G11 Inland fresh water bodies		
	22.4 Aquatic vegetation			
	23 Standing brackish and salt water			
C3 – Littoral zone of inland	53.11 Common reed beds	Q51 Tall-helophyte bed		

surface waterbodies					
	53.14 Medium-tall waterside communities	Q52 Small-helophyte bed			
	53.16 Reed canary-grass beds	Q53 Tall-sedge bed			
	53.17 Halophile clubrush beds				
	53.21 Large carex beds				
	53.3 Fen-sedge beds				
E – Grasslands and lands dominated by forbs	Mosses or lichens	34.3 Dense perennial grasslands and middle european steppes	R1A Semi-dry perennial calcareous grassland (meadow steppe)	9 Old pasture (3 years or older)	E10 Grassland with sparse tree/shrub cover
	37.1 Meadowsweet stands and related communities	R21 Mesic permanent pasture of lowlands and mountains		E20 Grassland without tree/shrub cover	
	37.2 Eutrophic humid grasslands	R22 Low and medium altitude hay meadow	E30 Spontaneously re-vegetated surfaces		
	37.7 Humid tall herb fringes	R34 Submediterranean moist meadow			
	38.1 Mesophile pastures	R35 Moist or wet mesotrophic to eutrophic hay meadow			
	81 Improved grasslands	R36 Moist or wet mesotrophic to eutrophic pasture			
	87.2 Ruderal communities	R55 Lowland moist or wet tall-herb and fern fringe			
	V37 Annual anthropogenic herbaceous vegetation				
G – Woodland	Forest and other wooded land	41.2 Oak-hornbeam forests	T13 Temperate hardwood riparian forest	C10 Broadleaved woodland	
	41.3 Ash forests	T21 Mediterranean evergreen Quercus forest	C32 Pine dominated mixed woodland		

	42.81 Maritime pine forests				
	44.3 Medio-european stream ash-alder woods				
	44.4 Mixed oak elm-ash forests of great rivers				
	83.15 Fruit orchards				
	83.32 Plantations of broad-leaved trees				
I – Regularly or recently cultivated agricultural	Horticultural and domestic habitats	82 Crops	V11 Intensive unmixed crops	1 Winter cereals	B11 Common wheat
	82.12 Market gardens and horticulture	2 Spring cereals	B12 Durum wheat		
	87.1 Fallow fields	3 Oats	B13 Barley		
	4 Grain legumes	B15 Oats			
	5 Mixture cereal and grain legumes	B16 Maize			
	6 Oilseed rape	B18 Triticale			
	7 Roots and tubers	B31 Sunflower			
	8 Young pasture (1–2 years)	B35 Other fibre and oleaginous crops			
	B41 Dry pulses				
	B43 Other fresh vegetables				
	B52 Lucerne				
	B55 Temporary grasslands				
J – Constructed	Industrial and other artificial habitats	86 Towns	villages	industrial sites	A11 Buildings with one to three floors
	A22 Non built-up linear features				
J5 – Artificial permanent surface waterbodies	89.1 Saline industrial lagoons and canals				
	89.2 Fresh-water industrial lagoons and canals				

Appendix P. Confusion matrix for habitat types during the 1984 – 2022 period derived from continuous change detection (rows) and reference data (columns).

	Reference								
Classification	A	B	C1J5	C3	E	G	I	J	Total
A	77	0	2	0	0	0	1	0	80
B	1	60	0	1	0	0	0	1	63
C1J5	0	0	116	0	0	0	0	0	116
C3	0	0	1	43	0	0	1	0	45
E	0	0	1	13	125	3	10	1	153
G	0	0	0	3	6	117	1	0	127
I	1	0	0	0	9	0	104	1	115
J	1	0	0	0	0	0	3	117	121
Total	80	60	120	60	140	120	120	120	820
UA	0.96	0.95	1.00	0.96	0.82	0.92	0.87	0.97	
PA	0.96	1.00	0.97	0.72	0.89	0.98	0.87	0.98	
F1-score	0.96	0.98	0.98	0.82	0.85	0.95	0.89	0.97	

Appendix Q. Visual comparison between the LULC maps obtained from the CCDC (up) and Corine Land Cover product (bottom) in 1990 and 2000 after legend harmonisation. Intermediate years in 1992, 2994, 1996, and 1998 are given to show the subtle differences that cannot be seen with the CLC product. Black circles (A and B) indicate a LULC change in both maps.

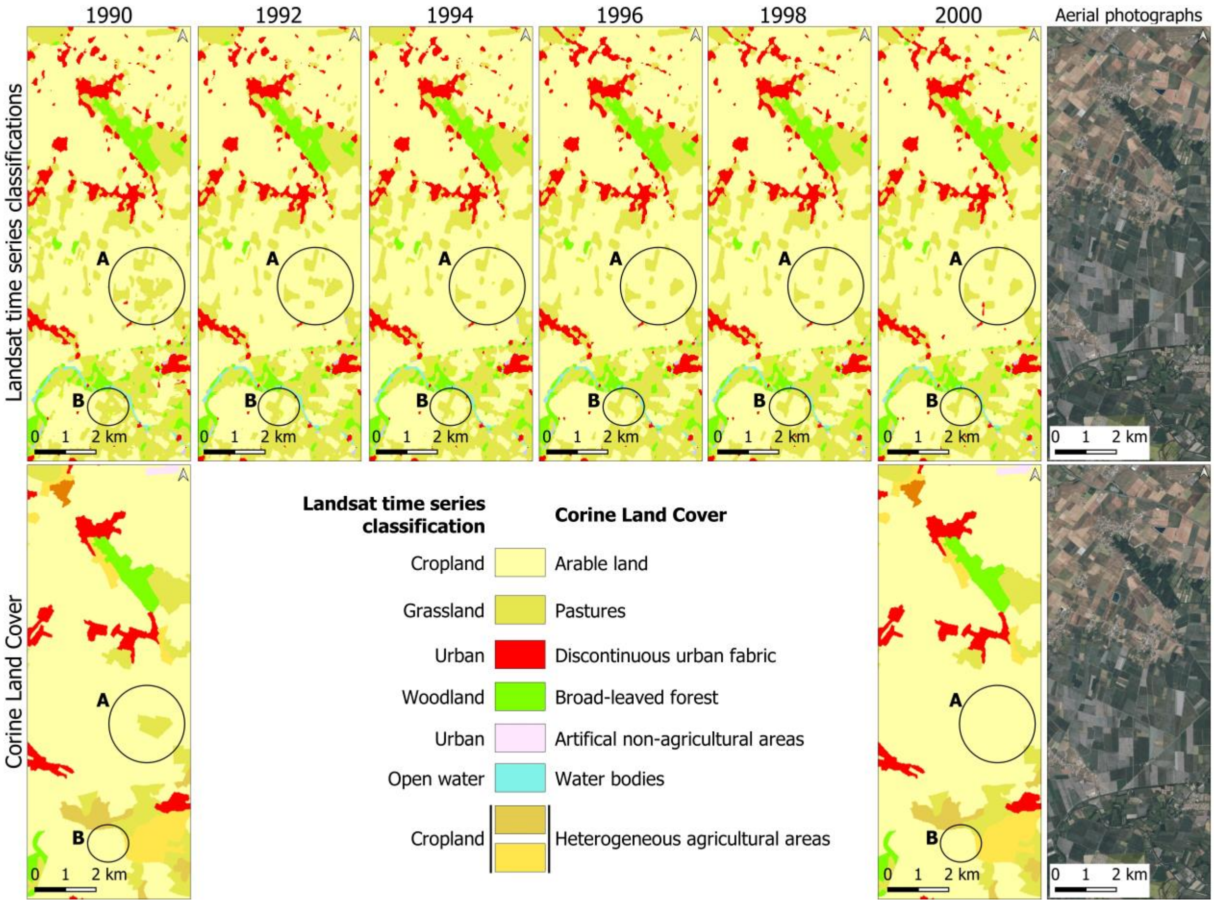

RESUME ETENDU (FRANÇAIS)

Après avoir été longtemps décrites comme des milieux insalubres auxquels étaient attribuées légendes et superstitions, les zones humides, situées à l'interface des milieux terrestres et aquatiques, sont aujourd'hui reconnues comme des écosystèmes uniques présentant un fort intérêt socio-écologique. Présentes partout sur le globe excepté en Antarctique, elles représentent entre 5 et 8% de la surface terrestre (Mitsch et al., 2013; Mitsch and Gosselink, 2015). Ces milieux sont définis différemment selon les régions et législations à travers le monde (Gardner and Davidson, 2011). A l'échelle internationale, la convention internationale de Ramsar adoptée en 1971 définit les zones humides comme *« des étendues des étendues de marais, de fagnes, de tourbières ou d'eaux naturelles ou artificielles, permanentes ou temporaires, où l'eau est stagnante ou courante, douce, saumâtre ou salée, y compris des étendues d'eau marine dont la profondeur à marée basse n'excède pas six mètres*". Les zones humides présentent donc une importante diversité d'habitats littoraux et continentaux allant des mangroves jusqu'aux tourbières, en passant par les marais et les prairies humides (Finlayson et al., 2018).

Les zones humides figurent parmi les socio-écosystèmes les plus menacés au monde avec une diminution de leur surface estimée à environ 3.4 millions de km² depuis 1700 à l'échelle globale. Une accélération de cette diminution a été observée à compter de la moitié du 20ème siècle, avec des pertes annuelles estimées entre -1.3 et -2.2% par an dans le monde (Davidson, 2014; Fluet-Chouinard et al., 2023). Cette diminution, répartie de façon inégale dans le monde, est particulièrement importante en Asie et en Europe (Hu et al., 2017). Les causes de la perte de zones humides ont une double origine : anthropique, surtout à travers l'extension des terres cultivées et l'urbanisation (Davidson and Finlayson, 2018; Moomaw et al., 2018), et climatique, à travers la hausse des températures, la modification du régime des précipitations et la hausse du niveau de des océans observées dans le contexte du changement climatique global (L. Chen et al., 2024; Lu and Xiao, 2024; Salimi et al., 2021). La diminution des zones humides s'accompagne d'une dégradation des zones humides restantes, avec une modification de leur structure (composition, fragmentation…) et de leur fonctionnement (baisse de biodiversité, moindre efficacité pour le filtrage d'éléments polluants…)(Davis and Froend, 1999; Erwin, 2009; Ramsar Convention Secretariat, 2018).

Ces menaces sont d'autant plus problématiques que les zones humides exercent de nombreuses fonctions hydrologiques, biogéochimiques et écologiques qui sont sources de bénéfices pour les sociétés humaines, comme par exemple l'atténuation du débit de crue, la séquestration du carbone ou le support d'habitats pour la biodiversité (Maltby, 2018; Ramsar Convention Secretariat, 2018). Ainsi, la valeur des services rendus par les zones humides dans le monde dépasse de près de cinq fois celle de ceux rendus par les forêts tropicales (Ramsar Convention Secretariat, 2018). Ces services tendent à diminuer avec la réduction des surfaces en zones humides et leur dégradation, faisant planer des risques importants pour le bien-être et la santé des populations humaines à large échelle (Millennium Ecosystem Assessment, 2005). Par conséquent, il apparaît primordial d'effectuer un suivi des zones humides afin de décrire leurs dynamiques spatiotemporelles tant en termes de structure que de fonctions, et de caractériser leur état écologique (Strauch et al., 2022).

Le suivi des zones humides est défini dans cette thèse comme un moyen de produire des indicateurs spatiotemporels qui servent à caractériser leur évolution dans l'espace et sur le long terme. La forte variabilité des dynamiques spatio-temporelles des zones humides, notamment à une échelle spatiale fine, entraîne des difficultés pour effectuer un suivi régulier et caractériser ces écosystèmes en utilisant des approches uniquement basées sur l'observation et la mesure *in situ*, en particulier lorsqu'il s'agit de zones humides de grande dimension (Rebelo et al., 2017). La télédétection, qui permet d'obtenir des informations sur un objet à la surface terrestre depuis des capteurs placés sur des plateformes mobiles telles que des satellites ou des drones, pallie en grande partie ces difficultés, tout en économisant des moyens humains et financiers (Corbane et al., 2015; Vanden Borre et al., 2011). Elle a été particulièrement utilisée ces dernières décennies pour le suivi de zones humides (Mahdavi et al., 2018), en exploitant des images satellitaires optiques (e.g. C. Chen et al., 2024; Jie and Wang, 2024; Yang et al., 2020) et radar (e.g. Betbeder et al., 2015; Huang et al., 2024; Zhang et al., 2024), ou des images optiques acquises par drones (e.g. Doughty et al., 2021; Fu et al., 2024; Van Alphen et al., 2024). Cependant, les études utilisant ces données se sont en très grande majorité focalisées sur l'analyse d'une image à une seule date ou d'images acquises sur des périodes temporelles relativement courtes, préférant favoriser la résolution spatiale des images à la répétitivité de l'observation. Or, le suivi des zones humides sur le long terme (ici défini comme une période d'observation de plusieurs décennies) permet de décrire les dynamiques historiques de ces écosystèmes et d'identifier les facteurs de changements associés (Gallant, 2015).

La réalisation de suivis des zones humides sur le long terme est particulièrement importante d'une part pour déterminer les pressions qui s'exercent sur ces milieux et d'autre part pour mettre en place et évaluer les actions de conservation et de restauration (Ghoddousi et al., 2022; Gillespie et al., 2015). A l'échelle internationale, des objectifs de conservation et de restauration ont été définis afin de stabiliser et d'infléchir la dégradation de la biodiversité au sein de conventions et traités, à l'instar de la convention de Ramsar sur la conservation et l'usage raisonné des zones humides, la Convention on Biological Diversity (CBD) ou les Sustainable Development Goals (SDG) des Nations Unies (Chandra and Idrisova, 2011; Hák et al., 2016). Par exemple, la conservation et la restauration des zones humides fait partie intégrante de l'objectif SDG 6.6 (« *Protection and restoration of water-related ecosystems* »), tandis que les zones humides continentales sont explicitement citées parmi les habitats à conserver tels que définis dans les objectifs 1 (« *Ensure all land, inland water and sea areas globally are under integrated biodiveristy-inclusive spatial planning adressing land-, inland water- and sea-use change […]* ») et 3 (« *Ensure that at least 30 per cent globally of land, inland water and sea areas […] are conserved through […] systems of protected areas and other effective area-based conservation measures […]* ») du Post-2020 Global Biodiversity Framework de la CBD (Moberg et al., 2022; Yi et al., 2024). Dans ce contexte, si le nombre d'aires protégées ne cesse d'augmenter à l'échelle globale, il convient d'en effectuer le suivi et d'évaluer les pressions anthropiques qui s'y exercent afin d'estimer si les objectifs pour lesquels elles ont été créées ont été atteints (He and Wei, 2023). De même, les projets de restauration écologique des zones humides se multiplient, et il est nécessaire de décrire leur efficacité à partir d'indicateurs spatio-temporels fiables et pertinents afin d'adapter, si nécessaire, la gestion de ces écosystèmes (Liu and Ma, 2024).

Les archives d'images Landsat présentent un intérêt certain pour la réalisation de suivis de zones humides sur le temps long. En effet, il s'agit du plus long programme de données d'observation de la Terre couvrant la totalité du globe (Wulder et al., 2022). Initié en 1972, le programme Landsat a permis d'acquérir de façon continue depuis près de 50 ans des images de la surface de la Terre à haute résolution spatiale, qui ont été utilisées pour de nombreuses applications environnementales (Hemati et al., 2021; Ojima et al., 2022; Wulder et al., 2019). Ces données sont disponibles intégralement en accès ouvert et gratuit depuis 2008 (Wulder et al., 2012), favorisant l'intérêt scientifique porté à ces archives notamment vis-à-vis du suivi et de la caractérisation des zones humides (Mahdianpari et al., 2020). Les archives Landsat permettent d'avoir un recul temporel inédit pour effectuer le suivi de ces écosystèmes sur le long terme. Les méthodes d'analyse de ces séries temporelles sont nombreuses et se sont développées conjointement à celui de l'intelligence artificielle, en particulier du *machine* et du *deep learning* (DeLancey et al., 2020; Jafarzadeh et al., 2022). Dans ce contexte de *Big Data*, des méthodes récentes d'analyse continue des séries temporelles d'images ont été développées afin d'exploiter de façon optimale les séries temporelles d'images satellitaires. Ces méthodes, telles que *LandTrendR* (Kennedy et al., 2010), BFAST (Verbesselt et al., 2010), ou encore la *Continuous Change Detection and Classification* (CCDC) (Zhu and Woodcock, 2014) , offrent de nouvelles possibilités pour décrire les changements qui interviennent au sein des écosystèmes sur le long terme. La CCDC, qui a été développée pour exploiter les archives Landsat (Zhu and Woodcock, 2014), est l'une des méthodes les plus utilisées, permettant à la fois de produire des classifications d'habitats à la fréquence souhaitée sur l'ensemble de la période étudiée ainsi que de générer des images synthétiques sans nuages. Néanmoins, ces méthodes nécessitent une puissance de calcul importante et le téléchargement local des séries temporelles satellitaires peut constituer un frein à leur utilisation. Le développement récent de plateformes de *cloud-computing* a permis de faciliter l'accès à la fois aux données ainsi qu'aux algorithmes permettant de les analyser à travers l'accès à des calculateurs à distance, dont la plateforme *Google Earth Engine* (GEE) (Gorelick et al., 2017). L'implémentation récente de méthodes d'analyse continue telles que la CCDC (Arévalo et al., 2020) et LandTrendR (Kennedy et al., 2018) sur la plateforme GEE représente un potentiel important pour effectuer le suivi des zones humides sur le long terme à partir de séries temporelles d'images satellitaires (e.g. Fu et al., 2022).

C'est dans ce contexte que s'intègrent les travaux réalisés au cours de cette thèse et qui visent à évaluer l'apport des archives Landsat pour le suivi et la caractérisation des zones humides d'importance internationale Ramsar sur le long terme en appliquant une méthode d'analyse continue de séries temporelles d'images. La thèse est structurée en cinq chapitres.

Dans le premier chapitre, nous présentons un état de l'art de la littérature scientifique traitant de l'utilisation des archives Landsat pour le suivi à long terme des zones humides. L'objectif était de montrer comment les archives Landsat avaient été utilisées pour le suivi et la caractérisation des zones humides sur le long terme défini ici comme une période supérieure à 20 ans. Pour cela, nous avons effectué une méta-analyse de la littérature scientifique en sélectionnant des articles publiés depuis 2009, année de la mise à disposition gratuite et ouverte des archives Landsat par l'United States Geological Survey (USGS). Un total de 351 articles a été analysé selon une grille de lecture comportant 22 attributs répartis en cinq sujets traitants d'aspects thématiques (type de zone humide étudiée, localisation, période d'étude, …), techniques (produits Landsat utilisés, méthode d'analyse, données auxiliaires, …), et opérationnels (type de logiciel utilisé, utilisateurs finaux, …).

Les résultats ont montré que les archives Landsat en libre accès ont été utilisées pour effectuer des centaines d'études scientifiques sur le suivi à long terme des zones humides, et ce à travers le monde, en particulier dans les pays en développement où les gestionnaires disposent de ressources humaines et financières limitées. La continuité des missions Landsat depuis 1972 permet d'effectuer un suivi sur le long-terme des zones humides, de leur structure et de leurs fonctions, y compris de changements subtils qui auraient été difficiles à observer sur des périodes plus courtes et/ou à une résolution spatiale plus grossière.

D'un point de vie thématique, ces études ont permis de décrire les pressions anthropiques qui menacent les zones humides, en particulier l'intensification agricole et aquacole, l'urbanisation et l'industrialisation qui entraînent la disparition et la dégradation de ces milieux. Les pressions climatiques entraînent également une réduction des zones humides côtières en raison de la montée du niveau des océans, ainsi qu'une modification de leur régime hydrologique à travers les sécheresses par exemple. La méta-analyse que nous avons réalisée a montré qu'une forte proportion de zones humides dans le monde restait encore peu étudiée, telles que les zones humides boréales en Russie ou encore les zones humides continentales tropicales en Afrique.

D'un point de vue méthodologique, cet état de l'art a mis en évidence que bien que les progrès technologiques rendent les méthodes de traitement et d'analyse des données de télédétection basées sur l'intelligence artificielle (IA) de plus en plus puissantes et accessibles, un nombre important d'études sont encore menées en utilisant l'approche diachronique traditionnelle. Cette approche n'utilise généralement que deux ou trois images pour analyser l'évolution de l'occupation et de l'utilisation des sols, alors que les nouvelles méthodes d'analyse des séries temporelles utilisent de manière optimale les archives Landsat, car elles sont basées sur des approches continues. En particulier, plusieurs études ont démontré la valeur de la CCDC (Continuous Change Detection and Classification), qui peut être utilisée sur la plateforme informatique en nuage Google Earth Engine pour détecter les changements d'occupation des sols. Les progrès récents réalisés en intelligence artificielle et en apprentissage machine ont apporté de nouvelles perspectives d'analyse des archives Landsat, en particulier concernant l'analyse continue des séries temporelles satellites dans leur entièreté. Ces analyses peuvent à présent être réalisées sur des plateformes de *cloud-computing* qui permettent : (i) d'accéder directement aux archives Landsat sans besoin de les télécharger, (ii) d'utiliser des algorithmes implémentés sur des serveurs à distance sans nécessiter de ressources informatiques locales, et (iii) de couvrir de larges surfaces géographiques sur de longues périodes d'étude. De plus, cela ne limite plus la sélection d'images satellites uniquement à celles sans nuages comme cela est souvent le cas pour l'approche traditionnelle diachronique.

Ainsi, les recherches futures devraient porter sur l'étude approfondie de certaines régions ou de certains types de zones humides encore peu explorés, étendre la période de suivi, utiliser davantage les bases de données *in situ* d'archives pour mieux calibrer et valider les modèles, se concentrer sur la modélisation de profils temporels en utilisant la plupart des images disponibles dans les archives Landsat, établir des correspondances avec des cadres opérationnels communs tels que la procédure d'évaluation fonctionnelle ou les variables essentielles de la biodiversité, et combler le fossé entre les communautés scientifiques de l'environnement et de la télédétection.

La méta-analyse qua nous avons effectuée a permis de définir l'approche méthodologique développée au cours de la thèse, en favorisant l'utilisation d'algorithmes d'analyse de séries temporelles continues pour produire des indicateurs structurels et fonctionnels sur le long terme sur les zones humides en utilisant une plateforme de *cloud-computing*. Ce chapitre a fait l'objet de la publication suivante :

> Demarquet, Q., Rapinel, S., Dufour, S., Hubert-Moy, L., 2023. Long-Term Wetland Monitoring Using the Landsat Archive: A Review. *Remote Sensing* 15, 820. https://doi.org/10.3390/rs15030820

Dans le troisième chapitre, nous exposons la méthode d'analyse continue de séries temporelles que nous avons appliquée pour suivre le fonctionnement à long terme des zones humides à partir des archives Landsat. Plus précisément, la CCDC a été utilisée pour générer un indicateur fonctionnel des zones humides, à savoir le NDVI-I, qui est un indicateur de la productivité primaire annuelle nette. L'objectif poursuivi était double : (i) générer des images de synthèse à partir de régressions harmoniques appliquées aux séries temporelles Landsat, et (ii) tester la sensibilité de la méthode à des conditions d'occupation des sols contrastées et au nombre d'images Landsat utilisées afin d'évaluer la transférabilité de la méthode. Pour ce faire, nous avons mobilisé les archives Landsat sur la période 1984-2021 sur quatre sites Ramsar contrastés sélectionnés dans des régions boréale (Suède), tempérée (France), aride (Algérie) et tropicale (Brésil) et présentant des conditions contrastées d'occupation du sol et de couverture nuageuse.

Les résultats ont montré que la précision de l'indicateur NDVI-I est généralement constante dans le temps (1984-2021), mais pas dans l'espace, car elle est principalement influencée par le type d'occupation du sol et dans une moindre mesure par le nombre d'observations claires Landsat disponibles. Les variations inter et intra-sites des valeurs de NDVI-I sont élevées, mais montrent une tendance générale d'augmentation de la valeur du NDVI-I au cours du temps et sur le long terme, positivement corrélée avec les températures moyennes, ce qui coïncide avec le phénomène de « verdissement » global largement documenté dans la littérature et lié au changement climatique, en particulier dans les régions boréales. Cette étude montre que la méthode mise en œuvre pour le suivi à long terme du fonctionnement de l'écosystème des zones humides est robuste dans des conditions bioclimatiques contrastées.

L'approche que nous avons développée dans cette étude est basée sur l'utilisation d'un grand volume de données satellitaires et d'algorithmes en libre accès, ce qui en fait une approche facilement reproductible et utilisable pour améliorer le suivi et la gestion des zones humides sur le long terme, puisqu'elle prend en compte la dimension fonctionnement de ces écosystèmes.

Cette étude a fait l'objet de la publication suivante :

> Demarquet, Q., Rapinel, S., Arvor, D., Corgne, S., Hubert-Moy, L., 2024. Satellite Long-Term Monitoring of Wetland Ecosystem Functioning in Ramsar Sites for Their Sustainable Management. *Sustainability* 16, 6301. https://doi.org/10.3390/su16156301

Dans le chapitre 4, nous présentons l'application de l'algorithme CCDC pour étudier les changements de superficie et de composition des zones humides sur le long terme. Comme cela a été souligné dans l'état de l'art effectué dans le chapitre 1, l'analyse des archives Landsat peut être effectuée selon deux approches : l'approche diachronique et l'approche continue. Cependant, aucune comparaison n'avait encore été réalisée afin d'établir laquelle de ces deux approches était la plus performante pour la détection de changements sur une période de plusieurs décennies au sein des zones humides. Dans ce contexte, l'objectif de cette étude était de répondre à cette question en utilisant les archives Landsat. Nous avons ainsi appliqué l'approche diachronique (post-classification) et l'approche continue (CCDC) sur le site Ramsar du Marais Poitevin, la plus vaste zone humide du littoral atlantique français, afin de cartographier les changements intervenus au niveau des principaux types d'habitats au sein de cette zone humide entre 1984 et 2022. Puis, nous avons comparé la précision de détection des changements mis en évidence avec ces deux approches.

Plus précisément, un ensemble de données de référence a été collecté principalement à partir d'observations sur le terrain (relevés phytosociologiques, cartes d'habitats, observations LUCAS (*Land Use and Cover Area Frame Survey)*, Registre Parcellaire Graphique (RPG) ainsi que par photo-interprétation d'orthophotographies aériennes représentant un total de 4200 observations. La nomenclature d'habitats qui a été utilisée est la classification hiérarchique EUNIS (*European Nature Information System*) au niveau 1 (Davies et al., 2004), ce qui a nécessité une harmonisation des nomenclatures d'habitats et de LULC des différentes données de référence. Les classes EUNIS ont ensuite été regroupées en deux classes principales (*i.e.*, zones humides dégradées ou existantes, qui ont été fortement altérées ou protégées des activités humaines, respectivement) afin de décrire les changements au sein de la zone humide (Rapinel et al., 2018). Les données de référence ont été utilisées pour entraîner et valider un classificateur *Random Forest* (RF) fonctionnant directement sur la plateforme *Google Earth Engine*. L'évaluation de la précision des cartes d'habitats a été réalisée à partir des échantillons de validation n'ayant pas servi à entraîner le modèle RF, tandis que la validation des cartes de détection de changements a fait l'objet d'une validation supplémentaire telle que recommandée par Olofsson et al. (2014). Celle-ci est une estimation des précisions (utilisateurs – UA – et producteur – PA) ainsi que des surfaces non biaisées, *i.e.*, corrigée des erreurs inhérentes à la classification. Pour ce faire, un deuxième jeu de données différent du premier utilisé pour l'entraînement et la validation des modèles a été constitué. Un total de 326 échantillons a été généré (*i.e.*, 62, 54, 101, et 109 pour les classes de zone humide dégradée, zone humide restaurée, zone humide existante stable et zone humide dégradée stable, respectivement). Ces échantillons ont par la suite fait l'objet d'une validation par photo-interprétation d'images aériennes et satellitaires, et en utilisant le RPG, en plus de la visualisation des séries temporelles de NDVI grâce à l'API développée par Arévalo et al. (2020).

Les résultats ont montré que la carte des changements obtenue avec une approche continue (algorithme CCDC) avait une précision globale non biaisée beaucoup plus élevée (0,86 ± 0,02) que celle obtenue avec une approche diachronique traditionnelle basée sur une post-classification (0,51 ± 0,03). Cette différence de précision peut s'expliquer par le cumul des erreurs de classification issues de l'approche diachronique post-classification qui aboutit inévitablement à la détection de faux changements, ce qui entraîne une caractérisation inadéquate des changements pour des opérations de conservation des zones humides. La détection des changements par une approche continue a pour sa part permis d'éviter la plupart de ces erreurs de classification et de classer les profils temporels Landsat de l'ensemble de la période d'étude en utilisant toutes les images d'archives, y compris les images partiellement nuageuses et celles acquises par le capteur ETM+SLC-off. Un autre avantage de la détection continue des changements est qu'elle utilise le profil temporel de toute la période d'étude pour faire des prédictions pour les années sélectionnées (ici, 1984 et 2022) en utilisant des données de référence asynchrones. Ainsi, toutes les données de référence collectées au cours de la période d'étude (2000-2010) ont été utilisées pour classer les zones humides avant (1984) et après (2022) la collecte de ces données.

Sur un plan thématique, l'analyse des résultats de cette étude a montré que la perte de zones humides était beaucoup plus importante que le gain de zones humides (18 % et 2 % de la zone, respectivement) et que cette perte était principalement due à la conversion des prairies en terres cultivées et à l'urbanisation. Ces résultats sont en accord avec ceux d'études antérieures qui ont mis en évidence la dégradation de l'état des zones humides dans le Marais Poitevin en raison de la conversion des prairies en terres cultivées (Duncan et al., 1999 ; Godet et Thomas, 2013) et de l'urbanisation croissante de la zone littorale (Pouzet et al., 2015) depuis 1950.

Cette approche continue de détection de changements pourrait ainsi être reprise d'un point de vue opérationnel par les décideurs politiques et gestionnaires pour le suivi des zones humides Ramsar et la mise en œuvre de mesures de gestion et de conservation appropriées. Cette étude a fait l'objet de la publication suivante :

> Demarquet, Q., Rapinel, S., Gore, O., Dufour, S., Hubert-Moy, L., 2024. Continuous change detection outperforms traditional post-classification change detection for long-term monitoring of wetlands. *International Journal of Applied Earth Observation and Geoinformation* 133, 104142. https://doi.org/10.1016/j.jag.2024.104142

Une quatrième étude (chapitre 5) présente l'utilisation des cartes d'habitats EUNIS produites sur le Marais Poitevin dans le cadre du chapitre précédent pour l'évaluation de l'efficacité des politiques agro-environnementales et de la création d'aires protégées pour la conservation des prairies. Les prairies semi-naturelles représentent un fort enjeu de conservation à l'échelle du site, car elles ont été fortement dégradées au cours de ces dernières décennies, et ce malgré leur importance pour le maintien de la biodiversité et pour les services écosystémiques qu'elles procurent. Face à ces dégradations, deux stratégies de politiques de conservation ont été mises en place sur le site : la création d'aires protégées et des mesures agro-environnementales. La première, largement appliquée dans le monde depuis les années 1950, vise à conserver les écosystèmes à travers l'application d'un cadre légal ou contractuel sur un espace géographique défini avec la mise en place d'un plan de gestion. La seconde, mise en œuvre à partir des années 1990, a pour objectif de développer des pratiques agricoles respectueuses de l'environnement sur la base du volontariat et d'incitations financières. Cependant, l'efficacité de ces deux stratégies nécessite d'être évaluée afin de les adapter pour une conservation optimale, ce qui représente un défi méthodologique.

Grâce à leur importante couverture spatiale et leur fréquence d'observation, les données de télédétection satellitaires ou des produits qui en sont issus ont fréquemment été utilisées pour évaluer l'efficacité d'aires protégées. Jusqu'à présent, ce sont surtout les produits Corine Land Cover (mis à jour tous les 6/10 ans en moyenne depuis 1990 avec une résolution spatiale de 100 mètres), les produits LULC MODIS (fréquence quotidienne avec une résolution spatiale de 500 mètres), ou encore les données à haute résolution spatiale telles que les images Landsat ou SPOT (fréquence quasi-mensuelle avec une résolution de 20-30 mètres) qui ont été utilisés. Or, s'ils permettent d'étudier les zones humides sur une période longue, les observations sont effectuées soit de façon grossière spatialement soit de façon discontinue temporellement. Dans ce contexte, l'objectif de cette étude était de tester l'intérêt de l'utilisation des cartes d'habitats obtenues à partir de l'application de la CCDC sur les archives Landsat pour évaluer l'efficacité de politiques de conservation, ce qui n'avait, à notre connaissance, jamais été réalisé.

Nous avons compilé les données géographiques sur le Marais Poitevin relatives aux aires protégées (*i.e.*, Natura 2000, réserves naturelles, périmètres d'acquisition foncière des Conservatoires) et aux mesures agro-environnementales, *via* la base de données internationale *Protected Planet* et les gestionnaires locaux, respectivement. Des cartes d'habitats pour les prairies et les cultures ont été générées annuellement entre 1984 et 2022, à 30 mètres de résolution spatiale, en appliquant la CCDC. Puis, une série d'évènements chronologiques clés ayant *a priori* un effet sur les dynamiques à long terme des prairies et des cultures a été définie.

Les résultats montrent un effet d'anticipation de la réforme de la Politique Agricole Commune (PAC) européenne de 1992, qui a entraîné une importante conversion des prairies en cultures vers la fin des années 1980. C'est à notre connaissance la première fois que l'effet d'anticipation de cette réforme est montré sur une zone humide à dominante prairiale. Les aires protégées ont eu pour effet de stabiliser les dynamiques des prairies sur le long terme, bien qu'elles aient été créées sur des zones déjà peu sujettes aux pressions anthropiques. Les mesures agro-environnementales, quant à elles, ont eu pour effet d'augmenter les surfaces en prairies sur les parcelles agricoles contractualisées, bien qu'elles ne concernent qu'une faible proportion du site d'étude. Ainsi, cette étude montre que, malgré des objectifs et mises en œuvre différentes, ces deux types de politiques de conservation sont complémentaires. Pour les décideurs politiques, le suivi continu des dynamiques spatiotemporelles de la structure d'un écosystème prairial constitue un outil intéressant d'évaluation de l'efficacité des politiques de conservation mises en place depuis plusieurs décennies.

Cette étude fait l'objet de l'article suivant :

> Demarquet, Q., Gore, O., Rapinel, S., Hubert-Moy, L., Dufour, S. (Soumis). Evaluating the effectiveness of agri-environmental and protected area policies for grassland conservation using continuous long-term satellite monitoring: A case study in the Poitevin marsh (France). *Applied Geography.*

Nous avons ainsi répondu à l'objectif principal de cette thèse qui était d'évaluer l'apport des archives Landsat pour le suivi et la caractérisation des zones humides d'importance internationale Ramsar sur le long terme en appliquant une méthode d'analyse continue de séries temporelles, en l'occurrence la CCDC. Les résultats obtenus nous ont permis de soulever un certain nombre de questions et limites.

D'un point de vue méthodologique, nous avons montré l'intérêt de l'analyse continue des archives Landsat pour le suivi et la caractérisation des zones humides sur le long terme. La revue de la littérature présentée dans le chapitre 1 a mis en évidence l'utilisation jusqu'ici limitée des approches d'analyse de séries temporelles continues, parmi lesquelles la CCDC, au profit des approches diachroniques traditionnelles utilisant quelques images exemptes de nuages. Cependant, la CCDC, qui utilise toutes les images des archives Landsat, y compris celles qui sont couvertes par des nuages, présente deux avantages particulièrement intéressants : (1) la classification de segments temporels, qui permet de détecter avec précision les changements dans la structure des zones humides, et (2) la production d'images synthétiques, qui permet de dériver des indicateurs fonctionnels.

Dans les études présentées dans cette thèse, des indicateurs de la structure et de la superficie des zones humides ont été générés en continu à partir de la CCDC en classant des segments temporels. Par rapport aux méthodes traditionnelles, la CCDC a l'avantage d'utiliser toutes les images contenues dans les archives Landsat pendant la période d'étude, y compris celles ayant une forte couverture nuageuse et/ou présentant des bandes SLC-Off du capteur ETM+, ce qui permet de suivre la dynamique spatio-temporelle des zones humides de manière plus détaillée. Les indicateurs de structure et de superficie des zones humides que nous avons dérivés couvrent une large période (environ quarante ans) avec une fréquence de mise à jour élevée (annuelle). Ces caractéristiques expliquent l'intérêt suscité par la CCDC, notamment pour le suivi des écosystèmes forestiers (Chen et al., 2021) ou des zones humides (Yang et al., 2022). Par ailleurs, nous avons mis en évidence les avantages de la CCDC par rapport à une méthode diachronique traditionnelle basée sur une post-classification, encore largement utilisée, les cartes de détection de changement produites à partir de la CCDC ayant montré une meilleure précision.

De manière générale, la qualité des classifications dépend fortement de la disponibilité de données de référence de qualité (Friedl et al., 2022). L'accès à ces données, qui est essentiel pour l'entraînement et la validation des modèles de classification, est souvent difficile, surtout avant les années 2000. L'algorithme CCDC présente l'avantage d'être asynchrone entre l'année d'acquisition des données de référence et celle de l'indicateur produit par la classification des segments temporels. Il permet ainsi de s'affranchir de la contrainte de disponibilité de données de référence « historiques » (antérieures aux années 2000), ce qui nous a permis de détecter des changements dans les habitats naturels du Marais poitevin depuis 1984. La qualité de la classification de la CCDC dépend également de son paramétrage, qui a jusqu'à présent été peu étudié et décrit dans la littérature. Plusieurs études rapportent que la CCDC a été paramétrée soit par hyper-tuning (e.g. Yang et al., 2022), soit en ajustant les paramètres selon l'avis d'experts (e.g. Awty-Carroll et al., 2019). La seconde option a été appliquée dans cette thèse, en modifiant la valeur par défaut de certains paramètres proposés dans l'API (Arévalo et al., 2020). Ainsi, à ce jour, il n'y a pas de consensus sur la manière de paramétrer la CCDC de façon optimale. Comme la détection des ruptures est fortement dépendante de plusieurs paramètres tels que le *ChiSquareProbability* ou le nombre minimum d'observations consécutives *minObs*, il est possible de rendre la CCDC plus ou moins sensible à la détection du changement (Pasquarella et al., 2022).

L'application de la CCDC aux séries temporelles Landsat nécessite une puissance de calcul élevée (Zhu et Woodcock, 2014a) mais aussi l'accès aux centaines d'images contenues dans les archives, ce qui requiert beaucoup de ressources informatiques. Sa récente implémentation en *cloud-computing* à travers une API développée par Arévalo et al. (2020) et le dépôt des archives Landsat sur la plateforme *Google Earth Engine* permettent de s'affranchir de ces contraintes. Pour les besoins de cette thèse, le code source de l'API a été modifié en ajoutant deux fonctionnalités : (i) l'intégration des images du satellite Landsat 9, et (ii) la possibilité de sélectionner une zone d'étude en important directement une couche SIG dans GEE.

Cette thèse souligne également la contribution des archives Landsat analysées par la CCDC pour la production de variables essentielles de biodiversité (EBVs) (Pereira et al., 2013 ; Skidmore et al., 2021). Les cartes des habitats naturels et de la productivité primaire annuelle nette générées correspondent respectivement aux EBVs « distribution des écosystèmes » et « productivité primaire ». Ce travail de cartographie a notamment été présenté lors d'une conférence internationale (Demarquet et al., 2023).

D'un point de vue thématique, les résultats décrits dans cette thèse apportent deux éléments nouveaux. Tout d'abord, nous avons décrit et mis en évidence les tendances et les changements dans les zones humides de façon continue. Par rapport aux changements observés via des approches diachroniques traditionnelles, les dynamiques des zones humides mises en évidence par une approche continue apportent un éclairage nouveau grâce à la fréquence élevée de mise à jour (décennale et annuelle) des indicateurs produits. D'autre part, la production d'un indicateur fonctionnel (productivité primaire annuelle nette) sur le long terme et à haute résolution spatiale, jusqu'alors limité en termes de résolution spatiale et/ou de période de suivi, permet de mieux évaluer l'état de conservation des zones humides. Nous avons également identifié trois limites à la surveillance des zones humides avec la CCDC à partir d'images issues des archives Landsat. Deux limites sont dues aux caractéristiques des images Landsat elles-mêmes : (i) la résolution spatiale des images ne permet pas de distinguer les habitats linéaires des habitats distribués en petits patchs, et (ii) la résolution spectrale des images (les satellites Landsat-5/7 étant limités à 6 bandes contre 8 pour les satellites Landsat-8/9) ne permet pas de distinguer les habitats ayant une physionomie similaire. Une troisième limite est due au mode de fonctionnement de la CCDC, qui est plus adaptée à la détection de changements d'habitats abrupts (par exemple la transformation d'une prairie en terre arable) que de changements subtils (par exemple la fermeture progressive d'une prairie vers d'autres habitats avec le développement d'espèces arbustives et arborescentes).

Nous avons également montré que la description continue des caractéristiques des zones humides au cours du temps peut être utilisée pour évaluer l'efficacité des politiques publiques de conservation, sur la base de l'exemple du Marais Poitevin.

D'un point de vue temporel, le suivi à long terme fournit un aperçu intéressant de la dynamique des zones humides avant et après la mise en œuvre d'une politique publique. D'un point de vue spatial, la haute résolution spatiale (30 m) des indicateurs a permis, par exemple, de comparer l'intérieur et l'extérieur des zones protégées. Cependant, cela n'aurait pas été possible avec une approche diachronique, encore utilisée dans la majorité des études (e.g. Huang et al., 2019 ; Jia et al., 2016 ; Leberger et al., 2020).

Plus généralement, cette thèse met en évidence le fait que, bien que les politiques agro-environnementales et les politiques de création d'aires protégées aient des objectifs et des méthodes d'application différents, elles sont complémentaires lorsqu'il s'agit de conserver les prairies. La mise en œuvre de la première réforme de la PAC en 1992 a conduit à une baisse significative de la conversion des prairies en cultures dans le marais poitevin. Les MAE proposées aux agriculteurs dans les années 2000 ont permis de reconquérir des surfaces en herbe, même à l'issue des périodes contractuelles. Quant aux zones protégées, leur création a permis de stabiliser les surfaces en herbe. La principale limite de cette analyse est qu'elle ne permet pas d'établir un lien de causalité direct entre la mise en œuvre d'une politique publique donnée et son effet sur la conservation des prairies. En effet, les dynamiques spatio-temporelles d'un écosystème sont liées à un ensemble de facteurs socio-démographiques et économiques à plusieurs échelles, nécessitant l'acquisition de données et des analyses complémentaires.

Malgré ces limites, l'utilisation de l'algorithme CCDC combinée aux archives Landsat permet un suivi standardisé (*i.e.*, même source de données, même méthode, même résolution spatio-temporelle, et couverture exhaustive) de la structure et des fonctions zones humides, ce qui est essentiel pour connaitre leurs tendances (Skidmore et al., 2021). Pour les gestionnaires, cette approche de suivi continu est utile pour évaluer les effets de leurs plans de gestion vis-à-vis des pressions anthropiques et climatiques (Lu and Xiao, 2024; Salimi et al., 2021). Ce suivi standardisé peut également contribuer aux rapportages de conventions internationales, comme par exemples la convention de Ramsar ou encore la Directive européenne Habitats-Faune-Flore pour lesquelles les Etats signataires doivent renseigner l'évolution de leurs écosystèmes à intervalle régulier, ceci dans le but d'évaluer l'efficacité des mesures de conservation priss (Davidson et al., 2019; Delbosc et al., 2021). Bien que les approches terrain soient indispensables pour de tels suivis, les différences induites par l'utilisation de divers types de données et de méthodologies rendent la comparaison spatiotemporelle difficile. Ainsi, l'approche utilisée dans nos travaux peut aider à lever ce verrou, notamment grâce à sa disponibilité sur *Google Earth Engine*. En effet, l'API développée par Arévalo et al. (2020) permet une utilisation intuitive grâce à son interface graphique, combinée à l'accès ouvert des archives Landsat dans un format standardisé et déjà prétraité. En ce sens, cette approche peut être mobilisée par des gestionnaires et décideurs, et ce quelles que soient les ressources informatiques en leur possession.

Plusieurs perspectives de recherches sont ressorties des travaux de cette thèse. D'un point de vue méthodologique, la première serait d'ajouter d'autres sources d'images pour effectuer la classification avec la CCDC. Par exemple, l'ajout d'images Landsat MSS permettrait de remonter encore plus loin dans le passé (1972), ce qui serait très intéressant au vu des fortes pressions agricoles qui ont affecté les zones humides dans les années 1970. De plus, l'ajout d'images issues de l'archive ouverte SPOT World Heritage (Nosavan et al., 2018) qui contient des images SPOT acquises entre 1986 et 2015 à une résolution spatiale de 20 m, permettrait d'augmenter significativement le nombre d'observations claires et ainsi d'améliorer la qualité de l'interpolation temporelle réalisée par la CCDC. Cependant, l'ajout de ces images Landsat MSS ou SPOT, qui ont des caractéristiques spatiales et spectrales différentes des autres capteurs Landsat, nécessite une étape d'harmonisation préalable. Une deuxième perspective méthodologique serait d'améliorer le masque de nuages appliqué à chaque image durant l'application de la CCDC pour ne retenir que les pixels clairs. En effet, la méthode de détection des nuages mise en œuvre a tendance à masquer à tort les surfaces d'eau (Foga et al., 2017 ; Zhu et Woodcock, 2014b) qui ont une réponse spectrale similaire à celle des ombres portées. Une troisième perspective méthodologique consisterait à comparer la CCDC avec des méthodes alternatives qui améliorent notamment la détection de changements plus subtils. Par exemple, la méthode DECODE (*Detection and Characterisation of Coastal Tidal Wetland Change*) a été développée pour mieux prendre en compte les changements survenant dans les zones humides côtières, et notamment les marées (Yang et al., 2022). Ye et al. (2023) ont quant à eux développé l'algorithme OB-COLD pour *Object-Based Continuous Monitoring of Land Disturbance*, qui ajoute une composante de segmentation spatiale pour reconnaître les perturbations. D'autres solutions ont été développées pour l'analyse continue de séries temporelles satellitaires, telles que des approches par apprentissage profond (*e.g.*, Ji et al., 2024). Cependant, à notre connaissance, il n'existe pas encore d'applications graphiques qui facilitent leur utilisation sur les plateformes de *cloud-computing*, ce qui limite leur utilisation aux chercheurs ayant de solides compétences en programmation et des ressources informatiques importantes.

D'un point de vue thématique, une évaluation plus approfondie de l'efficacité de chaque politique de conservation pourrait être effectuée en combinant des indicateurs dérivés de données de télédétection et des observations sur le terrain. Si le suivi des prairies issu de l'analyse des données de télédétection est très utile pour évaluer l'efficacité des zones protégées, d'autres indicateurs issus d'observations *in situ* (enquêtes sur les espèces invasives, comptage des oiseaux nicheurs) ou de diagnostics socio-économiques (entretiens avec les parties prenantes, etc.) sont tout aussi pertinents. De plus, des efforts sont nécessaires pour transférer l'approche développée dans cette thèse aux gestionnaires et décideurs politiques (Pettorelli et al., 2014) afin d'améliorer et de gérer plus efficacement les zones humides.

COLLEGE DOCTORAL BRETAGNE — ESPACES SOCIETES CIVILISATIONS

Titre : Suivi sur le long terme des zones humides Ramsar à partir des archives Landsat

Mots clés : Télédétection, Ecologie, Calcul dans le cloud, Séries temporelles

Résumé : Alors que les zones humides fournissent un grand nombre de services écosystémiques, elles sont fortement menacées au niveau mondial par les activités humaines. Dans ce contexte, cette thèse vise à évaluer l'apport des séries temporelles satellite Landsat enregistrées depuis près de 50 ans afin d'effectuer un suivi des dynamiques structurelles et fonctionnelles des zones humides sur le long terme. L'état de l'art montre que les archives Landsat en libre accès représentent une source pertinente pour l'évaluation des zones humides notamment grâce aux progrès récents en matière d'intelligence artificielle et d'outils en *cloud-computing* qui ouvrent de nouvelles perspectives d'analyse. En particulier, la méthode *Continuous Change Detection and Classification* (CCDC) permet de produire des séries temporelles continues et de classer des profils temporels en utilisant la plateforme *Google Earth Engine*. L'utilisation de la CCDC dans 4 sites Ramsar permet de produire un indicateur du fonctionnement de la zone humide même pour des sites présentant des caractéristiques très contrastées. De plus, la CCDC donne de meilleurs résultats que la méthode de détection de changements diachronique traditionnelle pour le suivi sur 40 ans de l'évolution d'une zone humide littorale atlantique Ramsar (Marais Poitevin). L'utilisation de cette méthode montre que la réduction des zones humides est principalement due au retournement des prairies naturelles en cultures et à l'urbanisation. Enfin, elle permet de décrire l'évolution annuelle des pressions anthropiques sur ce même site entre 1984 et 2022, ce qui présente un intérêt pour évaluer l'efficacité des politiques publiques en matière de conservation. Cette thèse montre ainsi que l'analyse en *cloud-computing* de l'ensemble des archives Landsat avec de nouvelles méthodes d'analyse de profils temporels ouvre de nouvelles perspectives pour le suivi des zones humides, tant d'un point de vue scientifique qu'opérationnel.

Title: Long-term monitoring of Ramsar wetlands using the Landsat archive

Keywords: Remote sensing, Ecology, Cloud-computing, Time series

Abstract: Although wetlands provide a large number of ecosystem services, they are under serious threat worldwide from human activities. In this context, this thesis aims to assess the contribution of Landsat satellite time series recorded over almost 50 years to monitor the structural and functional dynamics of wetlands over the long term. The state of the art shows that open-access Landsat archives are a relevant source for assessing wetlands, thanks in particular to recent advances in artificial intelligence and cloud-computing tools, which open up new analytical perspectives. In particular, the Continuous Change Detection and Classification (CCDC) method can produce continuous time series and classify temporal profiles using the Google Earth Engine platform. The use of CCDC in 4 Ramsar sites makes it possible to produce an indicator of wetland functioning even for sites with very contrasting characteristics. In addition, the CCDC gives better results than the traditional diachronic change detection method for monitoring the evolution of an Atlantic coastal Ramsar wetland (Marais Poitevin) over 40 years. This method shows that the reduction in wetlands is mainly due to the conversion of natural grasslands to crops and urbanisation. Finally, it allows us to describe the annual change in anthropogenic pressures on this same site between 1984 and 2022, which is of interest for assessing the effectiveness of public policies in terms of conservation. This thesis shows that cloud-computing analysis of all Landsat archives using new methods for analysing temporal profiles opens up new prospects for monitoring wetlands, from both a scientific and operational point of view.